DEUTSCHES ELEKTRONEN-SYNCHROTRON
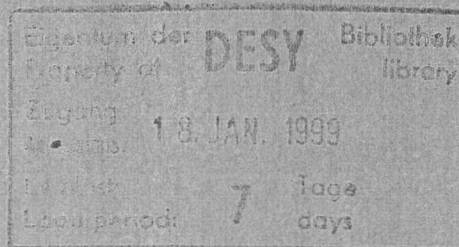
Measurement of the Strong Coupling Constant α_s from Jet Rates Using the $K_\perp$ Jet Algorithm at ZEUS

by

S. Eisenhardt

NOTKESTRASSE 85 - 22607 HAMBURG

To be sure that your reports and preprints are promptly included in the
HEP literature database
send them to (if possible by air mail):

DESY	DESY
Zentralbibliothek	Bibliothek
Notkestraße 85	Platanenallee 6
22603 Hamburg	15738 Zeuthen
Germany	Germany

Measurement of
the Strong Coupling Constant α_s
from Jet Rates using the $K_\perp$ Jet Algorithm
at ZEUS

INAUGURALDISSERTATION
zur Erlangung des Doktorgrades
der Fakultät für Physik
der
Albert-Ludwigs-Universität Freiburg i. Br.

vorgelegt von
Stephan Eisenhardt
aus Göttingen

Freiburg i. Br.
Dezember 1998

Measurement of
the Strong Coupling Constant α_s
from Jet Rates using the $K_\perp$ Jet Algorithm
at ZEUS

Abstract

The strong coupling constant α_s has been determined using the exclusive (2+1)-jet rate, R_{2+1}, in deep inelastic scattering data measured with the ZEUS detector at HERA. The $K_\perp$ jet finding algorithm has been used to identify the jets. The analysis was performed on the 1995 and 1996 data samples in the kinematic range of $44\,\mathrm{GeV}^2 < Q^2 < 3600\,\mathrm{GeV}^2$ in six bins of Q^2. The result obtained from the 1995 data in the full phase space of this analysis reads: $\alpha_s(M_z^2) = 0.1251 \pm 0.0012\,(\mathrm{stat})\,^{+0.010}_{-0.013}\,(\mathrm{syst})$, well in agreement with the current world average value. The data strongly favor the running of α_s as compared to the assumption of a constant α_s. Results are presented also for the determination of α_s from the exclusive (2+1)-jet cross section, $\sigma^{(2+1)}$, and the differential jet rate, D_2.

Contents

List of Figures

List of Tables

Chapter 1

Introduction

"What is the matter made of?" is simultaneously a very simple and fundamental question which generations of scientists have worked on. The general idea is to understand the matter from its building blocks and the interactions between them. With a tremendous experimental and theoretical effort since the beginning of the century the *Standard Model* of elementary particles has been developed from underlying symmetries and basic principles. It has been extremely successful in the description of the behavior of nature so far. No significant contradiction has been found up to today.

In the Standard Model the matter is described as consisting of the fermions *leptons* and *quarks*. The interactions between them are mediated by *gauge fields* via *gauge bosons*. In this framework the electromagnetic interaction is described by a quantized and renormalized gauge field theory, the *quantum electrodynamics* (QED). It was unified with the weak interaction in the *electroweak theory*. For the strong interaction, the *quantum chromodynamics* (QCD) has been developed in analogy.

But the Standard Model leaves open questions. It makes no prediction on the strength of the interactions or the mass of the constituents. They have to be measured. The question where the mass of the constituents arises from is predicted to be solved by the Higgs-mechanism which is still lacking experimental verification. Furthermore the Standard Model makes no prediction regarding very fundamental questions. Some of these are: Why are there only exactly three families of leptons and quarks in nature as it was experimentally concluded from results from the LEP collider at CERN? Are leptons and quarks really the fundamental particles or do they reveal a substructure? Is there a more general symmetry between fermions and bosons, known as supersymmetry?

Deep inelastic lepton-nucleon scattering (DIS) experiments have played a crucial role in the understanding of hadronic matter. Early fixed target scattering experiments at SLAC, followed by a series of other fixed target experiments, established the constituent structure of the proton. Together with the observation of the Bjorken scaling, this was first explained by the Quark-Parton model. The later observation of the scaling violations contributed to the development of the field theory of the strong interaction, the quantum chromodynamics. The first direct experimental confirmation of the QCD was found at the e^+e^- collider PETRA at DESY in 1979: the discovery of the *gluon* which mediates the strong interaction between the quarks. The strength of the coupling between the gluons and quarks is described by the *strong coupling constant* α_s which is, together with the quark masses, the only free parameter of QCD. A measurement of α_s, therefore, is a crucial test of the theory.

The first measurement of the strong coupling constant α_s was done in lepton scattering on nucleon targets at rest. Up to today a series of measurements of the strong coupling constant α_s was performed using different methods and various experiments (cf. table 2.4).

1

Nevertheless α_s is still the fundamental parameter of the Standard Model with the least accuracy (cf. table 2.3).

The ep-collider HERA, which started operation in 1992, opened a new kinematic window for lepton-nucleon scattering. With nominal beam energies of 27.5 GeV for the electrons and 820 GeV for the protons the maximum center of mass energy is $\sqrt{s} = 300$ GeV.

In fact, QCD predicts the strong coupling constant to be dependent on the scale of a reaction. At HERA a natural choice for this scale is the squared 4-momentum transfer, Q^2, so that α_s has to be measured at different values of Q^2, i.e. as $\alpha_s(Q^2)$. In pre-HERA physics the measurements were performed mostly at a fixed momentum transfer. An overall view concerning the scale dependence of α_s always introduced the difficult treatment of different systematic uncertainties of the various experiments involved. HERA now allows to measure physical observables from $Q^2 \approx 0$ GeV^2 up to, theoretically, $Q^2 \approx 90,000$ GeV^2 in one experiment. In this analysis α_s is determined from the jet rate of the hadronic final state in DIS in the range of $44 < Q^2 < 3,600$ GeV^2 using the HERA data collected with the ZEUS detector in the years 1995 and 1996 which corresponds to an integrated luminosity of $\mathcal{L}_{95} = 6.3$ pb^{-1} and $\mathcal{L}_{96} = 8.2$ pb^{-1}, respectively.

This thesis is organized as follows:

The second chapter gives a brief introduction to the main features of the Standard Model and QCD. The predictions for the coupling constant α_s made by QCD are discussed and it is referred to the measurements made of α_s within the last 25 years.

In the third chapter the experimental environment used for this analysis, the collider HERA and the ZEUS detector, is described.

In chapter four the domain of deep inelastic scattering is described. The kinematic variables and their reconstruction methods are defined and the description in terms of the fundamental partonic processes as well as in terms of structure functions is introduced.

Chapter five shows the different possible approaches to measure α_s at HERA. Particular emphasis is put on the methods using jets.

The status of the jet-cross section calculations in DIS is described in chapter six.

In chapter seven the concept of a jet is introduced by means of the picture of a full scattering process and the properties of the relevant jet finding algorithms are discussed.

The Monte Carlo models needed to relate the measured quantities to the predictions are introduced in chapter eight.

Chapter nine describes the analysis performed in this thesis. The structure of the analysis and the event selection are explained and the raw data are presented.

The detailed way, along which α_s is determined from the obtained data samples, is shown in chapter ten. The results of the α_s-determination are given for different approaches and data sets.

In chapter eleven the systematic studies are presented as well as details of the jet finding are investigated and the most suitable combination of Monte Carlo models for this analysis is selected.

The results are discussed together with the systematic checks carried out in chapter twelve.

A summary is finally given in chapter thirteen.

Chapter 2

The Strong Coupling Constant α_s

2.1   The Standard Model and QCD

In the Standard Model the elementary particles are spin $\frac{1}{2}$ *fermions* which appear as states and their anti-states connected by the exchange of all multiplicative quantum numbers. The states split up into two classes: six *flavors* of *quarks* and six *flavors* of *leptons*. The particles are grouped into three *generations* with equal properties but increasing mass. The integer spin *bosons* mediate the interactions between the particles and couple only to those particles which have the corresponding strong, electric or weak *charge*[1]. So, the quarks interact strongly and the leptons do not. Only the electrically charged ones interact electromagnetically and all particles interact weakly. See tables 2.1 and 2.2 for a summary of the fermion and boson properties, respectively. Of the fermions, only the ν_τ has not been observed directly in experiments so far. In addition, the spin 0 *Higgs boson* is predicted with the role of solving the problem of mass generation.

fermions	generation			el. charge	color charge	conservation numbers
	1	2	3			
leptons	ν_e	ν_μ	ν_τ	0		$L_e, L_\mu, L_\tau = 1$
	e	μ	τ	-1		
quarks	u	c	t	$+2/3$	red, green ,blue	$B = +1/3$
	d	s	b	$-1/3$		

Table 2.1: *Properties of fermions.*

interaction	gauge boson(s)	boson mass (mc^2)	dim-less coupling constant (M = nucleon mass)
strong interaction	8 gluons (g)	0	$\alpha_s = \frac{g^2}{4\pi} \sim 1$
elmag. interaction	photon (γ)	0	$\alpha_{em} = \frac{e^2}{4\pi\hbar c} \approx \frac{1}{137}$
weak interaction	$W^\pm, Z^0$	80.4, 91.3 GeV	$\frac{(Mc/\hbar)^2 G_F}{\hbar c} = 1.02 \times 10^{-5}$
gravitation	graviton (G)	0	$\frac{KM^2}{\hbar c} = 0.53 \times 10^{-38}$

Table 2.2: *Properties of bosons.*

Only the weak interaction can cause reactions where the flavor of a particle is changed. The exchanged bosons ($W^\pm$) in this case carry electric charge. Therefore, the process is

---
[1] The gravitation, even weaker than this by many orders of magnitude, is neglected in this picture.

called a *charged current* (CC) interaction. Non-flavor changing reactions are mediated by the weak (Z^0) as well as by the electromagnetic interaction (γ). These are electrical *neutral current* (NC) interactions. The electromagnetic interaction is described by a quantized and renormalized gauge field theory, the *quantum electrodynamics* (QED). It turns out that the electromagnetic and weak interaction can be described uniformly as the *electroweak* interaction. To achieve this uniform description the two neutral fields have to mix to give the physical states of the observed exchange bosons. The mixture can be described by only one *weak mixing angle* Θ_W, also called *Weinberg angle*.

To describe the strong interaction, a gauge field theory has been developed in analogy to QED which is also quantized and renormalizable: the *quantum chromodynamics* (QCD). Here the basic exchange between the *color* charges of the quarks is similar to the photon exchange of charged particles. But a fundamental difference is that there are three strong charges (and anti-charges), generally called red-green-blue (rgb and $\bar{r}\bar{g}\bar{b}$).

Mathematically the transformation between the strong charge states is described by the $SU(3)_C$ group. It gives eight linearly independent 3×3 hermitian matrices, the *color octet* state, and one *color singlet*, i.e. neutral, state. The eight matrices represent the eight gluons which mediate the strong interaction by exchanging the color charge. Since the gluons carry a color charge themselves they can interact with each other in a triple gluon vertex, in contrast to photons which cannot since they do not carry the electric charge[2]. A theory with self-coupling bosons is called *non-Abelian*.

In fact, in nature bound states of quarks are found only as color singlets, i.e. only colorless bound states are observed. This is accomplished by the two solely found configurations: *hadrons* formed from three (anti-)quarks ($q_r q_g q_b$) and *mesons* formed of quark-antiquark pairs ($q_c \bar{q}_{\bar{c}}$).

No color charge has been measured directly. It is an internal degree of freedom of the quarks only established through its consequences to the behavior of the interaction. The color degree of freedom also solves the problem of totally symmetric ground states of hadrons made of three quarks where they can be distinguished only by color, causing the total wave function to become asymmetric again in agreement with Fermi statistics.

The self-coupling of the gluons has substantial consequences. The coupling of electric charges becomes small at large distances, i.e. by using low-energy probes, and it increases with smaller distances, i.e. at higher energies. This is caused by vacuum polarization around the charges acting like in a dielectric medium, effectively reducing their visible charge with growing distance. This effect is called *screening*. The additional self-coupling of gluons turns this into an *anti-screening* for the strong interaction. By vacuum polarization, strong charges are surrounded predominantly by equal charges and the coupling is measured to be stronger at larger distances. In turn, at high momentum transfers, or small testing distances, the strong coupling decreases and the behavior is almost like for free particles. This is referred to as *asymptotic freedom*.

A second major consequence of the self-coupling by the gluons is the *quark confinement*. Two separated quarks form a color field between each other. Due to anti-screening the field energy increases with rising distance. And due to the self-coupling the field lines group into a tube-like *string* with almost constant field density per unit length, rather than spreading out as a Coulomb field does. With further increase of the distance the field energy grows up to a point where it becomes energetically favorable to produce the mass of an additional $q\bar{q}$ pair, providing the energy by cutting the long string into two shorter ones. This happens at a distance of about 1 fermi where α_s becomes $\simeq 1$. This is the reason why quarks are not

---

[2]$W^{\pm}$ and Z^0 also carry weak charge, but self-coupling is highly suppressed due to their large masses.

found as single, stable particles in nature. A single quark always would interact immediately with the surrounding matter and polarize the vacuum until all quarks are bound in states with low internal momentum and color field density.

To calculate an interaction in a gauge field theory one has to sum up all *Feynman graphs* which contribute to this particular interaction. The Feynman rules give exact instructions for the computations of the matrix element, the probability of the graphed process, once the graph is known. Due to the vacuum polarization, an infinite number of graphs contribute to each interaction. In quantum field theories therefore observables are expressed by the use of perturbation theory, i.e. as power series of the coupling constant which can be cut off at a particular order.

The vacuum polarization enters into the Feynman graphs as additional *loops* where the exchanged bosons fluctuate into pairs of field quanta which reannihilate. In fact, this polarization opens a recursive infinite path since any field quantum may fluctuate in this way. For a calculation, usually the maximum number of closed loops considered is given, referring to as *1-loop* or *2-loop* calculation. See figure 2.1 for the basic vacuum polarization processes of the strong interaction in the 1-loop approximation. The process on the left is similar to the splitting of a photon into a pair of leptons. The process on the right has no equivalent in the electromagnetic interaction and causes the substantial differences in the behavior of the two interactions.
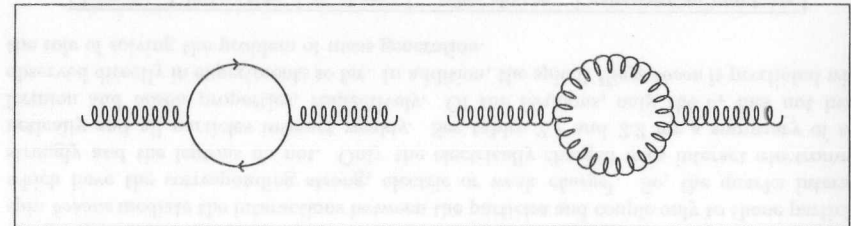
Figure 2.1: *Strong vacuum polarization in the 1-loop approximation: a gluon splits into a $q\bar{q}$ pair (left) or into two gluons (right).*

constant	value	rel. error ($\times 10^{-6}$)
fine structure constant $\alpha_{em}(m_{e^2})$	$1/137.0359895(61)$	0.045
Fermi constant G_F / GeV^2	$1.16639(1) \cdot 10^{-5}$	9
Weinberg angle $\sin^2 \Theta_W(\overline{MS})$	0.23124(24)	1000
strong coupling constant α_s (M_Z)	0.119(2)	17000

Table 2.3: *Fundamental constants [PDG98].*

From the above it is also clear that (anti-)screening causes the effective coupling to become dependent on the momentum transfer of the interaction, i.e. an *energy scale* of the physical process. The coupling constants α_{em} and α_s become *running coupling constants*. Their values normally are given at a fixed scale which is selected by convention. Table 2.3 quotes their actual world averages together with some fundamental constants in particle physics. It can be seen that α_s is much larger than α_{em}, making the strong cross sections typically 10^2 times larger than the electromagnetic ones. But the magnitude of α_s also causes perturbative QCD calculations (pQCD) to be much more complicated than in QED. Higher

orders do not vanish very fast but become important. Especially at low momentum transfer where α_s becomes large itself the pQCD calculations break down. This is one of the reasons why the relative error of α_s is much poorer than for the other fundamental constants.

The different scale behavior of the coupling constants α_{em} and α_s may result in a unification point at some very large energy scale where all forces act with the same strength. The extrapolation up to this scale needs as input precise values obtained from the low energy measurements. For example, predictions in the framework of supersymmetric theories, one major approach towards a grand unified field theory, suffer from the uncertainty of the value of α_s [ABF+92].

2.2 The Running of α_s

As stated, the running of the effective coupling constant $\alpha_s = \frac{g^2}{4\pi}$ (defined analogous to $\alpha_{em} = \frac{e^2}{4\pi}$) arises from the screening effects of the fields between interacting particles. In a quantum field theory, the infinite number of recursive fluctuations leads to ultraviolet divergences. This requires *renormalization* of the theory to get rid of them and to obtain finite results in the calculation of observables. In the renormalization procedure the modifications to the couplings of the bosons are calculated. Therefore, a mass scale, μ_r, has to be introduced at which the subtractions are performed to remove the ultraviolet divergences. The bare coupling constant turns into the renormalized one which is scale dependent and can be observed in experiments. This redefinition concerns masses, couplings and wave functions[3].

Since the value of the *renormalization scale* μ_r is arbitrary, no physical observable may depend on the choice made for it if the bare coupling is held fixed. Consider a dimensionless physical observable, R, which depends only on a single energy scale μ much bigger than any other dimensionful parameter in the process. Even if R scales with μ, in a renormalized quantum field theory it becomes dependent on the ratio μ^2/μ_r^2 and the renormalized coupling constant α_s. The total μ_r dependence of R is:

$$\left[\mu_r^2 \frac{\partial}{\partial \mu_r^2} + \mu_r^2 \frac{\partial \alpha_s}{\partial \mu_r^2} \frac{\partial}{\partial \alpha_s} \right] R(Q^2/\mu_r^2, \alpha_s) = 0 \qquad (2.1)$$

where the identification $Q = \mu$ has been made. This is usual in deep inelastic scattering where the momentum transfer Q^2 is the typical energy scale involved[4]. One sees that all of the scale dependence of R enters through the dependence of α_s on the renormalization scale μ_r, which is described through the *renormalization group equation* (RGE) or β function,

$$\beta(\alpha_s) \equiv \mu_r^2 \frac{\partial \alpha_s}{\partial \mu_r^2} . \qquad (2.2)$$

Eq. 2.1 can be solved by the implicit definition of a new function, the *running coupling* α_s

$$\ln \frac{Q^2}{\mu_r^2} = \int_{\alpha_s(\mu_r^2)}^{\alpha_s(Q^2)} \frac{dx}{\beta(x)} , \qquad (2.3)$$

relating the values of $\alpha_s(\mu^2)$ at two different scales μ. With that, QCD predicts the running of α_s but not the absolute value itself. As mentioned, this has to be obtained from experiment. Thus, it can be fixed at any convenient scale within the perturbative domain ($\alpha_s(M_Z^2)$ is

---

[3]For comprehensive descriptions of this and the following topics see [HM84, Per87, S+95, ESW96]

[4]There are also proposals to use p_t^2 and k_t^2 as scales [MZ96a].

conventional nowadays). And from there the value can be deduced for any other scale Q^2 within the perturbative regime.

The physical observable $R(Q^2/\mu_r^2, \alpha_s)$ has to be calculated at a particular scale Q in fixed-order perturbation theory by

$$R(Q^2/\mu_r^2, \alpha_s) = C_0 + C_1 \alpha_s(\mu_r^2) + C_2(Q^2/\mu_r^2)\alpha_s^2(\mu_r^2) + \dots \quad . \qquad (2.4)$$

Then the variation of R with Q can be predicted using the RGE. For that it is necessary to solve eq. 2.3. Due to the asymptotic freedom of QCD, this can always be achieved for sufficiently large Q and μ_r by using perturbation theory.

In QCD the RGE has the perturbative expansion

$$\mu_r^2 \frac{\partial \alpha_s}{\partial \mu_r^2} = \beta(\alpha_s) = -b_0 \alpha_s^2 (1 + b_1 \alpha_s + \mathcal{O}(\alpha_s^2)) , \qquad (2.5)$$

$$\text{where} \quad b_0 = \frac{(11 N_c - 2 N_f)}{12\pi}$$

$$b_1 = \frac{(17 N_c^2 - 5 N_c N_f - 3 C_F N_f)}{24\pi^2 b_0}$$

and $N_c = 3$ is the number of colors in QCD, N_f the number of active flavors, i.e. which mass can be produced at the scale Q, and $C_F = \frac{N_c^2 - 1}{2N_c}$ the Casimir factor.

Calculations are performed only to finite order: *leading order* (LO) calculations (1-loop) consider only terms with b_0, *next-to-leading order* (NLO) calculations (2-loop) take the terms with b_1 in addition. The coefficient b_2 is known but has not been used in general since most other quantities are not known to this order.

The β function in QED corresponding to eq. 2.5 is

$$\beta_{QED}(\alpha_{em}) = \frac{1}{3\pi}\alpha_{em}^2 + \dots , \qquad (2.6)$$

i.e. the b coefficients have opposite sign for physical N_f in QED and QCD. This is an effect of the non-Abelian interactions in the QCD.

Although not necessary, the definition of the renormalized coupling, α_s, in eq. 2.3 often is redefined by fixing one of the scales. Therefore, the dimensional parameter Λ_{QCD} is introduced and is defined as the integration constant of eq. 2.3 by setting

$$\ln \frac{Q^2}{\Lambda_{QCD}^2} = -\int_{\alpha_s(Q^2)}^{\infty} \frac{dx}{\beta(x)} = \int_{\alpha_s(Q^2)}^{\infty} \frac{dx}{b_0 x^2 (1 + b_1 x + \dots)} . \qquad (2.7)$$

Here Λ represents the scale at which α_s would diverge if extrapolated into the non-perturbative domain. It gives, therefore, the order of magnitude where $\alpha_s(Q^2)$ becomes strong.

With this definition the LO solution of eq. 2.5 is

$$\alpha_s(Q^2) = \frac{1}{b_0 \ln(Q^2/\Lambda^2)} . \qquad (2.8)$$

To NLO the exact solution of eq. 2.5 becomes

$$\frac{1}{\alpha_s(Q^2)} + b_1 \ln \left(\frac{b_1 \alpha_s(Q^2)}{1 + b_1 \alpha_s(Q^2)} \right) = b_0 \ln \frac{Q^2}{\Lambda^2} \qquad (2.9)$$

which allows the numerical determination of $\alpha_s(Q^2)$ to any desired accuracy. However, in this analysis the approximate solution in terms of powers of $\ln(Q^2/\Lambda^2)$ is applied consistently with the QCD predictions used

$$\alpha_s(Q^2) = \frac{1}{b_0 \ln(Q^2/\Lambda^2)} \left[1 - \frac{b_1}{b_0} \frac{\ln \ln(Q^2/\Lambda^2)}{\ln(Q^2/\Lambda^2)} + \dots \right] \quad . \tag{2.10}$$

For the limit $Q^2 \to \infty$, $\alpha_s(Q^2)$ vanishes logarithmically. This is the limit of the asymptotic freedom of QCD.

The value of Λ in eq. 2.10 differs from that in eq. 2.9 by a constant factor for the same value of $\alpha_s(Q^2)$ (it is about 10 % smaller for $N_f = 5$). Moreover, Λ is dependent on the number of active flavors, N_f, directly and, to NLO, is also dependent on the renormalization scheme chosen. Therefore, great care has to be taken to compare the right quantities when Λ is used.

In eq. 2.10 terms proportional to $(\ln \frac{Q^2}{\Lambda^2})^2$ are absorbed in the definition of Λ. This choice of renormalizing the coupling constant is called the *minimal modified subtraction scheme* ($\overline{\text{MS}}$) and the corresponding Λ is referred to as $\Lambda_{\overline{\text{MS}}}^{N_f}$. The systematic error due to the choice of the renormalization scheme is investigated in [IR94].

The number of active flavors depends on the energy scale of a particular process. Simply said, at an energy scale Q^2 lower than the mass m_f^2 of a quark with the flavor f there is not enough energy to produce this quark. Thus, it cannot be counted in the number of active quarks. In the perturbative expansion (eq. 2.5) α_s depends on the coefficients b_0 and b_1 which in turn depend on N_f. But α_s is a solution of the RGE and has to be continuous. Hence the values of $\Lambda_{\overline{\text{MS}}}$ have to change discretely if a quark mass boundary is crossed. This shows the importance of quoting Λ together with N_f for NLO calculations (changes in Λ only affect the higher orders). As a convention in the following $\Lambda_{\overline{\text{MS}}}^4$ is abbreviated with Λ unless stated differently.

In the literature different ways are described to calculate the $\Lambda_{\overline{\text{MS}}}$ at the thresholds. In this analysis the approach of [Mar84] is used, giving e.g. at the b quark threshold the relations:

$$\alpha_s \left(m_b^2, \left(\Lambda_{\overline{\text{MS}}}^5 \right)^2 \right) = \alpha_s \left(m_b^2, \left(\Lambda_{\overline{\text{MS}}}^4 \right)^2 \right)$$

$$\text{and} \quad \Lambda^4 \approx \Lambda^3 \left(\frac{\Lambda^3}{m_c} \right)^{\frac{2}{27}} \left[\ln \left(\frac{m_c^2}{(\Lambda^3)^2} \right) \right]^{\frac{-107}{2025}}$$

$$\Lambda^5 \approx \Lambda^4 \left(\frac{\Lambda^4}{m_b} \right)^{\frac{2}{23}} \left[\ln \left(\frac{m_b^2}{(\Lambda^4)^2} \right) \right]^{\frac{-963}{13225}} \tag{2.11}$$

$$\Lambda^6 \approx \Lambda^5 \left(\frac{\Lambda^5}{m_t} \right)^{\frac{2}{21}} \left[\ln \left(\frac{m_t^2}{(\Lambda^5)^2} \right) \right]^{\frac{-321}{3381}} \quad .$$

In the selected Q^2-range of this analysis, $44 < Q^2 < 3600 \, \text{GeV}^2$, five flavors are active throughout.

A peculiar feature of the RGE is the decrease of the relative error on an α_s determination when the result is evolved from a lower towards a higher scale. From eq. 2.5 one can derive with respect to the commonly used $\mu_r^2 = M_Z^2$

$$\frac{\delta \alpha_s(M_Z^2)}{\alpha_s(M_Z^2)} \sim \frac{\alpha_s(M_Z^2)}{\alpha_s(Q^2)} \frac{\delta \alpha_s(Q^2)}{\alpha_s(Q^2)} \quad , \tag{2.12}$$

which demonstrates this, since the β function decreases like α_s^2 when the scale is increased. Non-perturbative corrections which become important at lower scale do not share this feature, of course. And, since α_s itself becomes large at low scale, the justification to use perturbation theory gets weaker there, too. Therefore, the measurements of α_s at lower scales is typically less reliable.

2.3 The Status of α_s Determinations

Due to its importance, α_s has been determined using several observables in various reactions. Most of the experiments have measured α_s at a fixed center of mass energy, identifying the center of mass energy with the scale of the process μ. This experimental constraint allows access only to the value of α_s at a fixed scale μ^2. In order to compare the experiments, their results are evolved to a common scale, usually $\alpha_s(M_Z^2)$. In order to view the running of $\alpha_s(\mu^2)$ one has to consider carefully the intercalibration of the different experiments involving different sources and sizes of systematic uncertainties.

Table 2.4 gives a compilation of the present status based on [Sti97] and [PDG98] and references therein. Older standard reviews are [Bet95, Sch96, Bur97]. The values of $\alpha_s(M_Z^2)$ are given in table 2.4 in groups of related methods to determine α_s, ordered within by Q^2. The same values, globally ordered by Q^2, are shown in figure 2.2. The corresponding measurements are described very briefly in the following. The numbers in parentheses refer to the quoted values in table 2.4.

Sum rules: Deep inelastic scattering structure functions satisfy a number of sum rules corresponding to the conservation of various nucleon quantum numbers. Here the $\mathcal{O}(\alpha_s)$ corrections within the predictions can be used to extract α_s at a fixed scale Q^2. The **Bjorken Sum Rule (1)** [BjSR]

$$\int_0^1 dx(g_1^p(x) - g_1^n(x)) \equiv \frac{1}{3} \left| \frac{g_A}{g_V} \right| \left(1 - \frac{\alpha_s}{\pi} + \dots \right) + \Delta_{\text{HT}} \tag{2.13}$$

uses the polarized structure functions $g_1(x)$ for protons and neutrons derived from the difference in the cross section using parallel or antiparallel orientation between beam (e or μ) and target. With data from EMC/SMC and E142/143 from SLAC α_s has been determined at the lowest reported scale (1.58 GeV). The **Gross-Llewellyn Smith sum rule (2)** [GLS]

$$\int_0^1 dx(F_3^{\nu p} + F_3^{\bar{\nu} p}) = 6 \left[1 + \frac{\alpha_s}{\pi} + \dots \right] + \Delta_{\text{HT}} \tag{2.14}$$

provides a similar method for neutrino-nucleon scattering and has been used with data from CCFR. Despite the low scale, these methods are attractive since in both cases the theory is known up to NNLO. The higher twist (HT) contributions are understood relatively well but still dominate the systematic uncertainty.

Scaling violations: The classical way to measure α_s in deep inelastic scattering is from the strength of the scaling violations in the structure functions predicted by the DGLAP equations (cf. sec. 5.1.1). The value for the **neutrino scattering (3)** is that obtained from the CCFR collaboration. This has been updated for the new energy calibration of the detector. The result listed for the **muon scattering (4)** comes from the combined analysis of BCDMS and SLAC data.

no.	process	Q[GeV]	$\alpha_s(Q^2)$	$\alpha_s(M_Z^2)$	theory
1	DIS [BjSR]	1.58		$0.118^{+0.010}_{-0.024}$	NNLO
2	DIS [GLS]	1.72	$0.260^{+0.041}_{-0.046}$	$0.110^{+0.006}_{-0.009}$	NNLO
3	DIS [ν]	5.0		0.119 ± 0.005	NLO
4	DIS [μ]	7.1	0.180 ± 0.014	0.113 ± 0.005	NLO
5	DIS [jets]	22.1	0.148 ± 0.016	0.118 ± 0.009	NLO
6	τ [R_{had}]	1.77	0.33 ± 0.03	0.118 ± 0.004	NNLO
7	$Q\bar{Q}$ [1P,2S-1S]	3.6	0.1962 ± 0.0057	0.1180 ± 0.0027	LGT(NR)
8	$Q\bar{Q}$ [1P-1S]	5.0		0.116 ± 0.003	LGT(W)
9	$Q\bar{Q}$ [decay]	10.0	0.163 ± 0.014	0.110 ± 0.007	NLO
10	e^+e^- [σ_{had}]	31.6	0.163 ± 0.022	0.133 ± 0.015	NNLO
11	e^+e^- [shapes]	10.5	0.164 ± 0.015	0.113 ± 0.006	NLO
12	e^+e^- [shapes]	35.0	0.140 ± 0.020	0.119 ± 0.014	NLO
13	e^+e^- [shapes]	58.0	0.130 ± 0.008	0.122 ± 0.007	NLO
14	e^+e^- [shapes]	58.0	0.132 ± 0.008	0.123 ± 0.007	resum.
15	e^+e^- [fragm.]	22-91		0.124 ± 0.010	NLO
16	Z^0 [Γ_{had}]	91.2	0.123 ± 0.005	0.123 ± 0.005	NNLO
17	Z^0 [shapes]	91.2	0.118 ± 0.005	0.118 ± 0.005	NLO
18	Z^0 [shapes]	91.2	0.122 ± 0.006	0.122 ± 0.006	resum.
19	e^+e^- [shapes]	133	0.114 ± 0.007	0.121 ± 0.008	resum.
20	$p\bar{p}, pp \to \gamma + X$	4.0	$0.206^{+0.045}_{-0.032}$	$0.112^{+0.012}_{-0.010}$	NLO
21	$p\bar{p} \to b\bar{b}X$	20.0	$0.145^{+0.018}_{-0.019}$	0.113 ± 0.011	NLO
22	$p\bar{p} \to W + $ jets	80.6	0.123 ± 0.025	0.121 ± 0.024	NNLO
	world average			0.119 ± 0.002	

Table 2.4: *Summary of the α_s measurements, from [Sti97] and [PDG98]. The explanations in the text refer to the column 'no.'.*
The abbreviations are: (N)NLO = (next-)next-to-leading order; resum = resummed next-to-leading order; LGT(NR) = lattice calculation with an expansion around the non-relativistic limit; LGT(W) = lattice calculation using the Wilson formalism.
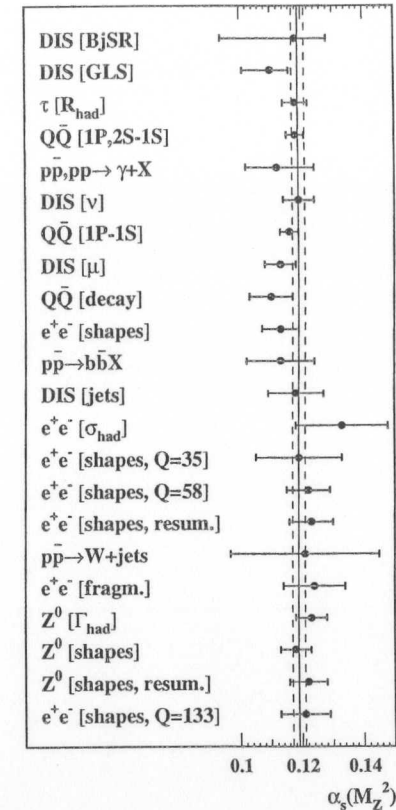
Figure 2.2: *Summary of the α_s measurements, from [Sti97] and [PDG98].*
The results from table 2.4 are ordered in increasing Q^2 and the lines correspond to the quoted world average and its error.

Jet rates (5): With HERA it has become possible to determine α_s from the jet production rate at high scales in deep inelastic scattering. There have been measurements reported by H1 [Nis94, H195] and ZEUS [ZEU95a, Tre96] using the JADE jet finding algorithm. Table 2.4 shows the averaged result for $\alpha_s(M_Z^2)$ and the ZEUS result for $\alpha_s(Q^2)$. This method has the great advantage of providing measurements of α_s in a wide range of Q^2 within one experiment. Therefore, the running of α_s can be demonstrated here without the problem of intercalibration between different experiments.

τ **decay (6):** The hadronic decay ratio of the τ lepton, R_τ, provides another measurement of α_s. The τ lepton can be measured well with vertex detectors, e.g. at LEP:

$$R_\tau = \frac{\Gamma(\tau \to \nu_\tau \to \text{hadrons})}{\Gamma(\tau \to \nu_\tau \bar{\nu}_e e)} = 3.058 \left(1 + \delta_{\text{pQCD}} + \delta_{\text{npQCD}}\right) \tag{2.15}$$

$$\text{with} \qquad \delta_{\text{pQCD}} = \frac{\alpha_s}{\pi} + 5.2 \left(\frac{\alpha_s}{\pi}\right)^2 + 26.4 \left(\frac{\alpha_s}{\pi}\right)^3 .$$

The non-perturbative correction, δ_{npQCD}, is small and the factor in front of the parentheses is different from $N_f = 3$ due to corrections known from QED. The value quoted in table 2.4 is based on the ALEPH and CLEO measurements.

Lattice calculations: With lattice calculations the states of quarkonium, a $q\bar{q}$ state with equal flavors, can be calculated with potentially high accuracy. E.g. the splitting between the 1S and the 1P state of the Charmonium is almost independent of the c-mass but depends on α_s. A result for this [1P-1S] split is given in table 2.4 using the **Wilson formulation** (7). A different approach, the expansion around the **non-relativistic limit** (8) calculated for Bottonium is also given. The scales $\alpha_s(Q^2)$ are derived from a conversion from the scale defined by the lattice spacing and differ from the J/Ψ-mass and Υ-mass.

Υ(1S) decay (9): Experimentally the decay of the $\Upsilon(1S)$ giving a single hard photon is a relatively clean measurement of α_s via

$$R_\gamma = \frac{\Gamma^{\gamma gg}}{\Gamma^{ggg}} = \frac{4}{5}\frac{\alpha_{em}}{\alpha_s(\mu^2)}\left\{1 - \left[2.6 - 2.1\ln\left(\frac{m_b^2}{\mu^2}\right)\right]\frac{\alpha_s(\mu^2)}{\pi}\right\} \quad , \qquad (2.16)$$

where CLEO has published the quoted result.

e^+e^- annihilation: From e^+e^- annihilation many further measurements are available. Here they are quoted in a more summarized from. Most of those in table 2.4 are derived from LEP and SLC data.

One of the most precise and reliable measurements comes from the Z^0 **hadronic width** which theoretically is calculated up to the complete third order (NNLO). Thus, the prediction is very stable with respect to variations in the renormalization scale. In particular the ratio of the hadronic Γ_{had} to the leptonic $\Gamma_{\ell\ell}$ partial width (16) is used:

$$R_Z = \frac{\Gamma(Z^0 \to \text{hads.})}{\Gamma(Z^0 \to l^+l^-)} = \frac{3\sum_q(v_q^2 + a_q^2)}{(v_v^2 + a_l^2)}\left[1 + \frac{\alpha_s}{\pi} + 0.85\left(\frac{\alpha_s}{\pi}\right)^2 - 15\left(\frac{\alpha_s}{\pi}\right)^3 + \dots\right] \quad .(2.17)$$

Using older data this has been done at intermediate scales, too (10).

By using the **event shapes** of the hadronic final state, like *thrust, sphericity, aplanarity, jet broadening, C-parameter* and others, α_s can be determined together with the size of the non-perturbative *power corrections* or hadronization. The predictions are known up to NLO and resummation techniques are used to minimize the contributions from higher orders (14). The data come from CLEO (11) (10.5 GeV), PEP/PETRA (12) (35 GeV), TRISTAN (13) (58 GeV), LEP (17) and SLC (18) (Z^0) and L3 (19) (133 GeV).

In e^+e^- annihilation α_s also has been derived from **scaling violations of the fragmentation functions** using data in the range $22 < Q < 91$ GeV from various experiments (15). Here similar scaling violations are introduced by QCD corrections as for the proton structure functions.

Hadron-hadron collisions: In hadron-hadron collisions (pp and $p\bar{p}$) α_s has been determined from comparing **direct photon** (20) (by UA6), **heavy quark** (21) (UA1) and W **boson plus jet cross sections** (22) (UA1 and UA2) to next-to-leading order predictions. The precision achieved so far is smaller than in e^+e^- and lepton-hadron processes due to larger experimental and theoretical uncertainties associated with the incoming hadrons. Measurements based on pure jet production can be compared only to leading order predictions so far, which does not allow a reliable α_s extraction.

The world average of $\alpha_s(M_Z^2) = 0.119 \pm 0.002$ is taken from [PDG98] where a χ^2 fit is performed and the error for the different degrees of correlation of the used results is rescaled. The central value has increased by $+0.003$ from that given in the issue two years before. This is mainly caused by the increase in the central value of the two lattice calculations (by $+0.003$ and $+0.004$) and by the increase ($+0.008$) of the CCFR result of the scaling violation due to the recalibration of the detector. Figure 2.2 shows the remarkable consistency of the results, in particular of those with the smallest uncertainties.

In order to view the running of $\alpha_s(\mu^2)$ one has to consider carefully the intercalibration of the different experiments involving different sources and sizes of systematic uncertainties. With its wide range of Q^2, HERA provides the possibility to test the running of α_s within one experiment.
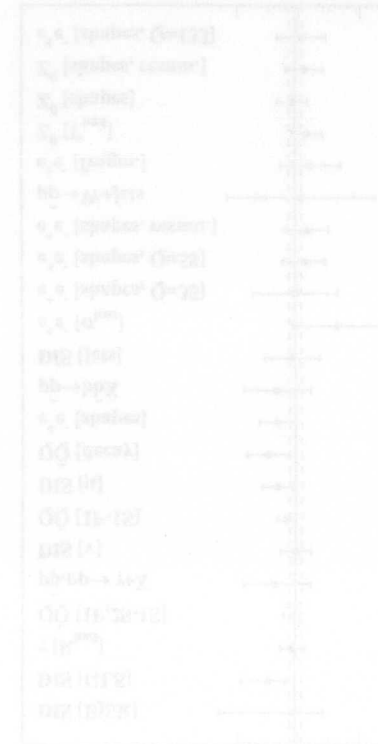
Chapter 3

HERA and the ZEUS Experiment

3.1 HERA
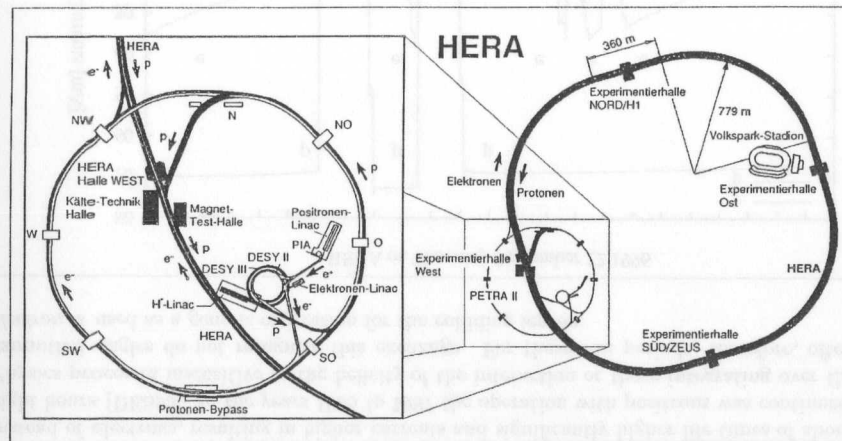
Figure 3.1: *The HERA accelerator.*

The *Hadron-Elektron-Ring-Anlage* HERA (cf. figure 3.1), the first electron-proton collider machine worldwide, is located at the *Deutsches Elektronen-Synchrotron* DESY at Hamburg, Germany. A summary of the most important parameters of the HERA accelerator is given in table 3.1.

Since the middle of 1992, collisions of electrons or positrons with protons have been provided for physics experiments at two interaction zones used by the multipurpose detectors of the two international collaborations H1 and ZEUS. There are two additional experimental zones. The HERMES experiment uses the electron beam of HERA, polarized with spin rotators, and a polarized gas target to measure the spin distributions of the quarks in the proton and neutron (data taking since 1995 in the East Hall). The HERA-B experiment uses the proton beam of HERA to study the CP violation in the $B^0\overline{B^0}$ system using a wire target in the proton beam halo to produce the B mesons (commence operation in 1998 in West Hall). Synchrotron radiation from the HERA preaccelerators is used at the

Hamburger Synchrotronstrahlungslabor HASYLAB at 40 experimental stations for fundamental and applied research in the fields of physics, biology, chemistry and crystallography, in materials and geological sciences as well as in medical applications.

HERA parameters	design		'95 run	
	electrons	protons	positrons	protons
nominal energy (GeV)	30	820	27.54	820.71
center of mass energy (GeV)	314		300.7	
number of bunches	210	210	174+15	174+6
injection energy (GeV)	14	40	12	40
injection time (min)	15	20	45	60
energy loss per turn (MeV)	127	$1.4 \cdot 10^{-10}$	127	$1.4 \cdot 10^{-10}$
current (mA)	58	160	30	55
magnetic field (T)	0.165	4.65	0.165	4.65
instantaneous luminosity ($cm^{-2}s^{-1}$)	$1.6 \cdot 10^{31}$		$4.3 \cdot 10^{30}$	
specific luminosity ($cm^{-2}s^{-1}mA^{-1}$)	$3.6 \cdot 10^{29}$		$5.0 \cdot 10^{29}$	
integrated luminosity per year (pb^{-1}/a)	35		12.5	
horizontal beam size σ_x at IP (mm)	0.301	0.276	0.239	0.185
vertical beam size σ_y at IP (mm)	0.067	0.087	0.055	0.085
longitudinal beam size σ_z at IP (mm)	0.8	11	0.8	11
bunch crossing time (ns)	96			
circumference (m)	6336			
experimental zones	4			

Table 3.1: *HERA design parameters and performance.*

HERA provides the electrons and protons by means of two independent systems of linear accelerators and storage rings (cf. figure 3.1) which bring the beams to collision at zero crossing angle at the interaction points (IP) of the North (H1) and the South Hall (ZEUS). The spacing of the particle bunches in HERA is 96 ns. Synchronized with the bunch crossing, the machine provides the *HERA clock* signal with a corresponding rate of 10.4 MHz.

The protons originate from negatively charged hydrogen atoms produced at LINAC III and are accelerated to 50 MeV. They are fed into DESY III where the electrons are stripped off by a thin metal foil. The left over protons are accelerated up to 7.5 GeV/c in 11 bunches already having the HERA bunch spacing of 96 ns and then passed to the proton line of PETRA II. There 70 bunches can be stored which are accelerated to 40 GeV/c and afterwards transferred to HERA. This procedure is repeated three times until the 210 proton bunches of HERA are filled. At design performance the total procedure needs about 20 minutes. The final acceleration up to about 820 GeV is done in the superconductive cavities of the proton storage ring of HERA, giving life times of the beam of more than 100 hours. The proton beam energy is limited by the bending field (4.65 T) of the dipole magnets[1].

Electrons or positrons are produced in the linear accelerator, LINAC II, and accelerated to 450 MeV. They are accumulated in the *positron intensity accumulator*, PIA, in a single bunch and fed to the DESY II ring which then accelerates them up to 8 GeV. Then they are transferred to the electron beam line of PETRA II. 70 bunches are accumulated, accelerated

---

[1]Within the lumi upgrade project some feasibility studies have been made to investigate the possibility of raising the proton energy up to 1 TeV [Hol97]

up to 14 GeV, and filled into HERA. Again, this procedure is repeated three times to fill the 210 electron bunches. At design performance this procedure needs about 15 minutes. After acceleration to its final energy, the electron (positron) beam has a life time of a few hours. The electron beam energy is limited by the radio frequency power which is needed to compensate the energy loss due to synchrotron radiation in the bending sections with a magnetic field of 0.165 T.

In practice not all electron and proton bunches are filled. Unpaired bunches, called pilot bunches, are used to estimate beam related backgrounds, while empty bunches allow to estimate the background from cosmic rays.

During the '94 run period severe lifetime problems of the electron beam were observed. The maximum electron current was limited to 25 mA and the typical life time was only two to three hours. The reason for this problem was the capture of positively charged dust by the electron beam which originates from the ion getter pumps of the HERA vacuum system. In the middle of '94 the HERA operation therefore was changed to accelerate positrons instead of electrons, resulting in higher currents and significantly higher life times of about eight hours [DES95]. In the years 1995 to 1997 the operation with positrons was continued. Physics processes insensitive to the helicity of the interaction or those integrating over the azimuthal angles do not recognize this exchange. For these run periods, therefore, often *electron* is used as a generic expression for the colliding lepton.
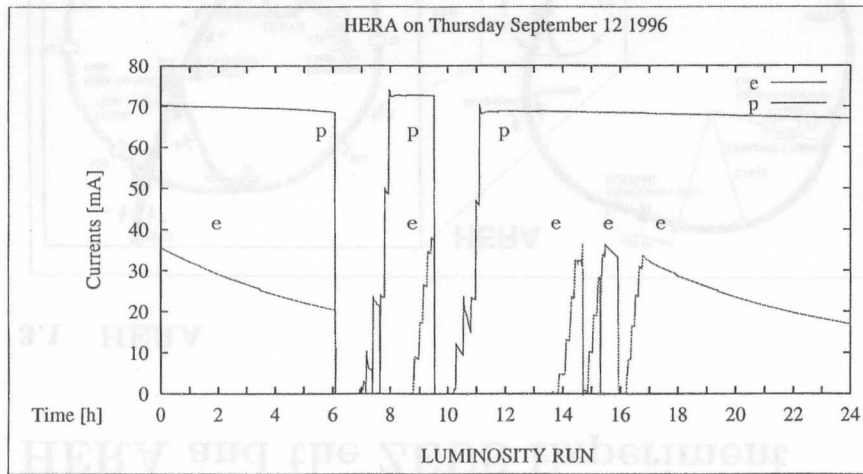
Figure 3.2: *Positron and proton current (mA) in HERA as a function of time (h) during an arbitrary 24 h luminosity operation.*

The luminosity delivered by HERA on an arbitrary day in 1996 (similar to 1995 operation) is shown in figure 3.2. One sees a dump of both beams at around 6:00 in the morning. A first try to refill the machine starting at about 7:00 for the protons and at about 8:45 for the electrons fails due to a proton beam loss while ramping the electrons at about 9:30. After refilling the protons it needs three attempts to fill and ramp the electrons successfully. A new luminosity run with stable beam conditions started around 17:00.

The integrated luminosity delivered by HERA in the years 1993 until 1997 is shown in figure 3.3. It shows a continuous increase year by year.
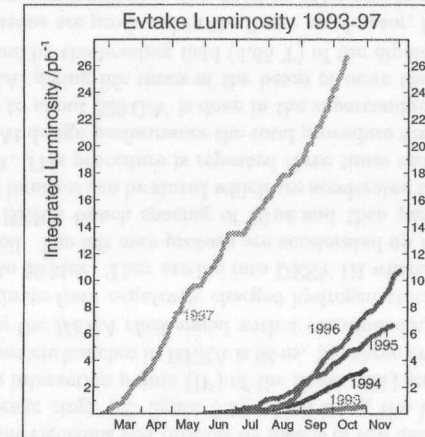
Figure 3.3: *Integrated luminosity delivered by HERA plotted as a function of time for the years 1993 to 1997.*

3.2   The ZEUS Detector

The ZEUS Collaboration is formed by about 450 physicists and an equal number of technicians, coming from 52 institutes of 12 nations.

The ZEUS detector is an asymmetric general purpose detector built to study lepton-hadron scattering and the structure of the proton. Figures 3.4 and 3.5 show cuts through the ZEUS detector along and perpendicular to the beam direction, respectively. The asymmetric layout of the detector reflects the difference in the electron and proton beam energies causing the center-of-mass system to move into proton direction relative to the laboratory system. With the exception of the holes for the electron and proton beams the detector is hermetic. The construction and installation of the detector was completed by fall 1991. Data taking started in the middle of 1992. Since then several detector upgrades and modifications have taken place as a consequence of physics requirements and the better technical understanding.

In the ZEUS laboratory system the direction of the incoming proton is defined as the positive z-axis, also referred to as *forward direction*. All polar scattering angles Θ are calculated with respect to this axis. The x-axis is pointing to the center of the HERA storage ring and the y-axis is pointing upwards. These directions are called *transverse*. Azimuthal angles ϕ are measured with respect to the x-axis. With this choice the 4-vectors of the incoming electron and proton become $k = (0, 0, -27, 27)$ GeV and $P = (0, 0, 820, 820)$ GeV.[2]

In the following a brief outline of the major detector components is given. A more detailed description of the components important for this analysis can be found in the remainder of this chapter. A detailed and general description is given in [ZEU93b].

---

[2]The exact values change from year to year.
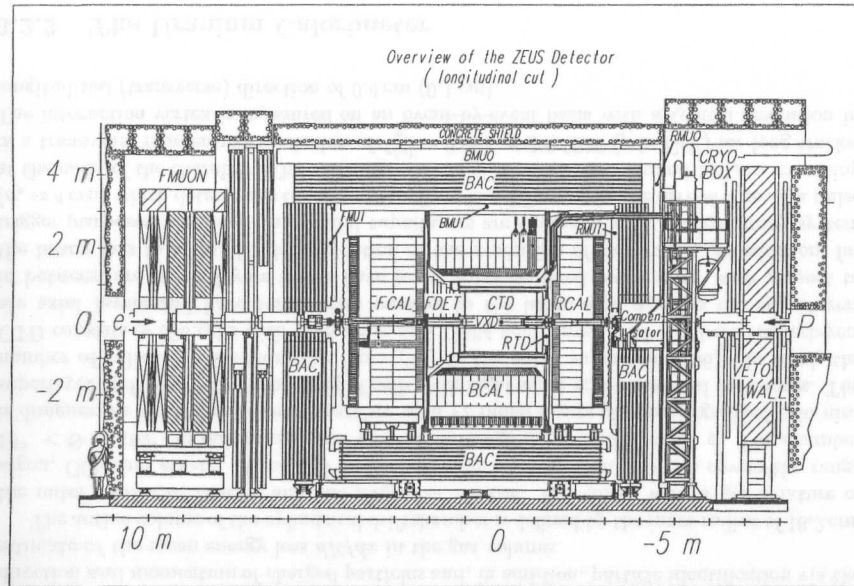
Figure 3.4: *The ZEUS detector from the side along the beam axis (cut along the yz-plane through the interaction point).*

The inner central part of the ZEUS detector consists of particle tracking detectors. Around the interaction point in the beam pipe a Vertex Detector (VXD) is mounted. The main tracking device is the Central Tracking Detector (CTD), a cylindrical drift chamber surrounded by a superconducting magnet providing an axial magnetic field of 1.43 T. In the forward direction three sets of planar drift chambers (FTD) are installed alternated with Transition Radiation Detectors (TRD). In the rear direction a single planar drift chamber (RTD) is installed. This tracking system yields the direction and momentum of charged particles originating from the collision or secondary vertices. Thus, a precise measurement of the event vertex is provided. By using the TRD and dE/dx measurements of the CTD particle identification is also possible. After high voltage problems and radiation damage in 1994 the VXD was not operational in 1995 and was removed during the winter shutdown of 1995/96. A micro vertex detector (μVTX) is planned to be installed for the 2000 run period.

The tracking system is surrounded by a high resolution uranium calorimeter (UCAL) which is subdivided into three parts: a forward (FCAL), a barrel (BCAL) and a rear calorimeter (RCAL). It is the prime device to measure the energy of particles produced by the collisions. Since installation, several subdetectors have been added to improve its performance. In 1994, outside the UCAL but still inside the iron yoke at $z = 5.1$ m, the Proton Remnant Tagger (PRT) was installed. It allows to obtain information about the hadronic final state in the forward direction at pseudorapidities[3] of $4.3 < \eta < 5.8$ and is used to tag diffractive events. For the 1994 run period, the Small angle Rear Tracking Detector

_____

[3]The pseudorapidity is defined as $\eta = -\ln\left(\tan\frac{\Theta}{2}\right)$ with the polar scattering angle Θ.
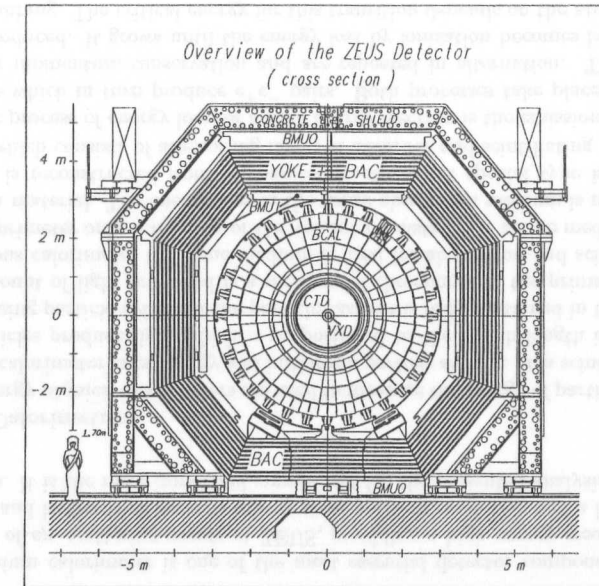
Figure 3.5: *The ZEUS detector perpendicular to the beam axis (cut along the xy-plane through the interaction point).*

(SRTD) was added to the RCAL to improve the spatial resolution in the measurement of the scattering angle of electrons near the beam pipe. It is mounted in front of the RCAL where it covers a radius of ~ 34 cm and consists of two layers of 1 cm wide scintillating strips. It also acts as a presampler, giving an energy correction to electrons which have showered in the dead material before entering the SRTD and the RCAL. Since 1995, the Presampler detectors (F/RPRES), consisting of a single layer of 20×20 cm^2 scintillator tiles, have been used to do such an energy correction for all electrons moving into FCAL and RCAL. A similar detector in front of the BCAL modules (BPRES) commenced operation in 1998. At a longitudinal depth of $3 X_0$ in the RCAL, the Hadron-Electron Separator (RHES), consisting of 3×3 cm^2 silicon diodes, was installed prior to 1995. It is used for the discrimination of electromagnetic and hadronic showers originating from low energy particles (< 5 GeV). A counter part in the FCAL (FHES) will become operational in 1998. Also starting up in 1995, a Beam Pipe Calorimeter (BPC) was installed in the beam hole of the RCAL, attached to the beam pipe. The two parts of the electromagnetic tungsten-scintillator sandwich calorimeter extend the acceptance for electrons scattered with a small angle. With the shift of the two central RCAL modules and the SRTD towards the beam line the gap in the acceptance between BPC and RCAL was closed in 1996. Finally, a Forward Plug Calorimeter (FPC), being a lead-scintillator shashlik calorimeter, started operation in 1998, too. It narrows the hole of the FCAL beam pipe from 20×20 cm^2 to a radius of ~ 2.5 cm and extends the acceptance of the calorimeter by one unit in pseudorapidity.

The UCAL is enclosed by streamer tubes (FMUI, BMUI, RMUI) on the inner side of the iron yoke for muon identification. The yoke itself is instrumented with proportional

chambers. This Backing Calorimeter (BAC) is used to measure the leakage from the main calorimeter and serves as return path for the solenoid magnetic field flux. Outside the yoke, a second layer of streamer tubes (FMUON, BMUON, RMUON) is installed. To measure the muon momentum in the forward direction drift chambers are mounted in a toroidal magnetic field of 1.7 T produced by two iron toroids.

Leaving the central detector in the electron direction, at $z = -7.3$ m an iron-scintillator VETO wall is used to reject beam-related background. Two small lead-scintillator electromagnetic calorimeters (LUMI) at $z = -35$ m and $z = -107$ m are used to measure photons from bremsstrahlung in the $ep \rightarrow ep\gamma$ reaction for luminosity measurements, to tag electrons from photoproduction events with $Q^2 \approx 0$ and for the investigation of radiative events. At $z = -8$ m and $z = -44$ m tungsten-scintillator electromagnetic calorimeters (TAGGER) were added to extend the acceptance of the electron tagging.

Moving from the central detector into the forward direction, six stations of silicon strip detectors, located at $z = 26 \ldots 96$ m, are mounted very close to the beam line: the Leading Proton Spectrometer (LPS) measures very forward scattered protons at a transverse momentum of $p_t < 1$ GeV/c. Finally, at $z = 105.6$ m the Forward Neutron Calorimeter (FNC) is set up, being a lead-scintillator sandwich calorimeter, designed to detect very forward produced neutrons.

Some scintillation counters attached to the beam collimators (C1,...,C5) are used to monitor the background and the timing conditions. The C5 counter, located upstream beyond the RCAL, is also used to reject background from beam-gas interactions.

3.2.1 The Central Tracking Detector

The central tracking detector (CTD) [F+93] provides a high precision measurement of the direction and momentum of charged particles and, in addition, particle identification via the estimate of the mean energy loss dE/dx in the gas volume.

The active volume of the cylindrical driftchamber is defined by the inner radius of 18.2 cm, the outer radius of 79.4 cm and the length of 205 cm. It is filled with a gas mixture of argon, CO_2 and ethane. Measured from the nominal interaction point, it covers the range $15° < \Theta < 164°$ in polar angle and has full coverage in azimuthal angle ϕ. The chamber is designed as a multi-cell stereo chamber with 72 radial layers of wires organized into nine superlayers (cf. figure 3.6) consisting of cells with eight sense and additional field wires. The number of cells increases from the inner (32) to the outer superlayers (96). In total, the CTD consists of 576 cells with 4608 sense and 19584 field wires. Odd numbered superlayers are axial layers and have sense wires parallel to the beam axis whereas the superlayers in between are stereo layers which have sense wires declined by $\sim \pm 5°$ with respect to the beam axis to allow the determination of the z-position of the tracks. In addition, for trigger purposes, the inner three axial superlayers are equipped with a z-by-timing system ($\sigma_z \approx 4$ cm) which determines the z-position from the difference in the arrival time of a pulse at the ends of the chamber. The resolution of the CTD in $r - \phi$ is around 230μm resulting in a transverse momentum resolution of $\frac{\sigma(p)}{p} = 0.005 \cdot p \oplus 0.0016$ (p in GeV) for long tracks. The interaction vertex is measured on an event-by-event basis with a typical resolution in longitudinal (transverse) direction of 0.4 cm (0.1 cm).

3.2.2 The Uranium Calorimeter

The ZEUS calorimeter is a high resolution uranium-scintillator compensating calorimeter [D+91, A+91, B+93a, Str91, Krü92].
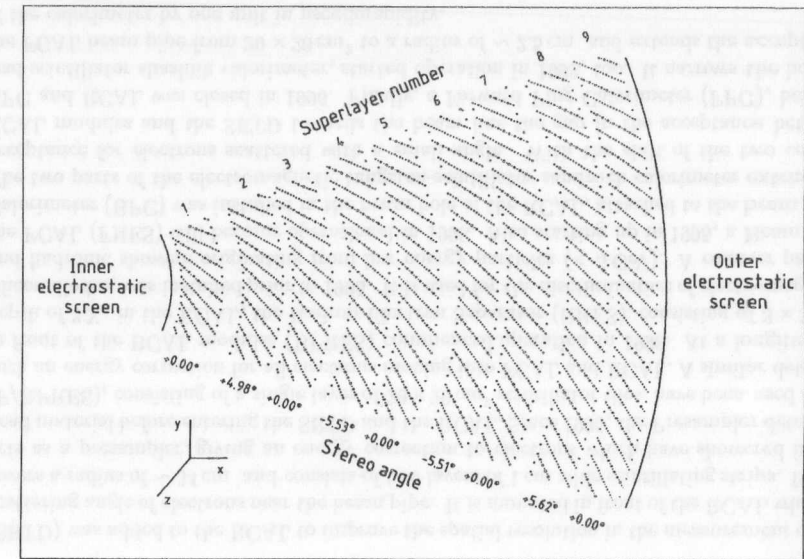
Figure 3.6: *CTD octant with sense and field wires. Also given is the stereo angle of each superlayer.*

The uranium calorimeter is one of the most essential detector components for the reconstruction of ep-scattering events at ZEUS, providing a high energy resolution for electromagnetic and hadronic showers, a mostly good position resolution and a hadron-electron identification. It is the most important component for the presented analysis.

Basics on Calorimetry:

In high energy physics, calorimeters are used to measure the energy of particles. A particle entering the calorimeter loses energy and initiates a *particle shower*. In a scintillator medium charged particles produce light which is proportional to their path length in the case of a minimal ionizing particle (MIP). If the particle cascade is fully contained in the calorimeter, the total amount of light produced is a measure of the energy of the primary particle. In a homogeneous calorimeter the same medium is used for absorption and scintillation. In a sampling calorimeter only a fraction of the volume consists of an active medium embedded in absorption material. The energy loss in the dense absorption medium is not visible. The total energy is reconstructed from the sample fractions. A special type is the *sandwich calorimeter* which consists of alternating layers of absorber and scintillating material.

The basic process of energy loss for a high energy electron is the emission due to Bremsstrahlung γ's which in turn produce e^+e^- pairs. Both processes take place in the field of a nucleus for momentum conservation and are repeated in alternation. Thus, a particle cascade is produced. It grows until the energy loss by ionization becomes larger than that by Bremsstrahlung. The critical energy for this transition depends on the atomic number Z of the absorber material ($E_C \sim 580$ MeV/Z). The longitudinal depth of an **electromagnetic shower** is measured in *radiation lengths* X_0: the path length where the energy of the

primary particle has dropped by Bremsstrahlung to $\frac{1}{e}$ in average. Thus, for electrons with $E \gg E_C$ one has:

$$-\frac{dE}{dx} = \frac{E}{X_0} \qquad (3.1)$$

In a simple view, a primary electron with energy E_0 radiates within the first radiation length a Bremsstrahlungs γ typically with $\frac{E_0}{2}$. The γ produces in the second radiation length an e^+e^- pair with $\frac{E_0}{4}$ each, while the primary electron radiates another γ now with $\frac{E_0}{4}$. Therefore, after two radiation lengths one can expect to have four particles with $\frac{E_0}{4}$ each, or after nX_0 radiation lengths $N = 2^n$ particles with almost equal numbers of electrons, positrons and photons. The shower maximum will be reached at a depth tX_0, where the particle energy has dropped to the critical energy yielding the number of particles N_{max}:

$$t = \frac{\ln \frac{E_0}{E_C}}{\ln 2} \qquad N_{max} = e^{t \cdot \ln 2} = \frac{E_0}{E_C} \qquad (3.2)$$

This coarse view on an electromagnetic shower neglects the spectrum of the Bremsstrahlung γ's, the Compton and photo effect and energy loss due to ionization. It also neglects the statistical fluctuations, which is the reason why in practice predictions are done with Monte Carlo calculations. But the qualitative picture is correct: the depth needed to absorb a shower completely (tX_0) grows logarithmically with the energy of the primary particle E_0. And the integral over the path of all particles is proportional to E_0. It is approximately:

$$L = \frac{2}{3} \int_0^{l_{max}} N dt = \frac{2}{3 \cdot \ln 2} \frac{E_0}{E_C} \sim \frac{E_0}{E_C} \qquad (3.3)$$

where the factor $\frac{2}{3}$ comes from the fraction of the charged particles. Thus, a signal produced[4] becomes proportional to the energy of the particle entering the calorimeter. To keep the shower short one chooses absorber materials with high atomic numbers Z.

Hadron showers have different properties than electromagnetic showers since hadrons predominantly interact by inelastic scattering with nuclei in the absorber material, i.e. by strong interaction, producing secondary hadrons. This cascade of particles ends when the particles have lost their kinematic energy or have been absorbed. Thus, for dense materials with high Z, the *nuclear absorption length* λ is much larger than the radiation length X_0. Compared to an electromagnetic calorimeter designed for the same particle energy, a hadronic one needs a much larger longitudinal depth and, due to diffusion processes, also a larger transverse size to contain the hadronic shower. And, compared to an electromagnetic shower, only about $\frac{2}{3}$ of the particle energy becomes visible in a calorimeter at all. The rest is lost in processes which do not produce a signal which can be measured:

- Neutral particles produce no signal in the scintillator. Only a fraction of their energy becomes visible via secondary reactions. The neutral fraction in a hadronic shower is larger than in an electromagnetic shower.

- π mesons are produced which mostly decay into muons and neutrinos. Both leave the calorimeter without deposition of their (full) energy.

---

[4]E.g. light in the case of a scintillation calorimeter as the ZEUS UCAL, charge in the case of ionization chambers as for the H1 liquid argon calorimeter.

- Hadrons may lead to fission of nuclei. Their fragments are stopped in the absorber after a very short distance and do not reach the scintillator. Also, the binding energy of the nucleus is lost. The highly excited fission fragments decay by emission of photons, pions and, mostly, by neutrons.

- Hadrons can cause spallation of nuclei. They induce the emission of secondary particles, mostly neutrons and pions, via an intranuclear cascade. In addition, an internuclear cascade may be induced since the secondary neutrons may induce spallation in other nuclei.

The π^0 mesons give an additional problem. Although being hadrons, they produce predominantly electromagnetic subshowers and the varying fraction of π^0 mesons in a hadronic shower induces an important spread.

In total, the visible fraction of energy of a hadron, h, is normally $10 \ldots 30\%$ less than that for an electron with the same energy, e. Thus, the energy resolution in the hadronic measurement is worse and the ratio of signals is $\frac{e}{h} > 1$.

In special layouts, **compensation** can be achieved for the missing hadronic energy in a scintillation measurement, i.e. the calorimeter layout is optimized in a way that electromagnetic and hadronic showers of equal energy yield, on average, equal response in the calorimeter. The key point is to use an organic scintillator since it has many hydrogen nuclei, i.e. almost free protons, which can act as recoil partners for the neutrons. The charged recoil protons in turn produce visible signals. Thus, with a suitable adjustment of the relative thickness of the absorber and scintillator volumes compensation in the light yield for hadronic and electromagnetic showers can be achieved for a minimum hadron energy of $5\,\mathrm{GeV}$. By using U^{238} as absorber material, the yield of neutrons in a hadronic shower is higher than for other absorbers, like lead or tungsten, due to the fission of U^{238}. And the neutrons produced in fissions can move almost free, with an absorption length of about $10\,\mathrm{cm}$, through the U^{238} absorber and reach the scintillator. Thus, for a compensating U^{238} calorimeter the scintillator volume can be chosen significantly smaller than for other absorber materials. At the same time the visible signal of an electromagnetic shower is smaller for an absorber with high Z since low energetic photons produce electrons by the photo effect which are more likely to remain in the absorber.
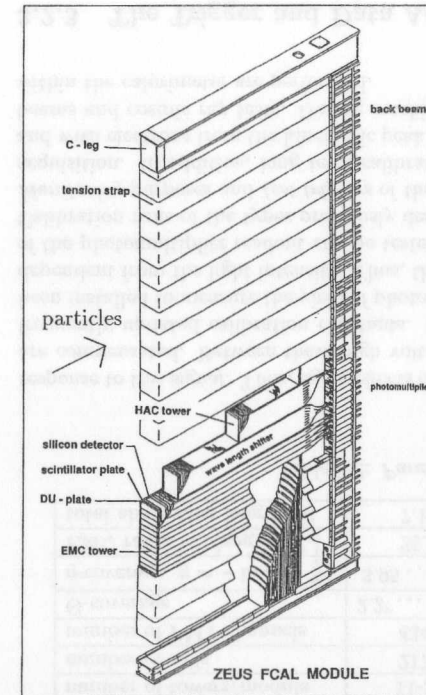
Figure 3.7: *3-dim view of a FCAL module.*

ZEUS UCAL peculiarities:

The UCAL is a sampling calorimeter, consisting of alternating layers of depleted uranium[5] as absorber and plastic scintillator[6] as active material. The thickness of the plates (3.3 mm uranium $\hat{=} 1\,X_0$ and 2.6 mm scintillator) has been chosen to optimize the compensation of the calorimeter ($\frac{e}{h} = 1.00 \pm 0.02$ for energies > 10 GeV). The energy resolution of the ZEUS calorimeter for electromagnetic particles and hadrons was measured at a test beam to be

$$\frac{\sigma^{\text{elmag}}(E)}{E} = \frac{18\,\%}{\sqrt{E}} \oplus 1\,\% \quad \text{and} \quad \frac{\sigma^{\text{had}}(E)}{E} = \frac{35\,\%}{\sqrt{E}} \oplus 2\,\% \tag{3.4}$$

where the energy E is measured in GeV [ZEU93b].

The UCAL is a 4π detector with the exception of the $20 \times 20\,\text{cm}^2$ holes to accommodate the beam pipe. It covers > 99.5 % of the solid angle. The three separate sections of the calorimeter are divided into vertical (FCAL, cf. figure 3.7, and RCAL) or radial (BCAL) modules. These in turn are subdivided into towers with lateral dimensions of approximately $20 \times 20\,\text{cm}^2$. The towers longitudinally are divided into three sections (only two in RCAL). The front section facing to the interaction point is used as an electromagnetic calorimeter (EMC) and is further subdivided into four cells of $\approx 5 \times 20\,\text{cm}^2$ front area (two cells of $\approx 10 \times 20\,\text{cm}^2$ in RCAL). The rear two sections (only one in RCAL) are used as hadron calorimeters (HAC1 and HAC2). They form a single cell each. Towers in the FCAL and RCAL with their front face hidden by the overlapping BCAL have a single (hadronic) cell in the front section (HAC0) instead of the four or two EMC cells. The longitudinal depth of the towers is chosen to ensure at least 95 % containment for 90 % of the particle showers with maximum energy. The EMC (HAC0) sections have a depth of $\sim 25\,X_0$ ($\sim 1\,\lambda$). The HAC sections have a depth of $\sim 3\,\lambda$ in FCAL and RCAL and $\sim 2\,\lambda$ in BCAL. The sampling fractions for minimal ionizing particles (MIP) are $\sim 6.2\,\%$ and $\sim 5.9\,\%$ in the EMC and in the HAC part, respectively. Further parameters are given in table 3.2.

Each cell is read out at two sides via wavelength shifters which are coupled to photomultiplier tubes (PMTs) for redundancy. By summing the signal from both PMTs of a cell, the energy measurement is independent of the impact point of the particle within the cell. The comparison of both signals allows the determination of the relative impact point of a particle between the two sides where the cell is read out. The nonlinearity of the PMTs is at most 2 % up to an anode charge of 2000 pC/pulse ($\hat{=} \sim 400\,\text{GeV}$ in FCAL).

The calorimeter also provides timing information with a resolution better than 1 ns for energy deposits > 4.5 GeV. The global time from a calorimeter section (F/B/RCAL) is obtained from an energy weighted average of the times of all PMTs with energy deposits > 200 MeV.

Calibration:

The absolute energy scale of the calorimeter has been determined after construction, in electromagnetic and hadronic test beam measurements of selected modules and also in cosmic ray tests for all modules, to about 1 %. During operation of ZEUS, the calorimeter is calibrated frequently on a channel-by-channel basis, mostly by in-situ testing methods. *Charge injection* test pulses are used to calibrate the electronic readout chain. The radioactive decay of U^{238} provides a small, constant reference signal, the *Uranium Noise*. The gain of the PMTs is trimmed by the adjustment of the HV from time to time to yield a defined

---

[5]An alloy of 98.1 % U^{238}, 1.7 % Nb and $\leq 0.2\,\%$ U^{235} with specific density of $\sim 18.5\,\text{g/cm}^3$.
[6]SCSN-38 (polystyrol)

CAL parameters	FCAL	BCAL	RCAL
number of modules	23	32	23
number of towers/module	11-23	14	11-23
number of cells	2172	2592	1152
number of PMT channels	4344	5184	2308
Θ-coverage	$2.2° \ldots 39.9°$	$36.7° \ldots 129.1°$	$128.1° \ldots 176.5°$
η-coverage $\eta = -\ln\left(\tan\frac{\Theta}{2}\right)$	$3.95 \ldots 1.01$	$1.10 \ldots -0.74$	$-0.72 \ldots -3.49$
EMC radiation length $[X_0]$	25.9	22.7	29.9
total absorption length $[\lambda]$	7.14	4.92	3.99

Table 3.2: *Parameters of the UCAL.*

response to this signal. Thus, aging effects of the scintillators, wavelength shifters and PMTs are compensated. Between these high voltage trims, changes in response are tracked with frequently updated calibration constants. A combined LED/Laser *light pulser system* has been installed to measure the yield of photoelectrons per GeV which is, to a large extent, independent from the light intensity. Thus, the linearity and the short and long term stability of the photomultiplier readout can be tested in the full dynamic range with high statistics. Calibration runs of the types previously described are taken at least daily for *Data Quality Monitoring* purposes and *test triggers* of these types are taken at low rate even during data acquisition. In addition, long term calibration is done with *cosmic* and *halo muon* events and with electrons from the kinematic peak which are compared to the results from the test beams and cosmic ray tests. During machine shutdowns, scans with movable Co^{60} *sources* within the calorimeter are performed.

3.2.3   The Trigger and Data Acquisition System

HERA has a short bunch crossing time of 96 ns, equivalent to a rate of $\sim 10\,\text{MHz}$. The total interaction rate is of the order of $10 - 100\,\text{kHz}$ and is dominated by background from interactions of the protons with the residual gas upstream in the beam pipe. Other sources of background reactions are electron beam gas collisions, beam halo and cosmic events. The rate of *ep* physics events in the ZEUS detector is only of the order of a few Hz. Since the ZEUS detector has 250,000 readout channels, it therefore produce 500 kByte/event, or a data load of > 5 TByte/s at the front end.

ZEUS employs a sophisticated 3-level trigger system [You92, S+89] in order to select *ep* physics events with an efficiency of 99 %, achieving a reduction of the total rate by a factor of 10^6. A schematic diagram of the ZEUS trigger system is shown in figure 3.8.

The *First Level Trigger* (FLT) is a hardware trigger, designed to reduce the input rate to 1 kHz. Each detector component has its own FLT and a 10.4 MHz pipeline to store the data and so avoid dead time losses. Each local FLT analyzes a particular event within the first 25 clock cycles after the interaction, yielding e.g. energy sums or differences, and sends its information to the *Global First Level Trigger* (GFLT). The GFLT issues, not later than $4.4\,\mu s$ after the interaction, a global trigger decision based on various logical combinations among the components' input. In the case of a positive trigger decision, the data stored in the pipelines of each component are copied to local buffers for further processing. For calorimeter signals at this stage the data are digitized and stored in digital signal processors (DSP), calibration constants are applied and energy and times values are calculated.
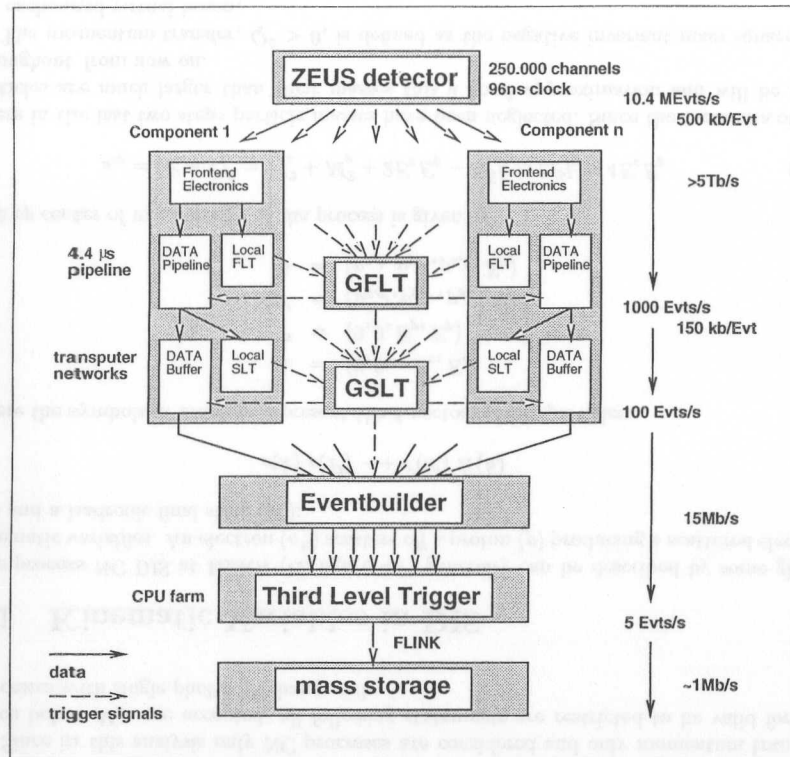
Figure 3.8: *Schematic diagram of the ZEUS trigger and data acquisition system.*

The *Second Level Trigger* (SLT) [Uij92] is designed to reduce the input rate to below 100 Hz. This trigger level is further subdivided in component related parts running on a network of Transputers [B+93b], but it is software-based. Thus, algorithms, like simplified jet finders, can be applied here already to identify desired event types. The result of the local SLTs are combined in the *Global Second Level Trigger* (GSLT) to execute a final decision.

If the event is accepted by the GSLT all detector components send their data to the *Event Builder* [BHV93] which produces the ADAMO event structure [Gre89, FP92] on which the *Third Level Trigger* (TLT) code runs and which is used offline in the analysis.

The TLT consists of a processor farm of Silicon Graphics CPUs. Part of the off-line reconstruction code runs on the TLT which filters out *ep* physics events and reduces the output rate to a few Hz. Accepted events are transferred to the computer center via an optical fiber link (FLINK) and stored on tape. The typical size of an event has been reduced to ~ 150 kByte and the amount of data to be stored is about $0.5 - 1.0$ MByte/s.

The *event selection* for measured data breaks up into two major parts. The first part is the on-line trigger decision and event classification in the reprocessing of the data. This part is defined in common for all users of the ZEUS data. The second part is the final event selection in the individual analysis code defined by each user.

The on-line trigger decision in general is based on relatively loose cuts to reduce background processes but ensure a high acceptance of the processes to be selected. The corresponding cuts in the final event selection are typically tighter unless they are available to the final accuracy already on trigger level.

The on-line event classification is coded as logical flags in a large number of so called *trigger bits* separately for the first, the second and the third level trigger. At ZEUS, in an off-line selection for an analysis, the trigger bits of the stored events can be read from a data base to select a suitable subset of the full data sample which is actually processed by the individual analysis code. This speeds up the selection process.

In addition, for about two years the object oriented data base ZES (*ZEUS Event Store* [Tas97]) has been available. It is generated from the off-line reconstructed data, i.e. with all calibration constants and correction procedures applied, and provides a simple interface to apply user-defined cuts on a large number of physical quantities before accessing the single events. Thus, strongly depending on the applied cuts, an additional significant reduction can be achieved in the number of events which actually have to be processed by the individual analysis code.
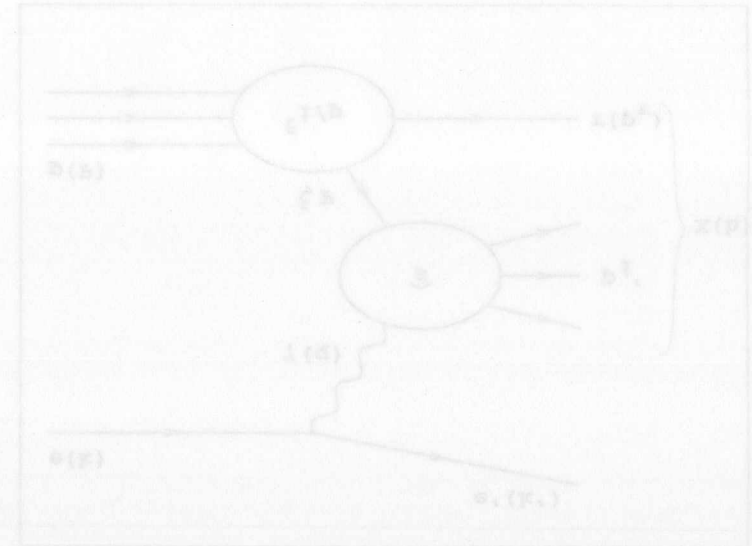
Chapter 4
Deep Inelastic Scattering

With the term *deep inelastic scattering (DIS)* a process is named where a lepton l scatters off a nucleon $\mathcal{N}$ with a large momentum transfer ($Q^2 \gg \Lambda_{\mathrm{QCD}}$). The lepton might be either a charged lepton (e, μ) or a neutrino (ν_e, ν_μ), the nucleon a proton (p) or a neutron (n) consisting of point-like constituents called *partons*. The interaction is mediated by a neutral (γ, Z°) or by a charged boson ($W^\pm$) and is called *neutral current (NC)* or *charged current (CC)* interaction, respectively.

Since in this analysis only NC processes are considered and only momentum transfers much below M_{Z° are accepted, all following statements are restricted to be valid for NC processes with single photon exchange only.

4.1   Kinematic Variables in DIS

The process NC DIS at HERA (cf. figure 4.1) generally can be described by some global kinematic variables. An electron ($e^\pm$) scatters off a proton (p) producing a scattered electron (e') and a hadronic final state (X):

$$e(k)\, p(P) \longrightarrow e'(k')\, X(h)$$

where the symbols in brackets represent the 4-vectors of the particles:

$$
\begin{aligned}
k &= (0, 0, -E_e, E_e) \\
P &= (0, 0, E_p, E_p) \\
k' &= (p_{x,e'}, p_{y,e'}, p_{y,e'}, E_{e'}) \\
h &= (p_{x,h}, p_{y,h}, p_{z,h}, E_h)
\end{aligned}
$$

The *ep* center of mass energy of the process is given by

$$s_{ep} = (P + k)^2 = M_e^2 + M_p^2 + 2E_e E_p - 2\vec{P}\vec{k} \approx 2Pk = 4E_e E_p \tag{4.1}$$

where in the last two steps particle masses have been neglected. Since the momenta of the particles are much larger than their masses this a good approximation and will be used throughout from now on.

The momentum transfer, $Q^2 > 0$, is defined as the negative invariant mass squared of the exchanged virtual boson,

$$Q^2 \equiv -q^2 = -(k - k')^2 \quad . \tag{4.2}$$
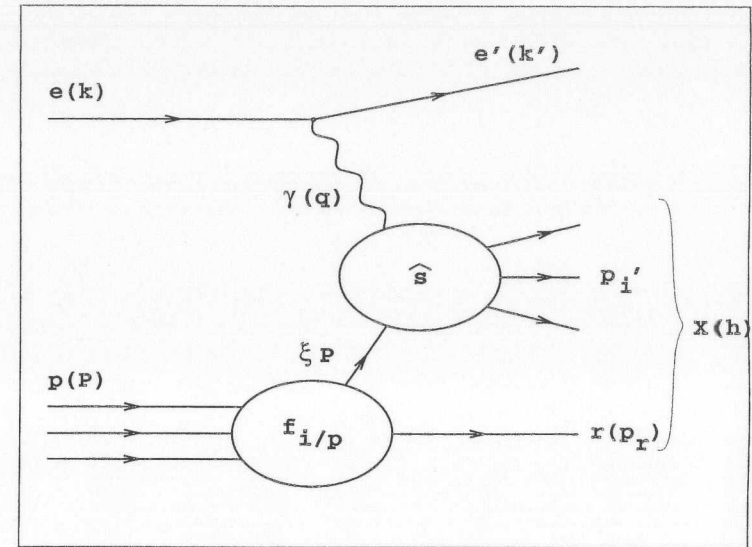
Figure 4.1: *The neutral current deep inelastic scattering process.*

The Bjorken scaling variables, x and y, are defined by [BN68]

$$x \equiv \frac{Q^2}{2Pq} \qquad y \equiv \frac{Pq}{Pk} \quad , \tag{4.3}$$

where x is the momentum fraction of the proton carried by the parton interacting with the virtual photon and y is the fraction of the electron momentum transferred to the proton. Combining the last three equations and ignoring the particle masses yields

$$Q^2 = x \cdot y \cdot s_{ep} \quad . \tag{4.4}$$

The total hadronic mass squared, W^2, is equivalent to the boson-proton center of mass energy $s_{\gamma p}$

$$
\begin{aligned}
W^2 &\equiv Q^2 \frac{1-x}{x} \\
&= y \cdot s_{ep} - Q^2 = 2Pq - Q^2 \approx (P+q)^2 = s_{\gamma p} \quad .
\end{aligned}
\tag{4.5}
$$

The beam energies at HERA are fixed, so s_{ep} is fixed too ($s_{ep} \approx 295\,\mathrm{GeV^2}$) and from equations 4.4 and 4.5 one can see that only two of these four variables are independent. To describe any DIS event one is free to choose a convenient pair. The mass squared of the hard subsystem is

$$\hat{s} = (\xi P + q)^2 \approx 2\xi Pq - Q^2 \tag{4.6}$$

where ξ denotes the momentum fraction of the proton carried by the incoming parton entering the hard interaction. Using eq. 4.3, one can show that only for a massless subsystem

($\hat{s} = 0$) the Bjorken-x equals ξ, otherwise $\xi > x$,

$$\xi \approx x \left(1 + \frac{\hat{s}}{Q^2}\right) \quad . \tag{4.7}$$

In the special case of a (2+1) partonic final state, or a (2+1) jet event (cf. chapter 7), the state has three additional degrees of freedom. They can be described with the following three scaling variables:

- The scaling variable x_p gives the momentum fraction of the parton within the proton in contrast to the momentum fraction x of the system $\hat{s}$ at the boson vertex:

$$x_p = \frac{x}{\xi} = \frac{Q^2}{2p \cdot q} = \frac{Q^2}{Q^2 + \hat{s}} \quad , \tag{4.8}$$

where x_p satisfies the condition $x < x_p < 1$.

- The scaling variable z_p gives the fraction of $E - p_z$ associated with the parton (jet) having the 4-momentum p_1 (p_2):

$$z_{p,1} = \frac{P \cdot p_1}{P \cdot q} = \frac{\sum_1 (E - p_z)}{\sum_{\text{all}} (E - p_z)} = \frac{1}{2} \cos(1 - \Theta_1^*) \quad . \tag{4.9}$$

Θ^* is the polar scattering angle of a parton (jet) in the γ^*-parton center of mass system, where γ^* is the exchanged virtual boson. The sum in the denominator is performed over *all* ($i = 1, 2$) scattered partons, i.e. the current part of the hadronic final state. z_p always satisfies the condition $0 < z_p < 1$ and for the two partons one gets two values symmetric around $z_p = 0.5$ so that $z_{p,1} + z_{p,2} = 1$. Therefore, it is sufficient to look only at the range $0 < z_p < 0.5$.

- The azimuth angle ϕ, is defined between the lepton plane $(\vec{k}, \vec{k}')$ and the plane defined by the proton and one of the two final state partons $(\vec{P}, \vec{p}_1)$.

Also useful is the relative transverse momentum p_t between the two final state partons (jets):

$$p_{t,21} = \sqrt{Q^2 \frac{z_p}{x_p} (1 - x_p)(1 - z_p)} \tag{4.10}$$

Finally, the *rapidity* y is given by

$$y = \frac{1}{2} \ln \left(\frac{E + p_z}{E - p_z}\right) \tag{4.11}$$

which in practice, by neglecting the masses, is approximated by the *pseudorapidity* η

$$\eta = -\ln \left(\tan \frac{\Theta}{2}\right) \quad , \tag{4.12}$$

with the polar scattering angle Θ defined with respect to the proton direction. Thus, the pseudorapidity, η, is the more convenient experimental variable.
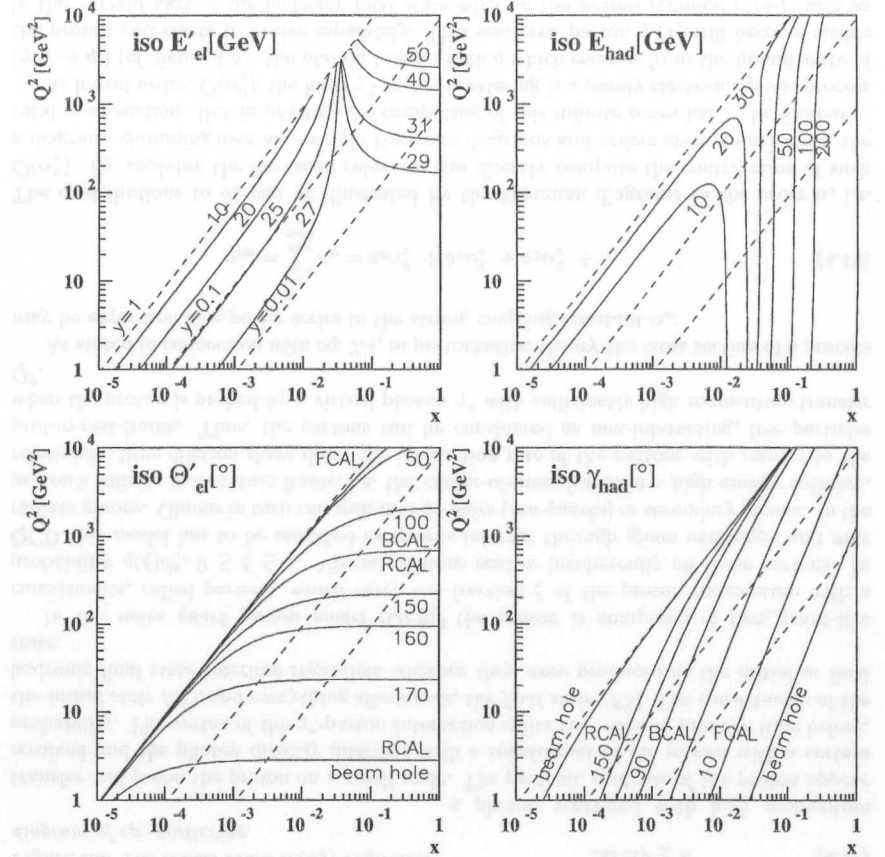
Figure 4.2: *Kinematic variables in the Q^2-x plane for a massless hard subsystem ($\hat{s} = 0$). In full lines: iso-energy lines (top) and iso-lines of the scattering angle (bottom) for the scattered electron (left) and the hadronic system (right). In dashed lines: Iso-y. For calorimeter acceptance limits see section 3.2.2.*

4.1.1 Reconstruction of Kinematic Variables

The relations between the scaling and kinematic variables of the final state are complex. Figure 4.2 shows, for a massless subsystem, the iso-lines of energy and scattering angle for the scattered electron and the hadronic system in the plane of Q^2 and x covered by HERA. Also, the iso-y-lines and calorimeter acceptance limits are given. Regions with a high resolution of a certain kinematic variable show narrow iso-lines.

Scaling variables can be reconstructed from kinematic variables by different methods. If

one measures both the scattered electron and the hadronic final state the event is overconstrained. For reconstruction it is in principle sufficient to know either the electron or the hadronic state, or another suitable combination of parts of them. It has to be decided in terms of resolution and systematic shifts for any kinematic region, which set of variables should be used. In the following, the methods used in this analysis are briefly introduced [Wol93] but there also exist various other methods [BEK91, Hoe91, CSZ91].

The *electron method* uses the energy E'_e and the angle θ of the scattered electron. This method is used at fixed target experiments to reconstruct x and Q^2. It is defined by [Wol93]:

$$
\begin{aligned}
Q^2_{el} &= 2E_e E'_e (1 + \cos\theta) \\
x_{el} &= \frac{E_e}{E_p}\left(\frac{E'_e \cos^2\frac{\theta}{2}}{E_e - E'_e \sin^2\frac{\theta}{2}}\right) \\
y_{el} &= 1 - \frac{E'_e}{E_e}\sin^2\frac{\theta}{2}
\end{aligned}
\tag{4.13}
$$

Its resolution in Q^2 and x becomes poor for low Q^2 and high x, i.e. for soft scattered electrons.

The *Jaquet-Blondel method* [JB+79] uses the total energy E_{had} and the angle γ_h of the visible part of the hadronic final state. There the approximation is made that the total transverse momentum of the particles escaping through the beam hole in proton direction and the total energy of the particles escaping through the beam hole in electron direction can be neglected.

$$
\begin{aligned}
y_{JB} &= \frac{\sum_h(E_h - p_{z,h})}{2E_e} = \frac{E_{had}(1 - \cos\gamma_h)}{2E_e} \\
Q^2_{JB} &= \frac{\left(\sum_h p_{x,h}\right)\left(\sum_h p_{y,h}\right)}{1 - y_{JB}} = \frac{E^2_{had}\sin^2\gamma_h}{1 - y_{JB}} \\
x_{JB} &= \frac{Q^2_{JB}}{s_{ep}\, y_{JB}}
\end{aligned}
\tag{4.14}
$$

while

$$
\cos\gamma_h = \frac{\left(\sum_h p_{x,h}\right)^2 + \left(\sum_h p_{y,h}\right)^2 - \left(\sum_h(E_h - p_{z,h})\right)^2}{\left(\sum_h p_{x,h}\right)^2 + \left(\sum_h p_{y,h}\right)^2 + \left(\sum_h(E_h - p_{z,h})\right)^2}
$$

The angle γ_h characterizes the transverse and longitudinal momentum flow of the hadronic final state. In the naive quark parton model it can be identified with the scattering angle of the struck quark. The resolution for x and Q^2 is worse at high y compared to that using the electron method due to the term $\frac{1}{1-y}$. For low y the resolution is very good. For CC DIS events (exchange of a $W^{\pm}$ boson), this is the only method to reconstruct x and Q^2.

The *double angle method* takes the two scattering angles from the two previous methods:

$$
\begin{aligned}
y_{DA} &= \frac{\sin\theta \cdot (1 - \cos\gamma_h)}{\sin\gamma_h + \sin\theta - \sin(\gamma_h + \theta)} \\
Q^2_{DA} &= 4\,E^2_e \frac{\sin\gamma_h\theta \cdot (1 + \cos\theta)}{\sin\gamma_h + \sin\theta - \sin(\gamma_h + \theta)} \\
x_{DA} &= \frac{E_e}{E_p} \cdot \frac{\sin\gamma_h + \sin\theta + \sin(\gamma_h + \theta)}{\sin\gamma_h + \sin\theta - \sin(\gamma_h + \theta)}
\end{aligned}
\tag{4.15}
$$

This method reduces the sensitivity to the uncertainties in the absolute energy measurements. The resolution in Q^2 and x is worse for low Q^2.

4.2   The Basic Partonic Processes
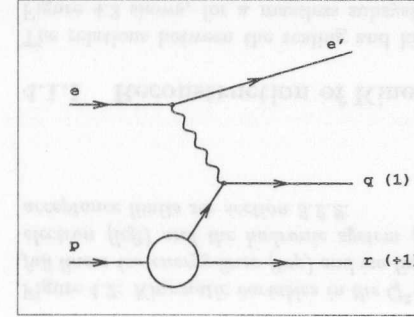
Figure 4.3: *The lowest order $\mathcal{O}(\alpha^0_s)$ Feynman diagram of ep-scattering.*

At HERA, in NC deep inelastic scattering, an electron ($e^{\pm}$) scatters off a proton (p) by exchange of a virtual γ^* producing a scattered electron (e') and a hadronic final state (X):

$$
e\, p \longrightarrow e'\, X\ . \tag{4.16}
$$

The regime of DIS is characterized by α_s being sufficiently small that perturbation theory is applicable. Due to the Heisenberg relation

$$
\Delta r \Delta p \geq \hbar \tag{4.17}
$$

a photon scattered with high momentum transfer will probe the proton on a small scale. The partonic contents of the proton appear resolved and the photon directly interacts with a constituent of the proton with a certain probability. The vertex of the γ^*-parton interaction splits the reaction into the time before, the *initial state (IS)*, and everything afterwards, the *final state (FS)*. The constituents of the hadronic final state interfere regardless whether they were produced at the initial or final state.

In the *naive quark parton model (QPM)* the proton is composed of free, point-like constituents, called partons, which carry the fraction ξ of the proton momentum with a probability $q(\xi)d\xi$, $0 \leq \xi \leq 1$. Virtual photons scatter incoherently off these partons. In QCD this model has to be modified as quarks interact through gluon exchanges and may radiate gluons. Gluons in turn can split into $q\bar{q}$-pairs (*sea-quarks*) or secondary gluons. In the proton's infinite momentum frame, i.e. the center-of-mass frame in a high energy collision, relativistic time dilation slows down the interaction rate of the partons with respect to the proton-rest-frame. Thus, the partons can be considered as non-interacting, free particles when the proton is probed by a virtual photon γ^* with sufficiently high momentum transfer Q^2.

As stated in connection with eq. 2.4, in perturbation theory the cross section of a process may be expressed as a power series in the strong coupling constant α_s:

$$
\sigma_{tot} = \sum_{n=0}^{\infty} \sigma_n = a_0\alpha^0_s + a_1\alpha^1_s + a_2\alpha^2_s + \ldots \tag{4.18}
$$

The contributions to σ_n can be illustrated by the Feynman diagrams to the order n, i.e. $\mathcal{O}(\alpha^n_s)$. By applying the Feynman rules one can directly compute the contribution of such a diagram. Summing over all possible Feynman diagrams and orders gives, in principle, the total cross section. But in practice the computing of this infinite series has to be limited.

At lowest order, $\mathcal{O}(\alpha^0_s)$, the hard γ^*-parton scattering is a purely electromagnetic process ($\gamma^*q \to q l$) (cf. figure 4.3): the photon hits a quark q which escapes from the bound state of the proton and starts to evolve separately. This scattered parton q (1) will become visible in the *current* part of the hadronic final state whereas the *proton remnant* r (+1) acts as spectator and continues on its way. In general in the remaining part of this thesis, a partonic state with n scattered partons will be referred to as $(n+1)$ state taking the proton remnant
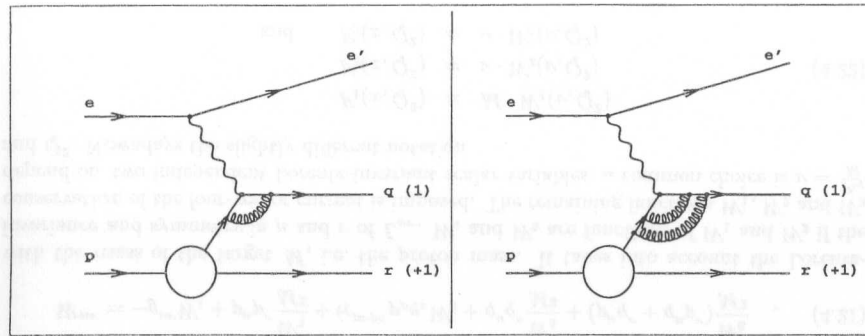
Figure 4.4: *Virtual corrections to the (1+1) parton final state in ep-scattering: a NLO virtual correction of the order $\mathcal{O}(\alpha_s)$ (left) and a NNLO virtual correction of the order $\mathcal{O}(\alpha_s^2)$ (right).*

Figure 4.6: *Virtual corrections to the (2+1) parton final state in ep-scattering: a NLO virtual correction $\mathcal{O}(\alpha_s^2)$ to the QCDC graph (left) and a NLO virtual correction $\mathcal{O}(\alpha_s^2)$ to the BGF graph (right).*

Figure 4.5: *First $\mathcal{O}(\alpha_s)$ Feynman diagrams of ep-scattering leading to (2+1) events: QCD Compton scattering (left) and boson gluon fusion (right).*
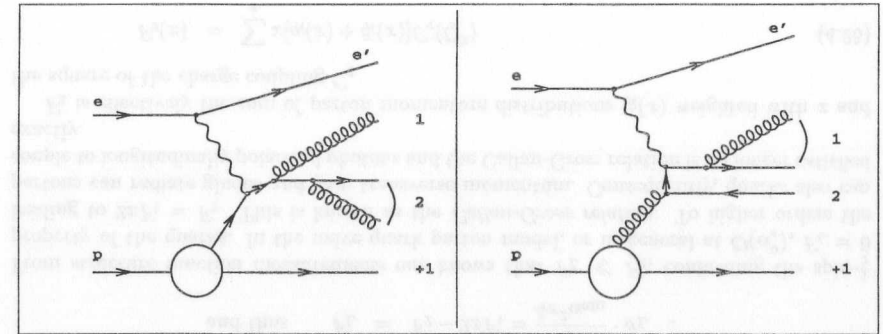
Figure 4.7: *Some generic second $\mathcal{O}(\alpha_s^2)$ Feynman diagrams of ep-scattering. Due to finite resolution these (3+1) parton final states might lead to (2+1) events as indicated here by the bent line.*

into account, since at HERA, parts of the proton remnant usually become visible. The further evolution of both into *jets* will be the subject of chapter 7.

Figure 4.3 only gives the $\mathcal{O}(\alpha_s^0)$ *leading order* (LO) process to the (1+1) parton final state. There are also diagrams with additional virtual QCD corrections, i.e. gluon and quark loops, leading to the (1+1) parton final state. In general each extra parton gives rise to an extra power of α_s in the order of the process. Figure 4.4 gives an example with one extra gluon and an example with two extra gluons. The corresponding orders in perturbation theory are $\mathcal{O}(\alpha_s^1)$ and $\mathcal{O}(\alpha_s^2)$, respectively, which are called *next-to-leading order* (NLO) and *next-to-next-to-leading order* (NNLO) contributions to the (1+1) parton state[1]. Note that both vertices of an extra gluon may be chosen arbitrarily on the quark line and previous gluon lines, they do not necessarily have to connect the initial and final state as shown in the

examples.

A (2+1) partonic final state needs at least a first order $\mathcal{O}(\alpha_s^1)$ hard γ^*-parton scattering. In general, this is the first order which contains a QCD process. Two graphs to order $\mathcal{O}(\alpha_s^1)$ exist (cf. figure 4.5). Both processes have an extra gluon with respect to the $\mathcal{O}(\alpha_s^0)$ graph which give rise to a factor α_s in the cross section:

- Analogous to the Compton scattering in QED the struck quark may radiate a gluon which is hard enough to get resolved. This is called a *QCD Compton* (QCDC) process. The radiation might happen at initial or final state. To get the QCDC cross section the amplitude of both subprocesses has to be added.

- Similar to photon radiation of charged particles, quarks may radiate and absorb gluons as long as the Heisenberg uncertainty relation is satisfied. A gluon in turn may fluctuate

---

[1]Alternatively these corrections also are called *1-loop* and *2-loop corrections*, respectively.

into a pair of sea quarks $q\bar{q}$. If the photon probes one of the quarks of such a $q\bar{q}$ pair, both quarks are kicked out of the proton since no reannihilation is possible. This is called a *boson gluon fusion* (BGF) process.

Both processes are LO with respect to the (2+1) parton final state. In general the rule holds that for a (n+1) partonic final state the LO contribution is of the order $\mathcal{O}(\alpha_s^{n-1})$.

Now figure 4.6 gives two examples of NLO virtual corrections to the (2+1) partonic final state, one for the QCDC and one for the BGF process. These corrections are of the order $\mathcal{O}(\alpha_s^2)$. Note that the order $\mathcal{O}(\alpha_s^2)$ is the lowest order which includes the *triple gluon vertex*, either as NLO correction to the (2+1) state or as NNLO order correction to the (1+1) state.

Real second order $\mathcal{O}(\alpha_s^2)$ processes usually lead to (3+1) partonic final states. But due to the finite resolution in the reconstruction of the hadronic final state, these generic (3+1) states may be reconstructed as (2+1) states (cf. figure 4.7) and contribute to the (2+1) cross section. In turn this may happen also for real $\mathcal{O}(\alpha_s^2)$ (2+1) states which might be reconstructed as (1+1) states. In addition, there are generally restrictions from the experimental side which also define whether a parton (or evolved jet) is accepted as resolved. Otherwise it is rejected and the (n+1) state migrates to a ((n-1)+1) state.

4.3 DIS Cross Section

A more general approach to describe the deep inelastic scattering which does not look into the details of the hadronic final state is the following. In the single boson exchange approximation the cross section in ep-scattering factorizes into a leptonic $L_{\mu\nu}$ and a hadronic tensor $W^{\mu\nu}$:

$$d\sigma \sim L_{\mu\nu} W^{\mu\nu} \quad . \tag{4.19}$$

The leptonic tensor can be calculated exactly by using QED:

$$L_{\mu\nu} = 2(k'_\mu k_\nu + k'_\nu k_\mu - g_{\mu\nu} Q^2/2) \quad , \tag{4.20}$$

where $g_{\mu\nu}$ is the metric tensor. In the hadronic tensor the ignorance of the structure of the proton and hence the details of the interaction is parameterized in terms of hadronic structure functions W_i. The most general parameterization for the part of $W^{\mu\nu}$ describing the single γ exchange is:

$$W^{\mu\nu} = -g^{\mu\nu} W_1 + p^\mu p^\nu \frac{W_2}{M^2} + i\epsilon^{\mu\nu\rho\sigma} p_\rho q_\sigma W_3 + q^\mu q^\nu \frac{W_4}{M^2} + (p^\mu q^\nu + q^\mu p^\nu) \frac{W_5}{M^2} \quad , \tag{4.21}$$

with the mass of the target M, i.e. the proton mass. It takes into account the Lorentz-invariance and symmetry in μ and ν of $L_{\mu\nu}$. W_4 and W_5 are functions of W_1 and W_2 if the conservation of the four-vector current is imposed. The remaining functions W_1, W_2 and W_3 depend on two independent Lorentz-invariant scalar variables; a common choice is $\nu = \frac{P \cdot q}{M}$ and Q^2. Nowadays the slightly different notation

$$
\begin{aligned}
F_1(x, Q^2) &= M \cdot W_1(\nu, Q^2) \\
F_2(x, Q^2) &= \nu \cdot W_2(\nu, Q^2) \\
\text{and} \qquad F_3(x, Q^2) &= \nu \cdot W_3(\nu, Q^2)
\end{aligned}
\tag{4.22}
$$

is widely used with the F_i^p referred to as *structure functions* (SF) of the proton. Roughly said, these structure functions describe how the target is seen by the probing boson. Summing

all orders of the basic processes introduced in sec. 4.2 leads to the total $ep \to e'X$ cross section:

$$\frac{d^2\sigma^{\mathrm{NC}}(e^\pm p)}{dxdy} = \frac{2\pi\alpha_{\mathrm{em}}^2}{x^2 y^2 s} \left[\left(1 + (1-y)^2\right) F_2 - y^2 F_L \mp \left(1 - (1-y)^2\right) x F_3 \right] \quad . \tag{4.23}$$

The structure function F_3 only becomes relevant at $Q^2 \approx M_Z^2$ since it describes the parity violation contributions. It does not play a role within the kinematic range used in this analysis.

In eq. 4.23 the definition $F_L = F_2 - 2x F_1$ has already been used which is suggested by the relation of the structure functions to the helicity cross sections of transverse, $\sigma_T^{\gamma^* p}$, and longitudinal, $\sigma_L^{\gamma^* p}$, polarized photons:

$$
\begin{aligned}
F_1 &= \frac{Q^2}{8x\pi^2\alpha_{\mathrm{em}}} \cdot \sigma_T \\
F_2 &= \frac{Q^2}{4\pi^2\alpha_{\mathrm{em}}} \cdot (\sigma_T + \sigma_L)
\end{aligned}
\tag{4.24}
$$

$$\text{and thus} \qquad F_L = F_2 - 2x F_1 = \frac{Q^2}{4\pi^2\alpha_{\mathrm{em}}} \cdot \sigma_L \quad .$$

From structure function measurements one knows that $F_L \ll F_2$, confirming the spin-$\frac{1}{2}$ property of the quarks. In the naive quark parton model, or in general at $\mathcal{O}(\alpha_s^0)$, $F_L = 0$ leading to $2x F_1 = F_2$. This is known as the *Callan-Gross relation*. To higher orders the partons can radiate gluons and gain transverse momentum. Consequently, quarks also can couple to longitudinally polarized photons and the Callan-Gross relation is no longer satisfied exactly.

F_2 is effectively the sum of parton momentum distributions $q_i(x)$ weighted with x and the square of the charge coupling C_q

$$F_2(x) = \sum_q x[q_i(x) + \bar{q}_i(x)] C_q(Q^2) \tag{4.25}$$

$$\text{with} \quad C_q(Q^2) = e_q^2 - 2e_q V_e V_q \left(\frac{Q^2}{Q^2 + M_Z^2}\right) + (V_e^2 + A_e^2)(V_q^2 + A_q^2) \left(\frac{Q^2}{Q^2 + M_Z^2}\right)^2$$

in the general case of the complete neutral current (γ and Z) exchange. Hence, for pure electromagnetic (γ^*) lepton-proton scattering , $lp \to lX$, with four flavors F_2 becomes

$$F_2^{em}(x) = x \left[\frac{4}{9}(u(x) + \bar{u}(x) + c(x) + \bar{c}(x)) + \frac{1}{9}(d(x) + \bar{d}(x) + s(x) + \bar{s}(x)) \right] \quad . \tag{4.26}$$

Here not only the *valence quarks* (uud for the proton) are considered but also the infinite number of sea quark pairs $q\bar{q}$. When the proton is probed at the momentum scale Q, the sea contains all quark flavors with mass $m_q \ll Q$.

In fact, the relations 4.24 to 4.26 have been given in the *Bjorken limit* ($Q^2 \to \infty$, $\nu \to \infty$ but $\frac{2M\nu}{Q^2}$ finite) where the structure functions *scale* with Q^2, i.e. $F_2(x, Q^2) \to F_2(x)$. This scaling behavior is plausible since the resolving power of a probing photon increases with Q^2 like:

$$\lambda = \frac{h}{|q|} \approx \frac{2Mx}{Q^2} \quad , \tag{4.27}$$

which does not change the view on point-like constituents.
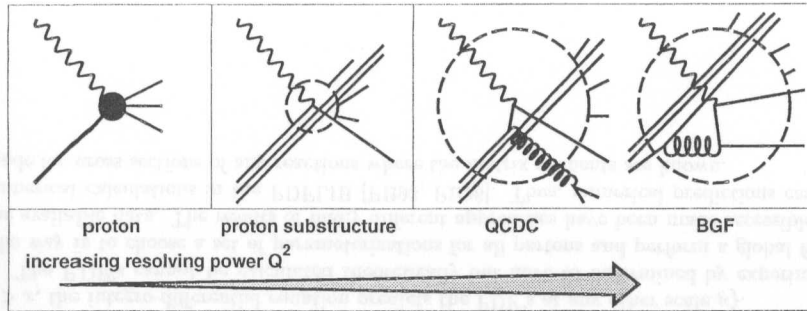
Figure 4.8: *The resolution of the proton constituents depends on Q^2 and causes scaling violations of $F_2(x, Q^2)$.*

At physical scales Q^2 one finds scaling violation for the structure functions requiring the generalized parton distribution functions $q(x, Q^2)$. This is interpreted as follows: At low Q^2 the resolution of the exchanged proton is rather broad and just the coarse valence quark substructure of the proton is seen (cf. fig. 4.8). With increasing Q^2 the resolution becomes finer and quarks, which have radiated a gluon before the interaction (QCDC), or $q\bar{q}$-pairs, originating from radiated gluons (BGF), may be resolved. This means that the history of a quark before it interacts with a photon becomes important. Then in general the Bjorken-x measured at the interaction vertex is smaller than the longitudinal momentum fraction ξ of the incoming parton entering the hard interaction. Therefore, the parton distributions $q(\xi, Q^2)$ for all momentum fractions ξ in the range $x < \xi < 1$ contribute to the considered process measured at x. At large x, where valence quarks dominate, the quark density, and hence F_2, falls with Q^2 since the probability rises that a quark with momentum ξ will be shifted below x by gluon radiation. At small x the amount of $q\bar{q}$ pairs and gluons in the partonic 'sea' increases and thus, with increasing resolution Q^2, F_2 rises. It is one of the main goals of HERA to measure F_2 down to very low x and up to highest Q^2. The described scaling violations, in conjunction with the strong rise of $F_2^{\gamma^*p}(x, Q^2)$ at small x at fixed Q^2, has been measured by ZEUS and H1 [ZEU93a, Qua96, Sur98, H193].

The formulation of the cross section $\sigma^{\mathrm{NC}}(e^\pm p)$ in terms of structure functions is very useful in order to measure and describe the total behavior of the ep-scattering to all orders. However, if one likes to study the internal structure of the hadronic final state in terms of the basic partonic processes of sec. 4.2, fixed order perturbation theory is needed for the calculations where the physical observables are formulated as power series of the coupling constant α_s. This approach is addressed in section 6.1.

4.4 Parton Density Functions

Relations like 4.26, obtained for various reactions, can in principle be inverted to give individual *parton density functions* $xq_i(x, Q^2)$ (PDF) in terms of the measured structure functions characteristic for the given target.

The introduction of PDF's in eq. 4.25 is an expression of the important *factorization theorem*. It states that a hadronic cross section, σ, is the sum over the cross sections of all subprocesses, $\hat{\sigma}$, of all partons, weighted with the probability distributions of the parton
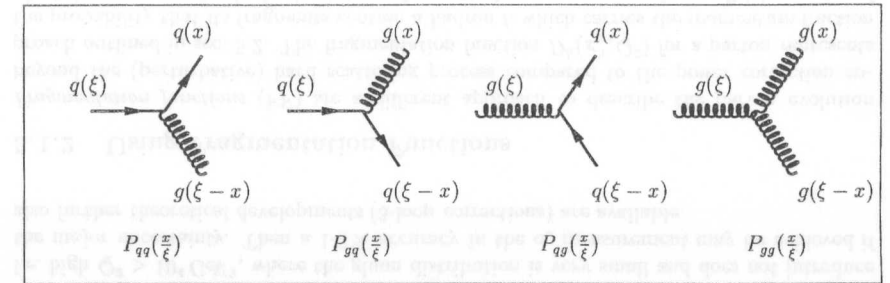
Figure 4.9: *The splitting functions $P_{ab}(\frac{x}{\xi})$. The two diagrams on the left show gluon radiation, the diagrams on the right gluon splitting.*

momenta in the target, the PDF's,

$$\sigma(x, Q^2) = \sum_{i=q,\bar{q},g} \int_0^1 d\xi \; \mathrm{PDF}_{i/h}(\xi, Q^2) \cdot \hat{\sigma}_i(x/\xi, Q^2) \; . \tag{4.28}$$

The $\hat{\sigma}$ is the matrix element of the partonic process, i.e. the γ^*-parton scattering at the characteristic scale Q^2. It describes the short distance cross section of the hard scattering and can be calculated perturbatively since the coupling is small. And it is independent of the type of the incoming hadron. The functions $\mathrm{PDF}_{i/h}(\xi, Q^2)$ describe the probability to find a quark of flavor i in the target h with a momentum fraction ξ at the energy scale Q^2. They depend on the type of the hadron, but not on the particular hard scattering process. Thus, they provide a universal description of the soft, long distance behavior of the partons.

The separation in short and long range physics is called *factorization* and the border is set by the *factorization scale* μ_f (cf. e.g. [S+95, ESW96]). This procedure works similarly to the renormalization of the coupling constant as discussed in sec. 2.2. On one side partons can acquire large transverse momentum, or virtuality k_t, by the emission of gluons up to $k_t^2 \approx Q^2$. On the other side the collinear emission of gluons ($k_t^2 \to 0$) leads to logarithmic singularities which have to be absorbed by a redefinition (renormalization) of the *bare* parton distribution functions $q_0(x)$. Roughly said, any propagator with virtuality $k_t^2 > \mu_f^2$ will contribute to the parton evolution in the hard scattering. Below this scale it will be absorbed into the PDF. Thus, all the infrared sensitivity and $Q^2 \equiv \mu_r^2$ dependence is enclosed in the PDF, as a specific feature of the hadron but universal in terms of the scattering processes.

Different *factorization schemes*, DIS and $\overline{\mathrm{MS}}$, are in use, which handle the *finite* corrections introduced by the QCD differently. But they can be converted into each other unambiguously. In this analysis, by default, the $\overline{\mathrm{MS}}$ scheme is used with the default choice $\mu_r^2 = \mu_f^2 = Q^2$.

It was found that by summing all quark density functions $xq_i(x, Q^2)$ and after integration over x, only about 50 % of the proton momentum can be explained. The missing momentum in the momentum sum rules for the quarks alone was a key hint for the existence of the gluon which mediates the strong interaction between the target constituents. A corresponding *gluon distribution function* $g(x, Q^2)$ describes their momentum distribution in the nucleon. It accounts for the missing part in the sum rules. Presently the gluon density $xg(x, Q^2)$ is still less well constrained as compared to the other parton density functions $xq_i(x, Q^2)$.

The evolution of the parton distribution functions is described by the DGLAP[2] equations [AP77]:

$$\mu_r^2 \frac{\partial}{\partial \mu_r^2} \begin{pmatrix} q_{i/h}(x,\mu_f,\mu_r^2) \\ g_h(x,\mu_f,\mu_r^2) \end{pmatrix} = \tag{4.29}$$

$$\frac{\alpha_s(\mu_r^2)}{2\pi} \sum_{q_i,\bar{q}_i} \int_x^1 \frac{\partial \xi}{\xi} \begin{pmatrix} P_{q_i q_j}\left(\frac{x}{\xi},\alpha_s(\mu_r^2)\right) & P_{q_i g}\left(\frac{x}{\xi},\alpha_s(\mu_r^2)\right) \\ P_{g q_j}\left(\frac{x}{\xi},\alpha_s(\mu_r^2)\right) & P_{gg}\left(\frac{x}{\xi},\alpha_s(\mu_r^2)\right) \end{pmatrix} \begin{pmatrix} q_{j/h}(x,\mu_f,\mu_r^2) \\ g_h(x,\mu_f,\mu_r^2) \end{pmatrix} \; .$$

The $P_{ab}\left(\frac{x}{\xi}\right)$ (cf. fig. 4.9) are called *splitting functions* or *evolution kernels* and are calculable as power series in α_s

$$P_{ab}(x,\alpha_s(\mu_r^2)) = P_{ab}^0(x) + P_{ab}^1(x)\,\alpha_s^1(\mu_r^2) + \dots \; . \tag{4.30}$$

To leading order they have the physical interpretation as the probabilities of finding a parton of type a in a parton of type b with a fraction $\frac{x}{\xi}$ of the longitudinal momentum of the parent parton and a transverse momentum of $k_t^2 \ll \mu_r^2$. They are known up to $\mathcal{O}(\alpha_s)$, i.e. NLO. At LO the QCD predicts the branchings $g \to q\bar{q}$, $q \to qg$, $q \to gq$ and $g \to gg$ as:

$$P_{qq}^0(x) = C_F\left[\frac{1+x^2}{(1-x)_+} + \frac{3}{2}\delta(1-x)\right]$$

$$P_{qg}^0(x) = \frac{1}{2}\left[x^2 + (1-x)^2\right]$$

$$P_{gq}^0(x) = C_F\left[\frac{1+(1-x)^2}{x}\right]$$

$$P_{gg}^0(x) = 2N_c\left[\frac{x}{(1-x)_+} + \frac{1-x}{x} + x(1-x) + \delta(1-x)\frac{(11N_c - 2N_f)}{6}\right] \; . \tag{4.31}$$

where the '+' distribution is defined in the way that its integral with any sufficiently smooth distribution f is

$$\int_0^1 \frac{f(x)}{(1-x)_+} = \int_0^1 \frac{f(x) - f(1)}{1-x} \tag{4.32}$$

with $(1-x)_+ = (1-x)$ for $0 \le x < 1$.

The predictive power of eq. 4.29 is strong. Once one knows the PDF's at a scale $\mu_{0,f}^2$ for $\xi > x$, the integro-differential equation predicts the PDF's at any other scale μ_f^2.

The PDF's cannot be calculated theoretically but have to determined by experiment. The way is to choose a set of parameterizations for all partons and perform a global fit to the available data. The results of many different approaches have been made accessible for numerical calculations in the PDFLIB [PB93, PB96]. Thus, numerical predictions can be made for cross sections of any reactions where the matrix elements are known.

---

[2]DGLAP = Dokshitzer-Gribov-Lipatov-Altarelli-Parisi.

Chapter 5

Strategies to Measure α_S at HERA

This chapter will give an overview about the possible ways to determine α_s from HERA data. Emphasis is placed on the methods which utilize jets.

5.1 α_s from Scaling Violations

5.1.1   Using Structure Functions

The classical method to determine α_s in DIS is to use the scaling violations of the structure functions. As described in sec. 4.4 the scaling of the structure functions is broken at NLO in QCD due to the scale dependence introduced by the DGLAP equations (4.29) and the power series expansion of the splitting functions.

α_s may now be derived from a global QCD fitting procedure performed on the data of the structure function measurements from one or many experiments. In such a fit, as an example, the parton density functions are parameterized by a chosen model with other variables held fixed to find a new optimized PDF. The variables which are let free or held fixed are chosen appropriate to the problem investigated. Presently, by using HERA data, α_s is not treated as free variable but the current world average is used as input. The reason lies in the gluon density function $xg(x,Q^2)$ which presently is not well enough constrained in the low x ranges, where most of the data is taken at HERA, to perform a reliable determination of α_s with a small systematic error.

Estimations exist [BKP96, B+96] for the expected accuracy of an α_s determination using this method when the total integrated luminosity at HERA will be accumulated to about $0.5 \ldots 1.0\,\text{fb}^{-1}$. Then enough statistics is available to restrict the kinematic range to high x, i.e. high $Q^2 > 10^4\,\text{GeV}^2$, where the gluon distribution is very small and does not introduce the major uncertainty. Then a 1-2 % accuracy in the α_s measurement may be achieved if also further theoretical developments (3-loop corrections) are available.

5.1.2   Using Fragmentation Functions

Fragmentation functions (FF) are a different approach to describe the parton evolution beyond the (perturbative) hard scattering process compared to the power correction approach outlined in sec. 5.2. The fragmentation function $D^h(x_p^h, Q^2)$ for a parton represents the probability that its fragments contain a hadron h which carries the momentum fraction x_p^h of the parton p. In the basic picture of a scattering process given in sec. 7.1 by means of fig. 7.1, fragmentation functions model the partonic fragmentation and the non-perturbative

hadronization, in one step. It is expected that FF are identical for parton splittings initiated by (anti-)quarks or gluons. Depending on the region of phase space, approximate scaling with Q^2 as well as scaling violations are expected for the fragmentation functions, where the latter implies sensitivity to α_s.

At HERA the measurement is performed by using the momentum of the charged particles in the current hemisphere of the Breit frame (cf. sec. 7.4.3), to compare with e^+e^- results, scaled by the hard scattering scale Q

$$x_p^c = |\vec{p}|^{\text{Breit}} \cdot \frac{2}{Q} \quad . \tag{5.1}$$

To derive α_s from the FF one has to follow a two-step procedure. First, one has to derive the fragmentation functions from the measured DIS cross section described by a convolution of the parton density functions, the perturbative hard scattering cross section and the non-perturbative fragmentation functions

$$\frac{d\sigma^{\text{meas.}}}{dx_p^c} \xleftarrow{\text{fit}} \frac{d\sigma^{\text{theo.}}}{dx_p^c} = \underbrace{PDF \otimes \left(\frac{d\sigma}{dx_p^c}\right)^{\text{NLO}} \otimes \underbrace{FF}_{\text{free}}}_{\text{input}} . \tag{5.2}$$

Each of the three components depends on α_s internally, but it is held fixed for this first step. In a second step the procedure is redone, now with known fragmentation functions from the first step and α_s as the only free parameter in all three contributions on the right hand side of eq. 5.2.

First measurements of the fragmentation functions at HERA ([H197a, ZEU97]) compared to e^+e^- results indicate their universality. To perform the second step parameterizations of fragmentation functions had to be provided which allow α_s to be varied. These have become available recently but a remaining problem is the treatment of the s quark in the fragmentation functions which needs to be different in e^+e^- and ep physics [OB98]. Unless this is solved the HERA data are not well enough described to perform a reliable determination of α_s.

5.2　α_s from Event Shapes

A different approach which still uses the hadronic final state is the determination of α_s from *event shapes*. As in e^+e^- physics (cf. sec. 2.3) infrared and collinear safe variables, F, are defined to describe the appearance of the hadronic final state. At HERA it is convenient to use the Breit system to separate the proton remnant from the rest of the hadronic final state. Thus, the event shapes of the current hemisphere of the BREIT frame can be compared to e^+e^- results easily. So far theoretical predictions are available only for a few variables in ep-scattering [DW98], unlike the situation in e^+e^- physics.

The basic principle of the analysis is as follows. From QCD there are predictions for mean values of event shape variables $\langle F \rangle$ to NLO. The remaining difference between these parton level predictions and the measured event shapes at hadron level, i.e. corrected for detector effects, is described by $\mathcal{O}(\frac{1}{Q})$ *power corrections*. No further assumption about fragmentation models are necessary. The power term parameterizes the hadronization corrections and depends only on α_s and an additional universal parameter $\overline{\alpha_o}$

$$\langle F \rangle^{\text{hadr.}} = \langle F(\alpha_s) \rangle^{\text{NLO}} + \langle F(\alpha_s, \overline{\alpha_o}) \rangle^{\text{power}} . \tag{5.3}$$

As an example the power correction part for the *thrust* $T = \max \frac{\sum_i |\vec{p}_i \cdot \vec{e}|}{\sum_i |\vec{p}_i|}$ is:

$$\langle 1 - T \rangle^{\text{power}} = -\frac{4 C_F \mu_I}{\pi Q} \left[\overline{\alpha_o}(\mu_I) - \alpha_s(Q) - b \left(\ln \frac{Q}{\mu_I} + 1 \right) \alpha_s^2(Q) \right] . \tag{5.4}$$

where the Casimir factor C_F and b are known. Here $\overline{\alpha_o}$ regulates the strength of the hadronization, i.e. the non-perturbative contributions to the event shape. Thus, pairs of values for α_s and $\overline{\alpha_o}$ are always derived from each event shape variable, while at the end, all values are expected to be consistent since both, α_s and $\overline{\alpha_o}$, are universal.

An equivalent view of $\overline{\alpha_o}$ is the following. The renormalized α_s diverges when it is extrapolated from the regime of pQCD into the non-perturbative region. Since the physical observables are finite there must be a finite *effective strong coupling* in the non-perturbative regime. No further statement about the size or the shape of this effective coupling is needed. The parameter $\overline{\alpha_o}$ is now the integral over this effective coupling up to a scale μ_I within the perturbative regime

$$\overline{\alpha_o}(\mu_I) = \frac{1}{\mu_I} \int_0^{\mu_I} \alpha_s^{\text{eff.}}(\mu) \, d\mu . \tag{5.5}$$

Good agreement data and predictions has been found in e^+e^- physics for $\overline{\alpha_o}(2\,\text{GeV}) = 0.52 \pm 0.04$ [A$^+$97]. For first results from HERA see [H197b, ZEU98].

5.3　α_s from (2+1) jet events

5.3.1　Using the Jet Rate Ratio R_{2+1}

Finally the total jet cross section can be identified with the total cross section of eq. 4.23 (cf. chapter 7 for the concept of a *jet*):

$$\begin{aligned}
d^2\sigma_{\text{tot}}^{\text{jet}} &= d^2\sigma^{\text{NC}}(e^{\pm}p) \\
&= \underbrace{d^2\sigma_{(0+1)} + d^2\sigma_{(1+1)}}_{\mathcal{O}(\alpha_s^0)} + \underbrace{d^2\sigma_{(2+1)}}_{\mathcal{O}(\alpha_s^1)} + \underbrace{d^2\sigma_{(3+1)}}_{\mathcal{O}(\alpha_s^2)} + \dots ,
\end{aligned} \tag{5.6}$$

with

$$\begin{aligned}
d^2\sigma_{(0+1)} + d^2\sigma_{(1+1)} &= a_{20}\alpha_s^0 &+ a_{21}\alpha_s^1 &+ a_{22}\alpha_s^2 &+ \dots \\
d^2\sigma_{(2+1)} &= &a_{31}\alpha_s^1 &+ a_{32}\alpha_s^2 &+ \dots \\
d^2\sigma_{(3+1)} &= & &a_{42}\alpha_s^2 &+ \ddots ,
\end{aligned} \tag{5.7}$$

$$\nwarrow \text{LO} \nwarrow \text{NLO}$$

with the coefficients $a_{ij} = a_{ij}(\mu_r^2, y_{\text{cut}})$, as the perturbative expansion. Here the $(0+1)$ cross section accounts for valid DIS events which do not lead to a *resolved and valid* current jet within the requirements as described in the context of fig. 4.7. This total cross section can be calculated order by order. Present calculations for ep-scattering cover the terms up to $\mathcal{O}(\alpha_s^2)$, i.e. NLO in the $(2+1)$ cross section.

As can be seen from fig. 4.5 the $\mathcal{O}(\alpha_s^1)$ Feynman graphs of the QCDC and the BGF process are the first which contain a QCD process. The exclusive $(2+1)$ cross section now has three additional degrees of freedom with respect to the total one; a convenient choice is

(x_p, z, ϕ) as defined in sec. 4.1. After integration over the additional variables the fivefold differential cross section $\frac{2\pi x_p d^5\sigma_{(2+1)}}{dxdydx_pdzd\phi}$ becomes:

$$\frac{d^2\sigma_{(2+1)}}{dxdy} = \frac{2\pi\alpha_{em}^2}{yQ^2}\frac{\alpha_s}{2\pi}\cdot\int\frac{dx_p}{x_p}\int dz\int\frac{d\phi}{2\pi}(I_q + I_g) \quad, \tag{5.8}$$

where I_q and I_g denote the quark- (and antiquark-) initiated (QCDC) and the gluon-initiated (BGF) processes, respectively [KMS89]. The integration over ϕ eliminates the helicity dependence of the contributions and the integration over x_p covers the integration over the parton density functions. Thus, $\sigma_{(2+1)}$ can be compared directly with σ_{tot} and the *dijet rate*, R_{2+1}, can be defined giving a direct measurement of α_s in the perturbative expansion:

$$\begin{aligned} R_{2+1} &\equiv \frac{d^2\sigma_{(2+1)}}{dxdy}\bigg/\frac{d^2\sigma_{tot}}{dxdy} \\ &= c_{21}\cdot\alpha_s + c_{32}\cdot\alpha_s^2 \quad, \end{aligned} \tag{5.9}$$

where the coefficients c_{21} and c_{32} are known. The jet rates of higher orders are defined analogously. The α_s^2 term in eq. 5.9 gives the NLO virtual corrections to the generic $\mathcal{O}(\alpha_s^1)$ processes and takes into account unresolved (3+1) states. In order to make a reliable comparison between the measurement, which is to all orders, and the $\mathcal{O}(\alpha_s^2)$ calculations, the rate R_{3+1} in the measurement has to be sufficiently small[1]. Otherwise the fixed order estimate of σ_{tot} would become significantly wrong due to the incompletely known contribution of $\sigma_{(3+1)}$.

Note that the QCDC and BGF contributions to $\sigma_{(2+1)}$ become divergent at some parts of the phase space since

$$d\sigma_{2+1}^{QCDC} \propto \frac{1 + x_p^2 z^2}{(1-z)(1-x_p)} \quad\text{and}\quad d\sigma_{2+1}^{BGF} \propto \frac{[z^2 + (1-z)^2][x_p^2 + (1-x_p)^2]}{z(1-z)} \quad. \tag{5.10}$$

The QCDC contribution diverges if the emitted gluon from figure 4.5 becomes collinear with the proton remnant r ($z \to 1$), if it becomes collinear with the scattered quark ($x_p \to 1$) or if it remains soft ($z, x_p \to 1$). The BGF contribution diverges if the quark either becomes collinear with the proton remnant r or remains soft ($z \to 0$) or if this happens to the antiquark ($z \to 1$).

When using a jet finding algorithm to identify the (2+1) configuration of a hadronic final state, one has to ensure that the phase space used does not include these divergences. The JADE algorithm therefore needs a cut in z, e.g. $0.1 < z < 0.9$. The $K_\perp$ algorithm depopulates the region $z \to 0$ and $z \to 1$ by itself and does not need this cut (cf. sec. 11.1.2 and 11.2). The region $x_p \to 1$ is depopulated at HERA for kinematic reasons.

Finally, α_s is determined by a fit of the measured dijet rate to the predicted rate, varying the strength of α_s:

$$R_{2+1}^{meas.}(\mu_r^2, y_{cut}) \xleftarrow{\text{fit}} R_{2+1}^{theo.}(\mu_r^2, y_{cut}, \alpha_s) = c_{21}(\mu_r^2, y_{cut})\cdot\alpha_s + c_{32}(\mu_r^2, y_{cut})\cdot\alpha_s^2 \quad. \tag{5.11}$$

This is the basic approach to determine α_s in this analysis.

Note that the coefficients c_{21} and c_{32} depend explicitly on the scale μ_r^2 describing the hard scattering process. For this analysis the renormalization scale is taken as $\mu_r^2 = Q^2$. The coefficients depend also on the resolution parameter y_{cut} of the jet finding algorithm. Thus, the analysis has to be performed with a defined jet finding algorithm at a fixed,

---

[1]By using MEPJET it should be $\sigma_{(3+1)} < 0.15\cdot\sigma_{(2+1)}$ [Mir97a]

properly chosen resolution parameter. Finally the coefficients c_{21} and c_{32} have a small intrinsic dependence on α_s itself which is not written in eq. 5.11. This arises from the parton density function which has been integrated over. In this analysis the dependence of the (2+1)-jet rate on the variation of α_s on the used parton density function is not investigated (cf. discussion in sec. 12.1).

5.3.2 Using the Differential Jet Rate $D_2(y_{cut})$

Another variable where α_s can be derived from is the *differential jet rate* $D_2(y_{cut})$ defined as:

$$D_2(Q^2, y_{cut}) \equiv \frac{R_{2+1}(Q^2, y_{cut}) - R_{2+1}(Q^2, y_{cut} + \Delta y_{cut})}{\Delta y_{cut}} \quad. \tag{5.12}$$

D_2 is the rate of events which make the transition from the (2+1) configuration to the (1+1) or (0+1) configuration when the jet resolution parameter is varied from y_{cut} to $y_{cut} + \Delta y_{cut}$. This is in contrast to the original approach [JAD91] where D_2 is normalized by the total number of events.

The advantage of this variable with respect to R_{2+1} is that the values of $D_2(y_{cut})$ viewed as a function of different y_{cut} are not correlated if Δy_{cut} is chosen such that the y_{cut} ranges do not overlap. Thus, not only the value at a particular y_{cut} but also the shape of the distribution $D_2(y_{cut})$ can be fitted.

The disadvantage is the need of higher luminosities to get comparable statistical errors since only a fraction of the events contributing to a value $R_{2+1}(y_{cut})$ is used to determine the corresponding value of $D_2(y_{cut})$, depending on the size of Δy_{cut}.

See sec. 10.4 for the results derived with this method in this analysis.

5.3.3 Using the (2+1) Jet Cross Section

There may be cases where the (2+1) jet cross section cannot be normalized reliably by the total cross section. In the future at ZEUS this probably will happen in the lower Q^2 ranges. To handle the increasing luminosity at HERA the ZEUS trigger branches for general DIS events will be highly prescaled up to medium Q^2, i.e. below a threshold only a fraction of the events will be saved for offline analyses. Special trigger branches with significantly lower rates, as for the class of (2+1) events, can be preserved without prescaling. But the comparison of the (2+1)-jet cross section with the total DIS cross section, obtained from different trigger branches, introduces a large additional uncertainty, due to the different trigger efficiencies and the high prescaling of the one quantity.

In this case α_s can be determined from $\sigma_{(2+1)}$ directly via:

$$\sigma_{(2+1)}^{meas.}(\mu_r^2, y_{cut}) \xleftarrow{\text{fit}} \sigma_{(2+1)}^{theo.}(\mu_r^2, y_{cut}, \alpha_s) = \tilde{c}_{21}(\mu_r^2, y_{cut})\cdot\alpha_s + \tilde{c}_{32}(\mu_r^2, y_{cut})\cdot\alpha_s^2 \quad. \tag{5.13}$$

The drawback of this approach is that one needs to know all efficiencies with high accuracy. In the case of using $R_{2+1}(Q^2, y_{cut})$ the trigger and electron tagging efficiencies cancel out as well as the uncertainties in the luminosity measurement. Here they become important and introduce additional systematic uncertainties.

The results obtained with this method are discussed in section 10.3.

Chapter 6

Status of Jet-Cross Section Calculations in DIS

This chapter will introduce the NLO QCD calculations used to make the predictions on DIS jet cross sections which the measured and corrected data are compared to. Refer to chapter 4 for the definitions of processes and kinematic variables.

6.1 Partonic Cross Section Calculations

The basic hypothesis is that the total cross section of a hadronic process can be written as the incoherent sum of the contributions given by the parton types which are found in a hadron. Each of the partons carries a fraction ξ of the hadron total momentum. In the general case in DIS, the reaction is mediated by an exchange of a vector boson $V = \gamma^*, Z, W$ and the hadronic cross section becomes:

$$d\sigma_H(P) = \sum_{i=q,\bar{q},g} \int_0^1 d\xi \; f_i^0(\xi, \mu_f^2) \cdot d\hat{\sigma}_i(\xi P, \alpha_s(\mu_r^2), \mu_r^2, \mu_f^2) \quad , \tag{6.1}$$

which is similar to equation 4.28. Here $d\hat{\sigma}_i$ is the parton cross section corresponding to a parton with flavor i and $f_i^0(\xi)$ is the bare parton distribution function.

This hadronic cross section now can be split up into a sum of a parity conserving (pc) and a parity violating (pv) part which in turn can be separated in a sum of flavor dependent terms. They are weighted by flavor dependent electroweak coupling coefficients given for the parity conserving case in eq. 4.25 as $C_i(Q^2)$.

The partonic processes in deep inelastic scattering at HERA have the structure

$$e(k) + p(P) \longrightarrow e'(k') + \mathcal{P}_1(p_1) + \ldots + \mathcal{P}_n(p_n) \quad ,$$

where the $\mathcal{P}_i$ denote the final state partons. The corresponding partonic cross sections $d\hat{\sigma}_i$ are products of the leptonic and the hadronic tensor as introduced in section 4.3. Thus, the total hadronic tensor $W^{\mu\nu}$ consists of flavor and parity dependent contributions $W_i^{\mu\nu}(P,q)^{(pc,pv)}$. Each of these parts of the hadronic tensor can now be expressed in terms of spin-averaged squares of the n-body final-state amplitudes $H_i^{\mu\nu}(n)$ via [KMS89]:

$$W_i^{\mu\nu}(P,q)^{(pc,pv)} = \frac{1}{4\pi} \sum_n d\Omega^{(n)} H_i^{\mu\nu}(P,q,p_1,\ldots,p_n)^{(pc,pv)} \quad , \tag{6.2}$$

---

where $d\Omega^{(n)}$ is the n-body Lorentz-invariant phase space. Thus, by using the gauge completed hatted tensors

$$\hat{g}^{\mu\nu} = g^{\mu\nu} + \frac{q^\mu q^\nu}{Q^2} \qquad \text{and} \qquad \hat{p}^\mu = p^\mu + \frac{p \cdot q}{Q^2} q^\mu \tag{6.3}$$

the parity conserving part of the hadronic tensor $H^{\mu\nu}$ consists for the first final state parton p_1 of five covariant hadronic structure functions:

$$H^{\mu\nu\,(pc)} = -\hat{g}^{\mu\nu} H_1 + \frac{1}{Pq} \hat{P}^\mu \hat{P}^\nu H_2 + \frac{1}{Pq} \hat{p}_1^\mu \hat{p}_1^\nu H_3 + \frac{1}{Pq} \left(\hat{P}^\mu \hat{p}_1^\nu + \hat{p}_1^\mu \hat{P}^\nu \right) H_4 \\ + \frac{1}{Pq} \left(\hat{P}^\mu \hat{p}_1^\nu - \hat{p}_1^\mu \hat{P}^\nu \right) H_5 \quad . \tag{6.4}$$

All loop corrections are contained in H_5 which therefore occurs first at $\mathcal{O}(\alpha_s^2)$, i.e. in NLO calculations. To $\mathcal{O}(\alpha_s)$ only $H_1, \ldots, H_4$ contribute and to $\mathcal{O}(\alpha_s^0)$ only H_1 and H_2. The parity violating part $(H_6, \ldots, H_9)$ is neglected in this analysis due to the single γ^*-exchange approximation and the limited phase space.

The five covariant hadronic structure functions are directly proportional to the helicity cross sections σ_{U+L}, σ_L, σ_T, σ_I and σ_A which can be measured. σ_{U+L} and σ_L correspond to the unpolarized and to the longitudinally polarized contribution to the cross section, respectively, σ_T and σ_I, σ_A correspond to the transverse and to the transverse-longitudinal interference contributions. Thus, the n-jet cross section in DIS reads [Mir97b]:

$$d\sigma_{\text{had}}(n_{jet}) \sim \sum_{i=q,\bar{q},g} L_{\mu\nu}^{(pc)} H_i^{\mu\nu\,(pc)} \sim \begin{array}{ll} & (1 + (1-y)^2) & \cdot \; d\sigma_{U+L}(n_{jet}) \\ - & y^2 & \cdot \; d\sigma_L(n_{jet}) \\ + & 2(1-y) & \cdot \cos 2\phi \; \cdot \; d\sigma_T(n_{jet}) \\ - & (2-y)\sqrt{1-y} & \cdot \cos \phi \; \cdot \; d\sigma_I(n_{jet}) \\ + & y\sqrt{1-y} & \cdot \sin \phi \; \cdot \; d\sigma_A(n_{jet}) \quad . \end{array} \tag{6.5}$$

As stated in section 5.3.1 for this analysis the jet cross section will be viewed after the integration over the azimuthal angle ϕ. In this case the contributions from σ_T, σ_I and σ_A cancel. In fixed order perturbation theory the $(2+1)$-jet cross section can be calculated by covariant projection of the hadronic tensor $H^{\mu\nu(pc)}$:

$$\begin{aligned} \sigma_{U+L} &= \left(-\frac{1}{2} g_{\mu\nu} + \frac{3x_p}{pq} p_\mu p_\nu \right) H^{\mu\nu(pc)}(n_{jet}) \\ \sigma_L &= \frac{2x_p}{pq} p_\mu p_\nu \; H^{\mu\nu(pc)}(n_{jet}) \quad . \end{aligned} \tag{6.6}$$

These matrix elements can be calculated up to $\mathcal{O}(\alpha_s^2)$ including real and virtual correction terms, i.e. to NLO QCD a complete calculation can be performed for the exclusive $(2+1)$-jet cross section in DIS ep-scattering. The following processes contribute in this case (cf. figures 4.5 to 4.7 for the corresponding Feynman graphs):

$$\begin{array}{llll} LO & : \; H^{\mu\nu}(\text{real}, \mathcal{O}(\alpha_s^1)) & : \; \gamma^* + q \to q + g \\ & & \quad\;\; \gamma^* + g \to q + \bar{q} \\[4pt] NLO & : \; H^{\mu\nu}(\text{virtual}, \mathcal{O}(\alpha_s^2)) \; \text{1-loop correction} & : \; \gamma^* + q \to q + g \\ & & \quad\;\; \gamma^* + g \to q + \bar{q} \\[4pt] NLO & : \; H^{\mu\nu}(\text{real}, \mathcal{O}(\alpha_s^2)) \quad \text{not resolved } 3^{rd} \text{ jet} : \; \gamma^* + q \to q + g + g \\ & & \quad\;\; \gamma^* + q \to q + q + \bar{q} \\ & & \quad\;\; \gamma^* + q \to q + \bar{q} + g \end{array} \tag{6.7}$$

and in addition the processes with the crossing $q \leftrightarrow \bar{q}$. The matrix elements for all contributions were discussed first in [BK92] and a full listing of all LO matrix elements

---

up to four final state partons can be found in [HZ89]. The major contribution to the (2+1)-jet cross section comes from the first projection ($\sim -g_{\mu\nu}$) in eq. 6.6 and was discussed first in [Gra91] and [Gra94]. The second projection in σ_{U+L} ($\sim p_\mu p_\nu$) contributes to 20 % to 30 % depending on the kinematic range. The contribution from σ_L is small for the kinematic range at HERA (< 1 %). This is caused by the y dependent coefficients $(1 + (1 - y)^2)$ and $-y^2$ and the small mean value of y in DIS ($\langle y \rangle \approx 0.1$).

The matrix elements for jet cross sections and 1-loop corrections can be calculated numerically. A jet finding algorithm is used to find those events with two resolved final state jets - which may consist of up to two partons for (2+1)-jet events to $\mathcal{O}(\alpha_s^2)$. It is essential to perform these calculations to NLO since to LO only a basic description of the cross section and distributions is provided which still is sensitive to uncalculated and potentially large infrared and ultraviolet logarithms. In a NLO calculation the ultraviolet divergences in the virtual 1-loop amplitudes are absorbed by the renormalization procedure (the $\overline{MS}$ scheme is used in this analysis). This introduces an explicit logarithmic dependence on the renormalization scale μ_r^2 and substantially reduces the μ_r^2 scale dependence with respect to LO calculations. The collinear divergences of the initial state are renormalized similarly which leads to the dependence on the factorization scale μ_f^2 with the same net effect. The infrared and collinear divergences of the real contributions to final state partons cancel with the corresponding divergences of the virtual 1-loop corrections for properly defined observables (infrared safe and collinear safe or factorizable), and thus by adding both one obtains finite results. The NLO bremsstrahlung contribution finally introduces an explicit logarithmic dependence on the jet resolution parameter which defines whether a parton is added to a jet.

Using a modified form of the matrix elements (eq. 6.6) a first generation of NLO programs was developed to make predictions on the (2+1)-jet cross sections: DISJET [BM94, BM95] and PROJET [Gra95]. In order to handle the complicated pattern of divergences described above, an implementation was chosen which limited the predictions to the use of the JADE jet finding algorithm. In addition, the jet definition used in both programs did not correspond to a defined recombination scheme (cf. table 7.1). Finally, terms proportional to y_{cut} were neglected. Now a second generation of NLO programs incorporating new theoretical developments is available (MEPJET, DISENT and DISASTER++) which overcomes these limitations.

6.2 Second Generation NLO Programs

MEPJET: MEPJET [MZ96a, MZ96b, MZ97b, Mir97b] provides full NLO calculations for (1+1)- and (2+1)-jet cross sections and distributions in DIS $e^\pm p$-scattering with complete neutral current (γ^* and/or Z) and charged current ($W^\pm$) exchange. It was the first program for NLO cross section predictions which allowed the implementation of an arbitrary jet definition scheme and overcame the other limitations of its predecessors DISJET and PROJET. To achieve this, MEPJET makes use of the *phase space slicing* method (s_{min}-technique) [GG92] and the technique of universal *crossing functions* [GGK93].

Without imposing any jet finding algorithm to define the (2+1) jet phase space the integration over the (3+1) partonic states has to be performed for the full phase space. Thus, the invariant theoretical parameter s_{min} is introduced to isolate the infrared and collinear divergences associated with the phase space regions where partons remain unresolved, i.e. at least one pair of (initial and final state) partons has $s_{ij} = 2p_i \cdot p_j < s_{min}$. An analytical integration is performed over these phase space regions for the final state partons covering the

infrared and collinear divergences. Adding the contributions which cover the corresponding divergences of the virtual corrections one obtains finite results. This contribution to the (2+1) jet cross section is negative and grows logarithmically with the decrease of s_{min}. This logarithmic growth is exactly canceled by the growth of the resolved (3+1) parton cross section. The remaining collinear initial state divergences are factorized into the bare parton densities. The integration over the finite resolved phase space with $s_{ij} > s_{min}$ is done numerically by Monte Carlo techniques. Thus, the 4-momenta of the partons are available and any jet finding algorithm with any set of acceptance cuts may be applied. The resolved and unresolved contributions to the jet cross section finally are added, which causes the dependence on the unphysical parameter s_{min} to disappear in the $s_{min} \rightarrow 0$ limit. In practice, the numerical results on an infrared safe observable are insensitive to the choice of s_{min} if it is sufficiently small.

The factorization of the collinear initial state divergences is handled by the technique of universal crossing functions $C_a(x, \mu_f, s_{min})$. A first contribution comes from the splitting of an initial state parton, p, into a resolved parton, a, and a collinear parton, u, where $|s_{pu}| < s_{min}$. Those parts of this contributions which cannot be factorized into the bare parton densities are absorbed into the crossing functions, which are effective parton functions, consisting of parton densities convoluted with the Altarelli-Parisi splitting functions $P_{p\rightarrow a}(x)$. A second contribution comes from the fact that the process $a \rightarrow up$ with two collinear final state partons ($s_{pu} < s_{min}$) cannot be distinguished from the crossed process $up \rightarrow a$, which leads to a wrong contribution in the parton densities. In the crossing function, $C_a(x, \mu f, s_{min})$, for the initial state parton a, this wrong contribution has been subtracted.

DISENT and DISASTER++: DISENT [CS96b, Sey97a] and DISASTER++ [Gra97] also provide NLO predictions for the dijet production in $e^\pm p$ DIS, but they are limited to the one-γ^* exchange approximation. Comparisons among these calculations and to MEPJET in the one-γ^* exchange approximation yielded so far satisfactory agreements [MZ97a, CS97].

Instead of the phase space slicing method, DISENT and DISASTER++ use the *exact subtraction method* as described in [KS92, CS96a, Sey96, CS97]. To apply it at NLO, two contributions to the (2+1)-jet cross section have to be considered. The first is the exclusive real cross section $d\sigma^R$ with $n+1 = 3$ partons in the current part of the final state; the second the 1-loop virtual correction $d\sigma^V$ with $n = 2$ partons:

$$\sigma^{NLO} \equiv \int d\sigma^{NLO} = \int_{n+1} d\sigma^R + \int_n d\sigma^V \ . \tag{6.8}$$

This sum is finite but each of its terms separately is divergent in $d = 4$ dimensions. By the established method of dimensional regularization $d = 4 - 2\epsilon$ the divergences are replaced by single $1/\epsilon$ and double poles $1/\epsilon^2$. With this alone, the limit $\epsilon \rightarrow 0$ is still singular. The main problem is now to find a proper approximation $d\sigma^A$ for $d\sigma^R$ which has the same pointlike singular behavior. By subtracting $d\sigma^A$ from $d\sigma^R$ the limit $\epsilon \rightarrow 0$ can be performed safely for this difference and one obtains:

$$\sigma^{NLO} = \int_{n+1} \left[d\sigma^R_{\epsilon=0} - d\sigma^A_{\epsilon=0} \right] + \int_n \left[d\sigma^V + \int_1 d\sigma^A \right]_{\epsilon=0} \ , \tag{6.9}$$

where all singularities are now associated with the two last terms in eq. 6.9, whereas the first integral can be integrated numerically in four dimensions. Now one is able to carry out the integration on $d\sigma^A$ over the one-parton subspace which leads to the ϵ poles to cancel them against those from $d\sigma^V$. Afterwards, the $\epsilon \rightarrow 0$ limit can be performed and the remaining integration over the n-parton phase space can be carried out numerically. Again

the numerical calculation via Monte Carlo techniques gives access to the four momenta of the partonic states and allows to impose any jet definition and to apply arbitrary acceptance cuts.

The key which allows to make use of this method and implement it into a NLO calculation is that nowadays there is a recipe for constructing suitable $d\sigma^A$, which meets the demands of this procedure, in a process and observable independent way [CS96a].

Chapter 7

Jet Finding and Jet Algorithms

In this chapter the concept of a *jet in DIS* will be discussed. The basic picture of a scattering process and the definition of a *jet* will be given. The structure of the jet analysis performed in this analysis, the relation of measured to theoretical quantities, will be explained. The demands on all jet finding algorithms in general will be described. And finally, the three major types of jet finding algorithms, cone, Jade and $K_\perp$, of which the latter is applied in this analysis, will be discussed.

7.1   The Basic Picture of a Scattering Process

As explained in section 4.2, at high energies in DIS the exchanged boson scatters off a parton in the proton. However, due to confinement, primary quarks and gluons emerging from hard scattering processes are not directly observable. Models are needed to describe the evolution from the primary partons to the hadronic final state.

Figure 7.1 shows schematically an *ep*-scattering process in DIS and the evolution of the partonic state. The fat lines in figure 7.1 show the basic matrix element process of a boson-gluon fusion as it was introduced with figure 4.5, together with a NLO (1-loop) correction. In a first stage the primary partons evolve by the perturbative emission of secondary partons which in turn evolve themselves. These partonic splitting processes (cf. fig. 4.9) occur in the initial and in the final state. The proton remnant evolves by the same splitting processes. Partons from initial and final state radiation and partons from the current and the remnant part can interfere. In each perturbative splitting the 4-momentum is conserved and, according to the DGLAP equations (eq. 4.29), energy and momentum of the secondary partons are determined by probability densities. Therefore, the primary parton can be reconstructed exactly if it is known which of the secondary partons evolved from it. This evolution process terminates when all particle energies have fallen below the regime of perturbative QCD.

In a next stage the hadronic states are formed from the remaining soft partons by soft, non-perturbative processes called *hadronization*. The origin of a particular hadron is not anymore well defined, i.e. it cannot be ascribed to a primary parton unambiguously. It might be composed of secondary partons evolved from different primary partons or from the color field between them [Sjö93]. Further decay of unstable hadrons might follow on a longer time scale. The totality of hadrons formed in this way is called the *hadronic final state (HFS)*.

A part of the HFS will show up in the detector and produce measurable signals. Due to limited detector resolution and energy losses only a fraction of the information about these
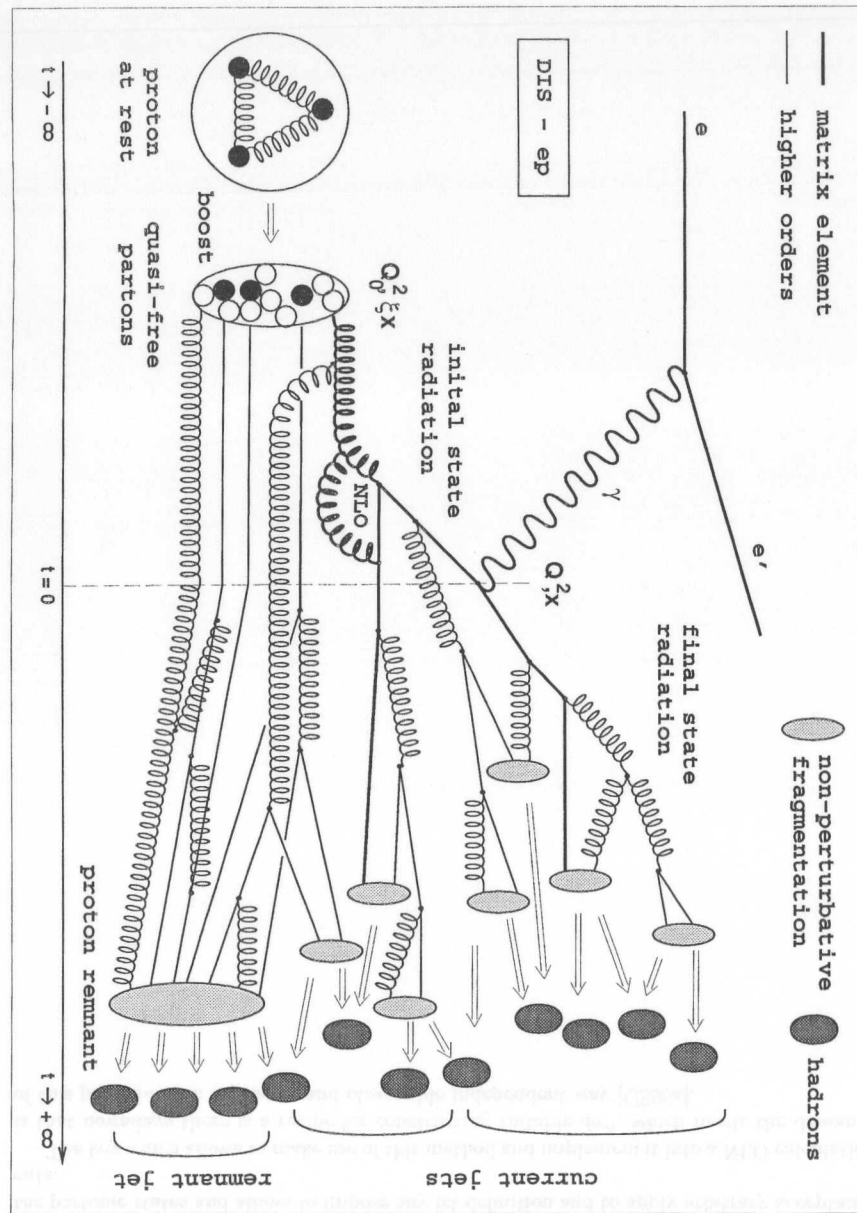
Figure 7.1: *An example process in DIS ep-scattering (here a boson-gluon fusion) and parts of the evolution of the partonic state. See text for explanations.*

hadrons is reconstructed and this information is possibly biased.

According to this picture the *parton*, *hadron* and *detector level* can be defined in the following way:

- The *parton level* contains all partons up to the order in α_s and the n-loop correction available by analytical pQCD calculations. If chosen, it also may contain partons from approximative calculations of higher orders.

- The *hadron level* corresponds to the hadrons making up the hadronic final state.

- And the *detector level* is the totality of the signals produced by the hadronic final state.

While the latter is model independent, the hadron and parton level depend on the model used to describe their generation[1]. The parton level may be chosen to contain only the partons from matrix element calculations. Then it is identical with the elements drawn with fat lines in figure 7.1. For this analysis it also contains partons from a phenomenological model to simulate the effect of higher orders. In this case the parton level contains also some elements drawn with thinner lines in figure 7.1. The motivation for this approach will be given in section 9.1.

The picture given so far is still not complete:

- Electrodynamic corrections, QED initial state radiation, vertex correction and self energy terms, affect the *ep*-scattering at parton level in Monte Carlo simulations and in real physics. They change the kinematic variables of the process, i.e. they shift the point in phase space where the scattering takes place. But the picture of the hadronic process itself is not changed.

- In a hard impact the boson probes the proton on a small scale, since it has a short de Broglie wavelength, and the partons evolve according to pQCD. In addition there may be soft, non-perturbative interactions between the partons with wavelengths at the scale of the proton size. These have small momentum transfers and do not significantly change the momenta from the perturbative interaction but e.g. may change the topology of the HFS.

7.2   What are Jets?

QCD makes predictions for partons, but according to the above picture one only observes detector signals. The aim is to relate the detector measurements to the corresponding quantities at hadron and parton level. For that an abstract construction, called a *jet*, is introduced. With this the final state can be described by *jet observables* which are determined at each level, regardless of which objects it is constructed from (partons, hadrons or detector signals). Thus, the different levels can be compared by means of the jet observables and relations between the levels can be studied (like purities, efficiencies and correction factors).

The concept of a *jet* has two sources of inspiration. On one side hard scattered primary partons mostly radiate collinear and soft secondary partons which leads to a collimated flow of particles. On the other side collimated flows of energy deposition are observed in the detectors for hard scattering processes. The latter can be regarded as a result of the first,

---

[1]For a description of the most important models used to describe the partonic, fragmentation, hadronization and detector processes mentioned in this chapter, see chapter 8.

where the deposed energy and position in the detector is thought to be strongly correlated to the momentum and direction of the primary hard scattered particle.

This correlation is strong as long as the transverse momentum, $p_{t,evol}$, of radiated partons relative to the axis of the primary parton is small with respect to the transverse momentum, $p_{t,parton}$, of the primary parton itself. In DIS ep-scattering this is true for events with large momentum transfer, Q^2, of at least several hundred GeV^2. And it certainly will fail at $Q^2 \approx 1$ GeV because there the transverse momentum produced by the parton evolution and hadronization is of the same order as the momentum of the scattered primary parton.

The concept of a jet has to be the same at each level. Therefore, a *jet* will be thought of as the following:

A jet is the totality of particles or measured signals which can be closely associated with a primary particle of a hard scattering process.

This means that a jet at parton level is built of the primary parton alone, following the hard scattering, of several partons in a later state of the evolution, of a number of hadrons after hadronization and also of a group of signals, possibly from different parts of the detector, when it is measured.

The following additional assumptions will be made:

- *Partons are massless.* Quarks and gluons are treated as massless particles in QCD and in all calculations.

- *The 4-vectors of the hard scattered partons are represented by jets at each level.* At parton level this statement is exact. But hadronization and detector effects turn this into an approximation because the clear assignment to the primary partons is lost.

7.3　Demands on Jet Finding Algorithms

Jet finding algorithms have to fulfill several demands when they are used as a tool to determine jet properties and to provide a mediation between the different levels. The main task is:

Jet finding algorithms have to find collimated structures in a set of 4-vectors, regardless of the source (partons, hadrons or detector signals).

Therefore, three decisions have to be made by the algorithm:

1. *Which* partons, hadrons or detector objects have to be combined next — this is the core of the algorithm.

2. *How* should the selected 4-vectors be associated with a jet to be recombined.

3. *When* has the procedure to be terminated — this is controlled by a *resolution parameter* which defines how close two partons may be to be resolved. It is the radius in cone algorithms and a cut-off parameter in cluster algorithms which is linked to an energy scale.

There are two additional demands from theory which also have their experimental correspondences. A jet finding algorithm has to be *collinear* and *infrared safe* [CDW92, Sey95]. The first requirement means that a parton splitting into two secondary partons with almost no relative transverse momentum, i.e. running in parallel, will give the same result as the original parton without splitting when it is treated by the jet finding algorithm. The second requirement means that secondary parton emission with almost no energy loss by the primary

particle also will not affect the result of the jet finding within the chosen resolution. The first requirement finds its experimental correspondence in the finite detector resolution; only sufficiently separated hadrons can be resolved as different signals. The second requirement corresponds to the experimental demand of noise suppression in the detector.

In theory both requirements serve as a cut-off against the singularities caused by the infinitely rising probabilities when approaching collinear splittings and infinitely soft emissions. In experiment they reflect the non-ideal conditions of measurement. It is required that the analysis is insensitive against the variation of the theoretical cut-off values and the variation of the noise suppression cut-off [2].

7.4　Jet Finding Algorithms

The commonly used jet finding algorithms can be separated in two classes: *geometrical* and *cluster algorithms.*

Geometrical algorithms assign objects to a jet which lie within a conical volume around the jet axis — therefore the name *cone algorithms* arises. The jet axis is found by an optimization procedure and jets get resolved if their axes are separated by at least a cone radius, which acts as distance parameter. The main features of the many different implementations are given in section 7.4.1.

In contrast, cluster algorithms merge together, step by step, pairs of objects (partons, hadrons or detector cells) into one object, until the inter-object separations exceed a given distance parameter. These remaining objects are identified with the found jets. The most common cluster algorithms (JADE and $K_\perp$) will be discussed in sections 7.4.2 and 7.4.3. Their definitions are less intuitive than those of the cone algorithms, but they have some advantages discussed below.

7.4.1　Cone Algorithms
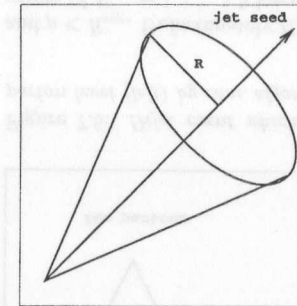
Figure 7.2: *Idea of a cone jet.*

The basic idea of cone algorithms [FM90, Sey95] is to maximize the flow of transverse energy, E_T, or total energy, E, through the base area of a cone with radius R around the jet axis (cf. figure 7.2, typically: $R = 0.7 \ldots 1.0$). A seed object is selected and the distance between this and other objects is given by

$$\Delta R = \sqrt{\Delta \eta^2 + \Delta \phi^2} \quad \text{with} \quad \eta = -\ln\left(\tan\frac{\Theta}{2}\right). \tag{7.1}$$

Here Θ and ϕ denote the polar and azimuthal scattering angle and η is the pseudorapidity. Objects within the cone are recombined to a jet.

This concept looks simple and intuitive in principle but turns out to be indetermined in some cases. This has to be cured by the invention of ad-hoc choices which lead to a larger number of existing implementations.

First, one has to generate a set of *jet seeds* to start the optimization procedure. For this, usually, the E_T or E is summed up in an arbitrary grid of η and ϕ. All entries above a chosen cut-off, E_T^{seed} or E_{seed}, are taken as primary seed jet axes around which the energy is summed up in an area (cone) with radius R. The arbitrariness of the seed thresholds

---

[2]The geometrical detector resolution usually is fixed.
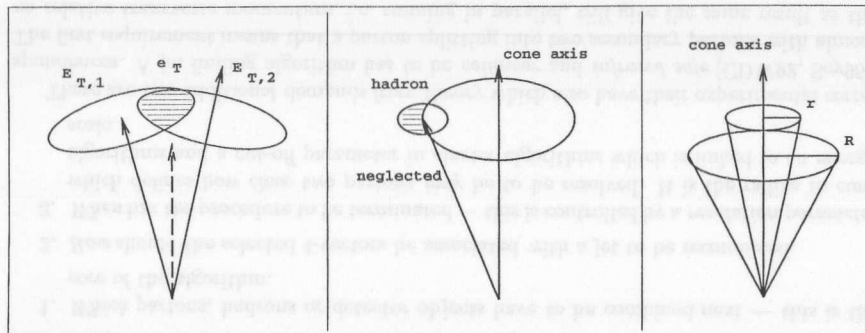
Figure 7.3: *Overlapping cone jets.*

Figure 7.4: *The Energy of a hadron is partially neglected if it is spread around a cone jet border.*

Figure 7.5: *Subcones as internal jet structures.*

Figure 7.6: *Dijet event which is misidentified on the parton level (left) by cone algorithms.*

Figure 7.7: *Introduction of parameter R_{sep}.*

(typically: $E_{T,seed} = 0.3 \dots 1.0\,\text{GeV}$) may cause a bias of the final results. The final jets will be required to have a minimum total energy E_T or E (e.g. $E_T^{min} = 3.0 \dots 6.0\,\text{GeV}$) to ensure their origin from pQCD processes.

At this point the procedure branches into two major types:
Fixed cone algorithms produce an (energy-)sorted list of the jets (objects in the cones around the initial seeds). Beginning at the most energetic jet they remove from further consideration *all* objects contributing to it, i.e. also seeds of less energetic jets, and count it as a final jet. This procedure is repeated with the remaining seeds and objects until no seed is left. *Iterative cone algorithms* calculate new, *weighted* η and ϕ values for the jet axes which are used as seeds in the next step until the procedure is stable. For this calculation the 'Snowmass Convention' [H+90] is mostly applied. With this also an energy corrections can easily be applied. The cone axis is re-evaluated after adding an object as:

$$E_T^{jet} = \sum_i E_{T,i} \quad , \quad \eta^{jet} = \frac{\sum_i E_{T,i}\,\eta_i}{\sum_i E_{T,i}} \quad , \quad \phi^{jet} = \frac{\sum_i E_{T,i}\,\phi_i}{\sum_i E_{T,i}} \quad , \qquad (7.2)$$

where summing is performed over all objects in the cone.

From the explanation above it is clear that not all input to the algorithm has to end up in a final jet. The remaining objects form the so-called *underlying event*.

The next choice to be made is the way those jets should be treated which have *overlapping regions* (cf. figure 7.3). A typical choice is to merge the two jets if more than 50% of the energy of the softer jet is shared by the harder jet. Otherwise they are separated and the common fraction of energy is split up in an arbitrary way.

Finally, there is a theoretical problem with the cone algorithm which leads to the introduction of the artificial parameter R_{sep} [EKS92, Sey95]. Figure 7.6 shows a dijet event with few partons (i.e. at the parton level) and after fragmentation (i.e. at the multi parton or hadron level). Cone algorithms now may fail to separate the two jets at the few parton level, as seen on the left, but reconstruct the jets properly at the multi objects level. In other words, they treat different levels of the evolution differently. This can be cured with a properly chosen parameter R_{sep} which is introduced into the calculation for few partons to resolve the hard radiation (cf. figure 7.7). Two partons will be treated as one jet if $r < R$
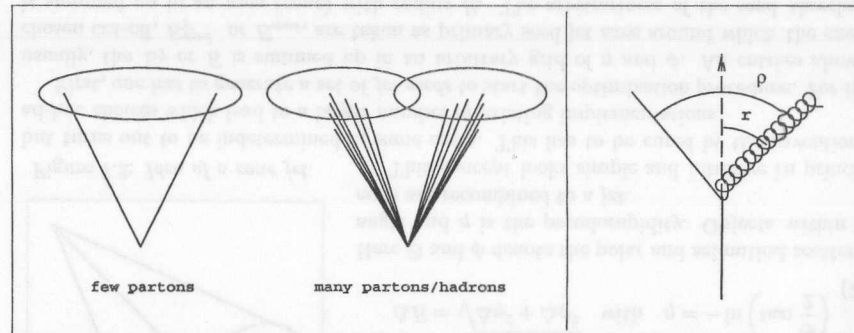
and $\rho < R_{sep}$. Unfortunately R_{sep} is not universal but different for every observable. Typical values of $R_{sep} = 1.2 \dots 1.5$ have been used to fit measurements of inclusive jet cross sections to calculations.

Two further features are worth to be noted:

- At detector level a hadron may spray its energy on both sides of the cone border (cf. figure 7.4). Only the inner part contributes to the jet regardless of whether the hadron 'belonged' to the jet at hadron level or not.

- The natural way of investigating internal jet structures is to look at the energy flow in a *subcone* with radius r (cf. figure 7.5) [Sey97b, Sey97c].

7.4.2   JADE Algorithm

The JADE algorithm [B+87, B+88] belongs to the class of cluster algorithms. Such algorithms merge, step by step, the 4-vectors of objects, i and j, which are close when compared to a chosen distance measure, d_{ij}. Figure 7.8 gives a flow diagram of the common structure. First the relative distance of all objects pairs and the distance of each object relative to the proton direction is calculated, then the minimal distance is searched. Objects associated to the remnant are removed from the procedure. Objects pairs are merged if their relative distance separation is below a *resolution parameter* y_{cut}. The clustering is terminated when all remaining combinations of objects are separated by more than the resolution parameter; these are the resolved jets. Cluster algorithms are *deterministic*, i.e. every object is assigned either to a final jet or to the remnant (jet) with no ambiguity or any ad-hoc parameter. A second, possibly different, resolution cut-off may be used to separate the remnant from the current region. To normalize the distance measure a physical energy scale is generally used.

The merging of the 4-vectors can be performed within different *recombination schemes*. Commonly used possibilities are listed in table 7.1. The E-scheme, with simple 4-vector addition, is the only Lorentz invariant scheme. But it causes the clustered objects to acquire mass when non-parallel 4-vectors are added. All other schemes avoid the acquisition of mass by either not conserving momentum (E0) or energy (P and P0) or by neglecting individual masses of the objects picked up at previous cluster steps (JADE). The schemes P and P0

differ in the way that the latter updates the physical scale every time the energy was not conserved.
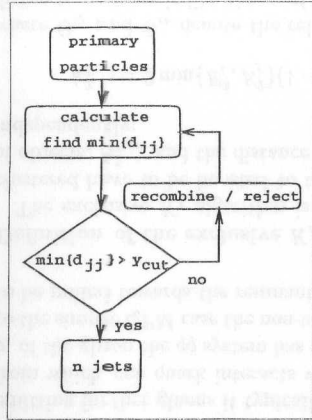
Figure 7.8: *Flow diagram of a cluster algorithm.*

The basic idea of the JADE algorithm is to use the *invariant mass*, m_{ij}^2, of each pair of objects as distance measure:

$$m_{ij}^2 = 2E_i E_j (1 - \cos \Theta_{ij}) \quad . \tag{7.3}$$

This means that particle masses are neglected. The minimum of $\{m_{ij}^2\}$ is tested with:

$$\frac{m_{ij}^2}{M^2} < y_{cut} \tag{7.4}$$

to see whether objects i and j should be merged. Here M denotes a *reference mass* or *scale* which introduces the physical energy scale (e.g. $M^2 \equiv W^2$ or $M^2 \equiv M_{vis}^2$, the visible invariant mass). y_{cut} is the chosen *resolution parameter* (with W^2 a $y_{cut} = 0.02$ is typical, i.e. 2 % of the total hadronic mass). The clustering procedure ends if all remaining pairs $\{ij\}$ fail the test equation 7.4. The proton remnant is included in this procedure and in DIS it is always found as a jet, too. This is the origin of the notation '(n+1)-jet event' for a n-current jet event.

Special treatment is needed when this algorithm is applied to detector level signals. There a non-negligible part of the event may be lost — for DIS events at HERA a major fraction, the proton remnant, escapes down the beam pipe. Therefore, a *pseudo particle* is introduced, built from the missing 4-momentum, which is added to the list of detector signals. This ensures the reconstruction of the proton remnant and the separation of current and remnant region of the signals at detector level.

Using JADE at detector level, the picture of the proton remnant is a jet from which a large fraction escapes through the beam hole. This is unlike the picture when using the cone algorithm where the underlying event simply is the left over fraction of the detector signals not assigned to a current jet. The cone algorithm does not care about objects near the proton direction since usually an angular cut is applied before the jet finding is performed.

scheme	4-vector recombination	remarks
E	$p_k = p_i + p_j$	• Lorentz invariant • jets get masses
E0	$E_k = E_i + E_j \qquad \vec{p}_k = \frac{E_k}{\|\vec{p}_i + \vec{p}_j\|}(\vec{p}_i + \vec{p}_j)$	• conserving E but not $\vec{p}$ • jets are massless
P	$E_k = \|\vec{p}_k\| \qquad \vec{p}_k = \vec{p}_i + \vec{p}_j$	• conserving $\vec{p}$ but not E • jets are massless
P0	$E_k = \|\vec{p}_k\| \qquad \vec{p}_k = \vec{p}_i + \vec{p}_j$	• as P but scale is updated
JADE	$p_k = p_i + p_j$	• E and $\vec{p}$ conserved • but individual masses m_{jj}^2 neglected

Table 7.1: *Recombination schemes for cluster algorithms.*

But the JADE algorithm acts on the full set of objects at parton and hadron level and gets the additional pseudo particle at detector level. Exclusion cuts for accepted current jets, either in pseudorapidity, i.e. angle, or in p_t, are applied afterwards. With JADE the found remnant jet always lies very close to the proton direction ($\eta \approx 8$).

A great theoretical advantage of the JADE algorithm with respect to the cone algorithms is its unique feature of *covariance*, i.e. it is defined in any reference system. This allows the factorization of phase-space for multiple parton emission as in fixed order QCD ME calculations. There it is well suited as cut-off against divergences (e.g. used in LEPTO).
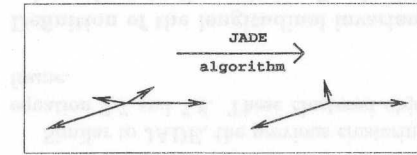
Figure 7.9: *Phantom jets in JADE.*

The invariant mass as distance measure makes the JADE algorithm sensitive to soft, non-perturbative parton radiation processes. And the remnant tends to grab objects from the hadronic final state which originally lay at lower η. Consequently large hadronization effects occur, especially for current jets reconstructed at high η ($\eta > 2$).

Finally, the distance definition in equation 7.3 is *non-local* in angle which may cause JADE to produce *phantom jets* out of soft partons originally emitted by different hard partons, although they have a large relative angle (cf. figure 7.9).

7.4.3 $K_\perp$ Algorithm

The $K_\perp$ algorithm is also a cluster algorithm. So the general features noted in section 7.4.2 are also valid here. Next to the original proposal, the *exclusive $K_\perp$ algorithm*[3] [CDW92], nowadays different approaches exist: the *longitudinal invariant $K_\perp$ algorithm* was proposed by [ES93] and the *angular ordered Durham* and *Cambridge algorithms* were proposed by [DLMW97]. In the following description emphasis is given to the exclusive $K_\perp$ algorithm as it is used in this analysis.

The BREIT frame:

In general, the special feature of the $K_\perp$ algorithm is its distance measure, k_T. In DIS it should be applied in the *BREIT frame* for reasons mentioned below. The BREIT frame is the *(γ^* parton) center-of-mass system*[4]. It is defined by the 4-vector of the exchanged virtual photon γ^* being spacelike:

$$q = (0, 0, 0, -Q) \qquad \text{or} \qquad E_{\gamma^*}' = 0 \quad . \tag{7.5}$$

In other words, within the quark parton model (QPM), the frame is chosen which aligns the virtual photon antiparallel to the struck parton. This causes the struck parton to be bounced directly backwards with no transverse momentum. The virtual photon transfers its full energy to the parton whose longitudinal momentum simply changes sign[5] (cf. figure 7.10) and the corresponding 4-vectors become:

$$p_{parton}^\mu = \left(0, 0, \frac{Q}{2}, \frac{Q}{2}\right) \qquad \text{and} \qquad p_{parton}^{\mu'} = \left(0, 0, -\frac{Q}{2}, \frac{Q}{2}\right) \quad .$$

---

[3]Also called *Durham algorithm* [Dok90].

[4]Another system, strongly related to the BREIT frame and commonly used at HERA, is the *hadronic center of mass system (HCM)*. It is the (γ^*p) center-of-mass system, which is distinct form the BREIT frame only by a longitudinal boost (i.e. in proton direction).

[5]Therefore, *brick wall system* is another name of this frame.
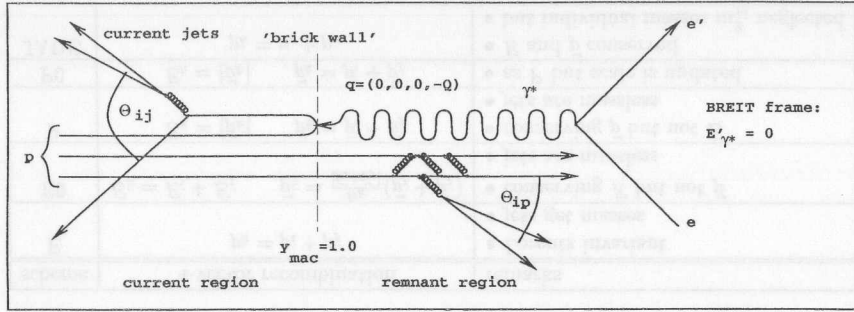
Figure 7.10: *A DIS event in BREIT frame as the $K_\perp$ algorithm sees it. See text for explanations.*

The proton remnant continues on its way. So the event breaks up into two hemispheres: on one side the *current region* where the scattered parton evolves (here the event structure is similar to that of e^+e^--physics) and on the other side the *remnant region* where the proton remnant will be found (which may be compared with event structures at hadron-hadron colliders). This picture does not change if there is a hard gluon emission by a final state quark (as shown in 7.10).

Initial state QCD radiation destroys this simple picture of collinear, antiparallel quark-boson interaction. In a QCD Compton scattering a quark may have emitted a gluon and have virtuality and p_t. Then it has an angle with respect to the proton direction when it is struck by the virtual photon. The virtuality will be canceled either by the momentum transfer of the interaction or by a subsequent final state gluon radiation. In a boson-gluon fusion the initial gluon gets emitted by a valence quark almost in the proton direction. By emitting further gluons it typically gains virtuality and p_t before it fluctuates into a $q\bar{q}$ pair from which one quark interacts with the virtual photon. In addition to the virtuality and p_t of the gluon the $q\bar{q}$ system has invariant mass and the q and $\bar{q}$ have relative p_t. Compared to the simple QPM case the non-zero invariant mass of the $q\bar{q}$ system causes the struck quark to be pulled towards the remnant direction.

Definition of the exclusive $K_\perp$ algorithm:

The exclusive $K_\perp$ algorithm is now defined in the following way: first all objects to be clustered have to be boosted to the BREIT frame. Then the relative distance of each pair of objects, $k^2_{T,ij}$, and the distance of all objects to the proton direction, $k^2_{T,ip}$, are calculated independently:

$$k^2_{T,ij} = 2\min\{E^2_i, E^2_j\}(1 - \cos\Theta_{ij}) \qquad \text{and} \qquad k^2_{T,ip} = 2\,E^2_i(1 - \cos\Theta_{ip}) \qquad (7.6)$$

where Θ_{ij} and Θ_{ip} denote the relative angles in the (η, ϕ)-space. For massless objects this distance measure is like the p_t of the softer relative to the harder object (at least for small angles). The remnant does not enter explicitly in the $K_\perp$ algorithm, i.e. an infinite momentum pointing into the proton direction is assumed. The distance between two objects, including the remnant, gets smaller either when they become more collinear or when the energy of the softer object gets smaller. When clustering is done in terms of minimal k_t the production of phantom jets, cf. fig. 7.9, is suppressed. The exclusive $K_\perp$ algorithm behaves

more like a cone algorithm with event-by-event adjusted cone size than the JADE algorithm because of the request of closeness in 3-dim space. But unlike the cone which tends to get as much E_T as possible from near the cone border the $K_\perp$ algorithm depends more on the center region of the jet.

According to fig. 7.8, the minimum of $\{k^2_{T,ij}, k^2_{T,ip}\}$ is found. If it is of the type $k^2_{T,ip}$ and

$$\frac{k^2_{T,ip}}{\text{scale}} < y_{mac} \qquad (7.7)$$

object i is removed from the list and added to the remnant. If it is of the type $k^2_{T,ij}$ and

$$\frac{k^2_{T,ij}}{\text{scale}} < y_{cut} \qquad (7.8)$$

objects i and j are merged according to a chosen recombination scheme to a new object k which replaces i and j in the list of objects. Here y_{mac} and y_{cut} are chosen *resolution parameters* while *scale* denotes a physical energy scale suitable for the scattering process:

- y_{mac} is the resolution parameter to separate the current from the remnant region, called *macro jets*. At $y_{mac} = 1.0$ the event is divided into two equally large hemispheres as shown in figure 7.10. This is the recommended case. Changing y_{mac} will cause a relative change of the sizes of the two hemispheres; one could think of bending the separating plane, indicated by the dashed line, into a cone shaped surface with its apex at the (γ^*parton) vertex.

- y_{cut} is the resolution parameter for the jet finding, i.e. the desired minimum separation of the current jets in order to be resolved. At HERA values between 0.1 and 1.5 are in use.

- The correct scale to be used with the $K_\perp$ algorithm in ep-scattering is controversial but has to be larger than Λ_{QCD}. Reasonable scales are linear combinations of Q^2, p^2_t and k^2_t or fixed values. From the theoretical point of view the uncertainties in renormalization and factorization scales are lower for p^2_t than for Q^2 and lowest for k^2_t [MZ96b, MZ96d].

Similar to JADE, the previous clustering step is repeated until all remaining objects fail equation 7.7 and 7.8. These clustered objects are the resolved current jets in the BREIT frame.

Definition of the longitudinal invariant $K_\perp$ algorithm:

In contrast to the exclusive $K_\perp$ algorithm (eq. 7.6), the distance measurement in the longitudinal invariant $K_\perp$ algorithm is defined as

$$^{linv}k^2_{T,ij} = \min\{E^2_{T,i}, E^2_{T,j}\}\frac{(\Delta\eta^2_{ij} + \Delta\phi^2_{ij})}{R^2} \qquad \text{and} \qquad ^{linv}k^2_{T,i} = E^2_{T,i} \quad , \qquad (7.9)$$

with a radius parameter R similar to that discussed for the cone algorithms.

Again, the minimum of $\{^{linv}k^2_{T,ij}, {}^{linv}k^2_{T,i}\}$ is found. If it is of the type $^{linv}k^2_{T,i}$, object i is removed from the list and kept as jet. If it is of the type $^{linv}k^2_{T,ij}$, objects i and j are merged by the E_T-weighted recombination scheme (eq. 7.2). That is, they are merged if

$$\sqrt{\Delta\eta^2_{ij} + \Delta\phi^2_{ij}} < R \quad . \qquad (7.10)$$

This means, the issue of which objects merge first depends on transverse energies and angles. But the issue of whether to merge two objects or not is solely a question of angle between them.

Thus, the longitudinal invariant $K_\perp$ algorithm essentially works like a cone algorithm without the disadvantages of the original cone implementations discussed above. Next to the physically interesting jets with large values of E_T it produces a larger number of 'minijets' with small E_T. This approach is suitable to study inclusive cross sections and originally was applied to hadron-hadron physics. Recently interest has grown to use it in ep-scattering, too. Here it is used with a radius parameter of $R = 1$.

Properties of the exclusive $K_\perp$ algorithm:

In addition to the found jets, there are a number of primary objects which are assigned to the remnant. Unlike the JADE algorithm, the $K_\perp$ algorithm in ep-scattering does not contain any pseudo particle information at the detector level. Consequently, in the laboratory frame the left over proton remnant found at detector level does not necessarily point into the proton direction. It rather behaves like the underlying event for the cone algorithm and is spread all over the detector (of course, the average deposited energy is pointing forward). At parton and hadron level, the full event information is available and the leading partons of the proton remnant will boost the remnant left over by the $K_\perp$ algorithm into the proton direction.

If in DIS the $K_\perp$ algorithm is applied in the BREIT frame, the factorization properties of cross section calculations become simple: in the perturbative QCD calculation of the n-jet cross section the jetrate coefficient functions do not explicitly depend on the kinematic variables x and y [CDW92]. This is true also if the $K_\perp$ algorithm is applied in frames derived from the BREIT frame by (x, y, Q^2)-independent Lorentz transformation, but not for different frames or e.g. for the JADE algorithm.

In addition the $K_\perp$ algorithm has the following other properties:

- It can be applied at the parton, hadron and detector level in *exactly* the same way. At the detector level, the left over remnant is not complete as it is for the parton or hadron level.

- The $K_\perp$ algorithm supports a different approach to internal jet structure studies than the cone algorithm. It allows to look for subjet structures within the jet at smaller resolution parameters y_{cut}. This approach corresponds to the partonic evolution described by Monte Carlo models.

- The JADE and $K_\perp$ algorithms only have $\approx 50\,\%$ overlap in phase space, i.e. only half of the events are classified equally by both algorithms, e.g. as dijet event.

- Due to the selection of $min\{E_i^2, E_j^2\}$ in equation 7.6 this algorithm is less sensitive to perturbation from soft particles than the JADE algorithm. Subsequently, smaller hadronization effects and model dependences as for JADE are expected. Additionally the uncertainties in renormalization and factorization scales can be reduced by choosing a proper energy scale [MZ96a, MZ96b, MZ96c, MZ96d, MWZ97].

- The jet cross sections are guaranteed to satisfy the factorization theorem. For that, absolute predictions using PDF's can be made [Sey95].

- And finally the use of $k_\perp$ as distance measure is suggested by the coherence properties of soft QCD emission processes [CDW92, C$^+$91, HIJJ94]. The $K_\perp$ algorithm is unique in meeting these properties.

For the last three points the $K_\perp$ algorithm is preferred by the authors cited above.

A standard implementation of the inclusive and exclusive $K_\perp$ algorithm, also used in this analysis, is supplied with the well documented KTCLUS package written by Mike Seymour [Sey97d]. It is applicable in all physics frames (e^+e^-, pp- and ep-scattering) with an exhaustive number of different modes defined also providing the membership of particles or detector objects to a jet (or remnant) and a facility to search for subjets.

The new developments, the *angular ordered Durham* and *Cambridge algorithms* preserve the advantages of the exclusive $K_\perp$ algorithm while reducing the effect of non-perturbative corrections and improving the subjet resolution [DLMW97].
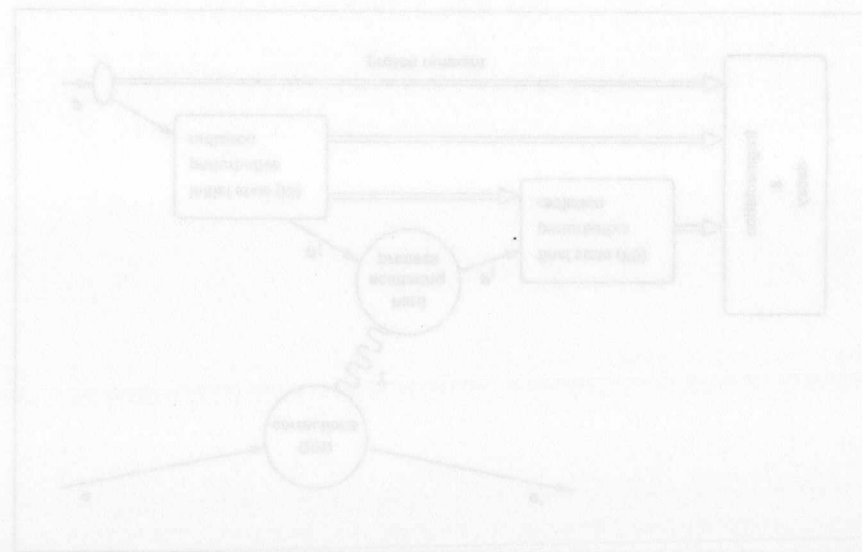
Chapter 8

Monte Carlo Simulation

In this analysis the comparison has to be made for deep inelastic ep-scattering events measured with the ZEUS detector and NLO predictions. Thus, the measured data have to be corrected for detector acceptance and smearing and for hadronization effects, before the comparison to the parton level predictions can be carried out. To obtain the needed corrections, numerical *Monte Carlo* (MC) simulations of ep-scattering events are used, since the totality of the processes is much too complex for a full analytical treatment. In MC programs, the knowledge about the underlying physical processes is implemented partially as the result of analytical calculations, e.g. for the matrix elements, and partially as models, e.g. to describe the non-perturbative particle evolutions or simplify the calculation of the detector response.

MC simulations are obtained by an event-by-event computation of the desired hard interaction followed by the step-by-step computation of the additional stages of the event evolution. For each event a point of phase space is randomly chosen within the allowed range and each decision in the calculations not analytically fixed is made according to probability distributions obtained from former measurements, or defined by model parameters. Thus, many simulated events are needed to model the distributions of measured or predicted observables.

In a first stage, a so called *generator* calculates the cross sections of the possible interactions in the phase space and gives, event-by-event, a list of 4-vectors of the produced particles. Such a generator itself may consist of several interacting parts, modeling different aspects of the interaction in question. Figure 8.1 gives an overview of the important subprocesses for this analysis: the *hard scattering* subprocess, QED corrections, perturbative QCD radiation from the *initial* (IS) and *final state* (FS), i.e. before and after the hard scattering, respectively, non-perturbative fragmentation and hadronization. Beside of the QED corrections, these subprocesses find their correspondence in figure 7.1 in section 7.1.

With the list of generated particles, a second computational stage, the *detector simulation*, is called to trace the 4-vectors through a numerical simulation of the detector, calculate the interactions with the detector material, the induced detector response and finally the signal processing by the data acquisition system.

Since all the information from the generator is stored together with the simulated detector response, measurable quantities can be related to the generated ones and acceptances, efficiencies and corrections can be obtained. As carried out in section 9.1, a MC simulation can be used to correct the measured data only if it describes the data at the level of measurement reasonably well. In this analysis the corrected data should be compared to QCD predictions in order to extract α_s as a free parameter. Thus, also the properties of the simulated parton level have to be consistent with those of the predictions. Otherwise the data would be
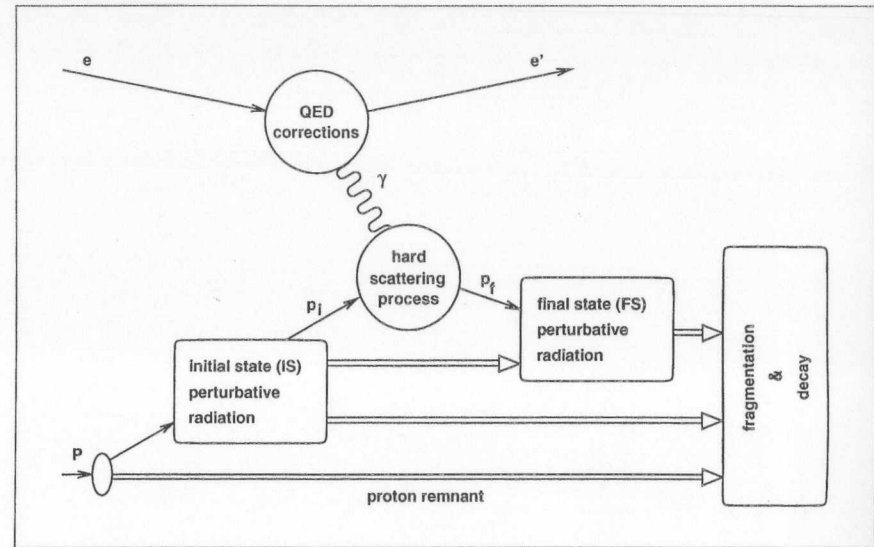
Figure 8.1: *Scheme of a MC generator for ep-scattering events in DIS.*

corrected back to a different state as defined by the prediction and the extraction of the variable observable within the prediction would not be reliable.

8.1 Monte Carlo Models for Perturbative Processes

8.1.1 Matrix Elements

The hard scattering subprocess of the $ep \to e'X$ interaction consists of a pure QED scattering $\gamma q \to q'$ together with QCD corrections, as introduced in section 4.2. The matrix elements (ME) for these processes can be calculated analytically in fixed order perturbation theory, where n in the $\mathcal{O}(\alpha_s^n)$ indicates the number of extra partons introduced by the QCD corrections.

In the presently available MC generators the matrix elements are implemented only to the first order in α_s, i.e. to LO, whereas the predictions are available to NLO. The corrections given by NLO calculations with respect to LO are not small and cannot be neglected in the predictions. The NLO predictions cannot be compared directly with the LO simulations of a MC generator. Thus, additional models are needed to simulate the orders beyond LO and approximate the level of the NLO predictions. This approximation works best if the first of the higher orders is comparable to the correction given by the next-to-leading order and the remaining orders can be neglected.

In this analysis the *Parton Shower* and the *Color Dipole Model* are used to simulate the higher orders. Recently it has become questionable whether these models give sufficiently good approximations of the NLO calculations [DDVZ97]. However, this will remain an open question until NLO MC generators or better models are available. Presently there

is no better way as the comparison of NLO QCD predictions to LO MC with additional simulation of higher orders.

8.1.2 Parton Showers

The *Parton Shower* (PS) approach [BIS87, BS88, IER96] is based on the iteration of the QCD parton branching processes ($q \to qg$, $g \to q\bar{q}$ and $g \to gg$): this is illustrated as higher orders in the example BGF event of figure 7.1. In contrast to the exact fixed order ME treatment, here only the leading $\log Q^2$ approximation of the DGLAP equations (eq. 4.29) is used, which in turn allows to simulate arbitrarily high orders. Thus, an approximate description can be achieved for the higher order effects due to multi particle emission. It is the nature of this approximation that the prediction becomes unreliable for hard parton radiation at large angles. In addition, in the LEPTO implementation of this model, the interference terms between initial and final state PS are neglected, preventing the model being gauge invariant. The latter approximation is forced by the separate procedures in the calculation of the initial and final parton showers.
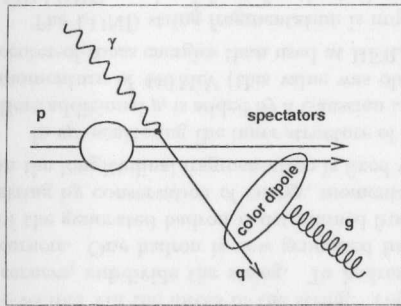
Figure 8.2: *Gluon emission in the Color Dipole Model.*

Since the Parton Shower model itself cannot account well for hard, large angle emissions it is preferable to use it in conjunction with matrix elements. In this combination the latter account for the proper description of the hard scattering whereas the PS model adds softer and collinear emissions. The maximum virtuality in the PS calculations is then set to the cut-off value of the matrix element in the case of $\mathcal{O}(\alpha_s^0)$. In the case of $\mathcal{O}(\alpha_s^1)$ the cut-off value is set to $\hat{s}$ for the final state shower and to the mass m_p^2 of the propagator of the struck parton just before the boson vertex for the initial state shower. This adjusts the border in phase space between the matrix element and the PS calculations such that double counting is avoided. The minimum limit for hard radiation, set by the cut-off in the ME, serves on the other side as maximum limit for the soft and collinear emitted partons by the PS.

The Parton Shower model as described above is implemented in the generator LEPTO [Ing91, IER95, IER96] together with the $\mathcal{O}(\alpha_s^1)$ matrix elements.

The generator HERWIG [M+92] also uses the the PS model in a different implementation together with matrix elements. This PS implementation additionally takes into account coherence between the initial and the final hadronic state.

8.1.3 The Color Dipole Model

In the *Color Dipole Model* (CDM) [ADKT85, Gus86, GP88, AGLP89, Lön95] only two basic assumptions are made. First it is assumed that all gluon emissions can be described by radiation from a color dipole field, stretched between the struck quark and the proton remnant, as illustrated in figure 8.2. Produced gluons may radiate softer gluons and split into $q\bar{q}$ pairs which form further approximately independent color dipoles. Second, the struck quark is considered as point-like, whereas the proton remnant is considered as an extended object. The latter implies coherence conditions which restricts the available phase space for

gluon radiation in deep inelastic ep-scattering unlike to the e^+e^- case, where all partons are point-like.

In contrast to the PS model, here no distinction is made between initial and final state radiation. In addition, partons are not produced with decreasing virtuality but with decreasing transverse momentum.

The Color Dipole Model alone gives rise only to the $\mathcal{O}(\alpha_s^0)$ or the QCDC partonic process. The BGF process, which becomes dominant at small Bjorken x, is missing in this model.

The Color Dipole Model supplemented by the matrix element calculations for the BGF process, to cover all processes to the order $\mathcal{O}(\alpha_s^1)$, is implemented in the generator ARIADNE [Lön92].

8.2 Monte Carlo Models for Soft Processes

The perturbation theory describes the production of colored quarks and gluons which are not observable due to the confinement. Phenomenological models are used to describe long-range phenomena and fragmentation, i.e. the non-perturbative parton evolution and the hadronization into observable, color-singlet hadrons.

8.2.1 Soft Color Interactions

The model of *Soft Color Interactions* (SCI) [EIR96, EIR97] was introduced as an alternative concept to simulate events with rapidity gaps, instead of the usage of parameterizations of an exchanged Pomeron.

The basic idea is that partons emerging from a hard scattering process (including higher order simulation like within the PS model) may interact soft, non-perturbatively with the color medium of the proton as they propagate through it. These soft interactions between any two of the current or remnant partons cause only small changes in the momentum of the partons, below the limit of pQCD, but exchange color. Thus, the color topology of a partonic state entering the hadronization may be significantly changed. In terms of the LUND string model (cf. sec. 8.2.3) this leads in some cases to configurations with color singlet subsystems which hadronize apart from each other, i.e. leading to gaps in the phase space where no hadrons are produced. The more probable case is the creation of topologies without gaps but with a string going back and forth between the partons leading to an enhanced production of hadrons between the regions of the current and the remnant jet.

The model of SCI is implemented together with the ME calculations and PS model in the LEPTO generator, starting from version 6.3, and can be switched on or off by a steering parameter. The strength of its effect is controlled by the probability of two partons to have a soft color exchange.

8.2.2 The Cluster Fragmentation Model

Fragmentation can be described by the decay of clusters [FW80]. Clusters are color-singlet objects which have been formed from groups of partons. The basic steps of this process used together with the PS model by Webber and Marchesini [Web84, MW84] are the following:

- All gluons decay in $q\bar{q}$ pairs which in turn are distributed to the clusters together with the other quarks from the perturbative evolution.

- Clusters with a mass larger than a limit decay iteratively into lighter clusters.

• The clusters decay to hadrons steered by the density-of-states for the particular hadrons.

This rather simple fragmentation model is used in HERWIG.

8.2.3 The LUND String Fragmentation Model

The LUND String Model [AGIS83, BS87, Sjö93] considers the potential of the QCD color forces between partons. Pairs of quarks and anti-quarks are thought to be connected by *strings* formed by the color forces. Additional gluons may be located on the string between the $q\bar{q}$ pair leading to kinks in the string. As the quarks leave each other, the intermediate field energy E rises proportional to their distance l: $E = \kappa \cdot l$, with the string constant κ of about $1\,\mathrm{GeV/fm} \approx 0.2\,\mathrm{GeV^2}$. If the field energy is high enough, the string will be cut into pieces by the production of a $q\bar{q}$ pair at each break in the string. Thus, iteratively, smaller substrings are formed which are treated independently.

While the particles and strings develop, *string motion* takes place. This means that the partons, linked to a string, exchange a continuous flow of infinitesimal fractions of their 4-vectors via the forces of the string. The leading and trailing edges of these flows, called *corners*, subdivide the string. To hadronize a string, it is broken up into pieces at the corners. One hadron is now generated from one broken piece of the string. The 4-vector of the generated hadron is determined from the vectors which belong to the corners of the string by conservation of energy, momentum and flavor. The remaining degree of freedom in the longitudinal fragmentation is fixed with a fragmentation function.

In ep-scattering the inner structure of the proton remnant has to be taken into account. Here additional p_t is added by a Gaussian transverse momentum distribution with an average momentum of 440 MeV (this value was obtained from lepton-nucleon interactions at lower center-of-mass energies than used at HERA).

The LUND string fragmentation is implemented in JETSET [Sjö93] which LEPTO and ARIADNE use by default for the hadronization. It is used with the default parameters throughout this analysis.

8.3 QED Corrections

Higher order corrections at the electron-boson vertex not only modify the cross section of the ep-scattering but also affect the relation between event quantities measured in the detector, such as electron angle and energy, as well as the event kinematics at the hadronic vertex. The latter means that the proton structure is probed at a different point in the phase space.

Figure 8.3 shows the NC Born level ep-scattering diagram together with the correcting diagrams to the order $\mathcal{O}(\alpha_{\mathrm{em}})$. Similar diagrams as (2-4) exist for the exchange of the Z^0 boson. The divergence of the vertex correction term (5) for vanishing photon energies cancels with those from the initial and final state radiation. Thus, a finite correction is obtained. Corrections from terms of the order $\mathcal{O}(\alpha_{\mathrm{em}}^2)$ and higher are neglected in this analysis.

These QED corrections are implemented in HERACLES [KSM92] and can be used together either with LEPTO or ARIADNE in the combined implementation DJANGO [SS91]. No combined implementation with HERWIG is available so far.
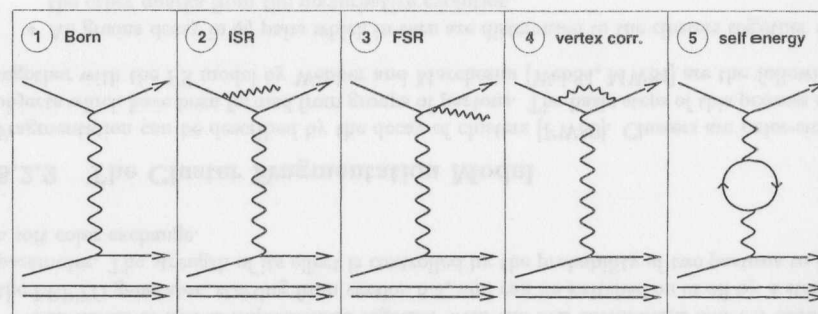
Figure 8.3: *Feynman diagrams of the NC Born-level eq → eq process (1) together with the QED corrections to the order $\mathcal{O}(\alpha_{\mathrm{em}})$: initial (2) and final state radiation (3), vertex correction (4) and the self-energy term (5).*

8.4 The Detector Simulation

Monte Carlo events from all generators have to be processed by the ZEUS detector simulation and offline reconstruction chain before they are comparable to measured data. The response of the different detector components is simulated by the software package MOZART [ZEU93b] which is based on the GEANT program [Bru87]. The former takes into account the material and geometry of the detector components and incorporates the present understanding of the detector and test beam results. The ZEUS trigger decision on the component signals is simulated by the program ZGANA. The full offline event reconstruction is performed by ZEPHYR. It takes into account the calibration constants and treats measured data and MC events in the same way.

The Monte Carlo samples considered in section 8.5 were processed by the FUNNEL versions *num95v2.1* and *num95v2.3*. The differences between them do not affect the components used in this analysis. With both, the trigger configuration *poct95* was used which has become the default one for '95 data analysis. Also with both, the vertex distribution *0.0:1995.0* was used. It has been fitted to the average vertex distribution found in that part of the 1995 data sample, which has been marked as *good for general data analysis*.

8.5 The Generators Used

Table 8.1 summarizes the different combinations of simulation models used within this analysis. They are ordered according to the quality in the description of data at detector level and the parton level predictions, as discussed in section 11.4. They will be refered to by *label* in the subsequent parts of this thesis.

Note that the HERWIG5.9 MC was only used to check the effect of the hadronization model, since QED corrections were not available for it and its description of the data was only fair compared to the samples 1) - 3). Technical problems in the data processing on this MC finally prevented a reliable extraction of the hadron level information. Thus, the hadronization correction caused by the cluster fragmentation could not be added as systematic check before this analysis was completed. The description of the data by the LEPTO6.5 MC was even poorer and the sample was rejected at an early stage of this analysis.

no.	label	parton model	hadronization	QED correction
1)	ARIADNE4.08	CDM + BGF ARIADNE 4.08	LUND string JETSET 7.409	$\mathcal{O}(\alpha_{\mathrm{em}}^1)$ HERACLES 4.5.2
2)	LEPTO6.3$^{\text{tuned}}$	ME + PS LEPTO 6.3	LUND string JETSET 7.401	$\mathcal{O}(\alpha_{\mathrm{em}}^1)$ HERACLES 4.5
3)	LEPTO6.3	ME + PS LEPTO 6.3	LUND string JETSET 7.401	$\mathcal{O}(\alpha_{\mathrm{em}}^1)$ HERACLES 4.5
4)	HERWIG5.9	ME + PS + coherence HERWIG 5.9	cluster fragmentation	—
5)	LEPTO6.5	ME + PS LEPTO 6.5	LUND string JETSET 7.409	$\mathcal{O}(\alpha_{\mathrm{em}}^1)$ HERACLES 4.5.2

Table 8.1: *Used combinations of MC generators. See text for details.*

parameter	meaning	ARIADNE4.08	LEPTO6.3$^{\text{tuned}}$	LEPTO6.3
"common"				
LST(12)	heaviest flavor in p sea	6 (4)		
LST(13)	heaviest quark flavor in BGF	5		
LST(15)	used PDF	GRV94$^{(\text{HO})}$		
LST(18)	α_{em}	α_{em} fixed $(\alpha_{\mathrm{em}}(Q^2))$		
LST(20)	cut-off scheme in ME	$m_{ij}^2 > y_{cut} W^2$		
PARL(3)	parton σ_{p_t} in p [GeV]	0.44		
PARL(5)	Weinberg angle $\sin^2 \Theta_W$	0.2271 (0.2319)		
"CDM"				
MSTA(32)	DIS ME for BGF by	LEPTO (ARI)		
PARA(3)	p_t^{max} in CDM rad. [GeV]	0.6		
PARA(5)	p_t^{max} in QED rad. [GeV]	0.6		
"tuning"				
PARL(7)	probability of SCI	—	0.5 (0.2)	0.2
PARL(8)	y_{cut}	0.005	0.005 (0.0001)	0.0001
PARL(9)	minimum absolute m_{ij} [GeV]	2.0	2.0 (1.0)	1.0
PARL(14)	σ_{p_t} of splitting remn. [GeV]	—	0.35 (0.44)	0.44

Table 8.2: *Parameters of the MC samples. Given are the used values and in parentheses the default values if different.*

The small changes between the implementations of JETSET 7.401 and 7.409 and between HERACLES 4.5 and 4.5.2 can be neglected for this analysis. The steering parameters have been chosen to be the same for each case, i.e. the default values of the older versions. Thus, all the differences in the behavior of the samples 1) - 3) and 5) have to be assigned to the models simulating the partonic distributions.

In the following, the important parameters for this analysis, presented in table 8.2, will be briefly discussed. In general the default values were used for all the models unless stated otherwise (in table 8.2 the default values are given in parentheses if they differ from the chosen values).

As many parameters as possible have been chosen to be the same for the three MC

samples finally used: LEPTO6.3$^{\text{tuned}}$, ARIADNE4.08 and LEPTO6.3. Among other parameters this applies to the number of active quark flavors, the used parton density function, the handling of α_{em}, the cut-off scheme against the divergences in the QCD matrix elements, the primordial transverse momentum of partons in the proton and the Weinberg angle[1]. This ensures that the three samples are comparable.

No changes at all have been applied to the parameters steering the Color Dipole Model. The ARIADNE4.08 MC was used in a common implementation with LEPTO6.5. This way the calculations for the BGF process to supplement the Color Dipole Model was provided by the LEPTO and not by the ARIADNE implementation. Thus, the LEPTO parameters affecting the BGF process, e.g. LST(20) and PARL(8,9), also affect the global behavior of the ARIADNE4.08 model.

Only the LEPTO6.3$^{\text{tuned}}$ sample has been subject to some kind of a *tuning* procedure. In fact, only the numerical parameters, PARL(7,8,9,14), simply were changed from the LEPTO6.3 to the LEPTO6.5 default values to obtain LEPTO6.3$^{\text{tuned}}$.

A significant change between LEPTO6.3 and LEPTO6.5 has been the introduction of the $z - \hat{s}$ scheme for cut-off against divergences in the QCD matrix element calculations in LEPTO6.5: LST(20), $(\hat{s} > \hat{s}_{min}, z_{q,min} < z_q < 1 - z_q)$. It is defined as default procedure in LEPTO6.5 and, thus, the BGF part of ARIADNE4.08 normally would be calculated with this cut due to the common implementation. In order to obtain comparable MC samples and to preserve the feature of the $k_\perp$ algorithm, which do not need any cut in z, this cut-off scheme was set back to the LEPTO6.3 default, $m_{ij}^2 > y_{cut} W^2$, for the production of the ARIADNE4.08 and the LEPTO6.5 sample. The steering parameters PARL(8,9) needed to be adjusted properly, too.

LEPTO6.5 has been developed from LEPTO6.3 by a new tuning to the measured data. The parameter changes for LEPTO6.3$^{\text{tuned}}$ take this into account. Two new major concepts had been introduced with the LEPTO6.3 release: the Soft Color Interaction and the dynamic sea quark treatment. By advancing from LEPTO6.3 to LEPTO6.5, nominally only the probability for the Soft Color Interaction increased from 20 % to 50 % (PARL(7)). Thus, from the point of application both major concepts are treated in the same way in LEPTO6.3$^{\text{tuned}}$ and LEPTO6.5, but the results on the hadronic final state differ significantly. The remaining documented changes between these two versions do not account for the big differences found. Therefore, it may be suspected that substantial undocumented additions or 'bug fixes' in the code were made.

One can state the following general features for MC samples which were processed by the ZEUS detector simulation:

- Monte Carlo's similar to LEPTO6.3 describe well the properties of the HFS concerning jets but significantly underestimate the measured energy flows in the *forward* region between current jet and proton remnant.

- LEPTO6.5, which was tuned under special consideration of the forward energy flow, fails to describe the jet properties well enough.

- The overall description is best done by ARIADNE4.08.

As will be seen in section 11.4, the combined view on the description of measured data and parton level prediction will favor in this analysis ARIADNE4.08 as the best MC for the correction in order to extract α_s from the 1995 data.

---

[1]By mistake, the Weinberg angle has been set to an older world average instead of the presently valid one. But the effect of this error on the final results is very small and can be neglected.

In order to determine α_s from 1996 ZEUS data a different MC sample of the type ARIADNE4.08 has been used, which has three significant differences to the 1995 version of ARIADNE4.08 discussed above:

- this MC sample was processed by the 1996 version of the ZEUS detector simulation to account for the changes introduced in the 1995/96 shutdown

- it was was produced with the default $z - \hat{s}$ -cut scheme (LST(20)) to cut against the matrix element divergences in the BGF processes

- by mistake, in the off-line analysis this sample was treated with the 1995 procedure for the noise reduction (but with 1996 run information) and with the nominal beam energies of 1995, which were slightly different.

The changes in the detector simulation between 1995 and 1996 are sufficiently small to be neglected, but the applied $z - \hat{s}$ -cut scheme prohibits the direct comparison of the 1995 and the 1996 MC and, therefore, the combination of both run periods. Due to the third point the reconstruction of the basic kinematic variables for this MC sample is less reliable.

Finally, the 1996 ARIADNE4.08 MC sample was generated with a threshold of $Q^2 > 70\,\text{GeV}^2$, i.e. the phase space of the 1995 analysis is not fully covered, but only the 4 bins with $Q^2 > 80\,\text{GeV}^2$ can be used to determine α_s.

Chapter 9

The Data Analysis

This section will explain the structure of this analysis and the selection performed on the data and MC samples. It will present the raw data and discuss its features. Finally, the correction procedure applied to the data to correct to parton level is presented.

9.1   Structure of this Jet Analysis

The structure of this jet analysis is shown as a principal sketch in figure 9.1.
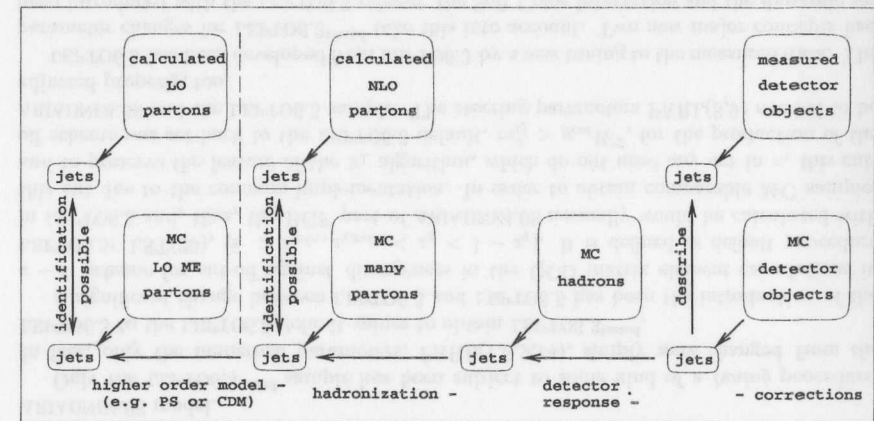
Figure 9.1: *Schematic structure of this jet analysis. See text for explanations.*

On one side there are *QCD predictions*, i.e. matrix element calculations, for inclusive DIS cross section and for exclusive (2+1)-jet parton level cross sections. In *ep*-scattering they are available up to *next-to-leading order* (NLO) and any jet finding algorithm may be implemented (cf. sec. 6.2). The predicted jet cross sections and distributions of kinematic variables need to be compared to the corresponding observed quantities on the other side.

In order to provide a link between predicted and observed quantities *Monte Carlo models* (MC) are used to simulate the basic physical processes, the higher orders of the evolution, the parton fragmentation and hadronization and the detector response to the final state hadrons (cf. ch. 8). By application of a jet finding algorithm the hadronic final state is described by

means of *jet observables*, i.e. the physical quantities determined by such an algorithm. This algorithm has to be applied in the same way to measured data, each MC data set and also to the theoretical calculations. Then by comparing different levels in the MC, the parton, the hadron and the detector level, correction factors or, more generally, unfolding matrices are derived. With this correction procedure the measured data are corrected to hadron and parton level in order to be compared to the theoretical predictions.

Several requirements have to be fulfilled to give confidence to this indirect way of comparing measured data and QCD predictions:

- the measured quantities have to be reproduced by the simulated detector level well

- the differences of reconstructed quantities between detector, hadron and parton level have to be sufficiently small (i.e. the purities and efficiencies for jet finding after hadronization and detector response have to be reasonable high in each single step)

- the parton level simulation has to describe the characteristics of the QCD predictions, i.e. the shape of the quantities but not necessarily the magnitude.

The last point depends the way the parton level is defined. In this analysis a comparison to NLO predictions has to be performed. As only a LO MC simulation of the hard scattering process is available the higher orders are simulated by the *Parton Shower* (PS) and the *Color Dipole Model* (CDM) (cf. sec. 8.1.2 and 8.1.3).

The key quantities measured in this analysis are the inclusive DIS cross section, the dijet cross section and the rate of (2+1)-jet events in the DIS regime, where the last two depend on α_s (cf. sec. 5.3). These quantities are compared to the predictions made by QCD NLO calculations with Λ_{QCD} as the only free parameter. Then α_s is derived from that value of Λ_{QCD} which gives the best fit between the measured quantities, corrected to the parton level, and the predictions.

9.2 Event Selection

The object of this section is to describe the *default DIS event selection* as well as the *default jet finding procedure* which are used throughout this analysis, unless stated differently.

As carried out in section 3.2.3, the event selection for measured data splits up into two major parts: first, the event classification by the on-line trigger system and the further possible specification after the event reconstruction and, secondly, the final selection in the individual analysis code. The cuts applied in the latter have to be at least as tight as all prior cuts in the data handling chain. But in general they are chosen tighter.

The classification by the trigger bits (cf. sec. 8.4) is also available for simulated MC events. But this trigger classification should not be used to preselect MC events like it is done for measured data. This would reject events which meet all requirements at parton and hadron level but fail on detector level. This class of events is needed to calculate the proper acceptance corrections between the detector and the generator levels.

The object oriented ZES data base (cf. sec. 3.2.3), used to speed up the selection of data, is not available for MC, although technically possible. But the gain in selection speed in MC is usually very small. The MC data samples generally are produced with specific sets of parameters suitable for the investigated processes and phase space of a few similar analyses or even only a single analysis. Thus, the fraction of generated events in MC which end up in the final selection is much higher than for measured data. Therefore, the final selection cuts is applied to MC samples directly.

The event selection criteria in the final off-line analysis applied to measured data and to simulated MC events can be grouped into three classes.

- The first class of cuts defines the *phase space* of the analysis. These cuts are independent of the particular shape of the hadronic final state and the definition of any jet finding algorithm. They are applied to all data sets in the same way, i.e. to the measured data, all MC levels and to the parton level predictions.

- The second class of cuts is applied together with a particular jet finding algorithm and defines which of the jets returned by the algorithm are accepted as *valid jets*. These cuts are applied to all data sets in the same way as well.

- The cuts of the third class finally serve to *clean up* the data samples from background, e.g. from different physical processes or misidentified events due to limitations and errors in the reconstruction at detector level. Thus, these cuts are only applied to measured data and to MC events at detector level, but not to the generator levels (parton and hadron) or to the parton level predictions. If a quantity is not modeled well enough in the MC simulation a necessary cut on this quantity may even be applied exclusively to measured data.

9.2.1 Electron identification

A key characteristic to identify a NC DIS event is the identified scattered electron, which is scattered under a sufficiently large scattering angle and is measured in the central part of the detector. In this analysis the default electron identification is based only on the calorimeter information.

Usually in NC DIS the scattered electron appears well separated from the hadronic part of the final state. Only for events with high Bjorken-y and low Bjorken-x, where the electron and the current jet are measured in the RCAL, the separation becomes difficult. In general the algorithms used within the ZEUS collaboration which consist of the following main steps:

- The first step is an algorithm which groups the energy deposited in the calorimeter cells into objects, i.e. *electron candidates*. For this a cluster-, island- or cone-algorithm is applied. The first looks for isolated clusters of cells with deposited energy. The second assigns the energy of each cell to a direct neighbor cell with higher energy, if available, until no further assignment is possible. And the third works in a similar way as the corresponding jet finding algorithm.

- In the second step the algorithm separates electromagnetic and hadronic shower objects by means of the shape of the shower in the calorimeter. Electromagnetic showers typically start immediately after the impact of the particle into the calorimeter. They have a restricted lateral extension.

- From the remaining electron candidates in the final step the algorithm selects the candidate either with the highest energy, highest p_t or lowest Q^2, depending on the algorithm.

The quality of an algorithm to find scattered electrons is determined with MC simulations and is expressed in terms of the purity and efficiency of the electron identification. The purity is the fraction of electrons correctly identified in all found electrons of the MC sample. The efficiency is the fraction of electrons correctly identified in all generated electrons of the

sample. The purity and efficiency of any electron finding algorithm becomes worse for low electron energies. Thus, to ensure a minimum quality in the jet finding typically a minimum energy of the reconstructed electron is required.

In fact, an additional approach has been performed at ZEUS. In the electron finder SINISTRA a neural network has been set up and trained to determine electron candidates and to assign probabilities to these candidates [ACS95]. The advantage of this method lies in the ability to separate distinct distributions in a multidimensional space of many variables rather than to reduce this space into few separated variables which causes the danger of loosing some information. This approach has been shown to give higher purities at any fixed efficiency, and vice versa, with respect to the traditional techniques. Thus, it has become default within the ZEUS DIS working group and is applied as the default method to identify scattered electrons in this analysis. Purities higher than 90 % with efficiencies significantly above 70 % are achieved by all the methods.

As an additional systematic check, the recently developed electron finder EM was used which basically combines a calorimeter based algorithm built upon the mentioned islands-method with charged track finding and a sophisticated matching procedure of both types of information.

Elaborated implementations of electron finders like SINISTRA and EM also involve internal calls to correction routines to account e.g. for cracks in the calorimeter structure or misalignments of detector components.

9.2.2 DIS Preselection

To perform an analysis in the regime of DIS, the first task in the handling of the measured data is to select a clean sample of DIS NC events with the minimum possible contamination by events from other physics processes: like photoproduction (PHP), from diffractive scattering processes and general background processes, e.g. beam-gas and beam-beam pipe interactions or halo- and cosmic-muon events.

The first step of preselection of DIS NC events in this analysis is based on the TLT trigger bit 'DIS bit 14' which in turn gives a subsample of the events selected by the more general 'DIS bit 11'. Both flags were defined by the DIS physics working group of the ZEUS collaboration as general purpose selection cuts to select DIS events.

The basic selection of 'DIS bit 11' consists of a complex combination of information from different branches of the trigger system. A main requirement for a DIS event is a found electron in the acceptance range of the calorimeter by at least one of four different electron finding algorithms (LOCAL, ELEC5, EEXOTIC, SINISTRA) with relaxed selection criteria. A fiducial cut is applied to the hit position of the electron at the calorimeter to ensure a minimal distance from the RCAL beam pipe and therefore its proper reconstruction (harder cuts on this quantity also serve as reduction of the rate of events at low momentum transfer Q^2). As an efficient cut against PHP events a cut on the quantity δ' is performed (cf. sec. 9.2.4). In addition, *global vetos* against test trigger, empty and so-called spark events and a rejection of muon induced events are applied. A timing cut on the calorimeter information is performed if applicable. 'DIS bit 14' defines some tighter thresholds than 'DIS bit 11' and introduces also a cut on the minimum electron energy to cut away the phase space regions where the electron finding algorithms have a low efficiency.

Together with the TLT trigger bit selection, at least one of the FLT trigger bits 'FLT 30' or 'FLT 44' have always been required since this was not requested in all branches used by 'DIS bit 11'. These two first level trigger bits require isolated clusters and minimal thresholds

for the energy deposition in the electromagnetic parts of the calorimeter, respectively. These are requirements to find electrons in a later stage of the event procession.

Within the trigger classifications of the events applied no tracking information was used in this analysis. A cut on the FLT information of the CTD in the '95 running period would have caused a < 1 to 3 % loss of 'good' DIS events — mainly events with an electron in the BCAL.

After the off-line reconstruction of the events the ZES data base was used to narrow the phase space of the preselected data sample which had to be processed by the final analysis code. Here moderate cuts, safely away from the final cut values, were applied on the phase space variables Q^2_{DA}, x_{DA}, y_{DA}, the uncorrected electron energy and on δ'. In addition, a cut on the z-position of the event vertex reconstructed by the tracking system was performed.

Almost all the cuts covered by this DIS preselection were more tightly defined in the individual code used for the final analysis to account for the changes which occur after the application of all corrections in the event reconstruction. Thus, they are not specified in detail here. Although, the cut on the z-position of the vertex in the ZES selection is an exception. It was applied already with the final cut value since the reconstruction for the ZES data base used the same data sources and the same reconstruction procedures as the final analysis code.

9.2.3 Applied Off-Line Corrections and Order of Procedures

After the preselection, the events are passed to the user defined analysis code. In the analysis code, before the final event selection is made, some final corrections to the reconstructed event properties may be applied. These may reflect special requirements by the analysis, the latest available knowledge or corrections not implemented into the general reconstruction procedure. This kind of correction is applied only to calorimeter information in this analysis.

In addition, the event analysis is sensitive to the order of application of the corrections within the essential steps of the processing. Thus, both, the corrections and the order of application, are described in conjunction in the following. All routines referred to are part of the PHANTOM library, a collection of analysis routines developed by the ZEUS collaboration to reconstruct and select physics events from data and MC samples.

Noise Suppression:

The first important step in the event analysis is the noise suppression. By using the routine NOISE95M, first isolated cells with energies above a threshold are removed (80 MeV for EMC and 140 MeV for HAC cells) and second a cut on the maximum imbalance of the two read-out channels of a cell is performed (70 % for cells with less than 0.7 GeV energy). In addition, cells are removed on a run-by-run selection which were found to be continuously noisy over some time. Since the noise in the calorimeter is simulated in the ZEUS MC this noise suppression is applied to the MC samples as well.

Having done this, the final electron identification (cf. sec. 9.2.1) provides the energy and position of the electron.

Corrections to the Electron:

The electron finding algorithms used at ZEUS typically make use only of the calorimeter information. Any correction using additional information by the SRTD or Presampler detectors to account for shower development of the electron in the dead material has to be applied afterwards. The corrections provided by the SRTD and Presampler are used mutually

exclusively. If the SRTD correction is available it provides the best energy correction and the best accuracy in the position reconstruction of the electron (routines: SRTDELEC and subsequently SRTDC95V2). Otherwise the Presampler is looked up which only can provide an energy correction to the found electron (routine: PRCLUS). If none of these additional sources of information are available (e.g. in the BCAL) no further improvement of the found electron is possible.

The energy correction performed with additional information from the SRTD or from the Presampler treats measured data and MC differently[1] for the same reason as the global hadronic energy correction had to be introduced (see below).

In the MC samples at generator level, the scattered electron from the generator table (FMCKIN) was corrected for final state bremsstrahlung in order to provide the correction back to the true vertex (routine: EBREMS).

Global Hadronic Energy Correction:

By comparing the p_t-balance between the electron and the hadronic system in DIS events $\delta p_t = p_t^{had}/p_t^{el}$ a significant discrepancy was found between measured data and MC simulation. The assumption is that the energy loss of particles in the dead material in front of the calorimeter is not modeled adequately in the MC. In fact, in the detector the distribution of dead material is a complicated function of the scattering angles (Θ, ϕ) which is modeled with several simplifications in the MC. This problem is complex and not completely understood so far. Thus, the ZEUS calorimeter group decided to provide a first approximate solution. A coarse global correction procedure was formulated in the routine CALCORR to account for the average systematic difference between data and MC: the reconstructed energy of calorimeter cells in measured data is scaled up by 5% for cells in BCAL and by 2.5% for cells in RCAL[2]. By this correction the reconstructed spectra, δp_t, of data and MC match reasonably well for all polar scattering angles Θ.

Having done this correction, the hadronic final state can be obtained from the calorimeter by the exclusion of those cells which contributed to the found electron. Now the kinematic variables can be finally reconstructed. On these the final event selection by phase space and cleaning cuts is performed. At this point the event selection of DIS events is completed and the further investigation of the hadronic final state may start.

Jet Energy Correction:

After the jet finding procedure cuts are performed on η_{max}^{jet} and $p_{t,min}^{jet}$ to select the accepted *valid jets*. It turns out that the $p_{t,det}^{jet}$ of a jet reconstructed at detector level is significantly lower than the $p_{t,had}^{jet}$ of a matching jet on hadron level. Thus, if a cut with the same threshold would be performed on both these p_t^{jet}-spectra, at detector level a much smaller sample would result. It is assumed that this energy loss is also an outcome of the dead material effects in the detector. Therefore, a correction procedure for the $p_{t,det}^{jet}$ has been developed from the average behavior of the jet momenta in MC (cf. sec. 11.3.4). In turn, it is applied to jets

---

[1]The energy measured in the Presampler associated with a found electron is converted from MIP to GeV and weighted with the factors 0.072 for data and 0.051 for MC before it is added to the electron energy. The SRTD correction is much more sophisticated and described by two sets of eight constants.

[2]Actually the correction factor for the BCAL cells originally was determined to 6% for the 1993 and the 1994 data sets. After a bug fix in the ZEUS detector MC, concerning the electron shower width and a shower termination parameter, this was reduced to 5% for analyses compared to MC samples produced for the 1995 running period.

found at detector level in MC as well as in data to correct the $p_{t,det}^{jet}$ towards $p_{t,had}^{jet}$ before the cut is performed.

9.2.4   Cleaning Cuts

Unless stated otherwise, the cleaning cuts are applied to the measured data as well as to the detector level information of simulated MC events. Generally a cleaning cut does not work perfectly and also removes data events which origin from the process to select. By applying it to the MC sample it removes similarly events from the generated process, if the quantities to cut on are modeled well in the MC. This way the acceptance correction obtained from the MC takes into account the errors introduced by the cleaning procedure.

In this section the properties of the main background processes are discussed. The applied cut values are summarized in section 9.2.4.1.

Photoproduction Events:

Photoproduction events are characterized by very low momentum transfer, $Q^2 \approx 0$, due to the exchange of a photon which is almost on mass shell, i.e. which is almost real. Thus, the scattering angle of the electron is very small and the electron escapes through the beam pipe or is tagged by one of the additional calorimeters which are attached directly to the beam pipe outside the main calorimeter (LUMI, TAGGER).

The quantities δ and δ' are used to separate PHP and DIS events:

$$\begin{aligned}
\delta &= E - p_z &&= \sum_i E_i(1 - \cos\Theta_i) \\
\delta' &= E - p_z + 2E_\gamma &&\; ,
\end{aligned} \tag{9.1}$$

where the sum runs over all cells of the calorimeter and E_γ is the energy measured in the LUMI and TAGGER system. These quantities peak at $\delta = 0$ for PHP events and at twice the electron beam energy $\delta \approx 2E_e$ for DIS events, with a minimum near the electron beam energy. In this analysis δ' is used in the trigger setup and the sharper cut against PHP events, δ, in the final analysis cut.

Photoproduction events may also produce electrons which are measured by the calorimeter, mainly via the pion decay $\pi^0 \to e^+e^-\gamma$. These electrons may be misinterpreted as the scattered electron from a DIS interaction. Such a fake electron mostly occurs in the forward direction with low energy and, thus, is characterized by a high Bjorken-y. Therefore, events with high y_{EL} are rejected. It turns out that at high Q^2 a residual background survives the cut on y_{EL}. Therefore, in this analysis an additional combined cut on forward directed electrons with low energy is introduced. This is discussed in section 11.1.3.

Diffractive Events:

Among the class of NC DIS events a subclass of diffractive events has been found which amounts to about 6% of the total sample (depending on the kinematic range). These events are characterized by a lack of hadronic energy deposition in the forward direction. The picture of this interaction is that the proton either keeps its identity or gets into an exited state and escapes completely through the beam pipe without the usual breakup of the proton remnant in the DIS interactions. Thus, a gap occurs in the rapidity of the energy deposition, between the current part of the hadronic final state and the proton direction. The diffractive interaction may be described by the exchange of a so-called *Pomeron* between the photon and the proton which, a remarkable feature, carries the quantum numbers of the vacuum (cf. [ZEU95b] and references therein).

Since his subclass of diffractive events is not simulated by the DIS MC generators it is removed from the data sample by a cut which requires a minimum hadronic energy deposition in the FCAL.

Beam-Gas and Beam-Beam Pipe Events:

Protons of the beam may interact with molecules of the residual gas or with the beam pipe itself. Due to the kinematic conditions, only those interactions are seen in the detector which took place upstream, i.e. before the protons reached the detector. In such interactions many secondary particles are produced which give many tracks in the tracking system and a high energy deposition in the calorimeter.

To reject events from these processes, the average arrival times of the signals are measured in the different parts of the calorimeter and are compared to the HERA clock signals. The relative calibration is chosen in such a way that interactions which take place at the nominal vertex would give signals in the calorimeter towers with average arrival times of '$t = 0\,$ns' relative to a HERA clock signal. Background events of the beam-gas and beam-beam pipe type give negative arrival times in the RCAL due to the very different z-position of the interaction; figure 9.2 illustrates this.
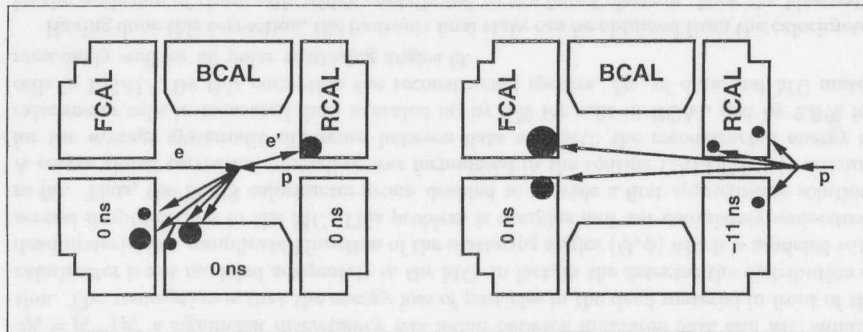
Figure 9.2: *Average timing of signals in the calorimeter for ep-scattering events (left) and for beam-gas and beam-beam pipe background events (right).*

Halo Muon and Cosmic Muon Events:

The proton beam is accompanied by a large number of muons extending in distance from the beam line up to the size of the HERA tunnel radius. These muons traverse the detector parallel to the proton beam. In addition, muons from cosmic rays cross the detector predominantly perpendicular to the beam directions. Muons from both processes may radiate photons and introduce electromagnetic showers in the calorimeter which could, in principle, be misidentified as scattered electrons. But, since these events are uncorrelated in time with the ep-collisions and due to the characteristic shape of the energy depositions in the calorimeter as well as due to the lack of an event vertex they can be identified and removed very efficiently.

Events with a Spark in a PMT:

Sometimes events are observed with a big energy deposition in an isolated calorimeter cell caused by a huge signal from only one of the two readout channels. This signature can

be caused by spark discharges in single photomultiplier tubes (PMT) but not by energy deposition of particles. Thus, events are rejected which contain cells with a big signal in only one PMT or with an unphysically large asymmetry in the two readout channels.

9.2.4.1   Applied Selections

In the following, those cut procedures and thresholds are listed which are valid for the final event selection. Again, all routines referred to are part of the PHANTOM library. Most of the given cut thresholds were developed in former analyses and studies performed within the ZEUS DIS working group and subsequently have become default to select general DIS events.

The selection cuts applied in this analysis are:
Applied to measured data only:

- The routine O1TTYP is used to reject test trigger events.

- The routine O1C5VT is used to reject beam-gas events tagged by the VETO wall or the C5 counter.

- The routines ALHALO2, COMCOS, ISITAMU and MUTRIG are used to reject halo-muon, QED Compton and cosmic-muon induced events, respectively.

- The routine RMSPARK is used to reject events with sparks in single photomultiplier tubes.

- The routine EVTAKE contains a history of all hardware and data acquisition problems during the running periods. Thus, complete runs as well as single events with significant problems are rejected.

- The following timing cuts on the average arrival times of the calorimeter signals $\langle t_i \rangle$ have been performed independently on the FCAL and RCAL signals if the timing for these calorimeter parts was available (which requires a minimum energy of 5 GeV):

$$|\langle t_{FCAL} \rangle| < 6\,\text{ns}$$
$$|\langle t_{RCAL} \rangle| < 6\,\text{ns}$$
$$|\langle t_{FCAL} \rangle - \langle t_{RCAL} \rangle| < 6\,\text{ns}$$

This cut rejects beam-gas and beam-beam pipe induced events but is not applicable for MC since the CAL timing is not modeled well.

Applied to MC and measured data:

- To reject diffractive events a minimum energy of 1 GeV is required in the FCAL.

- To reject events from photoproduction a cut on the quantity $\delta = E - p_z$ is performed:

$$35\,\text{GeV} < E - p_z < 60\,\text{GeV}$$

- Photoproduction events which produce a fake electron and which are still reconstructed within the defined phase space (cf. sec. 9.2.5) are suppressed by the rejection of events with a reconstructed electron in the forward direction ($\Theta_e < 1.0\,\text{rad}$) which in addition has low energy ($E'_e < 20\,\text{GeV}$). This cut has not been used in previous analyses, cf. sec. 11.1.3 for its discussion.

- At least one event vertex is required to be reconstructed by the tracking system to ensure a defined event reconstruction.

- The z-position of the event vertex is required to lie in the range $[-50\,\text{cm}, \ldots, 50\,\text{cm}]$. Outside this range, in the region of the so-called *satellite bunches*, the vertex distribution is not anymore well modeled by the MC.

- At least one found electron was required by the electron finding algorithm with a probability higher than the default threshold. By default SINISTRA was used. Alternatively EM was applied in one systematic check. The default probability thresholds are 90 % for SINISTRA and 5.0 rel. units for EM. All other steering parameters were also used with the recommended default values. If more than one electron candidate above the cut limit was found then only the most probable one was used in the event reconstruction.

- A fiducial cut was performed on the hit position of the reconstructed electron around the RCAL beam pipe: the event was rejected if the electron was reconstructed in a square of $30\,\text{cm} * 30\,\text{cm}$ around the beam axis. In this region the reconstruction of the angle and the energy of the electron is less accurate since a part of the electromagnetic shower may escape through the RCAL beam pipe. Actually, this cut is almost fully covered by the cut on the lower edge of the Q^2 range of this analysis, i.e. maybe no event is removed solely by this cut.

The behavior of the important quantities used by the cleaning cuts can be found in section 11.1.1.

9.2.5 Phase Space Cuts

In contrast to the cleaning cuts described above, the following *phase space* cuts are applied to all data sets including the NLO predictions:

- The momentum transfer, Q^2, is the key variable of the kinematic quantities in this analysis since the aim is to determine the strong coupling constant as function of it: $\alpha_s(Q^2)$. Its range has been limited to $44\,\text{GeV}^2 < Q^2 < 3600\,\text{GeV}^2$.

  The upper limit has been set due to the insufficient number of (2+1)-jet events above $3600\,\text{GeV}^2$. But, by using the exclusive $K_\perp$ algorithm in the BREIT frame even an increase of the available luminosity would not increase the number of reconstructed (2+1)-jet events at high Q^2 significantly. This algorithm shows a limitation in resolving of dijet configurations towards high Bjorken-x and thus at high Q^2 (cf. discussion in sec. 9.3).

  The lower limit has been set primarily to limit the amount of data since the total DIS cross section is almost proportional to Q^{-4}. In addition, it is known that the hadronization corrections in the jet finding become larger and more unreliable at low Q^2, this is discussed in section 9.4.1.

  The Q^2-range has been subdivided into six bins with the borders: 44, 56, 80, 160, 320, 640, 3600 GeV^2. Thus, with a resolution of the reconstructed Q^2_{DA} found to be RMS = 12.3 %, a minimal width of 2 * RMS for each bin is guaranteed.

- The range of Bjorken-x has been limited to $10^{-3} < x < 10^{-1}$.

  Beyond the upper limit at HERA DIS events become rare. With the extension of

the phase space in this direction one would gain only few events from measured data but become more sensitive to the MC prediction. In addition, at high x the resolution in x becomes poor.

The main reason for the lower limit is to restrict the fraction of BGF processes in the hard scattering which becomes dominant at low x. This process is strongly dependent on the gluon density $xg(x, Q^2)$ which is less well constrained in the PDFs. With this cut also the contribution from the parton shower model is limited [ZEU95a, Tre96]. Finally for low Bjorken-x and high Bjorken-y the electron identification becomes more difficult since the electron and the current part of the hadronic system end up in the RCAL.

With a RMS = 24.0 % x_{DA} provides the best resolution compared to the other reconstruction methods at detector level and is used throughout the analysis.

- The range of Bjorken-y has been limited to $0.04 < y < 0.95$.

  The upper limit serves as cut against photoproduction background in the measured data. But since this cut uses a basic kinematic quantity it has to be applied as phase space cut to all data sets.

  The lower limit guarantees a minimum energy transfer from the electron to the proton or, in other words, a minimum invariant mass W of the hadronic system. Thus, the jet structures in the hadronic final state are formed reasonably well.

  Although y_{EL} has the worst overall resolution (RMS = 28.5 %) in the total range it describes best the behavior of y in the range $y > 0.8$. Thus, it is used for the upper cut. The y_{JB} gives the best description at low y and shows the best resolution (RMS = 17.7 %). It is therefore used for the lower cut. As systematic check also y_{DA} was used, which gives a reasonable description in both cases.

- The energy of the electron E'_e is required to be larger than 10 GeV.

  Although motivated by the performance criteria of the electron finding algorithms at data and MC detector level, this cut is defined as a phase space cut since it cuts significantly in the selected phase space defined by the other cuts of this class.

The phase space cuts defined here together with the previously defined cleaning cuts are referred to as **default DIS selection** in the subsequent part of this thesis.

9.2.6 Jet Finding

The jet finding procedure is performed on the hadronic final state of an event, i.e. after the separation of the scattered electron and all final detector corrections. In this analysis the exclusive $K_\perp$ jet finding algorithm is used as it is implemented in the KTCLUS package [Sey97d].

The hadronic final state is obtained as a list of 4-vectors of particles or calorimeter cells in the laboratory frame. Since the jet finding is performed in the BREIT frame these 4-vectors have to be boosted first. For the boost the 4-vector of the scattered electron is needed to define the axis of the exchanged virtual boson. Therefore, the jet finding is very sensitive to the reconstruction of the scattered electron. By default in this analysis the electron was used which was found by the calorimeter based electron finder SINISTRA, corrected in energy and direction as described in section 9.2.3. As a systematic check, the electron energy reconstructed from the kinematic variables Q^2_{DA} and y_{DA} :

$$E'_{e,DA} = (1 - y_{\text{DA}})E_e + \frac{Q^2_{DA}}{4E_e} \quad , \tag{9.2}$$

with E_e the energy of the incoming electron, was used to alternatively construct the boost 4-vector. For the generator levels in the MC samples, the final state electron corrected for bremsstrahlung radiation was used.

As hard scale for the jet finding Q^2 was chosen in order to determine $\alpha_s(Q^2)$. At reconstructed level it was found that Q^2_{JB} gives a very similar behavior in the jet finding as Q^2_{true} does at the generator level for the favored MC sample (cf. the discussion in sec. 11.3.1). For this reason it was chosen as the default reconstructed hard scale Q^2 and the scales Q^2_{DA} and Q^2_{MIX} were taken for systematic checks.

The jet finding was performed at the fixed resolution parameter $y_{cut} = 0.5$ (cf. the discussion in sec. 11.3.2) which also was varied for systematic checks.

In addition to the *current jets* returned by the $K_\perp$ algorithm, the particles or cells which were discarded by the algorithm were reconstructed as the *proton remnant*. At the generator levels all partons and hadrons are available, while at detector level a large amount of energy of the proton remnant escapes through the beam pipe. Thus, at detector level, the remnant has a much smaller momentum when compared to the generator levels. In addition, the proton remnant at detector level may have a different direction than the remnant found at generator levels. The missing 4-momentum at detector level was reconstructed as the *pseudo particle*[3].

The returned jets were boosted back to the laboratory system without the application of any cut in the BREIT system. In order to obtain a sample of reliably reconstructed jets, cuts are applied in the laboratory frame on $\eta^{jet} < 2.436$ ($\hat{=} \Theta^{jet} > 10°$) and $p_t^{jet} > 4.0\,\text{GeV}$ to select the accepted *valid current jets* (cf. sec. 11.3.3 and 11.3.4 for a detailed discussion). By these restrictions the purities and efficiencies of the jet identification compared for different levels are maintained at reasonable levels (cf. sec. 9.4.1).

Before the cut on p_t^{jet} is applied, a correction is needed due to the systematically lower transverse jet momenta at detector level as compared to hadron level, which is interpreted as due to hadronic energy loss of the jets. Without such a correction this cut would spoil the relative fraction of accepted jets between detector and hadron level due to the of difference of the average p_t^{jet} distributions around the cut value. The measured p_t of a jet is scaled by the average systematic shift before the cut is performed. In average, this takes the effect out of the purities and efficiencies, which is due of the hadronic energy loss to the jets between the hadron level and the MC detector level. Subsequently, this effect is also removed from the correction factors of the jet rates. However, in principle it does not change the measured jetrate or cross section after the correction to a generator level, i.e. when it is compared to the NLO predictions. The question is, whether the correction either is formulated in one single step, by the correction factors alone, or in two, as it is done in this analysis. Within ZEUS the second solution is preferred since it is shown in ZEUS internal studies (e.g. [Rep96]) that the global hadronic energy correction of the calorimeter is not sufficient as discussed in section 9.2.3.

Thus, the **default jet finding procedure** of this analysis consists of the following elements: the exclusive $K_\perp$ algorithm (KTCLUS) is applied as jet finding algorithm which is operated at the resolution parameter $y_{cut} = 0.5$ with the hard scale Q^2 (reconstructed as Q^2_{JB} at detector level). After the jet finding by KTCLUS at detector level first the correction on p_t^{jet} is applied (cf. sec. 11.3.4) then, for all data sets at all levels, the cuts $\eta^{jet} < 2.436$ and $p_t^{jet} > 4.0\,\text{GeV}$ are applied to find the finally accepted *valid current jets*. Subsequently, this will be referred to as *default jet selection* unless stated otherwise.

---

[3]This pseudo particle is similar to the one which is needed for the JADE algorithm. But unlike there it has no effect to the jet finding here.

The valid current jets are counted and each event is assigned to one of the following classes: $(0+1)+(1+1)$-jet events, $(2+1)$-jet events and $(\geq 3+1)$-jet events. The exclusive *(2+1)-jet rate*, R_{2+1}, in a selected phase space is subsequently defined as:

$$R_{2+1} = \frac{\text{number of } (2+1)\text{-events}}{\text{number of all DIS-events}} \cong \frac{\sigma_{DIS}^{(2+1)}}{\sigma_{DIS}^{tot}}. \tag{9.3}$$

With this procedure it is possible that events with more than 2 current jets found by KTCLUS migrate to an accepted $(2+1)$-jet event. Similarly, events with 2 current jets found by KTCLUS may migrate to an $(1+1)$-jet or a $(0+1)$-jet event. This procedure is applied in exactly the same way to all data sets as well as to the NLO predictions.

9.3   The Selected Data and MC Samples

In the 1995 running period HERA delivered an integrated luminosity of $\mathcal{L} = 12.3\,\text{pb}^{-1}$. From that ZEUS was able to write $\mathcal{L} = 7.27\,\text{pb}^{-1}$ on tape. After application of EVTAKE this reduced to $\mathcal{L} = 6.62\,\text{pb}^{-1}$ which corresponds to 17,798,323 events from which about $7.3 * 10^6$ passed at least one of the DIS triggers. A small part of the 1995 running period was used to take data with the location of the nominal vertex shifted in beam direction by $+60\,\text{cm}$ and $-60\,\text{cm}$ to extend the kinematic range of the F_2 measurements. These special *shifted vertex* runs are not used in this analysis.

Thus, finally this analysis covered an integrated luminosity of $\mathcal{L} = 6.30\,\text{pb}^{-1}$ corresponding to 1,871,816 events which passed the *clean NC DIS* trigger 'DIS bit 14' and were processed. In fact, by the aid of the ZES preselection with additional constraints on some key variables like Bjorken-x, y and Q^2 to cut out unneeded phase space, the number of touched events was reduced to 239,951.

After the application of all cleaning and phase space cuts 80,514 events survived, which make up the final DIS data sample of the ZEUS 1995 running period used in this analysis in the chosen phase space. This sample is shown in figure 9.3 in the (Q^2, x)-plane together with the cuts which constrain the phase space of the analysis.

The default jet finding procedure of this analysis found 5955 events with a $(2+1)$-jet configuration in the hadronic final state within the final ZEUS 1995 DIS data sample. This $(2+1)$-jet event sample is shown in figure 9.4.

Note that the events in figures 9.3 and 9.4 are plotted with their reconstructed Q^2_{DA} and x_{DA} values. This causes the distribution to smear out over the borders given in terms of Bjorken-y and E'_e by the resolution of the different reconstruction methods.

From figures 9.3 and 9.4 one can obtain also the number of events which ended up in each Q^2-bin. These numerical results of the event selection are summarized in table A.1 in the appendix A. From these numbers the raw rate of dijet events can be obtained directly and with the additional information of the integrated luminosity $\mathcal{L}$ also the total DIS cross section $d\sigma_{DIS}^{tot}/dQ^2$ and the uncorrected exclusive $(2+1)$-jet cross section $d\sigma_{DIS}^{(2+1)}/dQ^2$ can be derived. They are given in table A.1, too. Given are also the propagated statistical errors for the jet rates and the cross sections. Note that for the calculation of the errors of the cross sections the error on the luminosity measurement, which is at ZEUS on the order of 1 %, was neglected. Analogously the numerical results on the event selection on the ZEUS 1996 data sample are summarized in table A.2. The results of the event selection for the MC samples used in this analysis (cf. sec. 8.5) are given in the tables A.3 to A.6.

These results of the event selection are shown graphically in figures 9.5 for the raw exclusive $(2+1)$-jet rate and in figure 9.6 for the total DIS and the exclusive $(2+1)$-jet cross
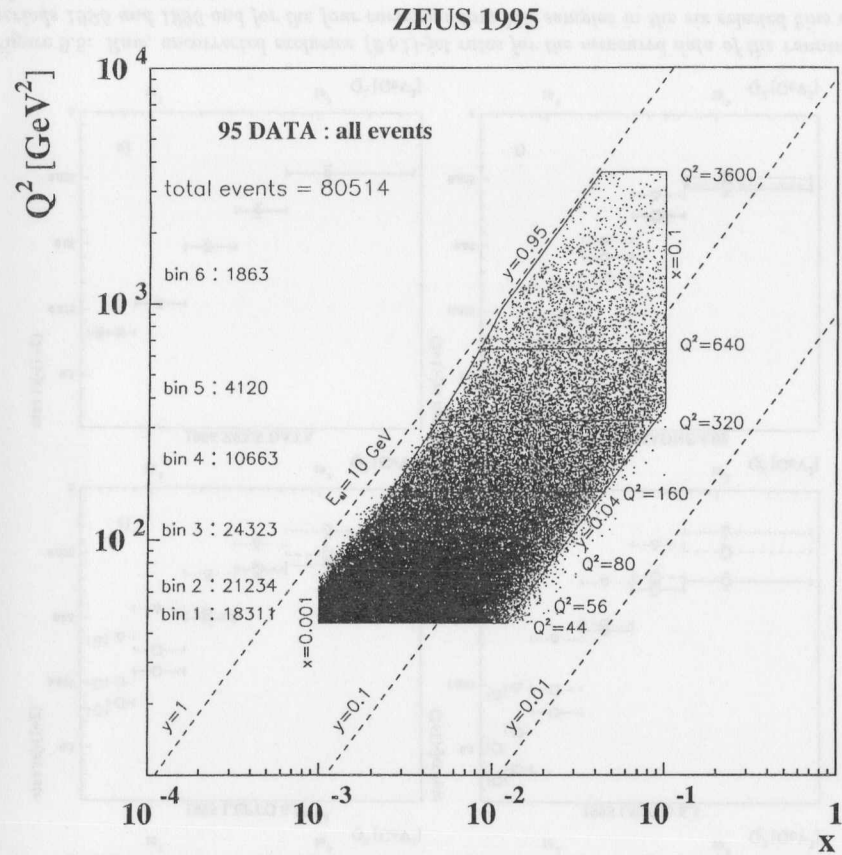
ZEUS 1995

Figure 9.3: *The selected DIS data sample from the ZEUS 1995 running period. Also given are the phase space cuts, the total number of selected events and the numbers of events in each Q^2-bin. The events are plotted with their reconstructed Q^2_{DA} and x_{DA} values. This causes the distribution to smear out over the borders by the resolution of the reconstructed Bjorken-y and E'_e.*

section. In these figures the upper four plots show the results (a) for the 1995 data in the six bins of Q^2 and, similarly, for the three 1995 MC samples used (b: ARIADNE4.08, c: LEPTO6.3^{tuned}, d: LEPTO6.3). The lower two plots show in addition (e) the 1996 data and (f) the only available MC sample for the 1996 configuration (ARIADNE4.08). For the MC samples the quantities are given for parton, hadron and detector level in each plot except for the total DIS cross section in figure 9.6 where by definition no difference is made between parton and hadron level.

Figure 9.7 compares the detector level results of the different data samples by drawing their ratios for the (2+1)-jet rates (top), the total DIS cross section (center) and the exclusive (2+1)-jet cross section (bottom). On the left the data samples are compared to the available
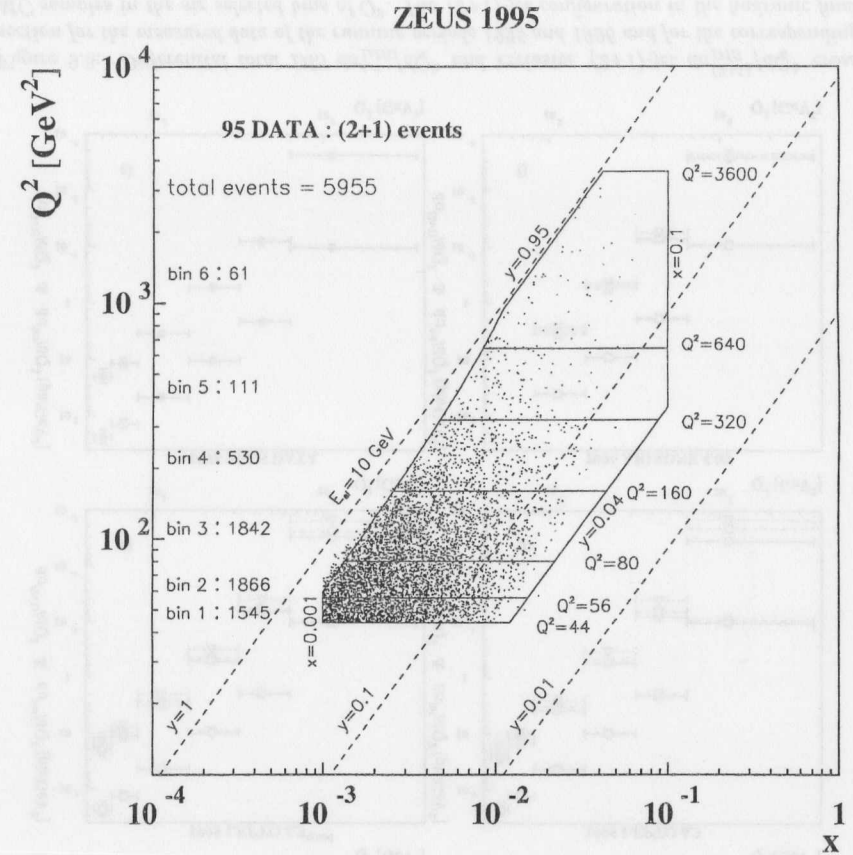
ZEUS 1995

Figure 9.4: *The selected DIS data sample from the ZEUS 1995 running period with a (2+1)-jet configuration in the hadronic final state identified by the default jet finding procedure. As in figure 9.3 the phase space cuts and the number of selected events are given.*

MC samples and on the right the 1996 results are compared with the 1995 results.

9.3.1 Properties of the Data and MC Samples

For the exclusive (2+1)-jet rate (fig. 9.5a), to first order, a monotonic fall off with Q^2 is expected under the assumption of a running α_s. But, by the application of a cut on the minimal transverse momentum of a jet, p_t^{jet}, the phase space for the (2+1)-jet configuration in the hadronic final state is reduced for events with small Q^2. Roughly said, a part of the momentum transfer Q^2 is needed to produce jets with a minimum p_t^{jet} and consequently some invariant mass. Only the remainder can be used to generate an invariant mass of the dijet system itself which in turn is needed to resolve the two jets as separate structures. Thus, the higher the $p_{t,min}^{jet}$-cut is chosen at a particular Q^2 or, vice versa, the lower Q^2 is

uncorrected (2+1)-jet rates
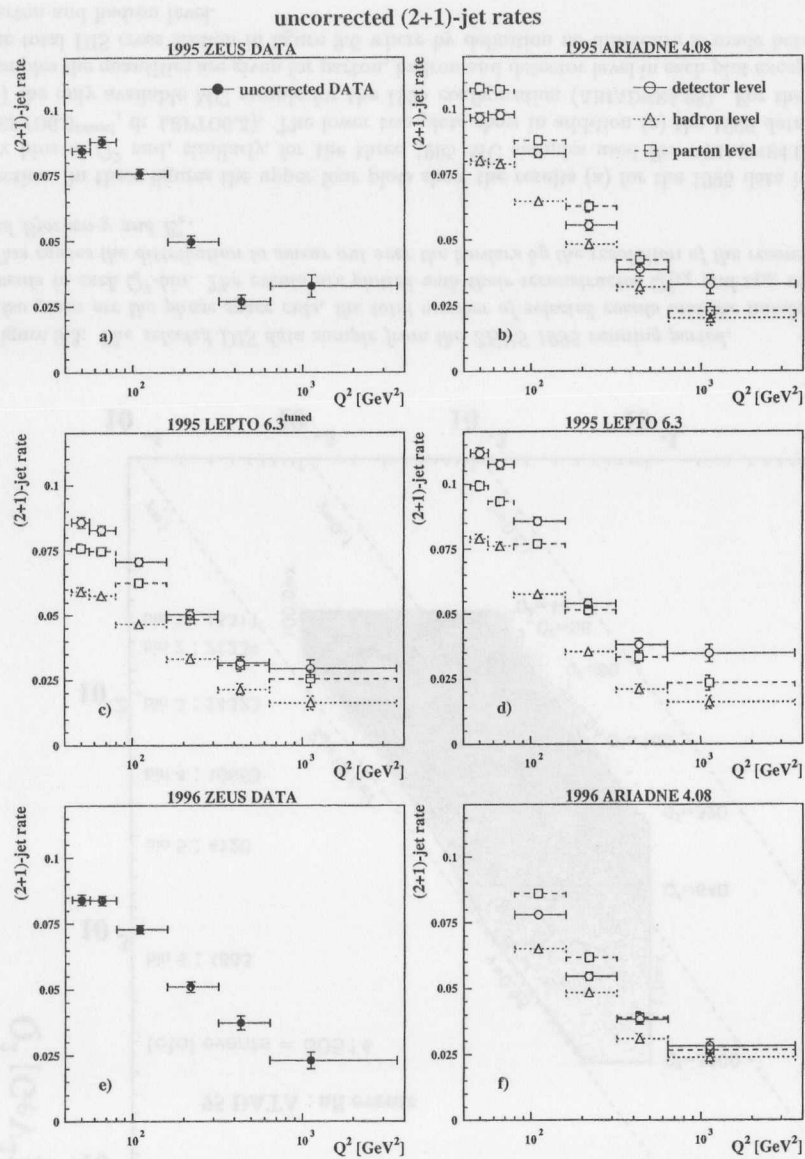
Figure 9.5: *Raw, uncorrected exclusive (2+1)-jet rates for the measured data of the running periods 1995 and 1996 and for the four corresponding MC samples in the six selected bins of Q^2. Only the statistical errors are given.*

differential total DIS & (2+1)-jet cross sections
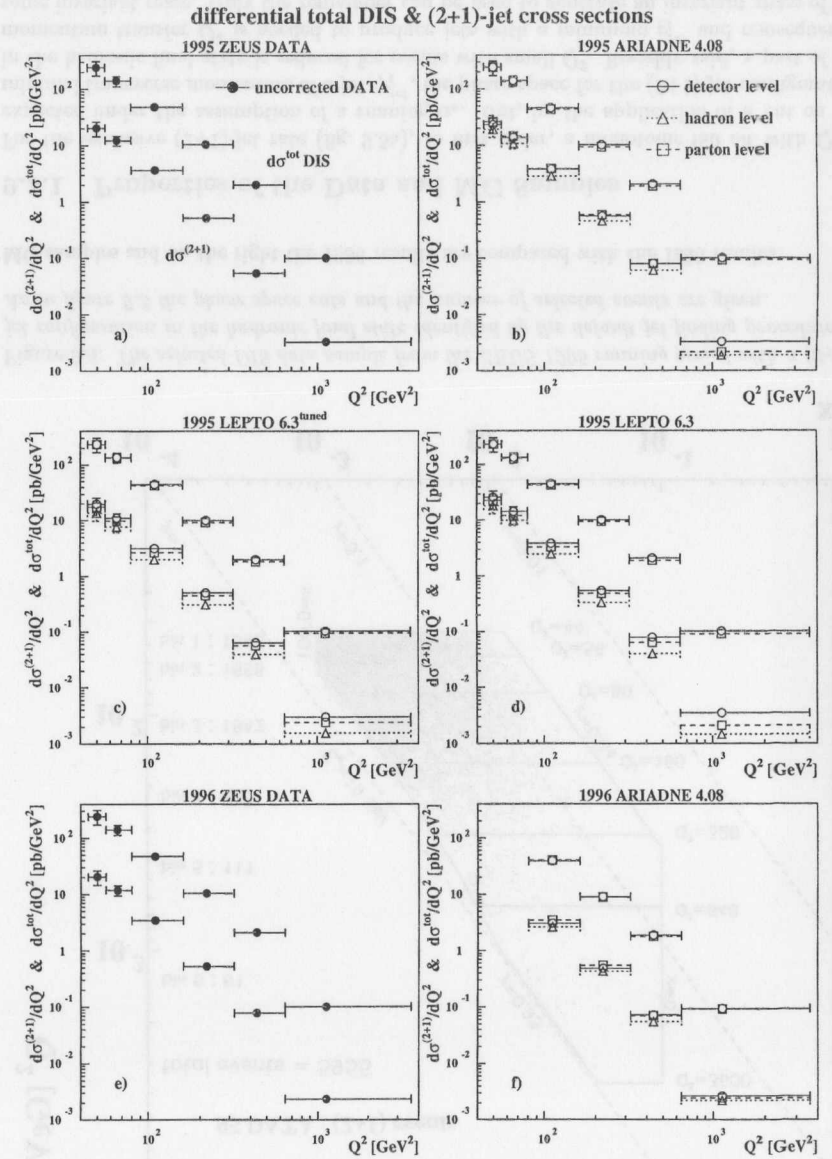
Figure 9.6: *Differential total DIS $d\sigma_{DIS}^{tot}/dQ^2$ and exclusive (2+1)-jet $d\sigma_{DIS}^{(2+1)}/dQ^2$ cross section for the measured data of the running periods 1995 and 1996 and for the corresponding MC samples in the six selected bins of Q^2. The (2+1)-jet configuration in the hadronic final state was identified by the default jet finding procedure. Only the statistical errors are given, especially the error on the luminosity measurement ($\approx 1\%$) was neglected.*

selected at a fixed $p_{t,min}^{jet}$-cut the smaller is the residual phase space to fit out a dijet system with an invariant mass. This may cause a drop of the (2+1)-jet rate towards low Q^2 which is clearly visible in the lowest Q^2-bin in the 1995 and in the 1996 data set (fig. 9.5a and 9.5e). This also can be seen in the NLO predictions (fig. 10.1). It is not as obvious in the three 1995 MC sets (fig. 9.5b-d) but relative to the rise of the (2+1)-jet rate extrapolated from the higher Q^2-bins the values in the lowest Q^2-bin are low, too. This effect cannot be seen in the 1996 MC sample (fig. 9.5f) due to its production cut-off at $70\,\text{GeV}^2$.

A similar effect leads to the depletion of the found number of (2+1)-jet events near the cut limit $y = 0.04$ clearly visible in figure 9.4. In this region the invariant mass W^2 of the total hadronic system is small and rarely sufficient to provide a resolvable dijet system.

In addition one can see in figure 9.4 that resolved (2+1)-jet configurations become rare at high Q^2 limiting the extension of the phase space towards higher momentum transfer compared to [ZEU95a] although the integrated luminosity is doubled. This behavior is seen in the MC samples as well. By applying the longitudinal invariant $K_\perp$ algorithm much more (2+1)-jet events are found in the high-Q^2 region allowing to set a reasonable upper limit for the used phase space e.g. at $20000\,\text{GeV}^2$ [Tas98]. This is interpreted as a feature of the exclusive $K_\perp$ algorithm which involves Q^2 in the denominator of the distance measurement (eq. 7.8). Hence, at high values of Q^2 jets do not get resolved any more which would be resolved at lower Q^2. In fact, if one looks at figure 9.4 one finds a depletion of (2+1)-jet events even at medium Q^2 and large values of Bjorken-x. For this region the high x-value boosts the particle in the BREIT frame towards the boson axis and a higher invariant mass is needed to bend them to the outside again in order to get resolved as separate structures. Only rarely this invariant mass can be provided at these relatively low values of Bjorken-y. The longitudinal invariant $K_\perp$ algorithm therefore should identify only few (2+1)-jet configurations in this region, too.

In the (2+1)-jet rate obtained from the measured 1995 data (fig. 9.5a) a turn-over is observed: the dijet rate in the fifth bin $(320\,\text{GeV}^2 < Q^2 < 640\,\text{GeV}^2)$ is found to be unexpectedly low compared to the MC predictions. This can be seen clearly from figure 9.7a where the rate in this Q^2-bin from 1995 data lies about 30 % lower than the rates from the simulations. This structure turned out to persist against any systematic check or correction. A comparison to the (2+1)-jet rate obtained from the measured 1996 data with the same selection procedure shows that this effect is not observed there. It therefore is neither of physical nature nor introduced by the event selection. The relative difference of the (2+1)-jet rates between the 1995 and the 1996 data set is $4.0\,\sigma_{95}$ for the fifth bin and $< 2.3\,\sigma_{95}$ in the other bins. This effect finally is interpreted as a statistical fluctuation in the data samples. Nevertheless, the statistical uncertainty is by no means the limiting factor of the accuracy of the determination of α_s in this analysis as the systematic uncertainty turns out to be larger by one order of magnitude.

Besides this statistical fluctuation in the data samples at high Q^2 the exclusive (2+1)-jet rates agree well for the 1995 and 1996 data and MC samples (fig. 9.7b). The simulation of the (2+1)-jet rates by the MC samples is less accurate. ARIADNE4.08 overestimates the (2+1)-jet rate by 10 to 15 %. So does LEPTO6.3 which in addition describes not well the shrinking of the phase space for (2+1)-jet configurations at low Q^2. This last problem is shared by LEPTO6.3$^{\text{tuned}}$ which in contrast matches better the (2+1)-jet rate.

By comparing the total DIS cross sections it turns out that the data samples agree very well within $1\,\sigma_{95}$ for the 1995 and 1996 data samples as well as when compared to each of the MC samples as can be seen from figures 9.7c-d[4]. Only the 1996 sample of

---

[4]All comparisons by means of the standard deviations do not refer to the errors given in figure 9.7, since

ARIADNE4.08 underestimates the total DIS cross section given by the other data and MC samples by typically $1.5\,\sigma_{95}$. This last point is not understood.

Thus, all differences in the (2+1)-jet rates between the samples discussed above can be traced back to the behavior of the exclusive (2+1)-jet cross section. Figures 9.7e-f show the same structures as discussed by means of figures 9.7a-b. This reflects that all the MC samples describe well the inclusive DIS quantities but differ in the description of the internal structure of the hadronic final state, i.e. the shape of the dijet system (cf. sections 11.1 and 11.2). The second reason is that the exclusive (2+1)-jet cross section is much smaller and, thus, has much higher statistical errors as compared to the total DIS cross section.

The results of the event selection and the jet finding presented in this section now are the base for the subsequent determination of α_s.

9.4 Correction to Hadron and Parton Level

The results from the event selection on the MC samples for the exclusive (2+1)-jet rate and the cross sections are used to obtain correction procedures which can be applied to the data samples in order to correct them to parton level.

In this analysis the simple *bin-by-bin* correction procedure was applied: the physical quantities R are determined in each chosen bin in phase space on each defined level in the MC sample. Then, in each bin i separately, the quantities R^{level} on different levels are related by scalar correction factors

$$R_i^{\text{generated}} = C_i * R_i^{\text{reconstructed}} \quad . \tag{9.4}$$

In this analysis, by convention, the correction factors have to be multiplied to the quantity R obtained from reconstructed level, i.e. to the more advanced level in the event evolution, to correct a quantity back to an earlier stage in the evolution. Thus, the hadron level is treated as the reconstructed level with respect to the parton level as the detector level is with respect to both.

Bin-by-bin correction factors do not take into account a possible migration between the bins in phase space. The following two cases give the same bin-by-bin correction factors:

- There is no migration, i.e. the resolution of the kinematical variables is perfect

- The migration has the same strength in all directions, i.e. for each pair of bins the sum of exchanged events is zero.

None of these situations can be expected for a real experiment.

To view the effects of migration in this scheme of correction one has to look at the purities and efficiencies of the event reconstruction in the bins of phase space. In this analysis the *purity*, p, of the reconstruction of a (2+1)-jet configuration in the hadronic final state is defined as the fraction of events which were generated with a (2+1)-jet configuration in the sample of events which were reconstructed with a (2+1)-jet configuration. The *efficiency*, ε, is analogously defined as the fraction of events which were reconstructed with a (2+1)-jet configuration in the sample of events which were generated with a (2+1)-jet configuration,

$$\text{purity} \quad : \quad p = \frac{\text{number of (2+1)-events}^{\text{gen}\oplus\text{rec}}}{\text{number of (2+1)-events}^{\text{rec}}}$$

$$\text{efficiency} \quad : \quad \varepsilon = \frac{\text{number of (2+1)-events}^{\text{gen}\oplus\text{rec}}}{\text{number of (2+1)-events}^{\text{gen}}} \quad . \tag{9.5}$$

---

there the errors are blown up by computing the ratio, but they refer to the statistical errors of the 1995 data sample (σ_{95}) given in the figures 9.5 and 9.6 and in the tables in appendix A.

detector level comparison of event samples
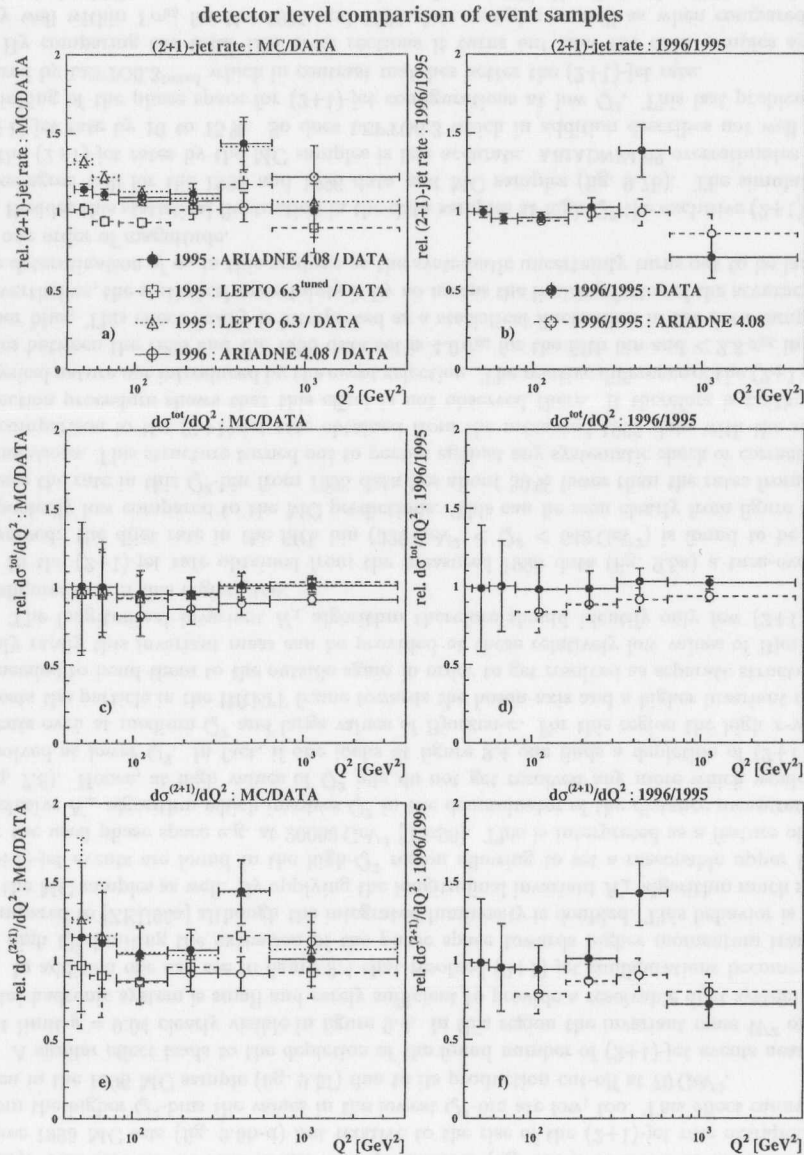
Figure 9.7: *Relative comparison on detector level of the results of the event selection for the (2+1)-jet rates (top), the total DIS cross section (center) and the exclusive (2+1)-jet cross section (bottom). On the left the data samples are compared to their corresponding MC samples, on the right 1995 and 1996 results are compared.*

Since the (2+1)-jet rate R_{2+1} is defined as the ratio of the number of the exclusive (2+1)-jet events and all DIS events (eq. 9.3) the correction factors for the dijet rate, ${}^{jr}C_i$, are defined differently to the correction factors used to correct the cross sections, ${}^{\sigma}C_i$,

$$ {}^{jr}C_i = \frac{\text{number of (2+1)-events}^{\text{gen}}}{\text{number of DIS-events}^{\text{gen}}} * \frac{\text{number of DIS-events}^{\text{rec}}}{\text{number of (2+1)-events}^{\text{rec}}} \qquad (9.6)$$

$$ {}^{\sigma_{2+1}}C_i = \frac{\text{number of (2+1)-events}^{\text{gen}}}{\text{number of (2+1)-events}^{\text{rec}}} \qquad {}^{\sigma_{\text{DIS}}}C_i = \frac{\text{number of DIS-events}^{\text{gen}}}{\text{number of DIS-events}^{\text{rec}}} . \qquad (9.7)$$

Thus, the ratio p/ε gives the values of the correction factors for any physical quantity considered. But the errors may not be derived from this ratio since only the 'generated and reconstructed' subsample would be considered and the error overestimated. In addition, the correction factors in this analysis are derived from correlated data samples. In this case an error calculation under the assumption of independent data set would strongly overestimate the size of the errors, too. Therefore, a method is utilized which is based on the Gaussian error propagation with consideration of the correlation of the data sets as it is discussed in [Rep98a] for correcting cross sections. It easily can be generalized to handle jet rates, i.e. ratios of cross sections, too. Consider a correction factor C as defined in equation 9.7 obtained from a MC sample. Now, the following subsamples are defined:

$$
\begin{aligned}
G &= \text{ number of generated events} \\
R &= \text{ number of reconstructed events} \\
D &= \text{ number of generated and reconstructed events} \\
E &= \text{ number of generated and not reconstructed events} = G - D \\
F &= \text{ number of reconstructed and not generated events} = R - D .
\end{aligned}
\qquad (9.8)
$$

For the errors of these samples Poisson errors are assumed: i.e. $\Delta D = \sqrt{D}, \Delta E = \sqrt{E} \ldots$. The correlation of the data sets is now taken into account by the definition of the correction factor,

$$ C = \frac{D + E}{D + F} , \qquad (9.9)$$

which is identified with the definitions given in equations 9.6 or 9.7, depending on which quantity has to be corrected. In fact, in the case of the (2+1)-jet rates to be corrected the identifications

$$
\begin{aligned}
D &= (2+1)\text{-jet rate}^{\text{gen}\oplus\text{rec}} = \frac{\text{number of (2+1)-events}^{\text{gen}\oplus\text{rec}}}{\text{number of DIS-events}^{\text{gen}\oplus\text{rec}}} \\
E &= (2+1)\text{-jet rate}^{\text{gen}\oplus\overline{\text{rec}}} = \frac{\text{number of (2+1)-events}^{\text{gen}\oplus\overline{\text{rec}}}}{\text{number of DIS-events}^{\text{gen}\oplus\overline{\text{rec}}}} \\
F &= (2+1)\text{-jet rate}^{\text{rec}\oplus\overline{\text{gen}}} = \frac{\text{number of (2+1)-events}^{\text{rec}\oplus\overline{\text{gen}}}}{\text{number of DIS-events}^{\text{rec}\oplus\overline{\text{gen}}}}
\end{aligned}
\qquad (9.10)
$$

have to be made. By application of the Gaussian error propagation the error of the correction factors, ΔC, becomes

$$ \Delta C = \sqrt{\sum_{i=D,E,F} \left(\frac{\partial C}{\partial i}\right)^2 (\Delta i)^2} $$

$$ = \sqrt{\frac{F^2(D+E) + E^2(D+F) + D^2(E+F) + 2 \cdot DEF}{(D+F)^4}} . \qquad (9.11)$$

Special care has to be taken on the right binning of the quantities. Quantities which make a statement about a particular level of reconstruction, like G and R, have to be classified by the kinematical variables on that level, i.e. in this analysis at detector level the events are binned in Q_{DA}^2 and at parton or hadron level in Q_{true}^2. Quantities which relate different levels are not defined in this sense. The followed rules here are:

- If the quantity is a ratio it is classified by the kinematical variables of the level considered in the denominator

- If the quantity express the same requirement at both levels, like D, it is classified by the kinematical variables of the level which appears first in the event evolution, i.e. parton before hadron or detector level, and hadron before detector level.

The last rule ensures that the correction factors are derived from quantities which are binned in the true variables which have perfect resolution. If this is done wrong significant changes to the correction factors and subsequently to the final results can be made especially at low Q^2 where the migration effects become larger. The first rule causes the efficiency to be binned also in the true variables but the purity to be binned in the reconstructed variables. This does not affect the correction factors which are derived independently from the purities and efficiencies.

9.4.1   Purities, Efficiencies and Correction Factors

The correction factors for the exclusive $(2+1)$-jet rates as well as for the corresponding cross sections already can be estimated from the results of the event selection given in the figures 9.5 and 9.6. From these plots it gets obvious that the $(2+1)$-jet rates and the dijet cross sections found for the hadron level are significant lower than for parton and hadron level. This is a remarkable feature as it indicates that although the correction factors between the detector and parton level may be close to 1.0 they involve a correction 'back-and-forth' via the hadron level leading to low purities and efficiencies. This can be seen in figure 9.8 for the purities and efficiencies of the exclusive $(2+1)$-jet finding which are shown in the six bins of Q^2 separately for the transitions between parton and hadron level, i.e. the hadronization, between hadron and detector level, i.e. the detector correction, and for the direct transition from parton to detector level. In addition the three 1995 MC sets are compared.

From figures 9.8a and 9.8b one can see the effect of the hadronization. The purities are of the order of 80 % while the efficiencies are lower, at the order of 60 %. This leads to hadronization correction factors of the order of 1.3 or higher, which are shown in figure 9.9a. Both, the purities and the efficiencies drop towards smaller values of Q^2 in a similar way which reflects the stronger migration there, i.e. stronger hadronization effects. But due to the similarity of the shapes of the purities and efficiencies they cancel to large extent in the correction factors. The residual effects lead to a rise of the correction factors towards higher Q^2 for the LEPTO MC samples and to a small tendency to drop for ARIADNE4.08. It is remarkable that the values for ARIADNE4.08 typically lie about 0.1 or even more higher than for the other both MC samples and the values for LEPTO6.3^{tuned} still lie about 0.05 higher than for the LEPTO6.3 sample.

The acceptance and smearing effects of the detector can be seen in figure 9.8c and 9.8d. The disturbance of the detector effects on the jet reconstruction is much stronger than for the hadronization effects. The average purities here are only around 30 % with efficiencies of about 45 %, again with ARIADNE4.08 higher than the other two by typically 0.1. This leads to correction factors of the order of 0.7. The purities and the efficiencies drop here
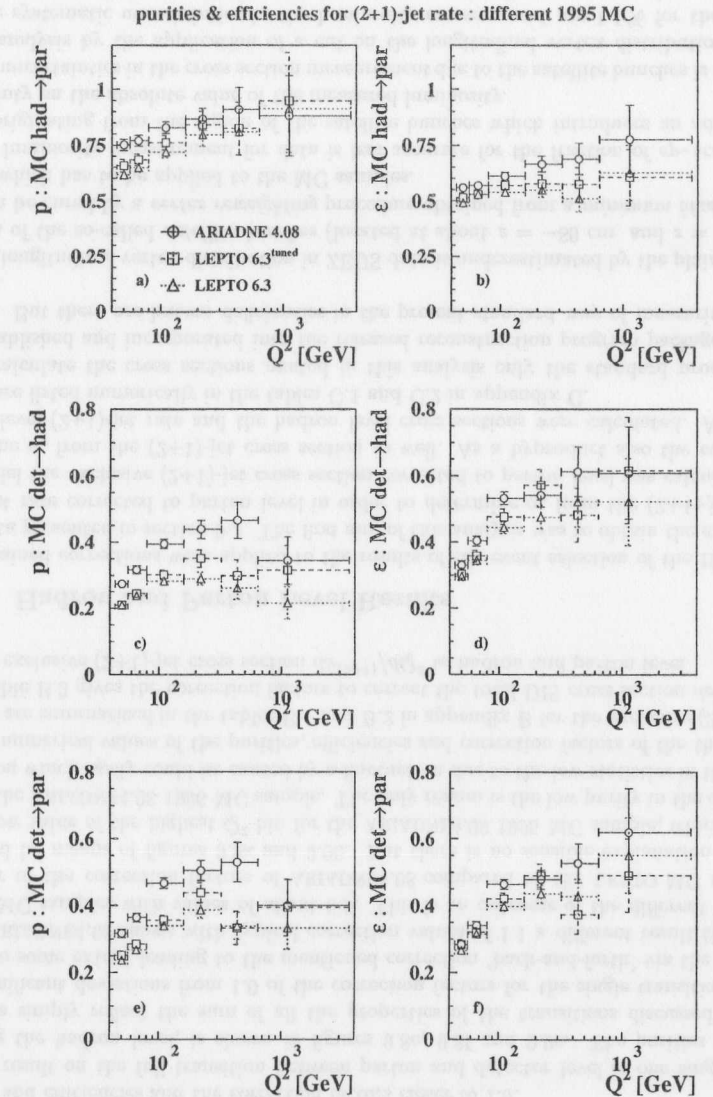
Figure 9.8: *Purities p (left) and efficiencies ε (right) for the exclusive (2+1)-jet rate in six bins of Q^2 using different 1995 MC. Separately given are the purities and efficiencies with errors from error propagation without regarding the correlation of the data sets for the transition between parton and hadron level (top), hadron and detector level (center) and the direct transition from parton to detector level (bottom).*
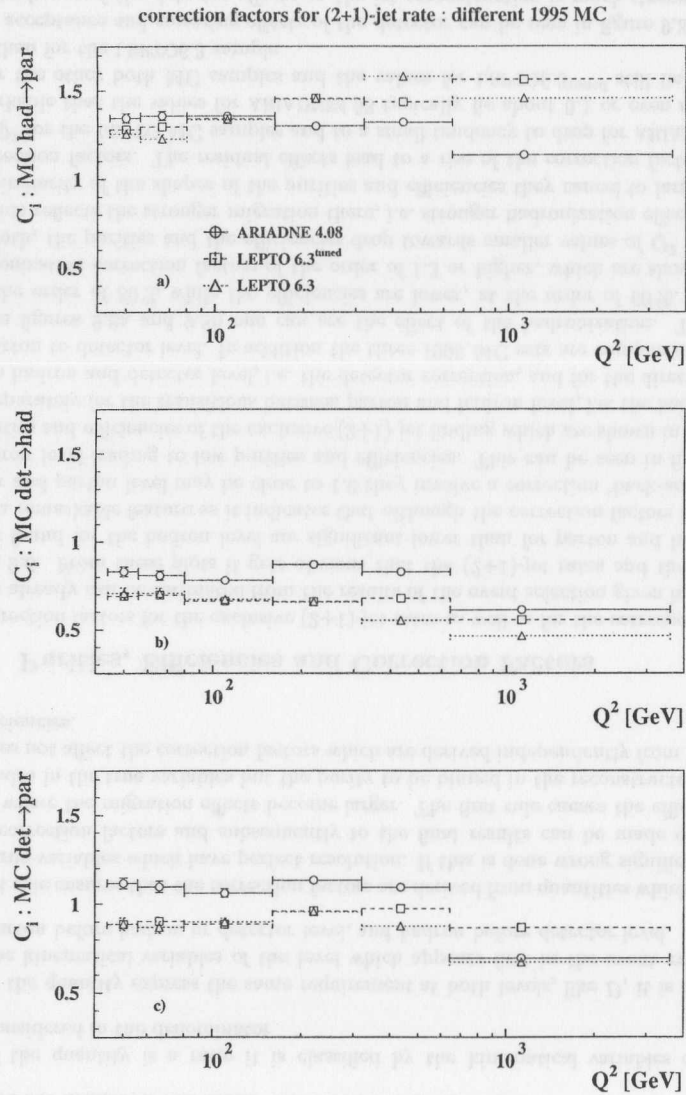
Figure 9.9: *Correction factors ^{ir}C for the exclusive (2+1)-jet rate in six bins of Q^2 using different 1995 MC. Separately given are the correction factors with errors calculated by equation 9.11 for the transition between parton and hadron level (top), hadron and detector level (center) and the direct transition from parton to detector level (bottom).*

towards lower Q^2, too, reflecting a deterioration of the reconstruction of the jets. Here the effect seems to be more pronounced as compared to the hadronization. But again, the shapes cancel to a large extent leaving only a slight drop of the correction factors (fig. 9.9b) towards higher Q^2, weakest for ARIADNE4.08 and most pronounced for LEPTO6.3.

In both cases, the hadronization and detector correction, ARIADNE4.08 provides highest purities and efficiencies and the correction factors closer to 1.0.

The result on the full transition between parton and detector level in one single step, omitting the hadron level, is shown in figures 9.8e, 9.8f and 9.9c. The purities and efficiencies simply reflect the sum of all the properties of the transitions discussed above. The significant deviations from 1.0 of the correction factors for the single transition steps cancel to some extent leading to the mentioned correction 'back-and-forth' via the hadron level. ARIADNE4.08 shows with typical correction values of 1.1 a different result than the LEPTO MC samples with values of about 0.9. This is an outcome of the different relative behavior of the correction factors of ARIADNE4.08 compared to the LEPTO MC samples discussed by means of figures 9.9a and 9.9b. But there is no sensible explanation for the rather low value of the highest Q^2-bin for the ARIADNE4.08 1995 MC sample, which is not seen in the ARIADNE4.08 1996 MC sample. The only reason is the low purity in the detector correction which easily could be caused by a fluctuation due to the low statistics in that bin.

The numerical values of the purities, efficiencies and correction factors of the three MC samples are summarized in the tables B.1 and B.2 in appendix B for the exclusive (2+1)-jet rate. Table B.3 gives the correction factors to correct the total DIS cross section $d\sigma^{tot}/dQ^2$ and the exclusive (2+1)-jet cross section $d\sigma^{(2+1)}/dQ^2$ to hadron and parton level.

9.4.2 Hadron and Parton Level Results

The obtained corrections were applied to the results of the event selection of the 1995 and 1996 data presented in section 9.3. The first aim of this analysis was to obtain the exclusive (2+1)-jet rate corrected to parton level in order to determine α_s from the (2+1)-jet rate. In parallel the exclusive (2+1)-jet cross section corrected to parton level was calculated to determine α_s from the (2+1)-jet cross section as well. As a byproduct also the corrected hadron level (2+1)-jet rate and the hadron level cross sections were calculated. All these results are listed numerically in the tables C.1 and C.2 in appendix C.

To calculate the cross sections quoted in this analysis only the standard procedures, well established and incorporated into the released reconstruction program packages, were applied. But there are known deficiencies in the present standard way of measuring cross sections.

The longitudinal vertex distribution in ZEUS data is underestimated by the plain MC in the area of the so-called *satellite bunches* (located at about $z = -80$ cm and $z = 70$ cm). This can be cured by a *vertex reweighting* procedure obtained from a *minimum bias sample* [AQ98] which has to be applied to the MC samples.

The luminosity measurement for data is less accurate for the fraction of ep-scattering events originating from the region of the satellite bunches which introduces an additional uncertainty on the absolute value of the measured luminosity.

The uncertainties in the cross section measurement due to the satellite bunches is reduced in this analysis by the application of a cut on the longitudinal vertex distribution. The absolute systematic uncertainties in the luminosity measurement are 1.1 % for the ZEUS 1995 data and 1.3 % for the ZEUS 1996 data. It was omitted to propagate these errors in the quoted hadron and parton level cross sections in appendix C.

Chapter 10

The Determination of α_s

In this chapter the α_s value is presented which was determined in this analysis. The method to determine α_s is described and is applied to the exclusive (2+1)-jet rate, R_{2+1}, as well as to the exclusive (2+1)-jet cross section, $\sigma^{(2+1)}$, found in the ZEUS 1995 and 1996 data samples. The question is discussed whether the data supports the running of α_s. An attempt is made to determine α_s also from the differential jet rate D_2 from the 1995 data.

10.1 Comparison to NLO Predictions

Figure 10.1 presents various sets of NLO predictions for the exclusive (2+1)-jet rate as they were obtained from MEPJET version 2.0 [MZ97b]. Figures 10.1a-b show the set obtained by applying the default phase space cuts and the default jet finding procedure and cuts, while figures 10.1c-f show different sets used for systematic checks. The same jet finding procedure, the KTCLUS implementation of the exclusive $K_\perp$ algorithm, was also used with MEPJET.

In order to provide predictions for different values of α_s, MEPJET version 2.0 was slightly modified. Normally MEPJET gets the value of $\Lambda_{\rm QCD}$, i.e. the value of α_s, from the selected set of parton density functions (PDF) and uses it internally for the matrix element calculations. For this analysis the possibility to override the value of $\Lambda_{\rm QCD}$ was added, a feature which became part of MEPJET with the release of version 2.1.

In each chosen Q^2-bin a set of predictions was obtained for the six values of $\Lambda_{\rm QCD}^4 = 100, 200, 300, 400, 600, 800$ MeV. In separate runs the total DIS and the exclusive (2+1)-jet cross sections were calculated for each value of $\Lambda_{\rm QCD}^4$ and each bin, together with their numerical errors. The exclusive (2+1)-jet rate subsequently was derived from their ratio.

By default the GRV(HO) [GRV95] parameterization of the parton density functions was used. With this set all the calculations were performed which were needed for the systematic checks. In addition the parameterization MRSA [MRS94] and CTEQ4M [LHK+97] were used with the default selections. The numerical results of the NLO predictions on the total DIS, the exclusive (2+1)-jet cross section and the exclusive (2+1)-jet rate using the default selections and the three PDFs GRV(HO), MRSA and CTEQ4M are given in the tables D.1 to D.3 in appendix D.

For the default selection, GRV(HO), the results on the exclusive (2+1)-jet rate are plotted in figure 10.1a. There the total data set is ordered in different subsets with varying $\Lambda_{\rm QCD}^4$. This way of plotting corresponds to the representation of the measured (2+1)-jet rates obtained from data given in figure 9.5. The (2+1)-jet rate strongly rises towards low values of Q^2, as it is predicted for the running of α_s. The rise becomes significant stronger with
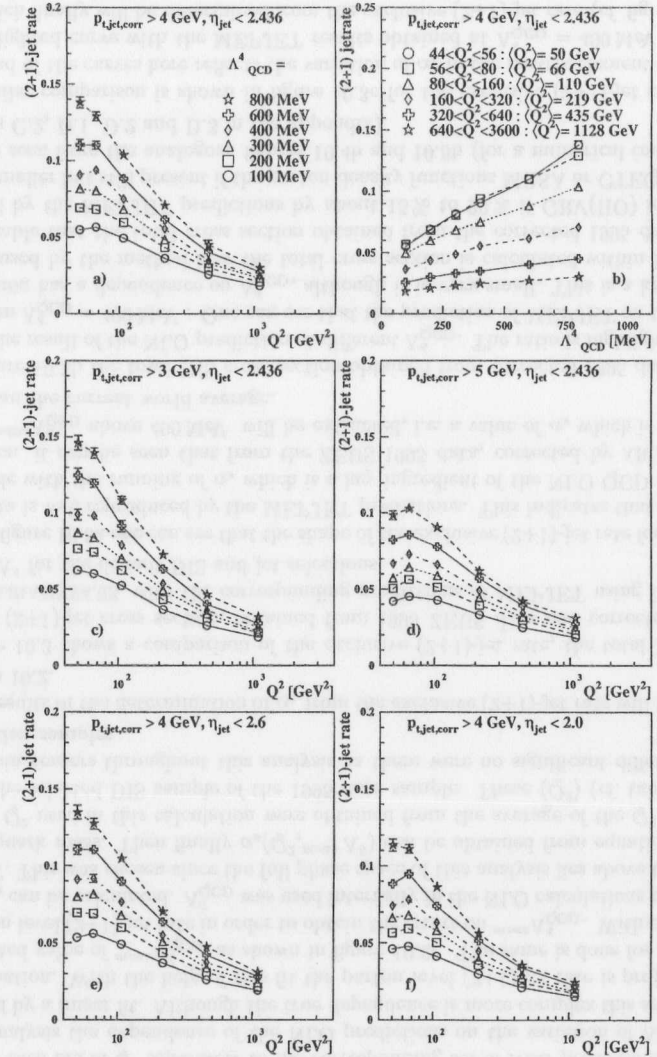
Figure 10.1: *MEPJET predictions on the (2+1)-jet rate for different $\Lambda_{\rm QCD}^4$ using GRV(HO). For the default jet selection (top) the (2+1)-jet rates are plotted versus Q^2 (left) and versus $\Lambda_{\rm QCD}^4$ (right). In addition, the (2+1)-jet rates are shown for the performed variations in p_t^{jet} (middle) and η^{jet} (bottom) in the jet selection.*

● ZEUS 95 DATA   ○ $44<Q^2<3600\ \mathrm{GeV^2}$
uncorrected

★ ZEUS 95 DATA   ☆ $44<Q^2<3600\ \mathrm{GeV^2}$
parton level, corr. by
ARIADNE 4.08 (CDM)

◇ MEPJET prediction (GRV(HO))

$\hookrightarrow \Lambda^5_{\mathrm{QCD}} \to \alpha_s(Q^2)$
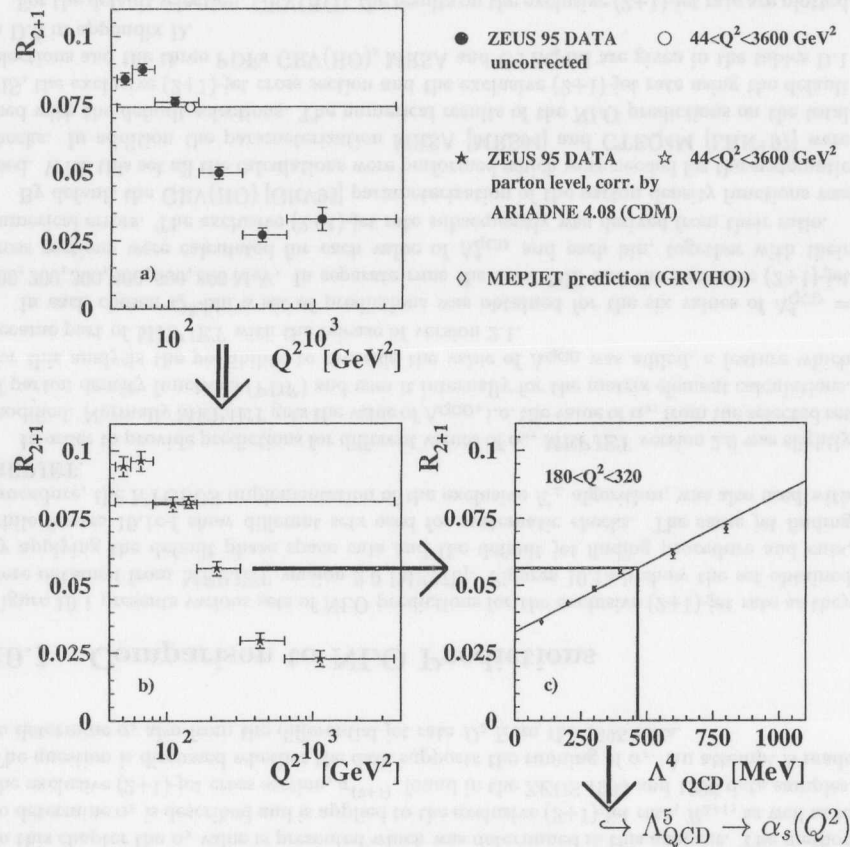
Figure 10.2: *Example procedure of the determination of α_s. See text for explanations.*

higher values of Λ^4_{QCD}. At low values of Q^2 a break-down of the (2+1)-jet rate can be observed, especially for small values of Λ^4_{QCD}. This is due to the phase space effect discussed in section 9.3.1. It becomes much more prominent when the cuts on the jets are tightened. This can be seen for a higher threshold for the p_t^{jet} in figure 10.1d and for a lower value of the maximum allowed pseudorapidity η^{jet} in figure 10.1f. This effect relaxes slightly when the cuts are widened (fig. 10.1c and 10.1e).

In figure 10.1b the same default data set is shown as in figure 10.1a, but now the rates are ordered in different subsets of Q^2-bins which are drawn as functions of Λ^4_{QCD}. This way the set of predictions with varied Λ^4_{QCD} can be compared to the measured exclusive (2+1)-jet rates in a single bin of Q^2, corrected to parton level. Thus, the measured $^{meas}\Lambda^4_{\mathrm{QCD}}$ can be interpolated. And from this, α_s can be calculated easily.

An example of the complete procedure to determine α_s from the measured quantities is visualized in figure 10.2. The raw uncorrected (2+1)-jet rates (fig. 10.2a) are corrected to parton level (fig. 10.2b) by the correction factors obtained from the selected MC sample (here the default choice ARIADNE4.08). The parton level (2+1)-jet rates in turn are compared for each bin of Q^2 separately to the corresponding set of NLO predictions (fig. 10.2c). In this analysis the dependence of the NLO predictions on the variation of Λ^4_{QCD} is parameterized by a linear fit. Although the true dependence is more complex this serves as good approximation. With the help of this fit the parton level (2+1)-jet rate is projected to the interpolated value of $^{meas}\Lambda^4_{\mathrm{QCD}}$, as shown in figure 10.2c. The same is done for the errors of the parton level (2+1)-jet rate in order to obtain the errors on $^{meas}\Lambda^4_{\mathrm{QCD}}$. With equation 2.11 $^{meas}\Lambda^5_{\mathrm{QCD}}$ can be calculated. Λ^5_{QCD} was used internally in the NLO calculations performed by MEPJET. This was chosen since the full phase space of this analysis lies above the threshold of the b-quark mass. Then finally $\alpha_s(Q^2, {}^{meas}\Lambda^5)$ can be obtained from equation 2.10. The values of Q^2 used in this calculation were obtained from the average of the Q^2 distribution $\langle Q^2 \rangle$ in the selected DIS sample of the 1995 data sample. These $\langle Q^2 \rangle$ (cf. table A.1) were used as bin centers throughout this analysis as there were no significant differences found for the other samples.

The results of the determination of α_s from the exclusive (2+1)-jet rate will be presented in section 10.2.

Figure 10.3 shows a comparison of the exclusive (2+1)-jet rate, the total DIS and the exclusive (2+1)-jet cross section, obtained from 1995 ZEUS data and corrected to parton level by ARIADNE4.08, with the corresponding predictions of MEPJET using GRV(HO) at different Λ^4 for the default DIS and jet selections.

From figure 10.3a one can see that the shape of the exclusive (2+1)-jet rate found from the ZEUS data is well reproduced by the MEPJET predictions. This indicates that the data are compatible with the running of α_s which is a key ingredient of the NLO QCD calculations. In addition, it can be seen that from the ZEUS 1995 data, corrected by ARIADNE4.08, a value of $^{meas}\Lambda^4_{\mathrm{QCD}}$ above 400 MeV will be extracted, i.e. a value of α_s which is significantly higher than the current world average.

In figure 10.3b the total DIS cross section obtained from corrected 1995 data is normalized by the result of the NLO prediction at different Λ^4_{QCD}. The ratio is highlighted with the result from $\Lambda^4_{\mathrm{QCD}} = 400$ MeV . One can see that the prediction of MEPJET on the total DIS cross section has a dependence on Λ^4_{QCD}, although it is very small. This is a known feature and is caused by the method how the total cross section is calculated within MEPJET. It is remarkable that the total cross section obtained from the corrected 1995 data is underestimated by the MEPJET predictions by about 15 % to 20 % if GRV(HO) is used. This effect is smaller but still present if the parton density functions MRSA or CTEQ4M are used as can be seen from the analogous figures 10.4b and 10.5b (for a numerical comparison see the tables C.2, D.1, D.2 and D.3 in the appendix).

A similar comparison is shown in figure 10.3c for the exclusive (2+1)-jet cross section. The spread of the curves here reflects the variation of α_s in the matrix element calculations. The highlighted curve with the MEPJET results obtained at $\Lambda^4_{\mathrm{QCD}} = 400$ MeV is near the result which finally will be determined from the exclusive (2+1)-jet rate (cf. fig. 10.3a). The MEPJET prediction on the exclusive (2+1)-jet cross section seems to underestimate the corrected cross sections from data in the same way as it was found for the total DIS cross section. Thus, in a determination of α_s from the (2+1)-jet rate these effects cancel. But if α_s is determined only from the exclusive (2+1)-jet cross section a value of $^{meas}\Lambda^4_{\mathrm{QCD}}$ will be preferred which leads to a ratio of about 1.0 in figure 10.3c. Therefore figure 10.3c shows
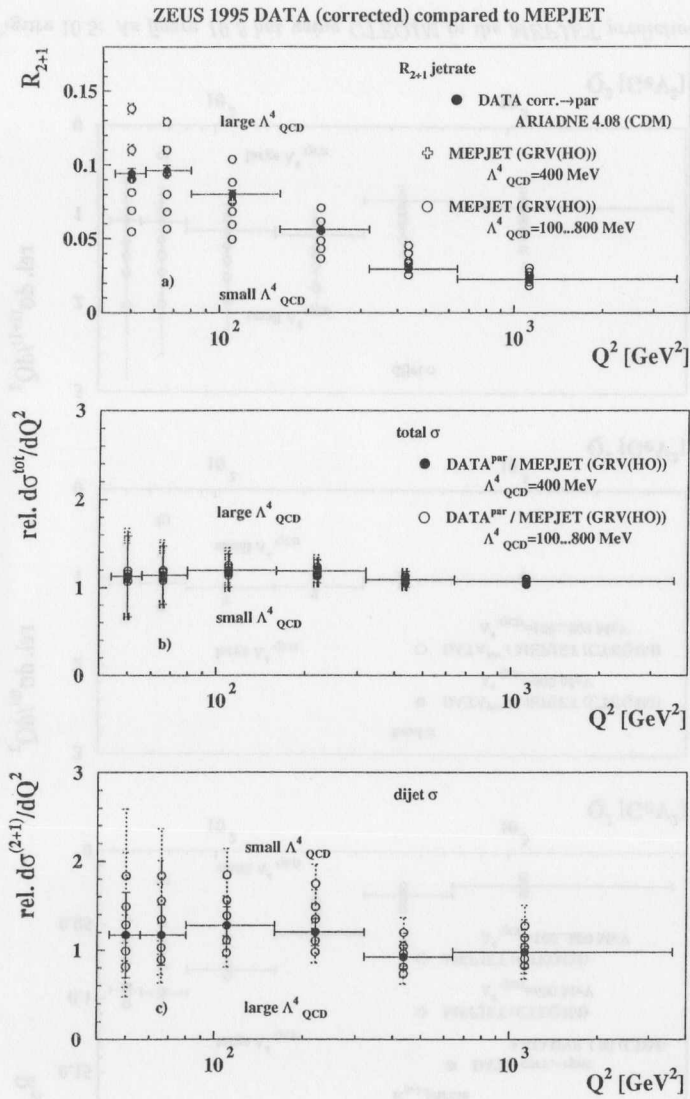
Figure 10.3: *Comparison of 1995 data corrected by* ARIADNE4.08 *to MEPJET predictions using GRV(HO) at different* Λ^4_{QCD} *for the default DIS and jet selections. In plot a) the corrected (2+1)-jet rate from data is plotted next to the MEPJET predictions from figure 10.1a. The relative magnitude of the cross sections data/MEPJET is given in b) for $d\sigma^{tot}/dQ^2$ and in c) for $d\sigma^{(2+1)}/dQ^2$.*
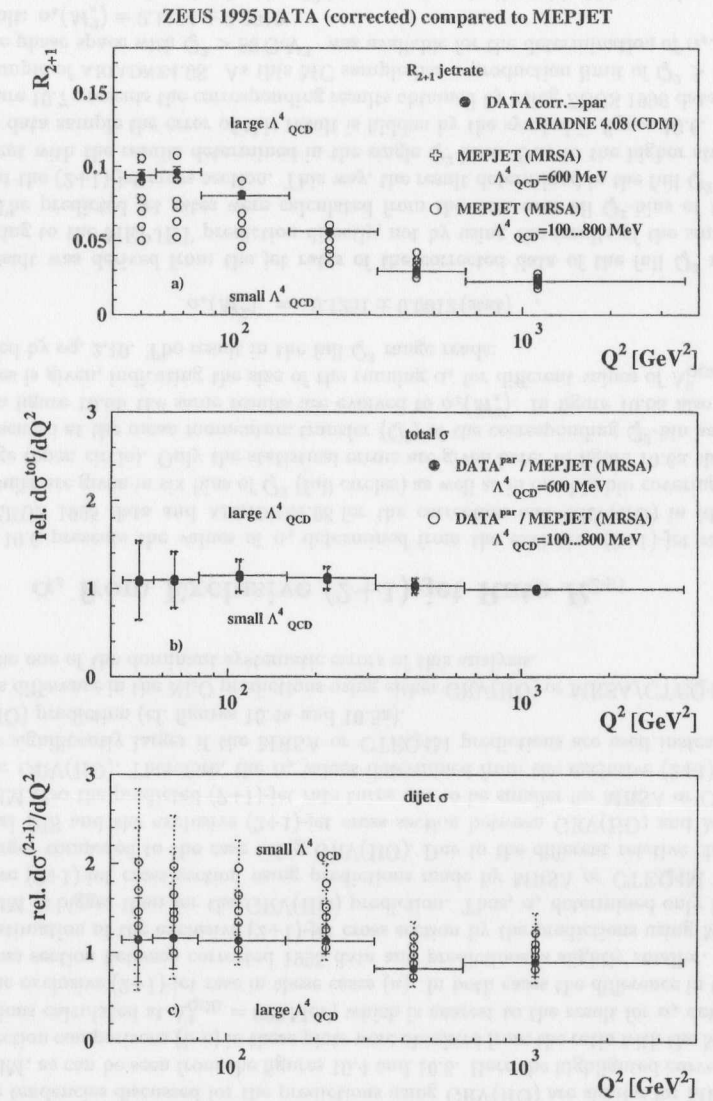
Figure 10.4: *As figure 10.3 but using MRSA in the MEPJET prediction.*

ZEUS 1995 DATA (corrected) compared to MEPJET
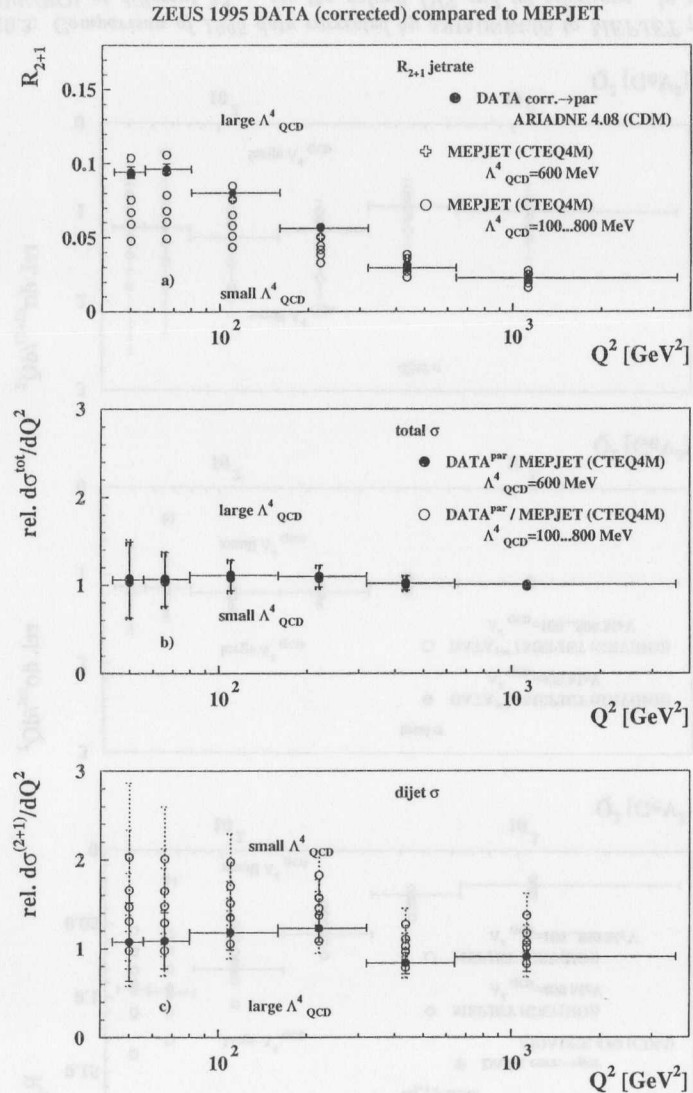
Figure 10.5: *As figure 10.3 but using CTEQ4M in the MEPJET prediction.*

that for the determination of α_s from the exclusive (2+1)-jet cross section alone a value for $^{meas}\Lambda_{\rm QCD}^4$ of about 600 MeV has to be expected; i.e. even significantly higher than from the exclusive (2+1)-jet rate.

The tendencies discussed for the predictions using GRV(HO) are similar for MRSA and CTEQ4M, as can be seen from the figures 10.4 and 10.5. Here the highlighted curves for the cross section comparisons (b-c) in these plots were obtained from the ratio with the MEPJET predictions calculated at $\Lambda_{\rm QCD}^4 = 600$ MeV, which is nearest to the result for α_s determined from the exclusive (2+1)-jet rate in these cases (a). In both cases the difference in the total DIS cross section between corrected 1995 data and predictions is slightly smaller. But the underestimation of the exclusive (2+1)-jet cross section by the predictions using MRSA or CTEQ4M is bigger than for the GRV(HO) prediction. Thus, α_s determined only from the exclusive (2+1)-jet cross section using predictions made by MRSA or CTEQ4M becomes even larger compared to the case using GRV(HO). Due to the different relative changes of the total DIS and the exclusive (2+1)-jet cross section between GRV(HO) and MRSA or CTEQ4M also the predicted (2+1)-jet rate turns out to be smaller for MRSA or CTEQ4M than for GRV(HO). Therefore, the α_s values determined from the exclusive (2+1)-jet rate become significantly larger if the MRSA or CTEQ4M predictions are used instead of the GRV(HO) prediction (cf. figures 10.4a and 10.5a).

This difference in the NLO predictions using either GRV(HO) or MRSA/CTEQ4M turns out to be one of the dominant systematic errors of this analysis.

10.2 α_s from Exclusive (2+1)-jet Rate R_{2+1}

Figure 10.6 presents the values of α_s determined from the exclusive (2+1)-jet rate R_{2+1} using ZEUS 1995 data and ARIADNE4.08 for the correction and GRV(HO) in MEPJET. The results are given in six bins of Q^2 (full circles) as well as in one big bin covering the full Q^2 range (open circle). Only the statistical errors are given here. In figure 10.6a the results are presented at the mean momentum transfer $\langle Q^2 \rangle$ of the corresponding Q^2-bin as $\alpha_s(Q^2)$, while in figure 10.6b the same results are evolved to $\alpha_s(M_z^2)$. In figure 10.6a also a group of curves is given, indicating the size of the running α_s for different values of $\Lambda_{\rm QCD}^5$ as it is predicted by eq. 2.10. The result in the full Q^2 range reads:

$$\alpha_s(M_z^2) = 0.1251 \pm 0.0012\,(\text{stat}) \ . \tag{10.1}$$

This result was derived from the jet rates of the corrected data of the full Q^2 range by comparing to the MEPJET prediction directly, not by using the results of the smaller Q^2-bins. The predicted jet rates were calculated from the sum over all Q^2-bins of the total DIS and the (2+1)-jet cross section. This way, the result determined in the full Q^2 range is consistent with the results determined in the single Q^2-bins. Due to the higher statistic of the full data sample the error of this result is hidden by the symbol in figure 10.6.

Figure 10.7 presents the corresponding results obtained by using ZEUS 1996 data and the 1996 sample of ARIADNE4.08. As this MC sample has a production limit of $Q^2 > 70$ GeV^2 only the phase space with $Q^2 > 80$ GeV^2 was available for the determination of α_s. It gives the result: $\alpha_s(M_z^2) = 0.1234 \pm 0.0010$.

The numerical results, also for the Q^2-bins, are given in the table 10.1 together with the corresponding values of $\Lambda_{\rm QCD}^4$ and $\Lambda_{\rm QCD}^5$ and the statistical errors. From these numbers one can see that both data sets agree very well with each other.

By comparing each single Q^2-bin one finds that the 1995 and 1996 results typically agree within 1.5 σ_{95}^{stat}. An exception is the bin 320 GeV$^2 < Q^2 < 640$ GeV^2 of the 1995 result. As

Figure 10.6: *(a): $\alpha_s(Q^2)$ with statistical errors only in six bins of Q^2 (full circles) and in one big bin (open circle) determined from the exclusive (2+1)-jet rate R_{2+1} using ZEUS 1995 data and ARIADNE4.08 for the correction and GRV(HO) in MEPJET. (b): the same data evolved to $\alpha_s(M_z^2)$. The statistical error of the result in the full phase space is small and hidden by the symbol.*

discussed in section 9.3.1 this bin exhibits most probably a statistical fluctuation. It differs from the other results by about $2.5\,\sigma_{95}^{stat}$ in the final results.

One further can see that the results in each single data set are consistent with a single value of $\alpha_s(M_z^2)$ within about $1\,\sigma_{95}^{stat}$, while these single values obtained independently from the two data sets agree with each other within $1.5\,\sigma_{95}^{stat}$.

Thus, in a global view, the results from both data sets exhibit a very good consistency.

10.2.1   The Running of α_s

The fact that the α_s-results of different, independent Q^2-bins are consistent with a single value of $\alpha_s(M_z^2)$, implies that they are consistent with the running of α_s. The evolution of
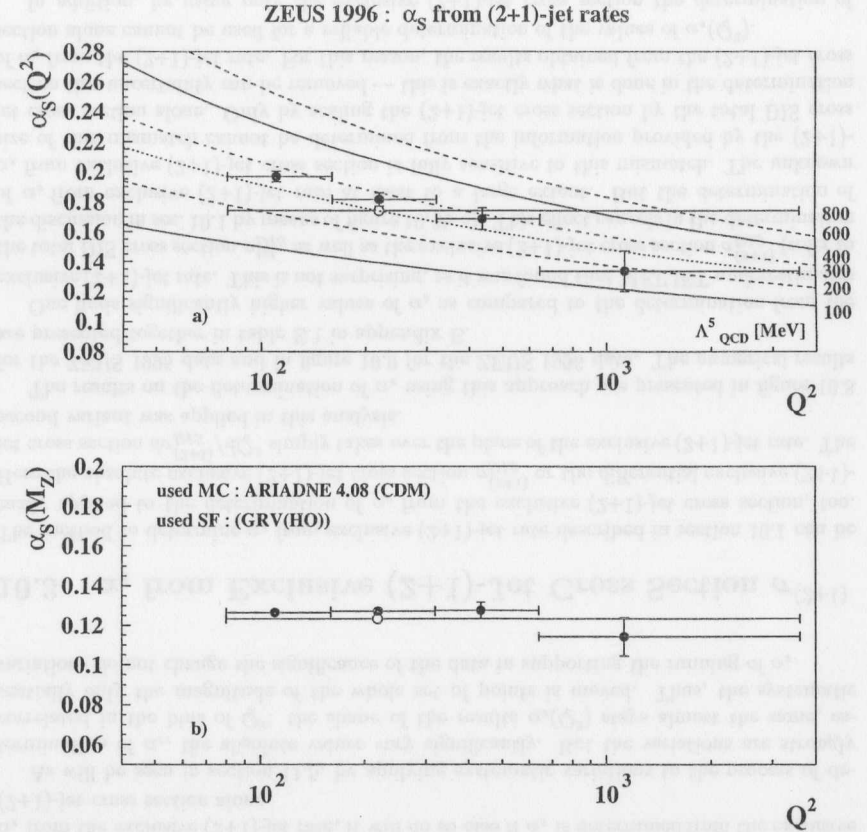
Figure 10.7: *Similar diagram as fig. 10.6, here for ZEUS 1996 data. Only the region $Q^2 > 80\,GeV^2$ can be used due to the limitation in the ARIADNE4.08 MC.*

the results to the Z° mass was done with eq. 2.10. The group of functions with constant Λ_{QCD}^5 in the figures 10.6a and 10.7a correspond to the prediction of the running of α_s. And judging by eye the determined results on α_s seem to agree well with this prediction.

To be more unbiased in judging, fits were performed to the individual α_s values depending on Q^2. The ansatz of a running α_s was checked against the ansatz of a constant α_s:

- By assuming a constant α_s, a constant value of $\alpha_s(Q^2)$ was fitted to the results presented in figures 10.6a and 10.7a, i.e. a horizontal line.

- By assuming a running α_s, a constant value of $\alpha_s(M_z^2)$ was fitted to the results presented in figures 10.6b and 10.7b.

The numerical results of these fits to the two data samples are listed in table 10.2. One finds that, if a constant α_s is assumed, the χ^2-values ($\chi^2/dof = 14/5$ for 1995 data and $\chi^2/dof = 10/3$ for 1996 data) are typically ten times larger compared to the assumption of

running α_s ($\chi^2/dof = 1.4/5$ for 1995 data and $\chi^2/dof = 0.58/3$ for 1996 data). Thus, the results on α_s from the 1995 & 1996 data samples support strongly the running of α_s.

This statement holds if LEPTO6.3$^{\text{tuned}}$ is used for the correction instead of ARIADNE4.08, but the difference in χ^2 reduces to a factor of about three (cf. table F.2 in appendix F). By looking at the corresponding figure F.3 one finds that this is caused mainly by the two bins with highest Q^2 and lowest statistics. Thus, the view is spoiled by these two bins. The four lower Q^2-bins look almost as consistent with the running of α_s as if ARIADNE4.08 is used. Therefore, the general picture is not changed.

This statement also holds for the determination of α_s from the exclusive (2+1)-jet cross section $\sigma^{(2+1)}$. From table E.2 in appendix E one finds differences in χ^2 by factors of four to ten. Here the absolute χ^2-values are reduced as compared to the ones found for the (2+1)-jet rate since the statistical errors are larger. But the running of α_s is supported by this way of determination of α_s, too (see also figures 10.8 and 10.9 in sec. 10.3). This does not surprise, as the ratios of corrected data cross sections over MEPJET predictions, as given in figure 10.3, essentially are constant with Q^2. The running of α_s enters only via the exclusive (2+1)-jet cross section. Thus, if the data is consistent with the running by determining α_s from the exclusive (2+1)-jet rate, it will do so also if α_s is determined from the exclusive (2+1)-jet cross section alone.

As will be seen in section 11.5, by applying systematic variations to the process of determination of α_s, the absolute values vary significantly. But the variations are strongly correlated in the bins of Q^2: the shape of the results $\alpha_s(Q^2)$ stays almost the same, essentially only the magnitude of the whole set of points is moved. Thus, the systematic variations do not change the significance of the data in supporting the running of α_s.

10.3 α_s from Exclusive (2+1)-Jet Cross Section $\sigma^{(2+1)}$

The method to determine α_s from exclusive (2+1)-jet rate described in section 10.1 can be easily applied to the determination of α_s from the exclusive (2+1)-jet cross section, too. Here the absolute exclusive (2+1)-jet cross section $\sigma_{DIS}^{(2+1)}$ or the differential exclusive (2+1)-jet cross section $d\sigma_{DIS}^{(2+1)}/dQ^2$ simply takes over the place of the exclusive (2+1)-jet rate. The second variant was applied in this analysis.

The results on the determination of α_s using this approach are presented in figure 10.8 for the ZEUS 1995 data and in figure 10.9 for the ZEUS 1996 data. The numerical results are presented together in table E.1 in appendix E.

One finds significantly higher values of α_s as compared to the determination from the exclusive (2+1)-jet rate. This is not surprising, as it was found that MEPJET underestimates the total DIS cross section σ_{DIS}^{tot} as well as the exclusive (2+1)-jet cross section $\sigma_{DIS}^{(2+1)}$ (refer to the discussion in sec. 10.1 by means of figure 10.3b-c). This effect cancels in the determination of α_s from exclusive (2+1)-jet rate at least to a large extent. But the determination of α_s from exclusive (2+1)-jet cross section is fully sensitive to this mismatch. The unknown size of this mismatch cannot be determined from the information provided by the (2+1)-jet cross section alone. Only by scaling the (2+1)-jet cross section by the total DIS cross section this uncertainty can be removed — this is exactly what is done in the determination of α_s from the (2+1)-jet rate. For this reason, the results obtained from the (2+1)-jet cross section alone cannot be used for a reliable determination of the values of $\alpha_s(Q^2)$.

In addition, by using only the exclusive (2+1)-jet cross section the determination of α_s becomes sensitive to uncertainties in the measurement of the luminosity. This is not

---

α_s from R_{2+1} using ZEUS 1995 data, ARIADNE4.08, GRV(HO)

Q^2-range [GeV^2]	bin 1 44…56	bin 2 56…80	bin 3 80…160	bin 4 160…320	bin 5 320…640	bin 6 640…3600	total 44…3600
$\langle Q^2\rangle$ [GeV^2]	50	66	110	219	435	1128	140
$\alpha_s(Q^2)$	0.2108±0.0048	0.2074±0.0047	0.1965±0.0040	0.1787±0.0050	0.139±0.011	0.1874±0.0028	
$\alpha_s(M_Z^2)$	0.1237±0.0016	0.1253±0.0016	0.1264±0.0016	0.1256±0.0024	0.1101±0.0070	0.1178±0.0089	0.1251±0.0012
$\Lambda^4_{\rm QCD,\overline{MS}}$ [MeV]	426±31	458±34	481±34	466±51	212±98	320±170	454±25
$\Lambda^5_{\rm QCD,\overline{MS}}$ [MeV]	306±25	332±27	351±28	338±42	140±74	220±130	329±20

α_s from R_{2+1} using ZEUS 1996 data, ARIADNE4.08, GRV(HO)

Q^2-range [GeV^2]	bin 2 56…80	bin 3 80…160	bin 4 160…320	bin 5 320…640	bin 6 640…3600	total 80…3600
$\langle Q^2\rangle$ [GeV^2]	66	110	219	435	1128	218
$\alpha_s(Q^2)$	0.1968±0.0036	0.1816±0.0045	0.1687±0.0074	0.134±0.014	0.1741±0.0020	
$\alpha_s(M_Z^2)$	0.1265±0.0014	0.1270±0.0021	0.1275±0.0041	0.1141±0.0097	0.1234±0.0010	
$\Lambda^4_{\rm QCD,\overline{MS}}$ [MeV]	484±31	495±46	505±94	270±160	420±20	
$\Lambda^5_{\rm QCD,\overline{MS}}$ [MeV]	353±25	362±38	370±78	180±130	302±16	

Table 10.1: $\alpha_s(Q^2)$ and $\alpha_s(M_Z^2)$ from exclusive (2+1)-jet rate R_{2+1} using ZEUS 1995 & 1996 data, ARIADNE4.08 for the correction and GRV(HO) in MEPJET. To correct the ZEUS 1996 data the 1996 sample of ARIADNE4.08 was used. Also given are the corresponding values for $\Lambda^4_{\rm QCD}$ and $\Lambda^5_{\rm QCD}$ in the $\overline{\rm MS}$ renormalization scheme. Only statistical errors are given.

fits to the results on α_s in bins of Q^2

sample	$\langle Q^2\rangle$	constant α_s assumed $\langle Q^2\rangle$	α_s	χ^2/dof	running α_s assumed α_s	χ^2/dof
ZEUS 1995	8315 GeV^2	140 GeV^2	0.1947±0.0022	14/5	0.1249±0.0010	1.4/5
ZEUS 1996	8315 GeV^2	218 GeV^2	0.1860±0.0026	10/3	0.1266±0.0011	0.58/3

Table 10.2: Fits to the results on α_s from exclusive (2+1)-jet rate R_{2+1} in bins of Q^2 in order to judge on the running of α_s using ARIADNE4.08 for the correction.

ZEUS 1995 : α_S from σ^{2+1}

ZEUS 1996 : α_S from σ^{2+1}
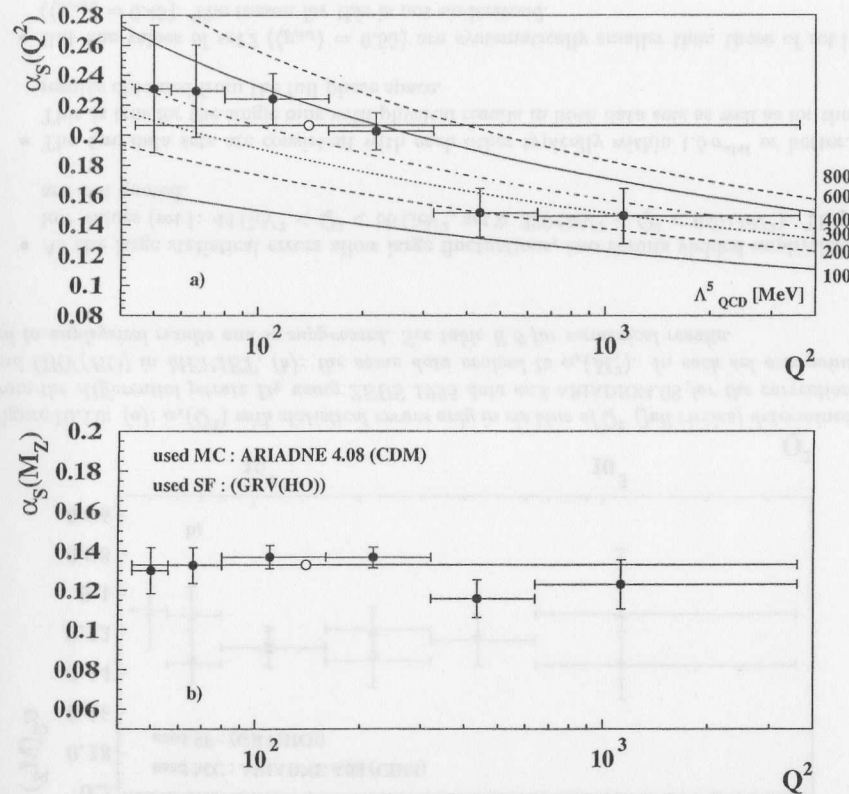
Figure 10.8: *(a): $\alpha_s(Q^2)$ with statistical errors only in six bins of Q^2 (full circles) and in one big bin (open circle) determined from the dijet cross section $\sigma^{(2+1)}$ using ZEUS 1995 data and ARIADNE4.08 for the correction and GRV(HO) in MEPJET. (b): the same data evolved to $\alpha_s(M_z^2)$. The statistical error of the result in the full phase space is small and hidden by the symbol. See table E.1 for numerical results.*

Figure 10.9: *(a): Similar diagram as fig. 10.8, here for ZEUS 1996 data.*

regarded further since this uncertainty (1.1 % in 1995 and 1.3 % in 1996) is much smaller than that introduced by the mismatch of the cross sections between data and MEPJET.

10.4 α_s from Differential Jet Rate D_2

Finally, the method to determine α_s from exclusive (2+1)-jet rate described in section 10.1 was utilized to determine α_s from the differential (2+1)-jet rate D_2. Here the differential rate D_2, obtained between two values of y_{cut} (eq. 5.12), simply took over the role of the exclusive (2+1)-jet rate, obtained at a fixed resolution parameter y_{cut}.

The main problem of this method is, that due to the calculation of the difference of two similarly large numbers, the resulting differential rates become small and the errors become

large. Thus, high statistics are needed to obtain reasonable results for single points of the measurement.

The determination of α_s was carried out in two ranges of y_{cut}:

- set 1: $0.4 < y_{cut} < 0.5$: i.e. $\langle y_{cut} \rangle = 0.45$, $\Delta y_{cut} = 0.1$,

- set 2: $0.5 < y_{cut} < 0.6$: i.e. $\langle y_{cut} \rangle = 0.55$, $\Delta y_{cut} = 0.1$.

This covers the range which was regarded as safe in the study of the behavior of the R_{n+1} jet rates with the jet resolution parameter y_{cut} varied (cf. sec. 11.3.2).

The results of this approach are presented graphically in figure 10.10 and numerically in table E.3 in appendix E.

One finds the following features:

- The statistical errors typically are five to ten times larger as compared to the determination of α_s from the exclusive(2+1)-jet rate.

ZEUS 1995 : α_S from differential jet rate D_2
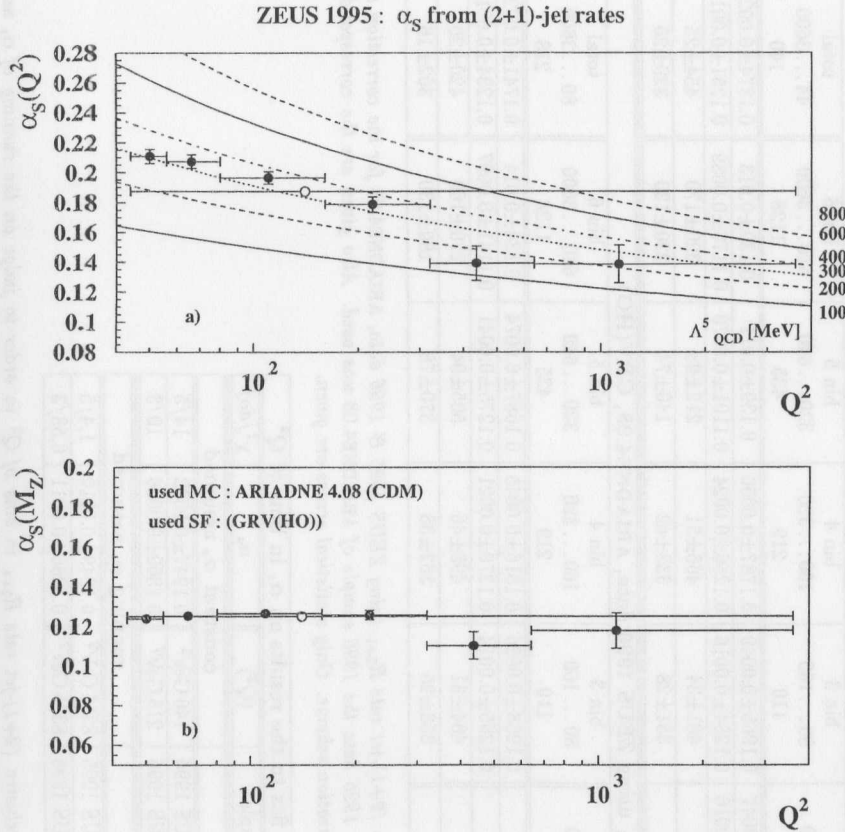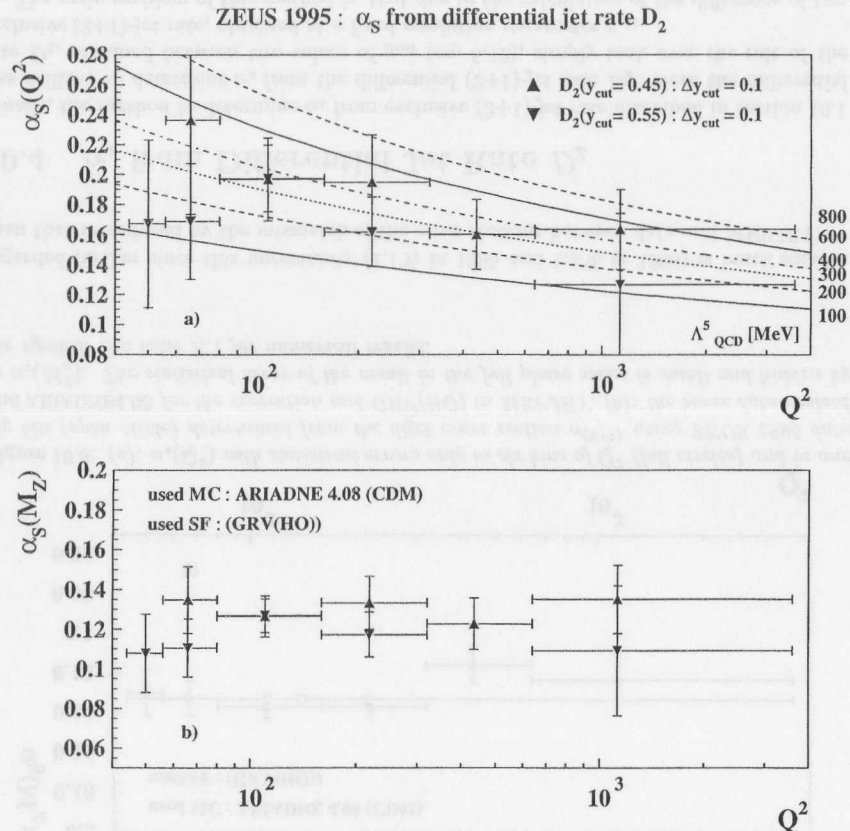

Figure 10.10: *(a): $\alpha_s(Q^2)$ with statistical errors only in six bins of Q^2 (full circles) determined from the differential jetrate D_2 using ZEUS 1995 data and ARIADNE4.08 for the correction and GRV(HO) in MEPJET. (b): the same data evolved to $\alpha_s(M_z^2)$. In each set one point led to unphysical results and is suppressed. See table E.3 for numerical results.*

As the statistical errors are so large no conclusion can be drawn from these results. To achieve more reliable results, more points at different resolution parameters $\langle y_{cut} \rangle$ are needed. With these additional, independent results a combined χ^2-fit could be performed, where the results from all $\langle y_{cut} \rangle$ are fitted to their corresponding predictions in one procedure. This should lead to reliable values of α_s at least for the results obtained in full Q^2-range, which provides the highest possible statistics, possibly also for results from single Q^2-bins.

- As the large statistical errors allow large fluctuations, two results yielded unphysical low values (set 1: $44\,\text{GeV}^2 < Q^2 < 56\,\text{GeV}^2$, set 2: $320\,\text{GeV}^2 < Q^2 < 640\,\text{GeV}^2$). They are not quoted.

- The two data sets are consistent with each other typically within $1.5\,\sigma^{stat}$ or better. This is true for the single bins with physical results in both data sets as well as for the results obtained from the full phase space.

- But the values of set 2 ($\langle y_{cut} \rangle = 0.55$) are systematically smaller than those of set 1 ($\langle y_{cut} \rangle = 0.45$). The reason for this is not understood.

- Due to the large errors no reliable statement on the running of α_s can be made (although, numerically the running of α_s is still favored).

Chapter 11

Systematic Studies

In this chapter the systematic studies are summarized which were performed in this analysis. The use of ARIADNE4.08 as the default MC sample in this analysis is justified and weighted against the other available MC samples defined in section 8.5. In addition, the MC studies to choose the jet selection parameters and cuts are discussed here. Finally, the results on the systematic studies performed on the determination of α_s from the exclusive (2+1)-jet rate are presented and the final result is discussed.

11.1 Comparisons at Detector Level

The first task of any MC sample, used to correct data which should be compared to NLO predictions (or to measure hadron level cross sections), is to describe the measured data well. This subsection presents the degree of description of the ZEUS 1995 data sample by the MC samples ARIADNE4.08, LEPTO6.3^{tuned} and LEPTO6.3.

11.1.1 Cut Variables

The match of the important kinematic variables between ZEUS 1995 data and any of the used MC samples is mostly well for the total DIS sample, especially in the important variables. For the exclusive (2+1)-jet subsample there are differences in the integrated cross section which are discusses in section 11.1.2 and, hence, in the magnitude of the compared distributions. But the shapes are modeled similarly well as for the total DIS sample.

Figures 11.1 and 11.2 present a selection of the most important kinematic variables in the phase space used in this analysis. In each plot a quantity is given measured in the total DIS sample (open dots) as well as measured in the exclusive (2+1)-jet sample (filled dots) together with the corresponding MC simulations. All quantities are given absolutely normalized to the luminosity measured in the ZEUS 1995 data. Thus, not only the shape but also the magnitude can be compared.

Figure 11.1 presents the distribution of the key variable for the binning in this analysis, Q^2_{DA}, and the variables used for kinematic cuts: x_{DA}, y_{JB} and y_{EL}. In general, a very good description of the measured data by the different MC is found. The small deviations in the medium ranges of the y_{JB} and y_{EL} distribution for the (2+1)-jet sample are not important (fig. 11.1c-d). These variables are used for cuts only and integrated over otherwise. The resolutions obtained for these quantities obtained from the RMS of the ratio 'reconstructed over true' in the ARIADNE4.08 sample are: 12.3 % for Q^2_{DA}, 24.0 % for x_{DA}, 17.4 % for y_{JB} and 28.5 % for y_{EL}. The systematic shift between hadron and detector level in the distribution for
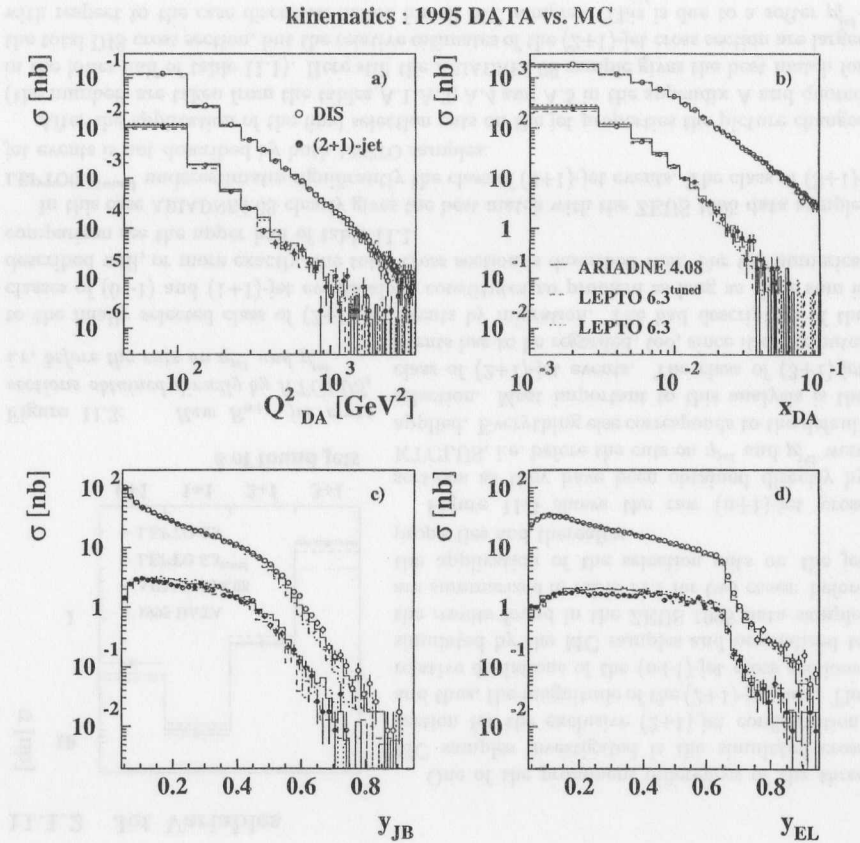
Figure 11.1: *Detector level comparison between 1995 data and different 1995 MC for the kinematic quantities Q^2_{DA}, x_{DA}, y_{JB} and y_{EL} for all DIS events and events with an identified (2+1)-jet state. The quantities are given in the range of the selection cuts.*

Q^2_{DA} is with +3.3 % small and almost constant over the full Q^2-range used in this analysis. It is by chance 0.0 % in average for x_{DA} but exhibits a slope. x_{DA} overestimates the true x at low Bjorken-x slightly and underestimates it at high values where the statistics are low. The systematic shift in the y_{EL}-distribution is +9.8 % in average but approaches 0.0 % for $y > 0.65$. Hence, it is the best variable to cut on at high values of Bjorken-y. Vice versa, the systematic shift in the y_{JB}-distribution is −16.7 % in average but approximately approaches 0.0 % around the lower cut border of Bjorken-y. The cut on y_{JB} at this border introduces the lowest bias to the data sample.

Figure 11.2 presents the distributions for the quantities of the reconstructed electron $E_{e'}$ and $\Theta_{e'}$ and two quantities used for cleaning cuts: $\delta = E - p_z$ and the longitudinal vertex distribution, vtx_z. The energy of the reconstructed and corrected electron, $E_{e'}$ (fig. 11.2a), is described reasonably well by the MC. The kinematic peak for the total DIS sample and the

kinematics : 1995 DATA vs. MC
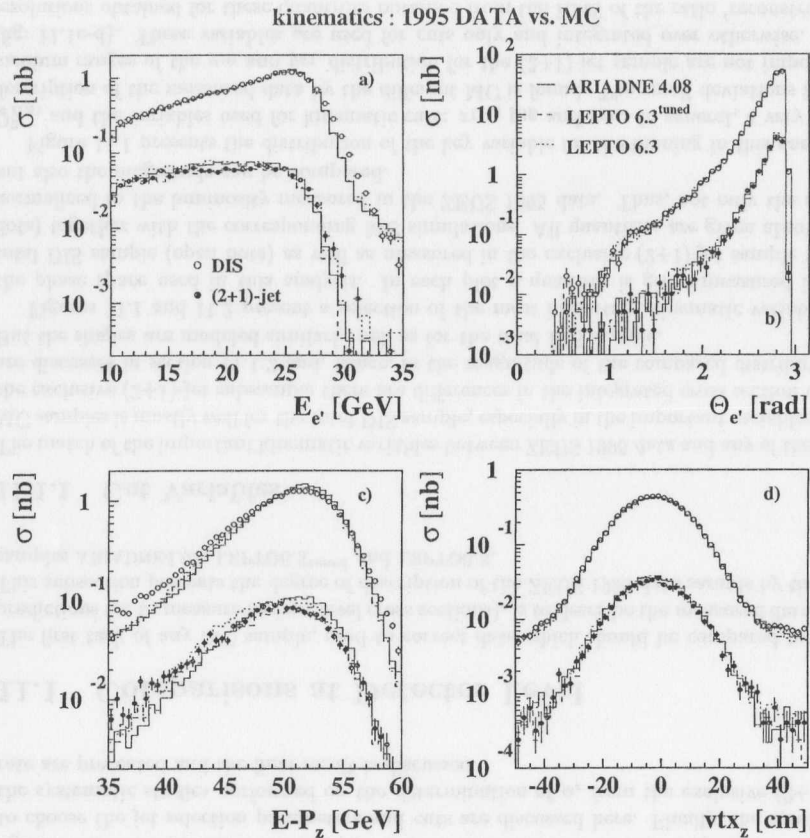
Figure 11.2: *Detector level comparison between 1995 data and different 1995 MC for the kinematic quantities $E_{e'}$, $\Theta_{e'}$, $E - p_z$ and vtx_z for all DIS events and events with an identified (2+1)-jet state. The quantities are given in the range of the selection cuts.*

medium energies for the exclusive (2+1)-jet sample are slightly overestimated by the MC. In addition, it is true that the average systematic shift between hadron and detector level is only +0.3 % with a resolution is of 9.7 % but the differential behavior is more complicated. The reconstructed $E_{e'}$ underestimates the true electron energy above the kinematic peak. At the kinematic peak it is still lower by typically 0.7 GeV. It matches the true electron energy around $E_{e,true} \approx 21$ GeV and overestimates it below. This way of behavior of the reconstructed electron energy is introduced by the SRTD and Presampler corrections which are tuned to correct a data sample in average and is seen in all ZEUS analyses within the DIS regime. The electron energy reconstructed from the double angle variables is, around the cut value of 10 GeV, typically 1-2 GeV lower than the reconstructed and corrected electron energy and provides there in average a better match with the generated electron.

The polar scattering angle of the electron, $\Theta_{e'}$ (fig. 11.2b), is modeled very well (with a

systematic shift of about -0.1 % at a resolution of 2.2 %).

The quantity $\delta = E - p_z$ is not very well described by any MC sample. This is due to the fact that this quantity is obtained from data and MC without applying the corrections to the electron, or the calorimeter cells which contribute to the electron. Thus, the different treatment for data and MC performed by the energy reconstruction in SINISTRA and the correction by the SRTD or the Presampler is not applied here. Figure 11.2c therefore shows the usual degree of description of δ achieved at ZEUS.

The longitudinal vertex distribution, vtx_z (fig. 11.2d), again is modeled very well within the region used in this analysis. At the forward edge ($vtx_z \approx 50\,cm$) in the total DIS sample a small effect may be suspected by one of the satellite bunches which is not well described in the MC.

Looking on the basic kinematic variables the MC samples ARIADNE4.08, LEPTO6.3^{tuned} and LEPTO6.3 do not differ significantly. As the degree of description of the data is mostly well and similar in all cases there are no means to favor one of the MC samples.

11.1.2   Jet Variables
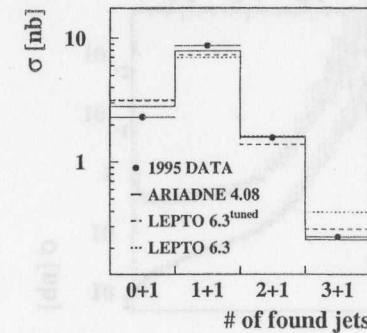
Figure 11.3:   *Raw R_{n+1} jet cross sections obtained directly by KTCLUS, i.e. before the cuts on η^{jet} and p_t^{jet}.*

One of the prominent differences of the three MC samples investigated is the simulated cross section for the exclusive (2+1)-jet configuration, and thus, the magnitude of the (2+1)-jet rate. The relative deviations of the (n+1)-jet cross sections, simulated by the MC samples and normalized to the results found in the ZEUS 1995 data sample, are summarized in table 11.1 for two cases: before the application of the selection cuts on the jet properties and thereafter.

Figure 11.3 shows the raw (n+1)-jet cross sections as they have been obtained directly by KTCLUS, i.e. before the cuts on η^{jet} and p_t^{jet} were applied. Everything else corresponds to the default selection. Most important to this analysis is the class of (2+1)-jet events. The class of (3+1)-jet events has to be regarded, too, since it contributes to the finally selected class of (2+1)-jet events by migration. The bad description of the classes of (0+1) and (1+1)-jet events alone constitutes no problem as long as their sum is described well, or more exactly, the total cross section is described well. For the numerical comparison see the upper half of table 11.1.

In this case ARIADNE4.08 clearly gives the best match with the ZEUS 1995 data sample. LEPTO6.3^{tuned} underestimates significantly the class of (2+1)-jet events. The class of (3+1)-jet events is not described by both LEPTO samples.

After the application of the final selection cuts on the jet properties the picture changes (the numbers are taken from the tables A.1,A.3, A.4 and A.5 in the appendix A and quoted in the lower half of table 11.1). Here still the ARIADNE4.08 sample gives the best match for the total DIS cross section, but the relative estimates of the (2+1)-jet cross section are larger with respect to the case discussed before for all MC samples. This is due to a softer p_t^{jet}-distribution in the subsample of (2+1)-jet events in data at low p_t^{jet} than simulated in the MC samples. The correction procedure for p_t^{jet}, presented in section 11.3.4, cannot account

relative (n+1)-jet cross section MC/data [%]				
generator	$(0+1) \vee (1+1)$	$(2+1)$	$(3+1)$	total DIS
before cuts on jets (cf. fig. 11.3)				
ARIADNE4.08	-2%	$+2\%$	-6%	
LEPTO6.3^{tuned}	-5%	-12%	$+15\%$	
LEPTO6.3	-8%	$+4\%$	$+58\%$	
with default jet selection				
ARIADNE4.08		$+10\%$		-2%
LEPTO6.3^{tuned}		-8%		-5%
LEPTO6.3		$+15\%$		-5%
typical absolute errors				
	$\leq 1\%$	$\leq 2\%$	$\leq 3\%$	$\leq 1\%$

Table 11.1: *Relative (n+1)-jet cross sections. Comparison between MC simulation and ZEUS 1995 data before the application of the selection cuts on the jet properties and thereafter.*

for this. A cut on a minimum p_t^{jet} removes more events in data than in the MC samples. This effect is weakest for the LEPTO6.3^{tuned} MC sample.

In a global view one has to conclude: none of the used MC samples describe well the relative size of the class of $(2+1)$-jet events. The LEPTO6.3 MC sample is slightly disfavored with respect to the other two as it gives the worst estimate in most cases.

In the following plots the features of $(2+1)$-jet events are presented and the degree of description of the ZEUS 1995 data sample by the used MC samples is investigated for the default jet selection. Since in these plots the MC simulation always is normalized to the luminosity measured in the 1995 data sample the discrepancies in the relative size of the class of $(2+1)$-jet events presented above will be visible as mismatch in the magnitude of the histograms.

Figure 11.4 presents the invariant quantities describing the internal properties of a $(2+1)$-jet configuration of a hadronic final state. The relative $\delta_{jet} = E_{jet} - p_{z,jet}$, z_p (eq. 4.9, fig. 11.4a), of the two jets holds $z_{p1} + z_{p2} = 1$. Therefore here only the spectrum of $z_{p1'} < z_{p2'}$ is plotted. It shows clearly the feature of the $K_\perp$ algorithm to be safe against the singularities at $z \to 0$ and $z \to 1$. The shape of the data is described reasonably well by all MC samples, but LEPTO6.3^{tuned} underestimate the data at low z_p $(0.0 < z_p < 0.2)$ while the other two overestimate the data in the other region $0.2 < z_p 0.5$.

The momentum fraction of the struck quark, x_p (eq. 4.8, fig. 11.4b), is described well by LEPTO6.3^{tuned} at low values, well by LEPTO6.3 at high values and to soft in the other cases.

The invariant mass of the dijet system, m_{jj} (fig. 11.4c), generally is simulated too hard. Still the best estimate is provided by ARIADNE4.08. The relative transverse momentum of the two jets, $p_{t,21}$ (eq. 4.10, fig. 11.4d), is simulated too hard in all cases, too. But the shapes still are described reasonably well in the both cases.

Although the description of the invariant $(2+1)$-jet variables in data by the MC samples is not well but only reasonable, there is no handle to rule out a particular MC sample judging from these variables.

Figure 11.5 presents the jet properties of the two current jets for events with an identified $(2+1)$-jet state using the default jet selection. The current jets are ordered by their pseudo-rapidity, η (eq. 4.12), in each event. Thus, *forward jet* refers to the current jet which is more
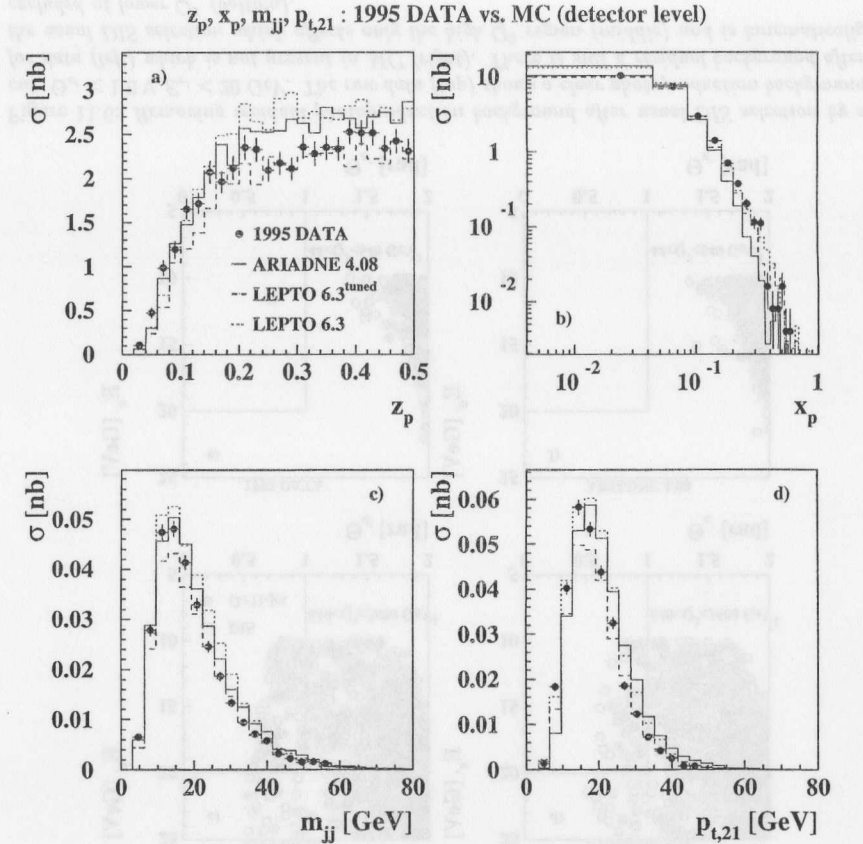
Figure 11.4: *Detector level comparison between 1995 data and different 1995 MC for the invariant quantities z_p, x_p, m_{jj} and $p_{t,21}$ of events with an identified (2+1)-jet state (default selection).*

directed towards the proton direction. Regarded are the pseudorapidities, η^{jet} (fig. 11.5a-b), and transverse momenta, p_t^{jet} (fig. 11.5c-d), of the two current jets.

The η^{jet} distributions are simulated significantly too much forward by the LEPTO6.3 MC in both cases: for the backward and the forward current jet of the $(2+1)$-jet events. Thus, not only the description of the magnitude but also that of the shape is bad, especially in the region where the cut on η^{jet} is applied. ARIADNE4.08 and LEPTO6.3^{tuned} describe the shape of the η^{jet}-distributions reasonably well, with advantages for ARIADNE4.08. The mismatch in the magnitude of the histograms, i.e. the $(2+1)$-jet cross section (cf. tab. 11.1), is most dominant in the transverse direction ($\eta^{jet} \approx 0$).

The match of the p_t^{jet}-distributions simulated by the LEPTO6.3 MC with data is similarly bad as seen for η^{jet}. Again, this mismatch is worst in the cut region disfavoring strongly this MC. In contrast, the ARIADNE4.08 and LEPTO6.3^{tuned} MC describe reasonably well the

η_{jet} & $p_{t,jet}$: 1995 DATA vs. MC (detector level)
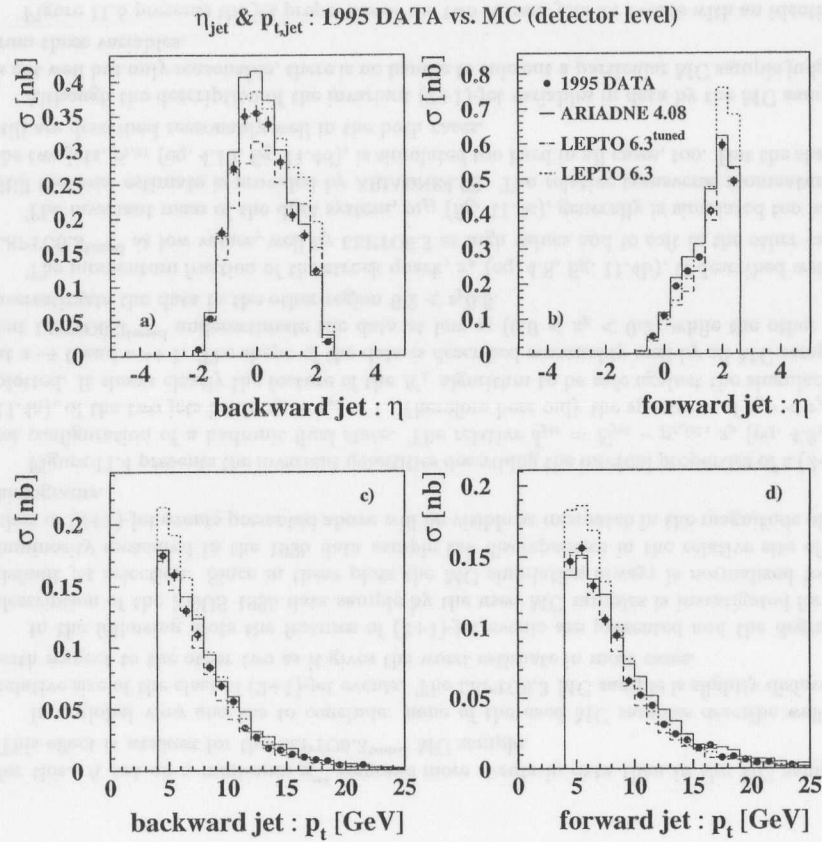
Figure 11.5: *Detector level comparison between 1995 data and different 1995 MC for the* η^{jet} *and* p_t^{jet} *of the reconstructed jets of events with an identified (2+1)-jet state (default selection). The two jets are ordered in* η*; „forward" refers to the higher* η *value.*

shape of the p_t^{jet}-distributions. ARIADNE4.08 exhibits spectra which are a bit harder than for data while the spectra of LEPTO6.3^{tuned} are a bit softer compared to data. Hence, a cut at a minimum p_t^{jet} supports a change in the relative (2+1)-jet cross sections for the transition „before" and „after" jet selection cuts as discussed by means of table 11.1.

Judging from the description of the jet properties, the LEPTO6.3 MC is ruled out for the correction of the data to parton level. ARIADNE4.08 and LEPTO6.3^{tuned} still give reasonable descriptions of the data with some advantages for ARIADNE4.08 (in the η^{jet}-distributions).

11.1.3 The Cut on $\Theta_{e'}$ and $E_{e'}$

In this analysis the cut „$\Theta_{e'} < 1.0\,rad \lor E_{e'} < 20\,GeV$" was applied in addition to the usual DIS event selection performed at ZEUS. It turned out to be necessary to remove some residual background in the high-Q^2 region as it spoiled strongly the exclusive (2+1)-jet rate

$\Theta_{e'}$-$E_{e'}$-cut : 1995 DATA vs. ARIADNE 4.08
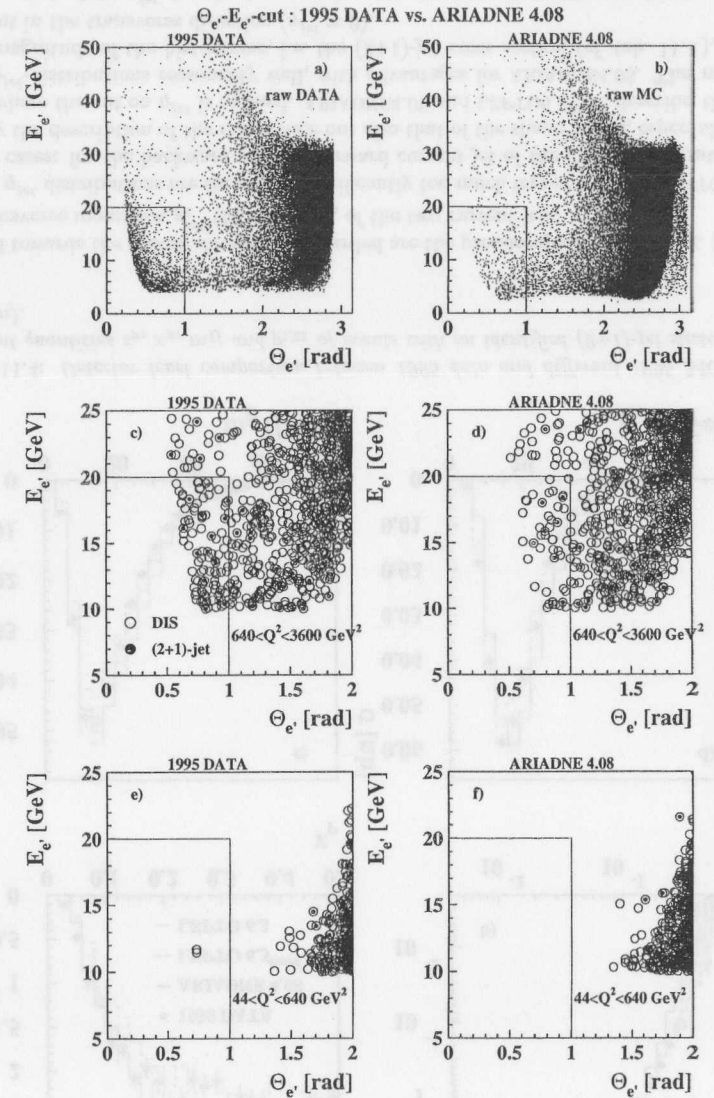
Figure 11.6: *Removing residual photoproduction background after usual DIS selection by a cut:* $\Theta_{e'} < 1.0 \lor E_{e'} < 20\,GeV$. *The raw data (top) shows a clear photoproduction background for data (left) which is not present in MC (right). There is still a residual background after the usual DIS selection which affects only the high* Q^2 *region (middle) and is kinematically excluded at lower* Q^2 *(bottom).*

in the highest Q^2-bin of this analysis ($640 < Q^2 < 3600\,\mathrm{GeV}^2$).

Figure 11.6 shows the signature of this background which is assumed to originate from photoproduction, although, it was not significantly reduced by cuts on lower y or higher δ values ($y_{EL} < 0.8$, $\delta = E - p_z > 40\,\mathrm{GeV}$). Compared are in separated scatter plots the selected events from the ZEUS 1995 data samples and those obtained from the ARIADNE4.08 MC sample. The top row presents the raw data right from the Ntuple, i.e. only with the (weak) DIS preselection cuts and the phase space limit $Q^2 > 40\,\mathrm{GeV}^2$, next to all events of the MC sample (fig. 11.6a-b). The cut borders „$\Theta_{e'} < 1.0\,rad \vee E_{e'} < 20\,\mathrm{GeV}$" are shown, too. One clearly sees the additional contribution in data at low $\Theta_{e'}$ and low $E_{e'}$ which is not modeled by the MC. By the application of the DIS selection cuts usually applied at ZEUS this contamination does not disappear completely as can be see in the center row (fig. 11.6c-d). In a close-up, the interesting region is inspected more detailed for the highest Q^2-bin of this analysis. Events accepted by the usual DIS selection are plotted with open circles, events with a (2+1)-jet configuration in the hadronic final state identified by the default jet selection are marked with a full dot in addition. The contamination is still visible. Note that the integrated luminosity of the ARIADNE4.08 MC sample is about 1.5 times larger than for 1995 data which would reduce the number of entries in the MC plot if it could be normalized to the luminosity of the data. The lowest row (fig. 11.6e-f) shows that the rest of the phase space used in this analysis is not affected by this contamination in the data since the problematic region is kinematically excluded.

Although the cut „$\Theta_{e'} < 1.0\,rad \vee E_{e'} < 20\,\mathrm{GeV}$" works reasonably well one clearly sees that this cut is not really suitable to the shape of this contamination (see fig. 11.6a). Judging from figure 11.6a a cut like $(E_{e'} - a)/b > \Theta_{e'}$ with constants like ($a = 30\,\mathrm{GeV}, b = -20\,\mathrm{GeV}$) would be much more suitable.

11.2   Comparisons at Parton Level
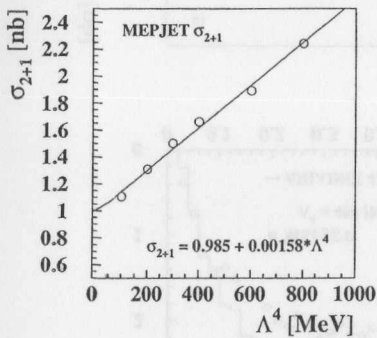
Figure 11.7: *MEPJET (2+1)-jet cross sections in $44 < Q^2 < 3600\,\mathrm{GeV}^2$ for different Λ^4. The fit is used to scale the MEPJET predictions for comparisons with MC.*

The main task of a MC model is to describe the measured data at detector level. Then the data is corrected to parton level. But the parton level simulated by a MC is dependent on the used model to simulate the higher orders in the parton evolution, i.e. the parton level the data is corrected to differs for different MC models. Since the corrected data is compared to NLO predictions at parton level a consistency between the parton level predictions and the MC simulations is required: the shape of the predicted distributions of the important quantities have to be modeled reasonably well by the MC. As the strong coupling α_s is derived from the relative size of the (2+1)-jet rate or cross sections found in the corrected data and in the NLO prediction, the relative magnitude of the quantities is the free parameter and cannot be used for strong conclusions.

Nevertheless, for the following parton level comparisons between MEPJET and the used MC samples the magnitude of distributions was looked at, too. This gives an idea whether the same result on α_s would be obtained for

other quantities if they would be used for the determination instead of R_{2+1}. For this check the MEPJET predictions should be viewed at that value of α_s, or Λ^4, which is determined when the data is corrected with the particular MC.

The MEPJET predictions used in this analysis have been calculated at discrete values of Λ^4. To avoid the CPU intensive recalculation at $^{meas}\Lambda^4$, the MEPJET histograms have been scaled in magnitude to that integrated cross section which corresponds to $^{meas}\Lambda^4$.

For that the integrated (2+1)-jet cross sections, calculated in the full phase space of this analysis at different values of Λ^4, were approximated by a linear fit as shown in figure 11.7. The result is:

$$\sigma_{2+1} = 0.985 + 0.00158 * \Lambda^4 \quad . \tag{11.1}$$

Then, to compare with the parton level MC simulation, the histograms of that MEPJET prediction were chosen which had been calculated with a value of Λ^4 nearest the found value $^{meas}\Lambda^4$. Subsequently, the integrated cross section of these histograms was scaled using the slope of equation 11.1.

Invariant Quantities:

In figure 11.8 the two invariant quantities z_p and m_{jj} of the (2+1)-jet state simulated by the usual MC samples are compared to the corresponding MEPJET predictions.

The shape of the variable z_p, as predicted by MEPJET, is described well by ARIADNE4.08 (fig. 11.8a), but the magnitude is significantly overestimated, much stronger than at detector level (fig. 11.4a). Thus, if z_p would be used instead of R_{2+1} to determine α_s, a significantly higher value of α_s would be obtained. Similarly well described is the shape by LEPTO6.3^{tuned} but here the match in the magnitude of the distribution is similar to the corresponding detector level comparison, too (fig. 11.8c, 11.4c). This indicates a good consistency between the parton level of LEPTO6.3^{tuned} and that of MEPJET. The LEPTO6.3 sample fails to describe the shape (fig. 11.8e) showing again that it is not suitable to be used for correction.

The m_{jj}-spectra predicted by MEPJET are described reasonably well by the ARIADNE4.08 and LEPTO6.3^{tuned} MC for $m_{jj} > 20\,\mathrm{GeV}$, below they are simulated a bit too soft (fig. 11.8b,d). Below $m_{jj} \approx 20\,\mathrm{GeV}$ the same is true for LEPTO6.3, but at higher values it tends to simulate the m_{jj}-spectrum too hard as well leading to a significantly too broad distribution.

Jet Quantities:

The η^{jet}-distributions (fig. 11.9) are shown analogously to the detector level comparison (fig. 11.5). All three MC samples exhibit a problem in the spectrum of the forward jet as they overestimate more or less strongly the region near the cut on η^{jet} while they tend to rather underestimate the more transverse region. As at detector level this problem is weakest for ARIADNE4.08 , only little worse for LEPTO6.3^{tuned} and most prominent for LEPTO6.3. The shape of the η^{jet}-spectrum of the backward jet is well described in all cases.

The NLO prediction of the p_t^{jet}-distributions (fig. 11.10) is very well described by the LEPTO6.3^{tuned} MC. The shapes still are described reasonably well by ARIADNE4.08 and LEPTO6.3, although the magnitudes are overestimated by the MC samples.

Judging only from the description of the shapes of the NLO predictions by the parton level MC samples, the LEPTO6.3 MC again is disfavored mainly by the z_p and the η^{jet} spectra, ARIADNE4.08 provides a reasonable description and turns out to be usable for a correction of data to parton level. While LEPTO6.3^{tuned} gives the best overall match.
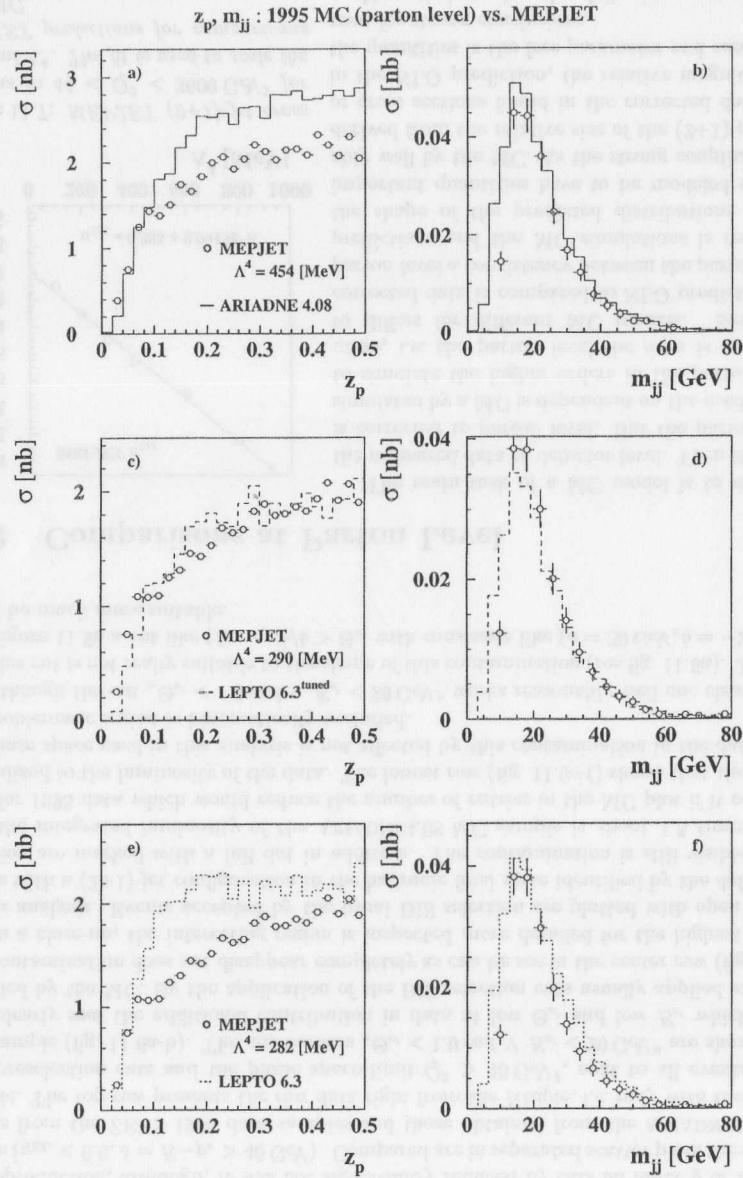
Figure 11.8: *Parton level comparison between MEPJET and different 1995 MC for the invariant quantities z_p and m_{jj} of events with an identified (2+1)-jet state (default selection). The MEPJET predictions were scaled according to eq. 11.1.*
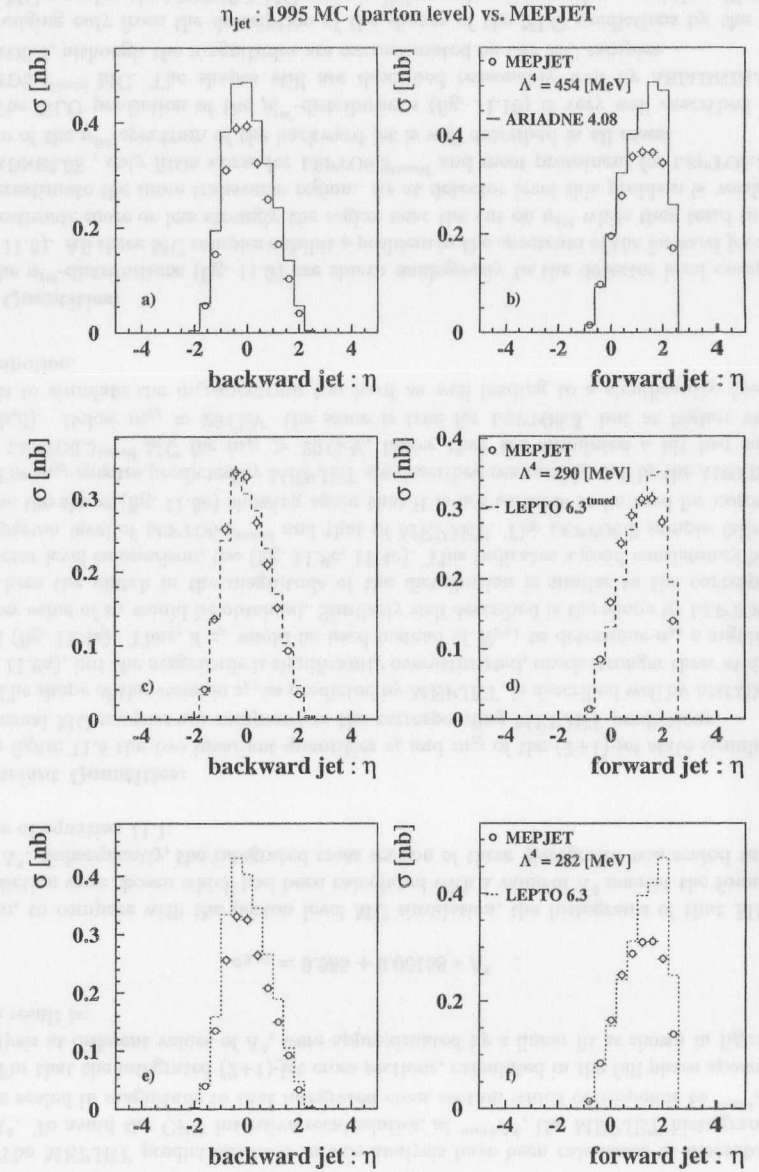
Figure 11.9: *Parton level comparison between MEPJET and different 1995 MC for the pseudo rapidities η^{jet} of the jets in events with an identified (2+1)-jet state (default selection). The MEPJET predictions were scaled according to eq. 11.1.*

$p_{t,jet}$: 1995 MC (parton level) vs. MEPJET
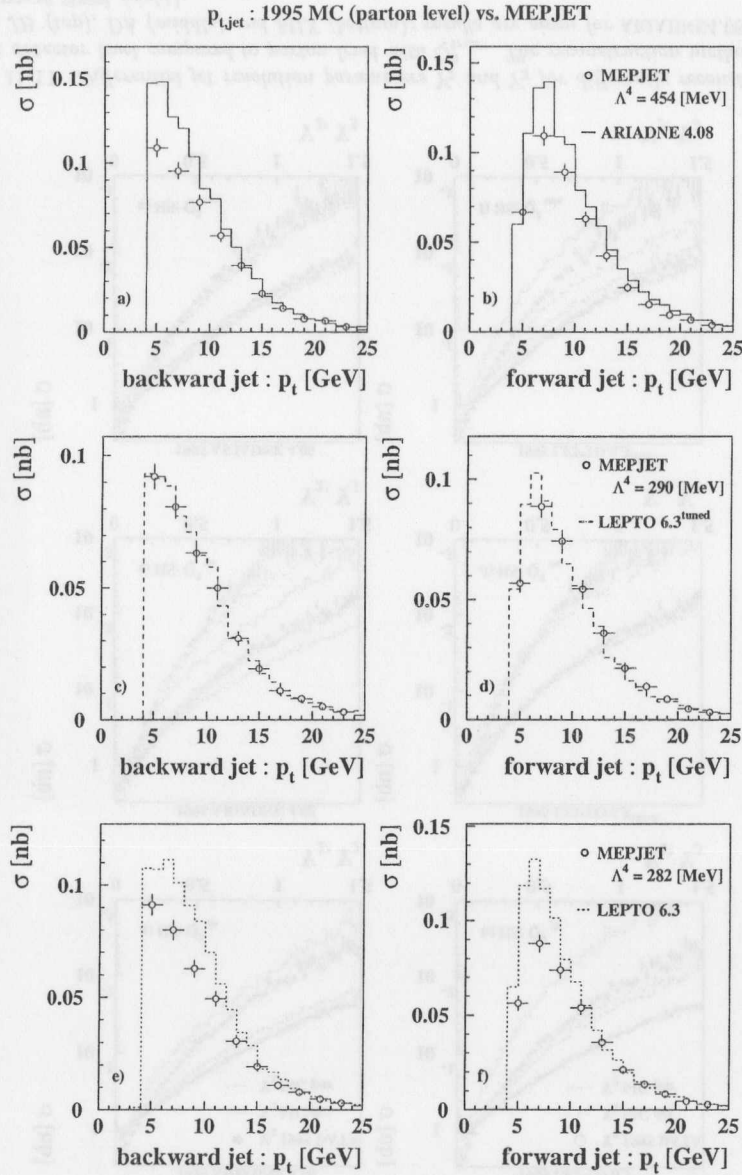
Figure 11.10: *Parton level comparison between MEPJET and different 1995 MC for the transverse momenta p_t^{jet} of the jets in events with an identified (2+1)-jet state (default selection). The MEPJET predictions were scaled according to eq. 11.1.*

Regarding also the matching of the magnitudes between MEPJET and MC simulations one finds that LEPTO6.3^{tuned}, i.e. the MEPS model tuned to the default parameters of LEPTO6.5, provides a parton level simulation which is very consistent with the NLO approximation calculated by MEPJET. In contrast, the ARIADNE4.08 MC, i.e. the Color Dipole Model supplemented by the matrix element calculations for the BGF process, tends to overestimate the NLO calculation. Therefore a correction of data performed by means of the ARIADNE4.08 simulation will tend to give high parton level (2+1)-jet cross sections resulting in high values of α_s.

11.3 Jet Finding

In this section the degree of description of the data by the used MC samples is investigated for the quantities which are important for the jet identification.

11.3.1 Choice of the Hard Scale

As pointed out in section 9.2.6, Q^2 was chosen as hard energy scale of the scattering process in order to determine $\alpha_s(Q^2)$. For measured data and MC detector level different reconstruction methods can be used to obtain Q^2. They are affected differently by the energy loss of the hadrons in the dead material before they enter the calorimeter.

Q_{DA}^2 (eq. 4.15) has the best resolution (12.3 %) and the minimum bias (+3.3 %), taken from the ratio 'reconstructed over true' in the ARIADNE4.08 MC sample. Q_{JB}^2 (eq. 4.14) has a much worse resolution (30.0 %). The striking feature of Q_{JB}^2 is the bias due to the energy loss of the hadronic final state in the dead material in front of the calorimeter (−34 %), since no correction for this energy loss is applied in the reconstruction of Q_{JB}^2. It was proposed to construct a reconstructed hard scale

$$Q_{MIX}^2 = s_{ep} * x_{EL} * y_{JB} \tag{11.2}$$

which combines quantities from different reconstruction methods [Mag96]. The idea is to combine two quantities where one depends on the energy scale of the electron measurement and the other depends on the hadronic energy scale. Thus, this scale depends on the difference of both energy scales. The achieved resolution for Q_{MIX}^2 is slightly better than for Q_{JB}^2 (26.4 %) and the bias is smaller (−25 %).

In the jet finding there is no chance to correct the energy loss of calorimeter cells due to dead material before the jet finding algorithm is applied. All methods to perform a correction for this energy loss rely on final objects like „particles" and „jets" but make no statement on the behavior of calorimeter cells. Hence, if Q_{JB}^2 is used as hard scale in the $k_\perp$-measurement of the $K_\perp$ algorithm (eq. 7.8) for single or grouped calorimeter cells, it is expected that the energy loss of the detector object cancel with that of Q_{JB}^2, i.e. the $k_\perp$-measurement is less biased by the energy loss problem as if e.g. Q_{DA}^2 would be used.

The differential jet resolution parameter Y_2 is for each single event that value of the resolution parameter y_{cut} of the exclusive $K_\perp$ jet finding algorithm where in the hadronic final state the transition from the (2+1)-jet to the (1+1)-jet configuration occurs, i.e. where the resolution becomes that coarse that the $K_\perp$ algorithm merges the two remaining jets to one. Analogously, Y_3 is that point of resolution where a (3+1)-jet configuration becomes a (2+1)-jet configuration. Thus, Y_2 and Y_3 define both borders of the exclusive (2+1)-jet class. In order to obtain these differential quantities they had to be defined without the default jet selection of this analysis, i.e. the jet identification is taken directly from KTCLUS.

Figure 11.11 presents the differential jet resolution parameters Y_2 and Y_3 for the three hard scales Q^2_{JB}, Q^2_{DA} and Q^2_{MIX} for ZEUS 1995 data and the MC samples ARIADNE4.08 and LEPTO6.3^{tuned} in the full phase space of this analysis. In each plot directly compared are the results obtained from data (Y_2: full dots, Y_3: open dots) with the simulation by the corresponding MC sample for the detector level as well as for the parton level.

The data is very well described by the ARIADNE4.08 MC by using Q^2_{JB} as hard scale (fig. 11.11a). The parton level simulation has the same slope as the data and the detector level simulation of Y_2 and Y_3. At detector level significantly more jets are found compared to the parton level. This can be related to the systematic bias of Q^2_{JB}, underestimating Q^2_{true}, giving rise to more jets to be resolved. But the principal behavior is the same. Beside of the statistics, one can expect to get similar results regardless which particular resolution parameter y_{cut} is chosen.

The picture changes if LEPTO6.3^{tuned} is used. The data used in figure 11.11b is the same as in figure 11.11a. Y_2 of the data is described well by LEPTO6.3^{tuned}, too, but Y_3 is slightly overestimated by the MC at high y_{cut}. The parton level simulation provided by LEPTO6.3^{tuned} exhibits a very different behavior than for ARIADNE4.08. It gives much less resolved jets and has much steeper slopes. Hence, a correction to parton level obtained from LEPTO6.3^{tuned} is strongly dependent on the resolution parameter.

The picture given above for Q^2_{JB} as hard scale is reversed if Q^2_{DA} is used instead (fig. 11.11c-d). Here the parton level simulations are the same as in figures 11.11a-b, but the data is reconstructed differently. It turns out that the number of found jets in data and at MC detector level, reconstructed with the hard scale Q^2_{DA}, matches very well the parton level simulation given by LEPTO6.3^{tuned}. Even the magnitude of the spectra fits very well, reflecting the fact that Q^2_{DA} provides an almost unbiased reconstruction of Q^2_{true}. Vice versa, for the ARIADNE4.08 MC now for Y_2 and Y_3 the parton and detector level differ in the slope. In addition, ARIADNE4.08 overestimates the Y_3 found in the data slightly at high y_{cut} as LEPTO6.3^{tuned} does it for the use of Q^2_{JB} as hard scale.

There is no explanation available why the parton level simulation given by ARIADNE4.08 corresponds to the data reconstructed with Q^2_{JB} as hard scale while that of LEPTO6.3^{tuned} to the data reconstructed using Q^2_{DA}. But judging from this comparison ARIADNE4.08 should be used with Q^2_{JB} as hard scale for the jet finding and LEPTO6.3^{tuned} with Q^2_{DA}.

Due to its construction the scale Q^2_{MIX} is rather similar to Q^2_{JB}, i.e. dominated by loss in the hadronic energy scale since it is much larger than for the electromagnetic energy scale. Thus, it exhibits a picture which is more similar to the case using Q^2_{JB} than the case using Q^2_{DA}. Due to the smaller bias a better match in magnitude is achieved between the parton and the detector level for the ARIADNE4.08 MC but the slopes turn out to be different and the match between data and MC is a bit worse. Using the LEPTO6.3^{tuned} MC neither the data is described nor the different slopes fit together. Q^2_{MIX} is not a convincing hard scale for the jet finding.

11.3.2 Jet Resolution Parameter y_{cut}

A priori there is no outstanding value of y_{cut} predestined to be used for the jet finding with the exclusive $K_\perp$ algorithm. Two opposite requirements have to be fulfilled. On the one hand one needs high statistics to reduce the error on the measurement, i.e. as many (2+1)-jet events in the event sample as possible. The rate of resolved (2+1)-jet events R_{2+1} in the event sample can be magnified by lowering the resolution parameter y_{cut}, at least up to a large fraction of the event sample. On the other hand, the corrected data, principally measured to

Figure 11.11: *Differential jet resolution parameters Y_2 and Y_3 for differently reconstructed Q^2_{rec} at detector level compared to parton level with Q^2_{true}. The reconstruction methods for Q^2 are JB (top), DA (middle) and MIX (bottom); results are given for ARIADNE4.08 (left) and LEPTO6.3^{tuned} (right).*
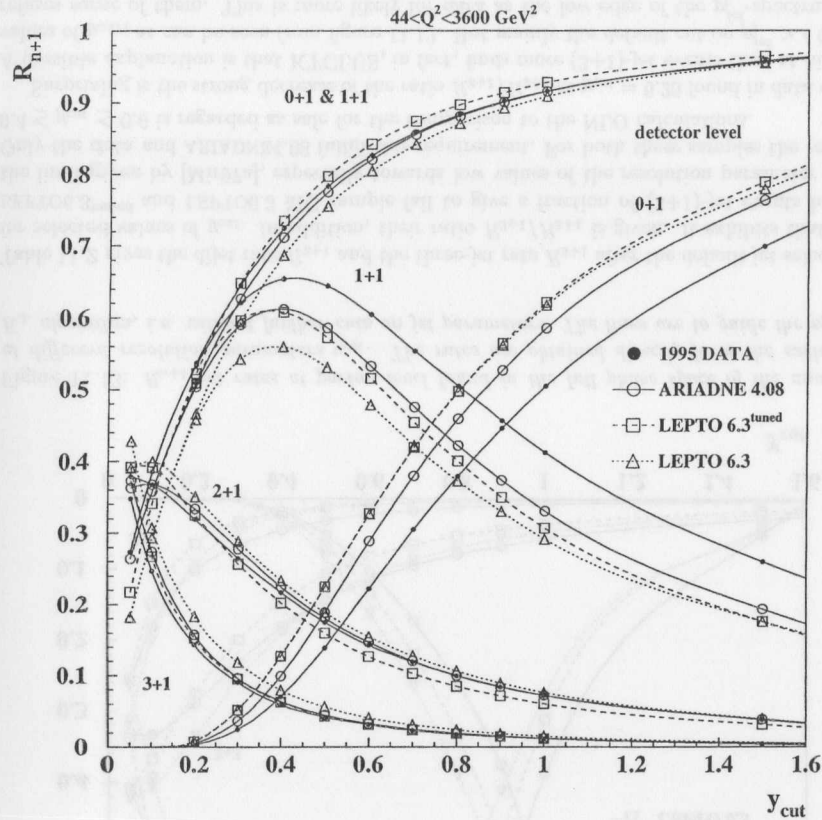
Figure 11.12: R_{n+1} jet rates at detector level found in the full phase space of the analysis at different resolution parameters y_{cut}. The rates are obtained directly form the exclusive $K_\perp$ algorithm, i.e. without further cuts on jet parameters. The lines are to guide the eyes.

infinite orders, should be compared to $\mathcal{O}(\alpha_s^2)$ predictions. As the virtual corrections and the higher order contributions to R_{3+1} are not covered by a NLO calculation the three-jet rate R_{3+1} may not become to large. [Mir97a] recommended to take care that $\sigma_{(3+1)} < 0.15 \cdot \sigma_{(2+1)}$ if MEPJET is used for the NLO calculations. R_{3+1} also grows towards low values of y_{cut}, below some threshold even faster than R_{2+1}. Thus, there is some optimum in fulfilling both requirements.

Figure 11.12 presents the R_{n+1} jet rates found in the ZEUS 1995 data sample in the full phase space of the analysis at different fixed resolution parameters y_{cut}. It compares them directly to the corresponding simulations at detector level provided by ARIADNE4.08, LEPTO6.3^{tuned} and LEPTO6.3. As for the view on the differential resolution parameters Y_2 and Y_3 (cf. sec. 11.3.1) the rates here are derived without the application of the default jet selection, i.e. the jet identification is taken directly from KTCLUS. Note that the sum of

R_{2+1} and R_{3+1} jet rates with jet selection				
	1995 data	ARIADNE4.08	LEPTO6.3^{tuned}	LEPTO6.3
$y_{cut} = 0.25$				
R_{2+1}	14.3 %	16.8 %	16.6 %	
R_{3+1}	0.04 %	3.7 %	4.5 %	
R_{3+1}/R_{2+1}	0.003	0.239	0.270	
$y_{cut} = 0.4$				
R_{2+1}	8.8 %	10.0 %	8.8 %	
R_{3+1}	0.9 %	1.3 %	1.7 %	
R_{3+1}/R_{2+1}	0.104	0.134	0.196	
$y_{cut} = 0.5$				
R_{2+1}	7.4 %	8.3 %	7.1 %	8.9 %
R_{3+1}	0.9 %	1.0 %	1.3 %	1.8 %
R_{3+1}/R_{2+1}	0.125	0.117	0.175	0.203
$y_{cut} = 0.6$				
R_{2+1}	6.3 %	7.0 %	5.9 %	
R_{3+1}	0.7 %	0.7 %	0.9 %	
R_{3+1}/R_{2+1}	0.113	0.101	0.154	
$y_{cut} = 1.0$				
R_{2+1}	1.1 %	1.2 %	0.9 %	
R_{3+1}	0.06 %	0.08 %	0.06 %	
R_{3+1}/R_{2+1}	0.050	0.063	0.0.74	

Table 11.2: R_{2+1} and R_{3+1} jet rates at detector level in the full phase space of the analysis with the default jet selection applied for selected values of y_{cut} comparing ZEUS 1995 data and the corresponding MC samples. The typical error on R_{3+1}/R_{2+1} from error propagation is ± 0.005. $y_{cut} = 0.5$ is the final working point of this analysis. The values of $R_{2+1}(y_{cut} = 0.5)$ are the same as given in the tables A.1, A.3, A.4 and A.5 in the appendix A.

these jet rates holds $\sum_i R_{i+1} = 1$.

The first observation is, that the rates R_{0+1} and R_{1+1} alone are not described by any of the MC samples. This is the same observation as it already was seen in figure 11.3 for the fixed $y_{cut} = 0.5$. Fortunately, only the sum of both, $R_{0+1} + R_{1+1}$, is important if R_{2+1} is of interest. This sum is described reasonably well by all MC samples. ARIADNE4.08 gives the best description for $y_{cut} \geq 0.4$.

The dijet rate R_{2+1} is described significantly to low by LEPTO6.3^{tuned} but well by the ARIADNE4.08 and LEPTO6.3 MC for $y_{cut} \geq 0.4$, again with ARIADNE4.08 giving the best match. The different magnitudes of these curves correspond to the discussion of the (2+1)-jet cross sections given in section 11.1.2 by the means of tab 11.1. For $y_{cut} < 0.4$ the slope found in the 1995 data is not anymore well described by the MC samples. As the higher jet rates become stronger at $y_{cut} \approx 0.1$ the dijet rate R_{2+1} saturates and starts to get smaller again towards lower values.

The three-jet rate R_{3+1} has two remarkable features. It becomes larger than the dijet rate R_{2+1} at about $y_{cut} \approx 0.05$. Thus, the finally used value of y_{cut} may not be chosen to low. And it does not vanish even for large resolution parameters like $y_{cut} = 1.5$. This is interpreted as a feature of the exclusive $K_\perp$ algorithm. This algorithm tends to produce more current jets than e.g. the JADE algorithm from the same hadronic final state. A significant fraction of these higher order jets survives also the default jet selection cuts defined for this analysis.
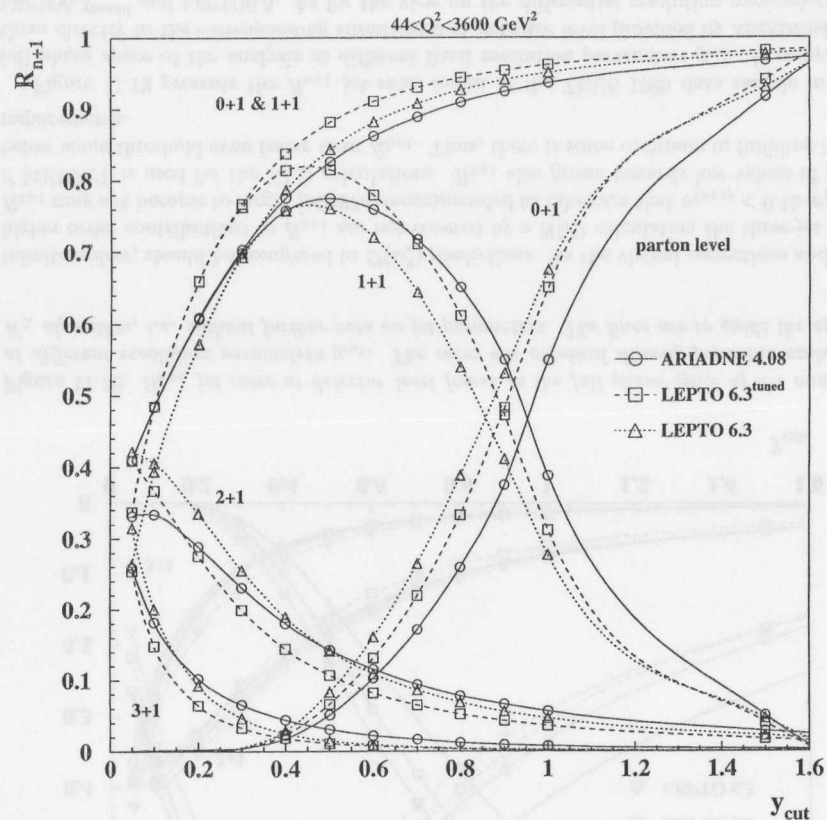
Figure 11.13: R_{n+1} jet rates at parton level found in the full phase space of the analysis at different resolution parameters y_{cut}. The rates are obtained directly form the exclusive $K_\perp$ algorithm, i.e. without further cuts on jet parameters. The lines are to guide the eyes.

Table 11.2 gives the dijet rate R_{2+1} and the three-jet rate R_{3+1} after the default jet selection for selected values of y_{cut}. In addition, their ratio R_{3+1}/R_{2+1} is given. It exhibits that the LEPTO6.3^{tuned} and LEPTO6.3 MC sample fail to give a fraction of (3+1)-jet events below the limit given by [Mir97a], especially towards low values of the resolution parameter y_{cut}. Only the data and ARIADNE4.08 fulfill this requirement. For both these samples the region $0.4 \leq y_{cut} \leq 0.6$ is regarded as safe for the comparison to the NLO calculations.

Surprising is the strong decrease of the ratio R_{3+1}/R_{2+1} at $y_{cut} = 0.25$ found in data only. A possible explanation is that KTCLUS, in fact, finds more (3+1)-jet events than at higher values of y_{cut}, as can be seen from figure 11.12. But mainly the default cut on $p_t^{jet} > 4$ GeV refuses some of them. This is more likely for data as the low edge of the p_t^{jet}-spectrum is underestimated by all MC simulations.

Figure 11.13 presents the parton level simulation of the R_{n+1} jet rates of the MC samples.
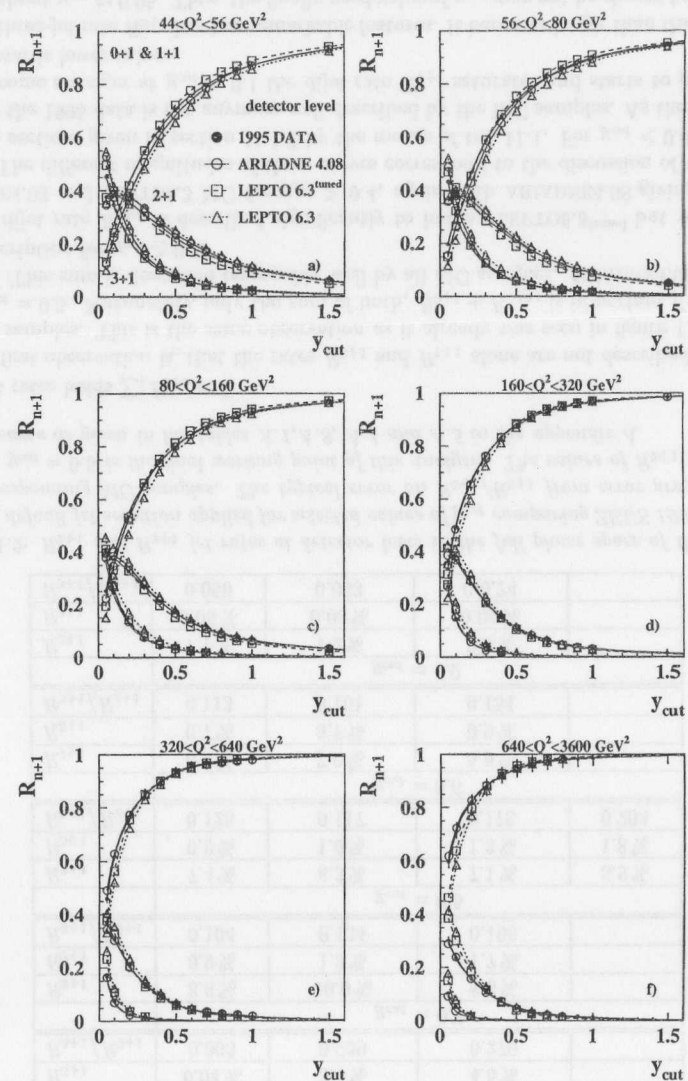
Figure 11.14: R_{n+1} jet rates at detector level found in the Q^2-bins of the analysis at different resolution parameters y_{cut}. The rates are obtained directly form the exclusive $K_\perp$ algorithm, i.e. without further cuts on jet parameters. The lines are to guide the eyes.

In general the R_{2+1} and the R_{3+1} jet rates are significantly lower than at detector level. In addition, the MC samples exhibit much more differences among the MC samples in the magnitudes as well as in the shapes of their jet rates. This figure in comparison to figure 11.12 illustrates a major problem of this analysis: different parton level simulations generated by different models lead to rather similar detector simulations. The MC models are tuned to describe the data as well as possible. Thus, it becomes difficult to judge on their validity from measurement.

Figure 11.14 splits up the data shown in figure 11.12 into the Q^2-bins of this analysis. Doing so, one can see that the underestimation of R_{2+1} by LEPTO6.3^{tuned} is concentrated in the lower Q^2 region (fig. 11.14a-c). Above, the data generally is described well by all MC models, but at high Q^2 (fig. 11.14e-f) the LEPTO MC samples fail to describe R_{2+1} for $y_{cut} < 0.3$. LEPTO6.3 fails in the full phase space to describe the magnitude of R_{3+1}.

One can summarize that ARIADNE4.08 gives the best description of the data in the full phase space for most values of y_{cut}. LEPTO6.3^{tuned} and LEPTO6.3 are disfavored to be used for a correction to parton level in order to compare to a fixed order prediction as the fraction of (3+1)-jet events is very high. The region $0.4 \leq y_{cut} \leq 0.6$ is regarded as safe for the comparison to NLO calculations if ARIADNE4.08 is used for the correction of the data. $y_{cut} = 0.5$ finally was chosen as the default resolution for this analysis and the values $y_{cut} = 0.4$ and $y_{cut} = 0.6$ were used for systematic checks.

11.3.3 η^{jet} Reconstruction

A cut on the pseudorapidity of the reconstructed jet, η^{jet}, has to be introduced to reduce the influence of the proton remnant on the jet finding. Especially the trend has to be avoided which has been found in the analysis [ZEU95a, Tre96] using the JADE algorithm: the jet finding by the JADE algorithm tends to grab energy from the proton remnant and, hence, bending current jets into the forward direction. A cut on $\eta^{jet} < 2.0$ had to be introduced to be reasonable safe against this effect. As the exclusive $K_\perp$ algorithm is less sensitive to energetic objects apart from the jet axis this cut can be relaxed with respect to the old limit.

Figures 11.15 and 11.16 present the reconstruction of η^{jet} between detector and hadron level in the ARIADNE4.08 MC sample achieved with the exclusive $K_\perp$ algorithm. Here the default DIS selection was used. As jet selection the default cut on p_t^{jet} was applied and the cut on η^{jet} was relaxed to $\eta^{jet} < 2.6$. Originally this study was performed without any cut on η^{jet}, as it should be. To save disk space thereafter the jets stored in the Ntuples were restricted to at most $\eta^{jet} \leq 2.6$. Since the old, unlimited MC was not available any more, unfortunately, only the limited phase space can be presented here.

Different subsamples are shown in the figures 11.15 and 11.16 (if more than one current jet is found at a level always the more forward jet is used for the comparison presented here):

(a) all events with at least one current jet found at the particular level, this is the major part of the data sample and includes all following samples

(b) exactly one current jet is found at both levels, this is the cleanest subsample with the high statistics

(c) two current jets are found at detector and only one at hadron level or vice versa, i.e. these are migration events, the most probable case for a misidentification of jets

(d) exactly two currents jets are found at both levels, a sample of forward going jets.
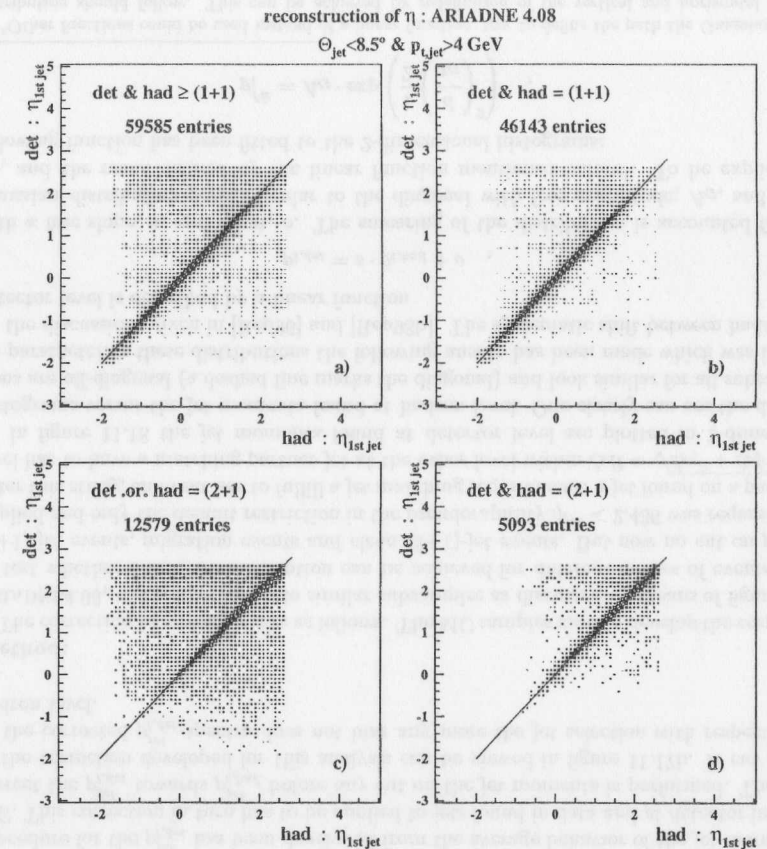
Figure 11.15: *Reconstruction of η^{jet} between detector and hadron level of ARIADNE4.08. Different subsamples are shown: a) all events with at least one current jet found at the particular level, b) exactly one current jet found at both levels, c) two current jets found at detector and only one at hadron level or vice versa and d) exactly two currents jets are found at both levels. If more than one current jet is found at a level the more forward jet is used for the comparison. The lines given with the slope of 1.0 are to guide the eyes.*

No other jet matching was performed.

From figure 11.15 one can see that, in general, the reconstruction of η^{jet} is very good and unbiased. There is no tendency visible to bend jets forward at detector level. Fitting a Gaussian shape to $\eta_{det}^{jet} - \eta_{had}^{jet}$ to either of the four samples leads to typical values of $|\mu_G| < 0.01$ and $\sigma_G \approx 0.06$ (exception: sample (d) with $\sigma_G \approx 0.12$). Of course, this leaves non-diagonal entries essentially unrecognized as the distributions are very sharp.

A better impression of the size of the contribution of the non-diagonal entries to the histograms of figure 11.15 is given by figure 11.16 which presents the same data.

As expected the non-diagonal tails are smallest for the clean „det & had = (1+1)-jet"

reconstruction of η : ARIADNE 4.08

$\Theta_{jet} < 8.5°$ & $p_{t,jet} > 4$ GeV
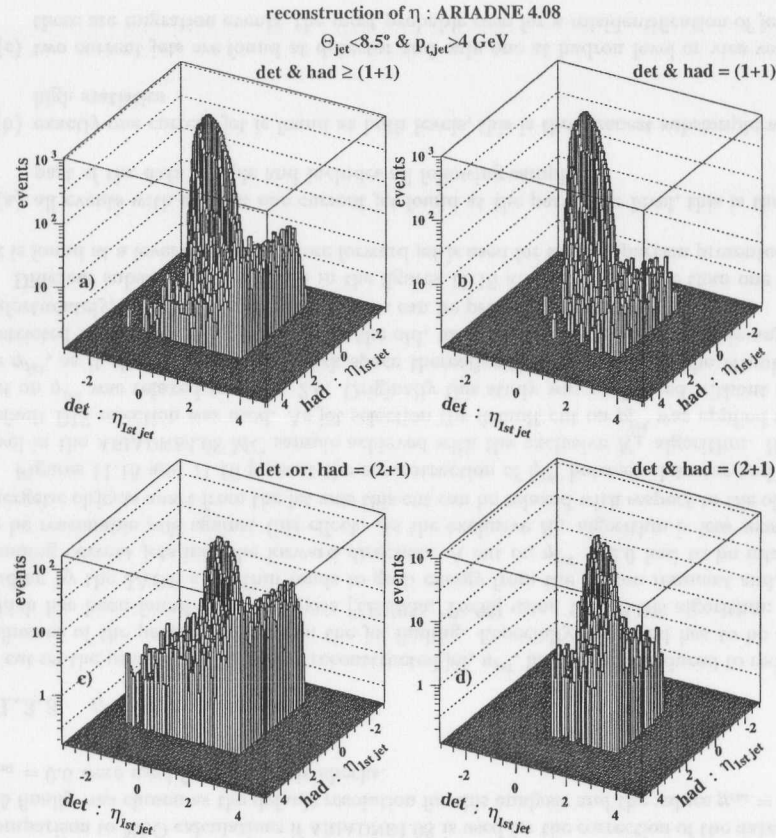
Figure 11.16: *Reconstruction of η^{jet} between detector and hadron level of ARIADNE4.08. The same data is shown as the corresponding plots of figure 11.15 here now in 3-dimensional histograms to illustrate the relative size of the non-diagonal tails.*

sample (fig. 11.15b and 11.16b). The tendency to bent a jet forward at detector level is the dominant contamination in the η^{jet}-resolution. This effect is not restricted to the forward region of the detector but occurs also for hadron level jets in the rear part of the detector. Therefore, it seems likely that in these cases the hadron level jet was not reconstructed or rejected by the p_t^{jet}-cut at detector level and an additional jet was formed at detector level instead. This type of contamination becomes effective for $\eta^{jet} > 2.0$ and plays a much bigger role in the „migration" sample (fig. 11.15c and 11.16c). The more critical forward jets in the „det & had = (2+1)-jet" sample (fig. 11.15d and 11.16d) again are reconstructed more cleanly.

The generation of additional forward jets at detector level becomes stronger for the region $\eta^{jet} > 2.6$ as is was visible in the former study using the unlimited MC sample. From that study it was judged that $\eta^{jet} < 2.436 \cong \Theta^{jet} > 10°$ provides a safe jet reconstruction by

allowing higher statistics. The cuts $\eta^{jet} < 2.6$ and $\eta^{jet} < 2.0$ were chosen to be used as check against the possible bias by the generation of additional forward jets at detector level.

11.3.4 p_t^{jet} Reconstruction and Correction

One remarkable feature of the $K_\perp$ algorithm is that it reconstructs jets with relatively low transverse momenta, p_t^{jet}, compared to other algorithms. Even jets with transverse momenta below 1 GeV are reconstructed by the algorithm, but with a very low rate. Jets with that low transverse momenta are not trusted to originate hard scattered partons. Therefore a minimum-p_t^{jet} requirement is introduced to ensure a reasonable hardness of the accepted jets.

Due to energy loss in the dead material of the detector, the $p_{t,det}^{jet}$ of a jet reconstructed at detector level is significantly lower than the $p_{t,had}^{jet}$ of a matching jet on hadron level. This can be seen from figure 11.17a where for 1995 data as well as for ARIADNE4.08 detector and hadron level the transverse momenta of the current jets are plotted if exactly one current jet is found. Thus, if a cut with the same threshold would be performed on both these p_t^{jet}-spectra, at detector level a much smaller sample would result. Therefore, a correction procedure for the $p_{t,det}^{jet}$ has been developed from the average behavior of the jet momenta in MC. This correction in turn has to be applied to jets found in data and at detector in MC to correct the $p_{t,det}^{jet}$ towards $p_{t,had}^{jet}$ before any cut on the jet momenta is performed. The result of the correction developed for this analysis can be viewed in figure 11.17b. A cut applied to the corrected $p_{t,det}^{jet}$-spectra does not bias any more the jet selection with respect to the hadron level.

Method:

The correction procedure works as follows. The MC samples used to develop the correction, ARIADNE4.08, was subdivided into similar subsamples as discussed by means of figure 11.15 to test whether a uniform description can be achieved for different classes of events: clean (1+1)-jet events, migration events and clean (2+1)-jet events. But now no cut on p_t^{jet} was applied and only the default restriction in the pseudorapidity $\eta^{jet} < 2.436$ was requested. To enter this study, an event has to fulfill a jet matching requirement: a jet found on a particular level has to have a matching partner jet at the other level within $\Delta R = \sqrt{\Delta \eta^2 + \Delta \phi^2} < 0.5$.

In figure 11.18 the jet momenta found at detector level are plotted in 2-dimensional histograms versus the jet momenta found at hadron level. One clearly can see the distributions are off-diagonal (a dashed line marks the diagonal) and look similar for all subsamples. To parameterize these distributions the following ansatz has been made which was inspired by the discussions given in [Rep96] and [Rep98b]. The systematic shift between hadron and detector level is described by a linear function

$$p_{t,det} = s \cdot p_{t,had} + o \quad , \tag{11.3}$$

with a free slope, s, and offset, o. The smearing of the distribution is accounted for by a Gaussian distribution perpendicular to the diagonal with free magnitude, A_G, and width, σ_G, and the mean defined by the linear function mentioned before[1]. To be explicit, the following function has been fitted to the 2-dimensional histograms:

$$p_t^{fit} = A_G \cdot \exp\left(\frac{1}{2}\left(\frac{d}{\sigma_G}\right)^2\right) \quad , \tag{11.4}$$

---

[1]Other functions could be used instead of a linear function, too, to define the path the Gaussian shaped distribution should follow. This can be achieved by redefinition of the vertical and horizontal distance measurements a and b in equation 11.5.
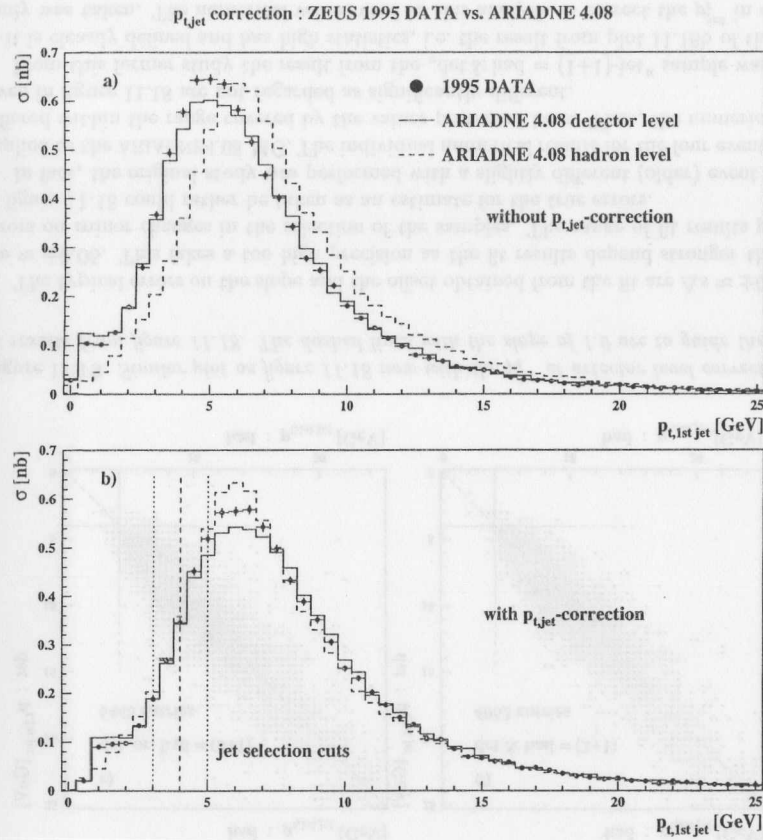
Figure 11.17: *Energy loss in the detector. Given are the transverse momenta p_t^{jet} of the reconstructed jets in 1995 data and for* ARIADNE4.08 *at detector and hadron level for events where exactly one current jet was found ($\eta^{jet} < 2.436$). No cut on p_t^{jet} was applied. Plot a) presents the data without any correction to p_t^{jet}, for plot b) the correction discussed in this section was applied.*

with the distance d between a point in the plane and the linear function one is interested in. This function is defined by:

$$d = b \cdot \sin\left(\arctan\left(\frac{a}{b}\right)\right)$$

$$\text{with} \quad a = |o + s \cdot p_{t,had} - p_{t,det}|$$

$$b = \left|p_{t,had} - \frac{p_{t,det} - o}{s}\right|. \tag{11.5}$$
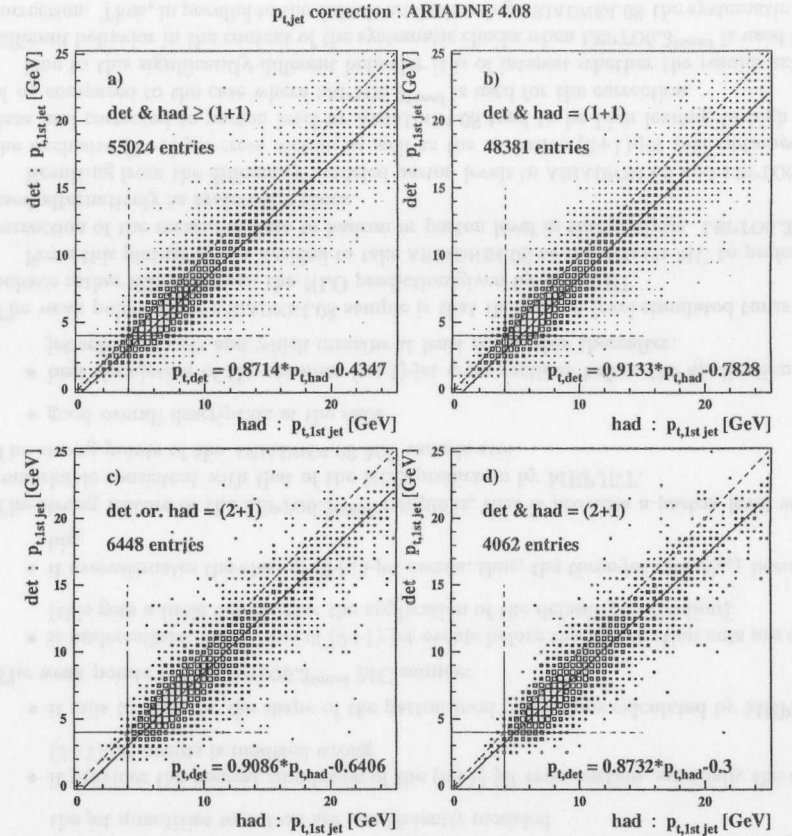
Figure 11.18: *Reconstruction of p_t^{jet} between detector and hadron level of* ARIADNE4.08. *Different subsamples are shown: a) the sum of the following samples, b) exactly one current jet at both levels, c) exactly 2 current jets either at detector or at hadron level, i.e. migration events and d) exactly 2 current jets at both levels. If more than one current jet is found at a level the more forward jet is used for the comparison. Jets are only plotted if they have a matching partner at the other level within $\Delta R = \sqrt{\Delta\eta^2 + \Delta\phi^2} < 0.5$. The systematic difference between the detector and hadron level is parameterized by a linear fit with the results given. The dashed lines with the slope of 1.0 are to guide the eyes. In addition, the cut lines of 4 GeV are given.*

Results:

The results of the fits to the different subsamples of the MC are shown in figure 11.18, too. The fits are plotted as well as the found parameters of the linear function are noted for each sample separately. The results are consistent with each other and the method works very well in principle as can be seen from figure 11.19. There the corrections obtained from 11.18 were applied to the corresponding sample.

corrected $^{corr}p_{t,jet}$: ARIADNE 4.08
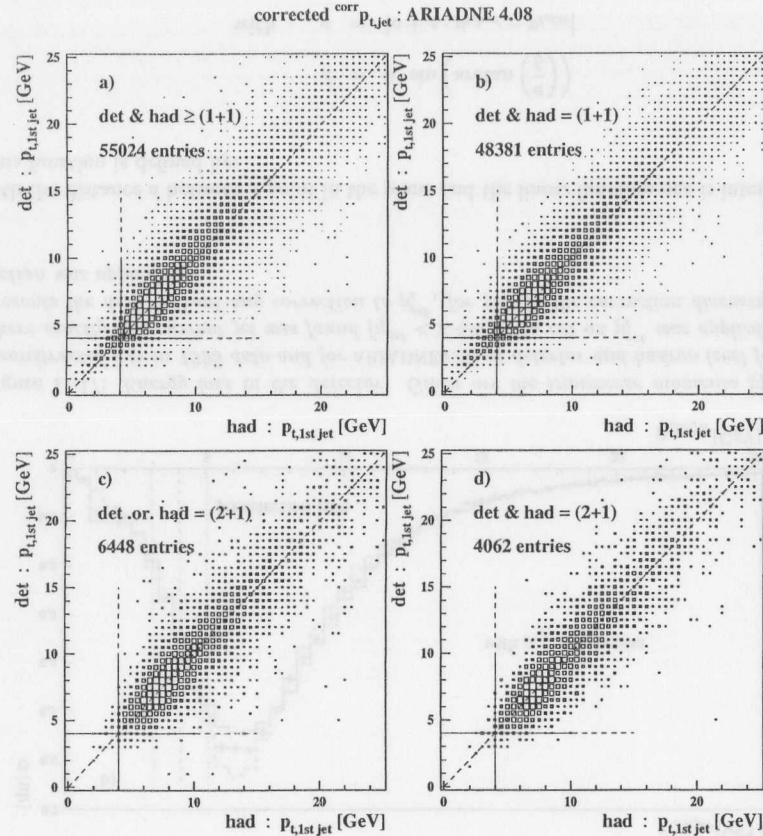
Figure 11.19: *Similar plot as figure 11.18 now with the p_t^{jet} at detector level corrected by the fit results from figure 11.18. The dashed lines with the slope of 1.0 are to guide the eyes.*

The typical errors on the slope and the offset obtained from the fit are $\Delta s \approx \pm 0.002$ and $\Delta o \approx \pm 0.05$. This fakes a too high precision as the fit results depend stronger than these errors on minor changes in the selection of the samples. The range of fit results presented in figure 11.18 could rather be taken as an estimate for the true errors.

In fact, the original study was performed with a slightly different (older) event selection applied to the ARIADNE4.08 MC. The individual numerical results for the four event samples differed within the range covered by the values presented here. Thus, the numerical values given in figure 11.18 are not regarded as significantly different.

From this former study the result from the „det & had = (1+1)-jet" sample was chosen, as it is cleanly defined and has high statistics, i.e. the result from plot 11.18b of the former study was taken. The numerical values used in this analysis to correct the p_t^{jet} in data and at detector level in MC are:

$$o_{def} = -0.4680 \qquad s_{def} = 0.8943 \tag{11.6}$$

Applying this correction to the data of figure 11.17a leads to the result presented in 11.17b. Now a cut on p_t^{jet} can be applied to all data samples in the same way without introducing a bias in the jet selection.

A default cut of $p_t^{jet} > 4\,\text{GeV}$ was chosen as default selection to guarantee a minimum hardness of the jets. The limits $p_t^{jet} > 3\,\text{GeV}$ and $p_t^{jet} > 5\,\text{GeV}$ were used to check against possible residual distortions introduced by this cut. The variation of this limit corresponds to the resolution of p_t^{jet} in the range of the cut.

11.4　Assessment of the MC Samples

In all studies presented in this chapter so far the ARIADNE4.08 MC sample gives the best or at least a reasonable description, while the LEPTO6.3^{tuned} and even stronger the LEPTO6.3 MC sample exhibit problems in at least some points.

Reasons to exclude the LEPTO6.3 MC sample:

- the description of the data is poor compared to the other used MC samples, especially the jet quantities to cut on are insufficiently modeled

- it provides the poorest simulation of the (n+1)-jet cross section, especially the class of (3+1)-jet events is modeled wrong

- it fails to describe the shape of the parton level predictions calculated by MEPJET.

The weak points of the LEPTO6.3^{tuned} MC sample:

- it underestimates the class of (2+1)-jet events before the jet selection cuts are applied (this gets a little better after the application of the default jet selection)

- it overestimates the class of (3+1)-jet events, thus, the three-jet rate R_{3+1} becomes to big.

The strong feature of the LEPTO6.3^{tuned} sample is, that it provides a parton level which is remarkable consistent with that of the NLO prediction by MEPJET.

The strong points of the ARIADNE4.08 MC sample are:

- good overall description of the data

- best simulation of the absolute (n+1)-jet cross sections before the application of the jet selection cuts and which remains at least reasonable thereafter.

The weak point of the ARIADNE4.08 sample is that the parton level simulated turns out to behave rather different than the NLO prediction given by MEPJET.

From this picture it was decided to take ARIADNE4.08 as the default MC to perform the correction of the measured data to hadron or parton level in this analysis. LEPTO6.3^{tuned} is used alternatively as systematic check.

Resulting from the differently modeled parton levels in ARIADNE4.08 and LEPTO6.3^{tuned} the exclusive (2+1)-jet cross section as well as the exclusive (2+1)-jet rate obtained from data and corrected to parton level by ARIADNE4.08 tend to be high leading to high values of α_s compared to the case where LEPTO6.3^{tuned} is used for the correction.

Due to this significantly different behavior it is of interest whether the results exhibit a different behavior in the context of the systematic checks when LEPTO6.3^{tuned} is used for the correction. Thus, in parallel to the default analysis using ARIADNE4.08 the systematic checks were also studied for the case using LEPTO6.3^{tuned} for the correction. The corresponding results are summarized in appendix F.

11.5 The Systematic Checks

This section gives a complete list of systematic checks which were performed in this analysis. The checks are defined analogously to the definition of the default selection procedures given in section 9.2. For each check the full analysis was repeated and the results for $\alpha_s(M_z^2)$ were stored. If necessary for a particular check, a different data or MC sample with the appropriate changes was used. Also the set of the NLO predictions was chosen appropriately, if needed.

The values of $\alpha_s(M_z^2)$ obtained from the systematic checks are presented graphically in figure 11.20 for the determination of α_s in the full phase space of this analysis and in figure 11.21 for the determination in the six bins of Q^2. The deviations from the default result, presented in section 10.2, are discussed in detail in the following together with the presentation of the systematic checks and are summarized in table 11.3.

To obtain the global systematic error, the variations from the default result of all systematic checks were added in quadrature. Two exceptions were made, where only the maximum error of mutual exclusive choices was taken (the choice of hard scale and the choice of the PDF). The systematic checks are combined into the four groups of:

- experimental uncertainties,

- jet finding uncertainties,

- hard scale uncertainties and

- theoretical uncertainties.

Experimental Uncertainties:

The experimental uncertainties comprise the variation of the important variables in the reconstruction and selection of events in data and at detector level in MC samples. The quantities typically are varied by about $1\,\sigma$ of their resolution to check whether a particular choice of a cut border might artificially spoil the picture the results give, i.e. to check whether the cut is made in a safe region. The experimental uncertainties consist of the following checks:

- Instead of the electron finder SINISTRA the electron finder EM was used, which incorporates additional information from the tracking system and an electron-track matching procedure.

- A slightly simplified electron-track matching procedure than used with EM was added to the electron finding performed by SINISTRA.

- The minimum required energy of the reconstructed electron was reduced from $E_{e'} > 10\,\text{GeV}$ to $E_{e'} > 8\,\text{GeV}$, i.e. towards the region where the electron finding becomes less efficient. This accounts for a possible misreconstruction of $E_{e'}$ near the cut limit.

- The z-position of the reconstructed vertex was shifted by $\pm 4\,\text{mm}$ to estimate the effect of a possible misreconstruction. This would put a significant bias to the reconstruction of the electron. Apart from the kinematical cuts this changes the boost to the BREIT frame and subsequently the jet finding which is very sensitive to the boost.

- A harder limit was put on the z-position of the reconstructed vertex, $|vtx_z| < 37.5\,\text{cm}$ instead of $|vtx_z| < 50\,\text{cm}$, to reduce the contribution of events which origin from regions where the description of the vtx_z-distribution by the MC becomes weaker.

- The energy scale of the calorimeter was shifted for the extracted hadronic final state, i.e. after the electron has been separated, by $\pm 3\,\%$. This was done to account for a possible uncertainty in the absolute energy scale of the calorimeter. For cross section measurements this usually is a major systematic error.

- The lower cut on Bjorken-y was changed by its resolution from $y_{JB} > 0.04$ to $y_{JB} > 0.05$ and $y_{JB} > 0.03$. In addition, it was changed to $y_{DA} > 0.04$.

- The upper cut on Bjorken-y was lowered from $y_{EL} > 0.95$ to $y_{EL} > 0.90$ to cut harder against the photoproduction background. In addition, it was changed to $y_{DA} > 0.95$.

- The lower cut on $\delta = E - p_z > 35\,\text{GeV}$ (eq. 9.1) was raised to $\delta > 40\,\text{GeV}$, again to cut harder against the photoproduction background.

- The cut against diffractive events with a large rapidity gap was varied by the hadronic energy resolution, from $E_{FCAL} > 1.0\,\text{GeV}$ to $E_{FCAL} > 0.6\,\text{GeV}$ and $E_{FCAL} > 1.4\,\text{GeV}$.

As can be seen from the figures 11.20 and 11.21, the overall systematic error introduced by this group of checks is small compared to the uncertainties given by the other checks in the full phase space of this analysis ($^{exp}\Delta\alpha_s = {}^{+0.0020}_{-0.0017}$). This is less than a factor of two bigger than the statistical error of the measurement ($^{stat}\Delta\alpha_s = \pm 0.0012$). The largest variations in this group occur in the two bins with the highest Q^2 and lowest statistics. Thus, even the biggest single variation, the use of the electron finder EM in the bin $320\,\text{GeV}^2 < Q^2 < 640\,\text{GeV}^2$ ($\Delta\alpha_s = -0.01$), can be interpreted as a statistical fluctuation since it is a singular behavior. In general, the experimental uncertainty introduced by the selection of DIS events in data is well under control.

Jet Finding Uncertainties:

In the second group of systematic checks the requirements are varied which were set to define a valid current jet. This group comprises the following variations:

- Instead of using directly the electron found by SINISTRA to obtain the boost vector to the BREIT frame, corrected as described in section 9.2.3, the electron energy was calculated from the kinematic variables reconstructed by the double angle method, $E'_{e,DA}$(eq. 9.2). For the direction of the electron the 3-vector from the SINISTRA electron was scaled appropriately. This way, the jet finding for a particular event may be significantly changed.

- The minimum transverse momentum of a jet, to be accepted as valid, was varied from $p_t^{jet} > 4.0\,\text{GeV}$ to $p_t^{jet} > 3.0\,\text{GeV}$ and $p_t^{jet} > 5.0\,\text{GeV}$. This corresponds to the jet energy resolution in this low-p_t^{jet} region.

- The maximum pseudorapidity allowed for a valid jet was varied from $\eta^{jet} < 2.436$ ($\stackrel{\wedge}{=} \Theta^{jet} > 10°$) to $\eta^{jet} < 2.0$ and $\eta^{jet} < 2.6$ which is larger than the resolution in η^{jet} is about 0.06 units. The variation of the cut was chosen to check against possible influences of the proton remnant and misreconstruction of forward jets.

The uncertainties introduced by the variation of the definition of the jet finding are typically not larger than the experimental error $^{exp}\Delta\alpha_s$. The larger positive error for this group of checks ($^{jet}\Delta\alpha_s = {}^{+0.0046}_{-0.0018}$) is mainly driven by the positive variation for $p_t^{jet} > 3.0\,\text{GeV}$ in the bin $44\,\text{GeV}^2 < Q^2 < 56\,\text{GeV}^2$ ($\Delta\alpha_s = +0.007$).
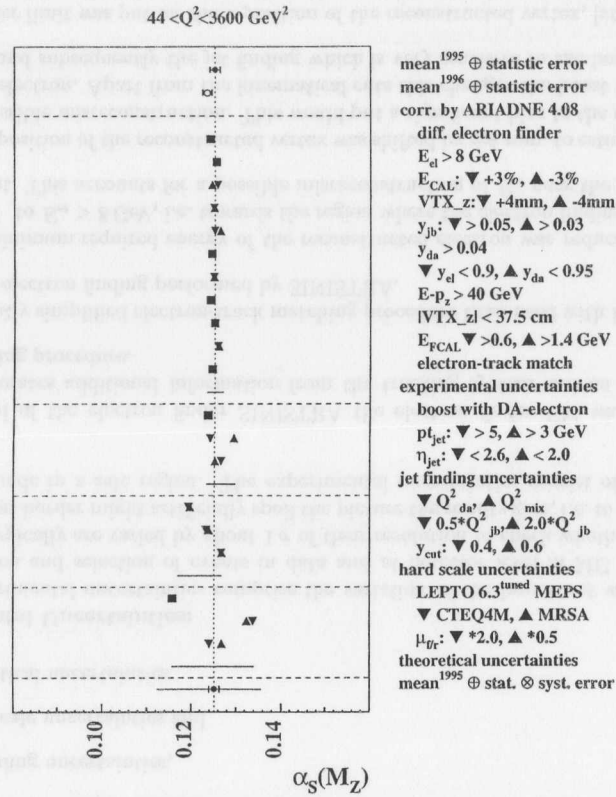
Figure 11.20: *Summary of systematic checks for the determination of $\alpha_s(M_z^2)$ in one big bin of Q^2 from the exclusive (2+1)-jet rate R_{2+1} using ZEUS 1995 data, ARIADNE4.08 for the correction and GRV(HO) in MEPJET. See text for discussion.*

In addition, the uncertainty was tested which is due to the migration of ($\geq 3+1$)-jet events identified by KTCLUS to (2+1)-jet events by applying the default jet selection. For this check this migration was forbidden while the migration from $(2+1)^{found}$ to $(1+1) \vee (0+1)^{accepted}$ was still allowed. Thus, the measured (2+1)-jet rate and subsequently the determined α_s was reduced. This type of definition of accepted (2+1)-jet events was used in [ZEU95a, Tre96]. It turned out that the size of the change introduced by this redefinition of a valid (2+1)-jet configuration was negligible small. Since this redefinition introduces an inconsistency in the jet identification, between data and MC samples on the one side and the MEPJET NLO predictions on the other side, it was not included into the final list of systematic checks.

Hard Scale Uncertainties:

The jet finding with the exclusive $K_\perp$ algorithm involves a hard energy scale and a jet resolution parameter. Both quantities are linked: $k_{T,ij}^2 < y_{cut} \cdot scale$ (eq. 7.8). To check the

hard scale the following checks were performed:

- The choice of Q_{JB}^2 as the default hard scale was cross checked by replacing it with Q_{DA}^2 and Q_{MIX}^2, which have different reconstruction properties. As these choices are mutual exclusive, only the largest variation of this check was used in the calculation of the full error.

- The default hard scale Q_{JB}^2 was scaled by a factor of two in both directions ($0.5 * Q_{JB}^2, 2.0 * Q_{JB}^2$) in order to check the reliability of the scale at about 2σ of its resolution.

- Next to the default choice of the resolution parameter $y_{cut} = 0.5$ the analysis was performed with $y_{cut} = 0.4$ and $y_{cut} = 0.6$, too.

This group of checks ($^{scale}\Delta\alpha_s = ^{+0.0017}_{-0.0081}$) provides a significant contribution to the total systematic uncertainty. It is dominated by the uncertainty in the reconstruction of the hard scale (-0.0057). Both scales used for the check reduce the results correlated in all Q^2-bins in a similar way. Only in the highest Q^2-bin, where the statistics are low, one scale (Q_{MIX}^2) gives a slightly higher result than the default procedure, while the other scale(Q_{DA}^2) yields an unphysical low value, which is suppressed.

Looking at the higher Q^2-bins, the variation of the hard scale by a factor of two exhibits large variations of the results, but they show no correlation (here the check $2.0 * Q_{JB}^2$ gives an unphysical low value in the highest Q^2-bin — it has strongly reduced statistics). In the full phase space these variations cancel and lead to a small error. This gives an indication that at these points, corresponding to the resolution parameters $y_{cut} = 0.25$ and $y_{cut} = 1.0$, the limits of a reasonable determination of α_s are reached.

The variation of the resolution parameter y_{cut} within the region which was regarded as safe (cf. 11.3.2) yields only a small uncertainty in the results.

Theoretical Uncertainties:

Finally, the following checks were performed which are related to model dependencies and *theoretical uncertainties*:

- Instead of ARIADNE4.08, the LEPTO6.3^{tuned} MC was used for the correction of the data to the parton level.

- Instead of the GRV(HO) parameterization of the parton density functions in the NLO predictions obtained from MEPJET, the MRSA and the CTEQ4M sets were used. As these choices are mutual exclusive, here also only the largest variation of this check was used in the calculation of the full error.

- Finally, the renormalization scale μ_r^2 and the factorization scale μ_f^2 were varied together by a factor of two ($0.5 * \mu_{r,f}^2, 2.0 * \mu_{r,f}^2$). This way the uncertainty was estimated introduced in the theoretical calculations by restricting them to fixed order, i.e. the effect of the residual interference with higher order terms is tested.

This group of checks contains the two most important systematic uncertainties of this analysis.

Using the LEPTO6.3^{tuned} instead of the ARIADNE4.08 MC model one obtains significantly lower results (-0.0093). This shift is correlated in the bins of Q^2; only the highest Q^2-bin exhibits a different behavior, similar to the choice of the hard scale. But this bin gives

systematic errors on α_s from R_{2+1} using ZEUS 1995 data, ARIADNE4.08, GRV(HO)							
	bin 1	bin 2	bin 3	bin 4	bin 5	bin 6	total
Q^2-range	44...56	56...80	80...160	160...320	320...640	640...3600	44...3600
$\langle Q^2 \rangle$ [GeV^2]	50	66	110	219	435	1128	140
$\alpha_s(M_z^2)$	0.1237	0.1253	0.1264	0.1256	0.1101	0.1178	0.1251
statistical error $^{stat}\Delta\alpha_s$	±0.0016	±0.0016	±0.0016	±0.0024	±0.0070	±0.0089	±0.0012
experimental uncertainty $^{exp}\Delta\alpha_s$	+0.0028 −0.00097	+0.0028 −0.0012	+0.0016 −0.0016	+0.0024 −0.0027	+0.0057 −0.013	+0.0068 −0.0081	+0.0020 −0.0017
jet finding uncertainty $^{jet}\Delta\alpha_s$	+0.0076 −0.00088	+0.0046 −0.0014	+0.0023 −0.0021	+0.0037 −0.0056	+0.010 −0.0028	+0.0083 −0.0026	+0.0046 −0.0018
hard scale uncertainty $^{scale}\Delta\alpha_s$	+0.0068 −0.0028	+0.0027 −0.0091	+0.00 −0.013	+0.0031 −0.027	+0.0064 −0.015	+0.0090 −0.016	+0.0017 −0.0081
theoretical uncertainty $^{theo}\Delta\alpha_s$	+0.0099 −0.0099	+0.0084 −0.0088	+0.0084 −0.0093	+0.012 −0.0093	+0.0087 −0.012	+0.016 −0.00	+0.0089 −0.0093
systematic error $^{syst}\Delta\alpha_s$	+0.014 −0.010	+0.010 −0.013	+0.0092 −0.017	+0.014 −0.029	+0.016 −0.024	+0.021 −0.018	+0.010 −0.013
total error $^{tot}\Delta\alpha_s$	+0.015 −0.010	+0.010 −0.013	+0.0094 −0.017	+0.014 −0.029	+0.017 −0.025	+0.023 −0.020	+0.010 −0.013

Table 11.3: *Systematic errors on $\alpha_s(M_z^2)$ from exclusive (2+1)-jet rate R_{2+1} using ZEUS 1995 data, ARIADNE4.08 for the correction and GRV(HO) in MEPJET. The errors are added in quadrature.*
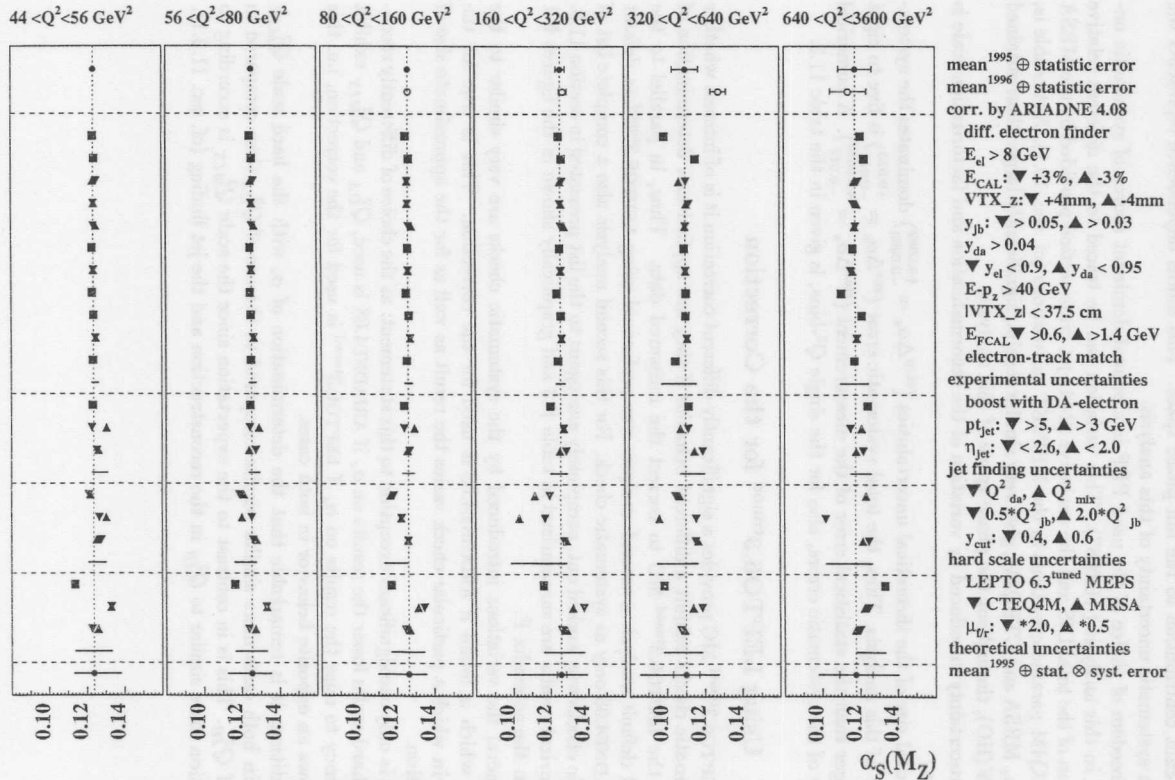
Figure 11.21: *Summary of systematic checks for the determination of $\alpha_s(M_z^2)$ in six bins of Q^2 from the exclusive (2+1)-jet rate R_{2+1} using ZEUS 1995 data, ARIADNE4.08 for the correction and GRV(HO) in MEPJET. See text for discussion.*

no significant contribution to the full phase space. This model dependence represents the dominant systematic uncertainty of this analysis.

The freedom of choice of the used PDF is a second dominant source of systematic uncertainty in this analysis (+0.0087). This variation can be traced to the different relative description of the total DIS and the exclusive (2+1)-jet cross section provided by the MRSA and CTEQ4M parameterizations in the MEPJET calculations (cf. sec. 10.1). Noticeable is, that both, MRSA and CTEQ4M, give very similar results, significantly larger than obtained from GRV(HO), throughout the phase space of this analysis.

The uncertainty introduced by variation of the renormalization and factorization scale is negligible.

The total size of the theoretical uncertainties ($^{theo}\Delta\alpha_s = {}^{+0.0089}_{-0.0093}$) dominates the systematic error of this analysis. Thus, the total systematic error ($^{sys}\Delta\alpha_s = {}^{+0.010}_{-0.013}$) is five to eight times larger than the statistical error of the measurement ($^{stat}\Delta\alpha_s = {}^{+0.0020}_{-0.017}$). A numerical summary of the systematic errors, also for the single Q^2-bins, is given in the table 11.3.

11.5.1 Using LEPTO6.3^{tuned} for the Correction

As the LEPTO6.3^{tuned} MC provides a significantly different correction it is of interest whether the systematic checks exhibit a different behavior if they are applied to a determination of α_s using the LEPTO6.3^{tuned} MC to correct the measured data. Thus, in parallel to the presented default analysis a second analysis was performed using LEPTO6.3^{tuned} as default and ARIADNE4.08 only as systematic check. For this second analysis also a complete list of systematic checks was worked out, completely analogous to the list presented in section 11.5. The numerical results are summarized in table F.3 and graphically shown in the figures F.1 and F.2 in the appendix F.

In general the variations introduced by the systematic checks are very similar to the behavior which is found if ARIADNE4.08 is used for the correction. This is true for the direction in which a particular check varies the result as well as for the approximate size of the variation.

There is only one significant exception to this statement: as the choice of differently reconstructed hard scales lower the results on α_s if ARIADNE4.08 is used, Q^2_{DA} and Q^2_{MIX} exhibit the tendency to raise the results on α_s if LEPTO6.3^{tuned} is used for the correction, i.e. this check shows an opposite behavior in both cases.

In addition, it is remarkable that the determination of α_s with the hard scale Q^2_{MIX} provides in both cases more similar results compared to the use of Q^2_{DA} than compared to the use of Q^2_{JB}. This is in contrast to the expectation since the scale Q^2_{MIX} is according to its definition more similar to Q^2_{JB} in the reconstruction and the jet finding (cf. sec. 11.3.1).

Chapter 12

Final Results

With the systematic errors obtained in section 11.5 the result on the determination of α_s from the exclusive (2+1)-jet rate (sec. 10.2) now can be completed. As the systematic checks were performed on the ZEUS 1995 data set only, only the corresponding figure 10.6 is updated.

The figure 12.1 presents graphically the final result of this analysis, including the statistical and the systematic errors. All errors are added in quadrature in order to calculate the total error, the size of the statistical errors is denoted in figure 12.1 by the tick marks. The fully detailed numerical result, determined from the 1995 data, can be obtained from table 11.3. In the full phase space of this analysis the final result on $\alpha_s(M_z^2)$ reads as follows:

$$\alpha_s(M_z^2) = 0.1251 \pm 0.0012\,(\text{stat})\;{}^{+0.0020}_{-0.0017}\,(\text{exp})\;{}^{+0.0046}_{-0.0018}\,(\text{jet})\;{}^{+0.0017}_{-0.0081}\,(\text{scale})\;{}^{+0.0089}_{-0.0093}\,(\text{theo})$$
$$= 0.1251 \pm 0.0012\,(\text{stat})\;{}^{+0.010}_{-0.013}\,(\text{syst})\;. \tag{12.1}$$

As in table 11.3, *stat* denotes the statistical error, *exp* the experimental uncertainty due to the selection of DIS events in the data, *jet* the uncertainty introduced by the variation of the definition of the jet finding, *scale* the uncertainty caused by the hard scattering scale and the choice of the jet resolution parameter, *theo* the model dependent uncertainty and *syst* the total systematic error.

The systematic errors are about ten times larger than the statistical error and are dominated by the dependence on the MC model, the choice of the parton density functions and the reconstruction of the hard scale.

Since the major systematic uncertainties exhibit a correlated shift of the results, the shape of the results on $\alpha_s(Q^2)$ is not significantly changed. Thus, the feature of the data to strongly favor the running of α_s, as discussed in section 10.2.1, is not significantly changed by the large systematic uncertainties.

The result presented in equation 12.1 is consistent with the current world average, $\alpha_s(M_z^2) = 0.119 \pm 0.002$, if the large systematic error of this determination of α_s is taken into account.

It is also consistent within $1.5\,{}^{stat}\sigma_{95}$ with the determination of α_s from the ZEUS 1996 data which give the result: $\alpha_s(M_z^2) = 0.1234 \pm 0.0010$. It is expected that the general behavior of the systematic uncertainties discussed for the 1995 data is not significantly different for the 1996 data, too.

By employing a different MC model for the simulation of the higher order parton evolution (LEPTO6.3^{tuned} instead of ARIADNE4.08) a result is found which lies at the lower limit of the systematic uncertainty of the presented result, i.e. below the world average:

$$\alpha_s^{\text{LEPTO}}(M_z^2) = 0.1158 \pm 0.0012\,(\text{stat})\;{}^{+0.0023}_{-0.00086}\,(\text{exp})\;{}^{+0.0044}_{-0.00}\,(\text{jet})\;{}^{+0.0045}_{-0.0018}\,(\text{scale})\;{}^{+0.0094}_{-0.0012}\,(\text{theo})$$
$$= 0.1158 \pm 0.0012\,(\text{stat})\;{}^{+0.012}_{-0.0023}\,(\text{syst})\;. \tag{12.2}$$

ZEUS 1995 : α_S from (2+1)-jet rates
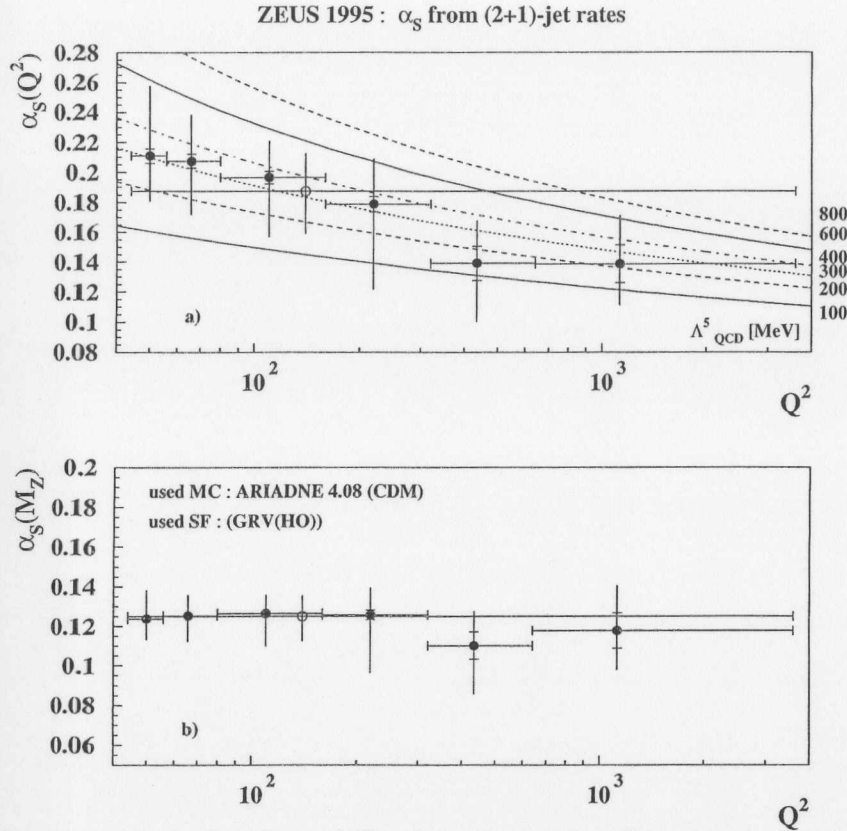
Figure 12.1: *(a): Final result on $\alpha_s(Q^2)$ with statistical (tick marks) and total errors, by addition in quadrature, in six bins of Q^2 (full circles) and in one big bin (open circle) determined from the exclusive (2+1)-jet rate R_{2+1} using ZEUS 1995 data, ARIADNE4.08 for the correction and GRV(HO) in MEPJET. (b): the same data evolved to $\alpha_s(M_z^2)$.*

Thus, the size of the systematic uncertainties is comparable to that found in the default analysis, but here their combination turns out to be very asymmetric. The use of this MC model is disfavored mainly due to the weak description of the R_{n+1} jet rates.

Recently H1 published two new results for the determinations of α_s [H198, Tob98]. Both utilize the JADE algorithm for the jet finding and the H1 1994 & 1995 data. Here LEPTO6.5 is used as the default MC for the correction. The first analysis determines α_s from the exclusive (2+1)-jet rate R_{2+1} and essentially updates the former analysis [H195]. The second analysis determines α_s form the differential (2+1)-jet rate D_2. The given results are:

H1: R_{2+1} : $\alpha_s(M_z^2) = 0.117 \pm 0.003\,(\text{stat})\,{}^{+0.009}_{-0.013}\,(\text{sys})$

H1: D_2 : $\alpha_s(M_z^2) = 0.118 \pm 0.002\,(\text{stat})\,{}^{+0.010}_{-0.010}\,(\text{sys})$.

The size of the systematic errors is comparable to the results found in this analysis. The

model dependence was found to be about half as large as in this analysis, with the relative change between the models inverted. Instead, the variations of the renormalization and the factorization scale contribute significantly.

12.1 Outlook

Beyond the scope of this analysis there are a number of interesting questions which should be briefly mentioned here. From the view of this analysis they have to be left as tasks for the future.

The systematic effect introduced by different hadronization models was not investigated in this analysis[1]. Here only a comparison can be made to the detailed determination of the hadronization uncertainty performed in [Tre96] using the JADE algorithm in a comparable phase space. There the biggest hadronization uncertainty was caused by the switch between the Lund fragmentation and the cluster fragmentation implemented in HERWIG. For the full phase space the uncertainty resulted in a $\Delta\Lambda^5 \approx 50\,\text{MeV}$. Towards low Q^2, where this analysis extends the phase space used in [Tre96], the hadronization effects grow. In fact, this was the reason to limit the phase space towards low Q^2 in [Tre96]. By using the exclusive $K_\perp$ algorithm from theoretical considerations (cf. discussion in sec. 7.4.3) the sensitivity to the hadronization is expected to be smaller than for the JADE algorithm. In addition, the biggest single uncertainties in this analysis correspond to a variation of $\Delta\Lambda^5 \approx 150\,\text{MeV}$. Therefore, for this analysis it is concluded that the hadronization uncertainty, if checked, would not belong to the major systematic uncertainties.

It would be interesting to use an alternative NLO program to explicitly cross check the predictions made by MEPJET. The use of DISENT or DISASTER++ would give an completely independent cross check, as they employ the phase space subtraction method to cut against the divergences in the matrix element calculations, instead of the phase space slicing method utilized by MEPJET. Nevertheless, no significant contribution to the systematic error of this analysis is expected from this source. Checks which were made, not regarding the phase space or special requirements of this analysis, showed that these different programs in general exhibit an excellent agreement at leading order and still a very satisfactory agreement at NLO [MZ97a, Gra97].

A comparison of LO predictions by MEPJET and LO MC simulations provides information on the consistency between the theoretical predictions and the MC implementations. Such an explicit comparison was performed for [ZEU95a], comparing the NLO programs of the first generation, DISJET and PROJET, with LEPTO6.1. For the phase space of this analysis such a study was performed by [Mus97] using MEPJET and the exclusive $K_\perp$ jet finding algorithm. Since it is not yet documented anywhere else the main results are summarized in the appendix G.

The method to determine α_s applied in this analysis does not take into account the variation of α_s within the PDF, which is a second source of dependence of the exclusive (2+1)-jet rate R_{2+1} on α_s. This effect is expected to be small for high Q^2 regions and will becomes more and more important towards lower Q^2. In [CR96] a study was presented for the JADE algorithm using PROJET4.1 and the MSRH parameterization of the parton density functions. They conclude that this effect can be neglected for $Q^2 > 1000\,\text{GeV}^2$ and become dominant with respect to the variation of α_s in the matrix element calculations

---

[1]The HERWIG MC, introduced in section 8.5, was planned to be used for such a check. Due to an unsolved technical problem this check was not finished by the time when this thesis was submitted.

below $Q^2 \approx 40\,\text{GeV}^2$. A similar study using the exclusive $K_\perp$ algorithm and a NLO program of the second generation is not yet available, although this might turn out to be a significant systematic effect. A study to clarify the size of this contribution to the α_s-dependence of the (2+1)-jet rate in the selected phase space of this analysis by using the exclusive $K_\perp$ algorithm is presently under study.

The longitudinally invariant $K_\perp$ algorithm recently has become of interest to be used in the DIS regime as it does not exhibit the depletion effect in the identification of (2+1)-jet configurations at high-Q^2 (high-x) as the exclusive variant of this algorithm does (cf. sec. 9.3.1). Thus, the phase space of the analysis can be extended to much higher values of Q^2. This interesting option is under study at ZEUS, too. The remarkable feature of this study is, that it seems to reveal a significant systematic dependence on the algorithm used in the identification of (2+1)-jet configurations in order to determine of α_s.

Chapter 13

Summary

A determination of the strong coupling constant α_s has been presented using the exclusive (2+1)-jet rate R_{2+1} determined by the $K_\perp$ jet finding algorithm in deep inelastic scattering data measured with the ZEUS detector at HERA.

The kinematic range of this analysis was chosen to:

$$44\,\text{GeV}^2 < Q^2 < 3600\,\text{GeV}^2, \qquad 0.001 < x < 0.1,$$
$$0.04 < y < 0.95, \qquad E_{e'} > 10\,\text{GeV} \quad .$$

The analysis was performed on the 1995 and the 1996 data samples measured by ZEUS, corresponding to the integrated luminosities of $\mathcal{L}^{95} = 6.30\,\text{pb}^{-1}$ and $\mathcal{L}^{96} = 8.16\,\text{pb}^{-1}$, respectively.

The jet finding by the $K_\perp$ algorithm was performed at a fixed jet resolution $y_{cut} = 0.5$ using Q^2 as hard scale of the scattering process. Jets found by the $K_\perp$ algorithm had to fulfill the requirements $\eta^{jet} < 2.436$ and $p_t^{jet} > 4\,\text{GeV}$ to be counted as valid. The measured data was corrected to the parton level by the ARIADNE4.08 MC model. At parton level the (2+1)-jet rate R_{2+1} from corrected data was compared to the NLO QCD predictions calculated by MEPJET for different values of Λ_{QCD}, i.e. different values of the strong coupling α_s. In this comparison that value of α_s was interpolated which gave the best fit to the corrected data. The analysis was performed in six bins of Q^2 as well as in the full Q^2-range. The results obtained at average values $\langle Q^2 \rangle$ were evolved to the Z° mass for the comparison with other measurements. A full set of systematic studies was carried out for the 1995 data sample only.

The result obtained from the 1995 data in the full phase space of this analysis reads:

$$\alpha_s(M_z^2) = 0.1251 \pm 0.0012\,(\text{stat})\ {}^{+0.0020}_{-0.0017}\,(\text{exp})\ {}^{+0.0046}_{-0.0018}\,(\text{jet})\ {}^{+0.0017}_{-0.0081}\,(\text{scale})\ {}^{+0.0089}_{-0.0093}\,(\text{theo})$$
$$= 0.1251 \pm 0.0012\,(\text{stat})\ {}^{+0.010}_{-0.013}\,(\text{syst}) \quad ,$$

where *stat* denotes the statistical error, *exp* the experimental uncertainty due to the selection of DIS events in the data, *jet* the uncertainty introduced by the variation of the definition of the jet finding, *scale* the uncertainty caused by the hard scattering scale and the choice of the jet resolution parameter, *theo* the model dependent uncertainty and *syst* the total systematic error.

The total systematic error is about ten times larger than the statistical error and is dominated by the dependence on the MC model, the freedom of choice of the parton density functions and the reconstruction of the hard scale.

This result is well in agreement with the current world average value of $\alpha_s(M_z^2) = 0.119 \pm 0.002$, which has been calculated from many approaches to determine α_s and, thus, has a relatively small total error.

The result from the 1996 data $(\alpha_s(M_z^2) = 0.1234 \pm 0.0010\,(\text{stat}))$ is consistent with that obtained from the 1995 data within $1.5\,{}^{stat}\sigma_{95}$. As the systematic errors are expected to be similar to those of the 1995 data, this result is regarded as consistent with the current world average, too.

The data strongly favor the running of α_s as compared to the assumption of a constant α_s. Since the major systematic uncertainties exhibit a correlated shift of the results, the shape of the results on $\alpha_s(Q^2)$ is not significantly changed. Thus, this feature of the data is not significantly changed by the large systematic uncertainties.

The chosen MC model for the correction of the data provides the major systematic uncertainty of this analysis. The Color Dipole Model and the MEPS model provide significantly different simulations of the parton level to which the data are corrected. For both cases a full set of systematic checks was worked out. It was found that, besides one, all checks behave very similar in direction and size of the variation. Only the variation in the reconstruction of the hard scale, the third biggest systematic uncertainty in this analysis, changes the direction in which the result is varied.

The use of the MEPS MC for the correction of the data was disfavored mainly due to its weak description of the R_{n+1} jet rates.

The second major uncertainty is the freedom of choice of a parton density function. Next to the default choice, GRV(HO), the parameterizations MRSA and CTEQ4M were checked. Both give very similar results on α_s, but significantly different than for GRV(HO). This behavior can be traced to the different relative description of the total DIS and the exclusive (2+1)-jet cross sections in the MEPJET calculations. In general, MEPJET underestimates these cross sections when it is compared to corrected data. The amount depends on the chosen parton density function. By using the (2+1)-jet rate as quantity to determine α_s this misdescription cancel, at least to a large extent.

Consequently, the determination of α_s from the exclusive (2+1)-jet cross section yields very large values of α_s. The systematic errors are expected larger than presented above due to additional uncertainties. But due the size of the misdescription of the cross sections in MEPJET, inconsistency with the world average can be expected for this approach.

The determination of the strong coupling constant α_s from the (2+1)-jet configuration of the hadronic final state in ep-scattering is dominated by the systematic errors related to MC models and to the parameterizations of the parton densities. New ideas are needed for a significant reduction of these uncertainties to overcome this limitation in the determination of α_s.

Appendix A

Results of the Event Selection

This chapter gives the numerical results of the event selection on the used data samples:

- ZEUS data 1995 running period
- ZEUS data 1996 running period
- 1995 MC ARIADNE4.08
- 1995 MC LEPTO6.3$^{\text{tuned}}$
- 1995 MC LEPTO6.3
- 1996 MC ARIADNE4.08

The numerical results cover:

1. the measured number (#) of found DIS events in the chosen phase space

2. the number of events with an additional (2+1)-jet configuration in the hadronic final state identified by the default jet finding procedure ($K_\perp$ algorithm, $y_{cut} = 0.5$, hard scale: Q^2_{JB}).

These results are given in the chosen Q^2-bins and in addition in one big bin which covers the full phase space for 1995 data and only the region $Q^2 > 80\,\text{GeV}^2$ for 1996 data. The latter restriction was invented in order to compare to the 1996 sample of the ARIADNE4.08 MC which has been produced with a threshold of $Q^2 > 70\,\text{GeV}^2$. For the MC samples the parton, hadron and detector level results are given. The quoted bin centers $\langle Q^2 \rangle$ were taken from the mean of the Q^2 distribution of the selected DIS events in the bins found with the 1995 data sample.

For each data sample the measured integrated luminosity $\mathcal{L}$ is quoted. For the MC samples an effective integrated luminosity $\mathcal{L}^{eff}$ was used, i.e. the generated luminosity times the fraction which had passed the ZEUS MC chain.

The following quantities can be derived directly from these data:

- the raw, uncorrected rate of (2+1)-jet events R_{2+1}

- the DIS cross section $\dfrac{d\sigma^{(2+1)}_{DIS}}{dQ^2} = \dfrac{1}{\mathcal{L}}\dfrac{\#\,\text{of (2+1)-events}}{\Delta Q^2}$

- the dijet cross section $\dfrac{d\sigma^{tot}_{DIS}}{dQ^2} = \dfrac{1}{\mathcal{L}}\dfrac{\#\,\text{of DIS-events}}{\Delta Q^2}$,

which are given too with statistical errors only. Especially the errors given for the cross sections measured from ZEUS data do not take into account the total systematic error on the luminosity measurement which is about 1.1 % in 1995 and 1.3 % in 1996.

1995 MC ARIADNE4.08							
	bin 1	bin 2	bin 3	bin 4	bin 5	bin 6	total
Q^2-range [GeV^2]	$44 \ldots 56$	$56 \ldots 80$	$80 \ldots 160$	$160 \ldots 320$	$320 \ldots 640$	$640 \ldots 3600$	$44 \ldots 3600$
bin center $\langle Q^2 \rangle$ [GeV^2]	50	66	110	219	435	1128	140
det : # of DIS events	26946	31078	33985	14911	6057	2734	115711
det : # of (2+1)-jet events	2600	3037	2816	827	234	90	9604
det : (2+1)-jet rate R_{2+1} [%]	9.65±0.20	9.77±0.19	8.29±0.16	5.55±0.20	3.86±0.26	3.29±0.35	8.300±0.088
had : # of DIS events	26944	30233	32265	13883	5563	2535	111423
had : # of (2+1)-jet events	2159	2386	2089	671	178	51	7534
had : (2+1)-jet rate R_{2+1} [%]	8.01±0.18	7.89±0.17	6.47±0.19	4.83±0.15	3.20±0.24	2.01±0.28	6.76±0.080
par : # of DIS events	26944	30233	32265	13883	5563	2535	111423
par : # of (2+1)-jet events	2903	3237	2834	872	235	58	10139
par : (2+1)-jet rate R_{2+1} [%]	10.77±0.21	10.71±0.20	8.78±0.17	6.28±0.22	4.22±0.28	2.29±0.30	9.100±0.094
eff. luminosity $\mathcal{L}^{eff}$ $\left[\frac{1}{\text{pb}}\right]$	9.2235						
det : $d\sigma_{DIS}^{tot}/dQ^2$ [pb/GeV^2]	243±70	140±29	46.1±5.2	10.10±0.80	2.05±0.12	0.1001±0.0027	3.528±0.060
det : $d\sigma_{DIS}^{(2+1)}/dQ^2$ [pb/GeV^2]	23.5±6.8	13.7±2.8	3.81±0.43	0.560±0.048	0.0793±0.0068	0.00330±0.00035	0.2928±0.0057
had : $d\sigma_{DIS}^{tot}/dQ^2$ [pb/GeV^2]	243±70	137±28	43.7±4.9	9.40±0.75	1.88±0.11	0.0929±0.0025	3.397±0.058
had : $d\sigma_{DIS}^{(2+1)}/dQ^2$ [pb/GeV^2]	19.5±5.6	10.8±2.2	2.83±0.32	0.455±0.040	0.0603±0.0056	0.00187±0.00026	0.2297±0.0047
par : $d\sigma_{DIS}^{tot}/dQ^2$ [pb/GeV^2]	243±70	137±28	43.7±4.9	9.41±0.75	1.88±0.11	0.0929±0.0025	3.397±0.058
par : $d\sigma_{DIS}^{(2+1)}/dQ^2$ [pb/GeV^2]	26.2±7.6	14.6±3.0	3.84±0.44	0.591±0.051	0.0796±0.0068	0.00212±0.00028	0.3091±0.0060

Table A.3: *Results of the event selection on the 1995 MC sample* ARIADNE4.08 *using the default selection and jet finding procedure.*

ZEUS 1995 uncorrected data							
	bin 1	bin 2	bin 3	bin 4	bin 5	bin 6	total
Q^2-range [GeV^2]	$44 \ldots 56$	$56 \ldots 80$	$80 \ldots 160$	$160 \ldots 320$	$320 \ldots 640$	$640 \ldots 3600$	$44 \ldots 3600$
bin center $\langle Q^2 \rangle$ [GeV^2]	50	66	110	219	435	1128	140
# of DIS events	18311	21234	24323	10663	4120	1863	80514
# of (2+1)-jet events	1545	1866	1842	530	111	61	5955
(2+1)-jet rate R_{2+1} [%]	8.44±0.22	8.79±0.21	7.57±0.18	4.97±0.22	2.69±0.26	3.27±0.42	7.396±0.099
luminosity $\mathcal{L}$ $\left[\frac{1}{\text{pb}}\right]$	6.30 (±1.1 % absolute, neglected)						
$d\sigma_{DIS}^{tot}/dQ^2$ [pb/GeV^2]	242±70	140±29	48.3±5.4	10.58±0.84	2.04±0.12	0.0999±0.0030	3.594±0.062
$d\sigma_{DIS}^{(2+1)}/dQ^2$ [pb/GeV^2]	20.4±5.9	12.3±2.5	3.65±0.42	0.526±0.047	0.0551±0.0061	0.00327±0.00042	0.2658±0.0056

Table A.1: *Results of the event selection on the uncorrected 1995 data sample using the default selection and jet finding procedure.*

ZEUS 1996 uncorrected data							
	bin 1	bin 2	bin 3	bin 4	bin 5	bin 6	total
Q^2-range [GeV^2]	$44 \ldots 56$	$56 \ldots 80$	$80 \ldots 160$	$160 \ldots 320$	$320 \ldots 640$	$640 \ldots 3600$	$80 \ldots 3600$
bin center $\langle Q^2 \rangle$ [GeV^2]	50	66	110	219	435	1128	218
# of DIS events	23468	27606	30921	13613	5497	2464	52495
# of (2+1)-jet events	1973	2314	2254	694	205	57	3210
(2+1)-jet rate R_{2+1} [%]	8.41±0.20	8.38±0.18	7.29±0.16	5.10±0.20	3.73±0.27	2.31±0.31	6.11±0.11
luminosity $\mathcal{L}$ $\left[\frac{1}{\text{pb}}\right]$	8.16 (±1.3 % absolute, neglected)						
$d\sigma_{DIS}^{tot}/dQ^2$ [pb/GeV^2]	240±69	141±29	47.3±5.3	10.42±0.83	2.10±0.12	0.1020±0.0028	1.827±0.032
$d\sigma_{DIS}^{(2+1)}/dQ^2$ [pb/GeV^2]	20.1±5.8	11.8±2.4	3.45±0.39	0.531±0.047	0.0785±0.0070	0.00236±0.00032	0.1117±0.0027

Table A.2: *Results of the event selection on the uncorrected 1996 data sample using the default selection and jet finding procedure.*

1995 MC LEPTO6.3							
	bin 1	bin 2	bin 3	bin 4	bin 5	bin 6	total
Q^2-range [GeV^2]	44...56	56...80	80...160	160...320	320...640	640...3600	44...3600
bin center $\langle Q^2 \rangle$ [GeV^2]	50	66	110	219	435	1128	140
det : # of DIS events	29683	34333	38550	17317	7122	3192	130197
det : # of (2+1)-jet events	3318	3689	3301	934	271	111	11624
det : (2+1)-jet rate R_{2+1} [%]	11.18±0.20	10.74±0.19	8.56±0.16	5.39±0.18	3.81±0.24	3.48±0.34	8.928±0.086
had : # of DIS events	29653	33610	36616	16083	6465	2865	125292
had : # of (2+1)-jet events	2342	2556	2108	570	136	46	7758
had : (2+1)-jet rate R_{2+1} [%]	7.90±0.17	7.60±0.16	5.76±0.13	3.54±0.15	2.10±0.18	1.61±0.24	6.192±0.072
par : # of DIS events	29653	33610	36616	16083	6465	2865	125292
par : # of (2+1)-jet events	2943	3137	2815	828	215	67	10005
par : (2+1)-jet rate R_{2+1} [%]	9.92±0.19	9.33±0.17	7.69±0.15	5.15±0.18	3.33±0.23	2.34±0.29	7.985±0.083
eff. luminosity $\mathcal{L}^{eff}$ $\left[\frac{1}{pb}\right]$	10.722						
det : $d\sigma_{DIS}^{tot}/dQ^2$ [pb/GeV^2]	231±67	133±27	44.9±5.0	10.09±0.80	2.08±0.12	0.1006±0.0026	3.415±0.058
det : $d\sigma_{DIS}^{(2+1)}/dQ^2$ [pb/GeV^2]	25.8±7.5	14.3±2.9	3.85±0.44	0.544±0.047	0.0790±0.0065	0.00350±0.00034	0.3049±0.0058
had : $d\sigma_{DIS}^{tot}/dQ^2$ [pb/GeV^2]	230±67	131±27	42.7±4.8	9.37±0.74	1.88±0.11	0.0903±0.0024	3.286±0.056
had : $d\sigma_{DIS}^{(2+1)}/dQ^2$ [pb/GeV^2]	18.2±5.3	9.9±2.0	2.46±0.28	0.332±0.030	0.0396±0.0041	0.00145±0.00022	0.2035±0.0041
par : $d\sigma_{DIS}^{tot}/dQ^2$ [pb/GeV^2]	230±67	131±27	42.7±4.8	9.37±0.74	1.88±0.11	0.0903±0.0024	3.286±0.056
par : $d\sigma_{DIS}^{(2+1)}/dQ^2$ [pb/GeV^2]	22.9±6.6	12.2±2.5	3.28±0.37	0.483±0.042	0.0627±0.0055	0.00211±0.00026	0.2624±0.0051

Table A.5: *Results of the event selection on the 1995 MC sample* LEPTO6.3 *using the default selection and jet finding procedure.*

1995 MC LEPTO6.3$^{\text{tuned}}$							
	bin 1	bin 2	bin 3	bin 4	bin 5	bin 6	total
Q^2-range [GeV^2]	44...56	56...80	80...160	160...320	320...640	640...3600	44...3600
bin center $\langle Q^2 \rangle$ [GeV^2]	50	66	110	219	435	1128	140
det : # of DIS events	23611	27678	30457	13648	5510	2591	103495
det : # of (2+1)-jet events	2024	2289	2150	687	174	76	7400
det : (2+1)-jet rate R_{2+1} [%]	8.57±0.20	8.27±0.18	7.06±0.16	5.03±0.20	3.16±0.24	2.93±0.34	7.150±0.086
had : # of DIS events	23625	27155	29158	12678	5047	2399	100062
had : # of (2+1)-jet events	1400	1565	1360	421	108	39	4893
had : (2+1)-jet rate R_{2+1} [%]	5.93±0.16	5.76±0.15	4.66±0.13	3.32±0.16	2.14±0.21	1.63±0.26	4.890±0.072
par : # of DIS events	23625	27155	29158	12678	5047	2399	100062
par : # of (2+1)-jet events	1792	2026	1821	613	155	61	6468
par : (2+1)-jet rate R_{2+1} [%]	7.59±0.19	7.46±0.17	6.25±0.15	4.84±0.20	3.07±0.25	2.54±0.33	6.464±0.083
eff. luminosity $\mathcal{L}^{eff}$ $\left[\frac{1}{pb}\right]$	8.5226						
det : $d\sigma_{DIS}^{tot}/dQ^2$ [pb/GeV^2]	231±67	135±28	44.7±5.0	10.01±0.80	2.02±0.12	0.1027±0.0028	3.415±0.058
det : $d\sigma_{DIS}^{(2+1)}/dQ^2$ [pb/GeV^2]	19.8±5.7	11.2±2.3	3.15±0.36	0.504±0.044	0.0638±0.0060	0.00301±0.00035	0.2442±0.0050
had : $d\sigma_{DIS}^{tot}/dQ^2$ [pb/GeV^2]	231±67	133±27	42.8±4.8	9.30±0.74	1.85±0.11	0.0951±0.0026	3.302±0.056
had : $d\sigma_{DIS}^{(2+1)}/dQ^2$ [pb/GeV^2]	13.7±4.0	7.7±1.6	1.99±0.23	0.309±0.029	0.0396±0.0044	0.00155±0.00025	0.1615±0.0036
par : $d\sigma_{DIS}^{tot}/dQ^2$ [pb/GeV^2]	231±67	133±27	42.8±4.8	9.30±0.74	1.85±0.11	0.0951±0.0026	3.302±0.056
par : $d\sigma_{DIS}^{(2+1)}/dQ^2$ [pb/GeV^2]	17.5±5.1	9.91±2.0	2.67±0.31	0.450±0.040	0.0568±0.0056	0.00242±0.00031	0.2134±0.0045

Table A.4: *Results of the event selection on the 1995 MC sample* LEPTO6.3$^{\text{tuned}}$ *using the default selection and jet finding procedure.*

Q^2-range [GeV²] bin center $\langle Q^2 \rangle$ [GeV²]	bin 1 44...56 50	bin 2 56...80 66	bin 3 80...160 110	bin 4 160...320 219	bin 5 320...640 435	bin 6 640...3600 1128	total 80...3600 218
			1996 MC ARIADNE4.08				
det: # of DIS events			50603	23461	9833	4534	88431
det: # of (2+1)-jet events			3950	1279	377	128	5734
det: (2+1)-jet rate R_{2+1} [%]	±	±	7.81±0.13	5.45±0.16	3.83±0.20	2.82±0.25	6.484±0.088
had: # of DIS events			52386	23248	9452	4480	89566
had: # of (2+1)-jet events			3412	1124	292	107	4935
had: (2+1)-jet rate R_{2+1} [%]	±	±	6.51±0.12	4.83±0.15	3.09±0.18	2.39±0.23	5.510±0.081
par: # of DIS events			52386	23248	9452	4480	89566
par: # of (2+1)-jet events			4514	1436	369	119	6438
par: (2+1)-jet rate R_{2+1} [%]	±	±	8.62±0.17	6.18±0.17	3.90±0.21	2.66±0.25	7.188±0.093
eff. luminosity $\mathcal{L}^{eff}$ $\left[\frac{1}{pb}\right]$					16.389		
det: $d\sigma_{DIS}^{tot}/dQ^2$ [pb/GeV²]	±	±	38.6±4.3	8.95±0.71	1.87±0.11	0.0935±0.0022	1.533±0.026
det: $d\sigma_{DIS}^{(2+1)}/dQ^2$ [pb/GeV²]	±	±	3.01±0.34	0.488±0.041	0.0719±0.0055	0.00264±0.00024	0.099±0.0021
had: $d\sigma_{DIS}^{tot}/dQ^2$ [pb/GeV²]	±	±	40.0±4.5	8.87±0.70	1.80±0.10	0.0924±0.0022	1.553±0.027
had: $d\sigma_{DIS}^{(2+1)}/dQ^2$ [pb/GeV²]	±	±	2.60±0.29	0.429±0.036	0.057±0.0045	0.00221±0.00022	0.0855±0.0019
par: $d\sigma_{DIS}^{tot}/dQ^2$ [pb/GeV²]	±	±	40.0±4.5	8.87±0.70	1.80±0.10	0.0924±0.0022	1.553±0.027
par: $d\sigma_{DIS}^{(2+1)}/dQ^2$ [pb/GeV²]	±	±	3.44±0.39	0.548±0.046	0.0703±0.0054	0.00245±0.00023	0.1116±0.0023

Table A.6: Results of the event selection on the 1996 MC sample ARIADNE4.08 using the default selection and jet finding procedure.

Appendix B

Purities, Efficiencies and Correction Factors

This chapter gives the numerical results for the purities, efficiencies and correction factors for the exclusive (2+1)-jet rate R_{2+1} obtained from the MC samples

- 1995 MC ARIADNE4.08
- 1995 MC LEPTO6.3^tuned
- 1995 MC LEPTO6.3
- 1996 MC ARIADNE4.08

by the default event and jet selection. They are listed for the three transitions

- between parton and hadron level, i.e. the hadronization correction
- between hadron and detector level, i.e. the detector correction
- the direct transition from parton to detector level which was applied to obtain the final results.

In addition, the correction factors are given which are used to correct the total DIS cross section $d\sigma_{DIS}^{tot}/dQ^2$ and the exclusive (2+1)-jet cross section $d\sigma_{DIS}^{(2+1)}/dQ^2$ to hadron and parton level.

These quantities are given in the chosen Q^2-bins and in addition in one big bin which covers the full phase space for 1995 data and only the region $Q^2 > 80$ GeV² for 1996 data. As before, the latter restriction was invented since the 1996 sample of the ARIADNE4.08 MC has been produced with a threshold of $Q^2 > 70$ GeV².

The errors given for the purities and efficiencies are obtained from simple Gaussian error propagation without regarding the correlation of the data sets while for the correction factors the method of error calculation discusses in conjunction with equation 9.11 was applied.

Purities, Efficiencies and Correction Factors for the exclusive (2+1)-jet rate						
	bin 1	bin 2	bin 3	bin 4	bin 5	bin 6	total
Q^2-range [GeV^2]	44…56	56…80	80…160	160…320	320…640	640…3600	44…3600
1995 MC LEPTO6.3^{tuned}							
p : had↔par	0.657±0.028	0.684±0.027	0.761±0.031	0.841±0.061	0.82±0.12	0.95±0.22	0.717±0.016
ε	0.513±0.021	0.529±0.020	0.568±0.022	0.577±0.039	0.574±0.076	0.61±0.13	0.542±0.011
^{jr}C	1.280±0.016	1.295±0.016	1.339±0.012	1.4561±0.0073	1.4352±0.0037	1.5641±0.0026	1.322±0.012
p : det↔had	0.210±0.011	0.245±0.012	0.301±0.014	0.351±0.026	0.299±0.047	0.316±0.074	0.2635±0.0067
ε	0.304±0.017	0.358±0.018	0.476±0.023	0.572±0.046	0.481±0.081	0.62±0.16	0.399±0.011
^{jr}C	0.691±0.021	0.697±0.020	0.661±0.015	0.6597±0.0092	0.6776±0.0046	0.5542±0.0037	0.684±0.016
p : det↔par	0.251±0.012	0.284±0.013	0.356±0.015	0.438±0.030	0.333±0.051	0.395±0.085	0.3127±0.0074
ε	0.283±0.014	0.321±0.014	0.421±0.018	0.491±0.035	0.374±0.058	0.49±0.11	0.3578±0.0087
^{jr}C	0.885±0.024	0.902±0.023	0.885±0.018	0.961±0.011	0.9725±0.0055	0.8669±0.0047	0.904±0.018
1995 MC LEPTO6.3							
p : had↔par	0.617±0.021	0.648±0.020	0.719±0.024	0.796±0.050	0.81±0.10	0.91±0.19	0.673±0.012
ε	0.491±0.016	0.528±0.016	0.538±0.017	0.548±0.032	0.512±0.060	0.63±0.12	0.5221±0.0089
^{jr}C	1.257±0.025	1.227±0.023	1.335±0.016	1.4526±0.0080	1.5809±0.0038	1.4565±0.0025	1.290±0.017
p : det↔had	0.2089±0.0087	0.2385±0.0089	0.283±0.010	0.290±0.020	0.262±0.035	0.216±0.049	0.2472±0.0052
ε	0.296±0.013	0.344±0.013	0.444±0.017	0.475±0.035	0.522±0.076	0.52±0.13	0.3705±0.0081
^{jr}C	0.707±0.031	0.708±0.030	0.672±0.021	0.657±0.010	0.5528±0.0055	0.4617±0.0044	0.694±0.022
p : det↔par	0.2360±0.0094	0.2678±0.0096	0.340±0.012	0.387±0.024	0.339±0.041	0.333±0.063	0.2910±0.0057
ε	0.266±0.011	0.315±0.011	0.398±0.014	0.436±0.027	0.428±0.053	0.55±0.11	0.3380±0.0067
^{jr}C	0.888±0.035	0.869±0.033	0.898±0.024	0.955±0.012	0.8740±0.0069	0.6725±0.0053	0.894±0.025

Table B.2: *Purities p, efficiencies ε and correction factors ^{jr}C for the exclusive (2+1)-jet rate R_{2+1} obtained from different MC samples for different bins in Q^2 using the default DIS and jet selection. Contination from table B.1.*

Purities, Efficiencies and Correction Factors for the exclusive (2+1)-jet rate						
	bin 1	bin 2	bin 3	bin 4	bin 5	bin 6	total
Q^2-range [GeV^2]	44…56	56…80	80…160	160…320	320…640	640…3600	44…3600
1995 MC ARIADNE4.08							
p : had↔par	0.751±0.025	0.770±0.024	0.829±0.027	0.866±0.049	0.910±0.099	0.88±0.18	0.793±0.014
ε	0.558±0.017	0.568±0.017	0.611±0.019	0.666±0.036	0.689±0.070	0.78±0.15	0.5895±0.0096
^{jr}C	1.345±0.026	1.357±0.026	1.357±0.019	1.300±0.012	1.3202±0.0066	1.1374±0.0030	1.346±0.020
p : det↔had	0.273±0.012	0.317±0.012	0.395±0.014	0.439±0.028	0.466±0.054	0.344±0.072	0.3424±0.0069
ε	0.329±0.014	0.403±0.015	0.532±0.020	0.541±0.035	0.612±0.074	0.61±0.14	0.4364±0.0091
^{jr}C	0.830±0.027	0.808±0.027	0.781±0.021	0.871±0.012	0.8282±0.0069	0.6111±0.0047	0.815±0.022
p : det↔par	0.317±0.013	0.364±0.013	0.468±0.016	0.505±0.030	0.530±0.059	0.400±0.079	0.3982±0.0076
ε	0.284±0.011	0.342±0.012	0.465±0.015	0.479±0.029	0.528±0.059	0.621±0.13	0.377±0.0072
^{jr}C	1.117±0.032	1.096±0.032	1.060±0.025	1.132±0.014	1.0935±0.0079	0.6950±0.0050	1.096±0.025
	bin 1	bin 2	bin 3	bin 4	bin 5	bin 6	total
Q^2-range [GeV^2]	44…56	56…80	80…160	160…320	320…640	640…3600	80…3600
1996 MC ARIADNE4.08							
p : had↔par	±	±	0.829±0.021	0.873±0.038	0.846±0.073	0.925±0.13	0.842±0.018
ε	±	±	0.627±0.015	0.683±0.028	0.669±0.055	0.83±0.11	0.646±0.013
^{jr}C	±	±	1.323±0.019	1.278±0.012	1.2637±0.0061	1.1122±0.0039	1.305±0.015
p : det↔had	±	±	0.450±0.013	0.446±0.022	0.432±0.041	0.438±0.070	0.448±0.011
ε	±	±	0.521±0.015	0.508±0.026	0.558±0.055	0.523±0.086	0.520±0.013
^{jr}C	±	±	0.834±0.020	0.887±0.012	0.8058±0.0067	0.8460±0.0044	0.850±0.015
p : det↔par	±	±	0.509±0.014	0.521±0.025	0.477±0.043	0.414±0.068	0.508±0.012
ε	±	±	0.446±0.012	0.464±0.022	0.488±0.044	0.445±0.074	0.452±0.010
^{jr}C	±	±	1.104±0.023	1.133±0.014	1.01823±0.0076	0.9409±0.0046	1.109±0.017

Table B.1: *Purities p, efficiencies ε and correction factors ^{jr}C for the exclusive (2+1)-jet rate R_{2+1} obtained from different MC samples for different bins in Q^2 using the default DIS and jet selection. Continued with table B.2.*

Appendix C

Hadron and Parton Level Results

This chapter gives the numerical results for exclusive (2+1)-jet rate R_{2+1} corrected to hadron and parton level by

- 1995 MC ARIADNE4.08
- 1995 MC LEPTO6.3$^{\text{tuned}}$
- 1995 MC LEPTO6.3
- 1996 MC ARIADNE4.08

Again, the default event and jet selection was used.

In addition, the measured total DIS cross section $d\sigma^{tot}_{DIS}/dQ^2$ and the exclusive (2+1)-jet cross section $d\sigma^{(2+1)}_{DIS}/dQ^2$ corrected to hadron and parton level are given.

As before, these quantities are given in the chosen Q^2-bins and in addition in one big bin which covers the full phase space for 1995 data and only the region $Q^2 > 80\,\text{GeV}^2$ for 1996 data — due to the restriction $Q^2 > 70\,\text{GeV}^2$ in the MC.

The errors given for the (2+1)-jet rate were calculated by error propagation including the method presented in section 9.4 to account for the correlation of the MC samples the correction factors were obtained from.

The same is done for the errors given for the cross sections but they do not incorporate the uncertainties from the luminosity measurement as discussed in section 9.4.2.

	Correction Factors for the total DIS and the exclusive (2+1)-jet cross section						
	bin 1	bin 2	bin 3	bin 4	bin 5	bin 6	total
Q^2-range [GeV^2]	44 . . . 56	56 . . . 80	80 . . . 160	160 . . . 320	320 . . . 640	640 . . . 3600	44 . . . 3600
1995 MC ARIADNE4.08							
$^{\sigma\text{DIS}}C$: det↔had/par	0.9999±0.0052	0.9728±0.0042	0.9494±0.0031	0.9310±0.0045	0.9184±0.0070	0.9272±0.0091	0.9629±0.0020
$^{\sigma_{2+1}}C$: det↔had	0.830±0.020	0.786±0.017	0.742±0.016	0.811±0.030	0.761±0.052	0.567±0.074	0.7845±0.0095
$^{\sigma_{2+1}}C$: det↔par	1.117±0.025	1.066±0.022	1.006±0.020	1.054±0.036	1.004±0.064	0.644±0.078	1.056±0.012
1995 MC LEPTO6.3$^{\text{tuned}}$							
$^{\sigma\text{DIS}}C$: det↔had/par	1.0006±0.0055	0.9811±0.0043	0.9574±0.0033	0.9289±0.0047	0.9160±0.0072	0.9259±0.0092	0.9668±0.0021
$^{\sigma_{2+1}}C$: det↔had	0.692±0.021	0.684±0.019	0.633±0.017	0.613±0.029	0.621±0.060	0.513±0.077	0.661±0.010
$^{\sigma_{2+1}}C$: det↔par	0.885±0.025	0.885±0.023	0.847±0.021	0.892±0.036	0.891±0.079	0.80±0.10	0.874±0.012
1995 MC LEPTO6.3							
$^{\sigma\text{DIS}}C$: det↔had/par	0.9990±0.0049	0.9789±0.0039	0.9498±0.0029	0.9287±0.0042	0.9078±0.0065	0.8976±0.0084	0.9623±0.0019
$^{\sigma_{2+1}}C$: det↔had	0.706±0.017	0.693±0.015	0.639±0.014	0.610±0.026	0.502±0.043	0.414±0.061	0.6674±0.0082
$^{\sigma_{2+1}}C$: det↔par	0.887±0.019	0.850±0.017	0.853±0.017	0.887±0.033	0.793±0.057	0.602±0.071	0.8607±0.0097
	bin 1	bin 2	bin 3	bin 4	bin 5	bin 6	total
Q^2-range [GeV^2]	44 . . . 56	56 . . . 80	80 . . . 160	160 . . . 320	320 . . . 640	640 . . . 3600	80 . . . 3600
1996 MC ARIADNE4.08							
$^{\sigma\text{DIS}}C$: det↔had/par	±	±	1.0352±0.0027	0.9909±0.0039	0.9613±0.0058	0.9881±0.0078	1.0128±0.0020
$^{\sigma_{2+1}}C$: det↔had	±	±	0.864±0.015	0.879±0.026	0.775±0.043	0.836±0.079	0.861±0.012
$^{\sigma_{2+1}}C$: det↔par	±	±	1.143±0.018	1.123±0.031	0.979±0.052	0.930±0.089	1.123±0.015

Table B.3: *Correction factors $^{\sigma\text{DIS}}C$ and $^{\sigma_{2+1}}C$ for the total DIS and the exclusive (2+1)-jet cross section obtained from different MC samples for different bins in Q^2 using the default DIS and jet selection.*

Total DIS and exclusive (2+1)-jet cross sections from 1995 and 1996 data corrected to hadron and parton level							
Q^2-range [GeV^2]	bin 1 $44\ldots56$	bin 2 $56\ldots80$	bin 3 $80\ldots160$	bin 4 $160\ldots320$	bin 5 $320\ldots640$	bin 6 $640\ldots3600$	total $44\ldots3600$
[pb/GeV^2]	1995 MC ARIADNE4.08						
$d\sigma_{DIS}^{tot}/dQ^2$: had/par level	240±70	137±28	45.8±5.1	9.85±0.79	1.88±0.11	0.0926±0.0029	3.461±0.060
$d\sigma_{DIS}^{(2+1)}/dQ^2$: had level	17.0±4.9	9.7±2.0	2.71±0.31	0.427±0.042	0.0419±0.0054	0.00185±0.00034	0.2085±0.0051
$d\sigma_{DIS}^{(2+1)}/dQ^2$: par level	22.8±6.6	13.2±2.7	3.68±0.43	0.554±0.054	0.0553±0.0070	0.00210±0.00037	0.2806±0.0067
[pb/GeV^2]	1995 MC LEPTO6.3$^{\text{tuned}}$						
$d\sigma_{DIS}^{tot}/dQ^2$: had/par level	240±70	138±28	46.2±5.2	9.83±0.78	1.87±0.11	0.0925±0.0029	3.475±0.060
$d\sigma_{DIS}^{(2+1)}/dQ^2$: had level	14.1±4.1	8.4±1.7	2.31±0.27	0.322±0.033	0.0342±0.0050	0.00168±0.00033	0.1758±0.0046
$d\sigma_{DIS}^{(2+1)}/dQ^2$: par level	18.1±5.3	10.9±2.3	3.10±0.36	0.469±0.046	0.0490±0.0069	0.00263±0.00048	0.2323±0.0059
[pb/GeV^2]	1995 MC LEPTO6.3						
$d\sigma_{DIS}^{tot}/dQ^2$: had/par level	240±70	137±28	45.8±5.1	9.82±0.78	1.86±0.11	0.0897±0.0028	3.459±0.060
$d\sigma_{DIS}^{(2+1)}/dQ^2$: had level	14.4±4.2	8.6±1.8	2.33±0.27	0.321±0.032	0.0276±0.0038	0.00136±0.00026	0.1774±0.0043
$d\sigma_{DIS}^{(2+1)}/dQ^2$: par level	18.1±5.3	10.5±2.2	3.12±0.36	0.466±0.045	0.0437±0.0057	0.00197±0.00035	0.2288±0.0055
Q^2-range [GeV^2]	bin 1 $44\ldots56$	bin 2 $56\ldots80$	bin 3 $80\ldots160$	bin 4 $160\ldots320$	bin 5 $320\ldots640$	bin 6 $640\ldots3600$	total $80\ldots3600$
[pb/GeV^2]	1996 MC ARIADNE4.08						
$d\sigma_{DIS}^{tot}/dQ^2$: had/par level	±	±	49.0±5.5	10.33±0.82	2.02±0.12	0.1007±0.0029	1.850±0.032
$d\sigma_{DIS}^{(2+1)}/dQ^2$: had level	±	±	2.98±0.34	0.467±0.043	0.0608±0.0064	0.00197±0.00032	0.0961±0.0027
$d\sigma_{DIS}^{(2+1)}/dQ^2$: par level	±	±	3.94±0.45	0.596±0.055	0.0768±0.0080	0.00219±0.00036	0.1254±0.0035

Table C.2: *Total DIS $d\sigma_{DIS}^{tot}/dQ^2$ and exclusive (2+1)-jet cross sections $d\sigma_{DIS}^{(2+1)}/dQ^2$ from 1995 and 1996 data corrected to hadron and parton level by correction factors obtained from different MC samples for different bins in Q^2 using the default DIS and jet selection.*

Exclusive (2+1)-jet rate from 1995 and 1996 data corrected to hadron and parton level							
Q^2-range [GeV^2]	bin 1 $44\ldots56$	bin 2 $56\ldots80$	bin 3 $80\ldots160$	bin 4 $160\ldots320$	bin 5 $320\ldots640$	bin 6 $640\ldots3600$	total $44\ldots3600$
1995 MC ARIADNE4.08							
R_{2+1} [%] : had level	7.01±0.30	7.10±0.30	5.92±0.21	4.33±0.20	2.23±0.22	2.00±0.26	6.03±0.18
R_{2+1} [%] : par level	9.42±0.37	9.63±0.36	8.03±0.27	5.63±0.26	2.95±0.28	2.28±0.30	8.11±0.21
1995 MC LEPTO6.3$^{\text{tuned}}$							
R_{2+1} [%] : had level	5.83±0.23	6.12±0.23	5.00±0.17	3.28±0.15	1.83±0.18	1.81±0.24	5.06±0.14
R_{2+1} [%] : par level	7.47±0.28	7.93±0.28	6.70±0.21	4.77±0.22	2.62±0.25	2.84±0.37	6.69±0.16
1995 MC LEPTO6.3							
R_{2+1} [%] : had level	5.96±0.31	6.22±0.30	5.09±0.20	3.27±0.15	1.49±0.14	1.51±0.20	5.13±0.18
R_{2+1} [%] : par level	7.49±0.36	7.63±0.34	6.80±0.24	4.74±0.22	2.35±0.23	2.20±0.29	6.62±0.21
Q^2-range [GeV^2]	bin 1 $44\ldots56$	bin 2 $56\ldots80$	bin 3 $80\ldots160$	bin 4 $160\ldots320$	bin 5 $320\ldots640$	bin 6 $640\ldots3600$	total $80\ldots3600$
1996 MC ARIADNE4.08							
R_{2+1} [%]: had level	±	±	6.08±0.20	4.52±0.19	3.00±0.22	1.96±0.26	5.20±0.13
R_{2+1} [%] : par level	±	±	8.05±0.24	5.78±0.24	3.80±0.27	2.18±0.29	6.78±0.16

Table C.1: *Exclusive (2+1)-jet rate R_{2+1} from 1995 and 1996 data corrected to hadron and parton level by correction factors obtained from different MC samples for different bins in Q^2 using the default DIS and jet selection.*

$\Lambda^4_{QCD} =$:	Q^2-range [GeV²]	bin 1 $44\ldots56$	bin 2 $56\ldots80$	bin 3 $80\ldots160$	bin 4 $160\ldots320$	bin 5 $320\ldots640$	bin 6 $640\ldots3600$
100 MeV :	$d\sigma^{tot}_{DIS}/dQ^2$ [pb/GeV²]	226 ± 65	127 ± 26	40.3 ± 4.5	8.72 ± 0.69	1.79 ± 0.10	0.0899 ± 0.0017
	: $d\sigma^{(2+1)}_{DIS}/dQ^2$ [pb/GeV²]	12.4 ± 3.6	7.2 ± 1.5	1.99 ± 0.22	0.318 ± 0.026	0.0461 ± 0.0028	0.001652 ± 0.000059
	: (2+1)-jet rate R_{2+1} [%]	5.485 ± 0.088	5.661 ± 0.080	4.949 ± 0.060	3.642 ± 0.071	2.579 ± 0.057	1.837 ± 0.056
200 MeV :	$d\sigma^{tot}_{DIS}/dQ^2$ [pb/GeV²]	222 ± 64	124 ± 25	39.5 ± 4.4	8.58 ± 0.68	1.755 ± 0.098	0.0889 ± 0.0017
	: $d\sigma^{(2+1)}_{DIS}/dQ^2$ [pb/GeV²]	15.3 ± 4.4	8.4 ± 1.7	2.36 ± 0.27	0.372 ± 0.030	0.0529 ± 0.0034	0.001848 ± 0.000063
	: (2+1)-jet rate R_{2+1} [%]	6.90 ± 0.12	6.82 ± 0.11	5.97 ± 0.11	4.338 ± 0.076	3.016 ± 0.095	2.080 ± 0.060
300 MeV :	$d\sigma^{tot}_{DIS}/dQ^2$ [pb/GeV²]	217 ± 63	122 ± 25	38.9 ± 4.3	8.45 ± 0.67	1.739 ± 0.098	0.0876 ± 0.0017
	: $d\sigma^{(2+1)}_{DIS}/dQ^2$ [pb/GeV²]	17.7 ± 5.1	9.8 ± 2.0	2.65 ± 0.30	0.410 ± 0.033	0.0576 ± 0.0039	0.00203 ± 0.00011
	: (2+1)-jet rate R_{2+1} [%]	8.15 ± 0.18	8.03 ± 0.14	6.83 ± 0.12	4.857 ± 0.093	3.31 ± 0.12	2.32 ± 0.12
400 MeV :	$d\sigma^{tot}_{DIS}/dQ^2$ [pb/GeV²]	215 ± 62	120 ± 24	38.4 ± 4.3	8.31 ± 0.66	1.719 ± 0.096	0.0866 ± 0.0016
	: $d\sigma^{(2+1)}_{DIS}/dQ^2$ [pb/GeV²]	19.5 ± 5.6	11.2 ± 2.3	2.87 ± 0.33	0.461 ± 0.038	0.0598 ± 0.0037	0.002154 ± 0.000080
	: (2+1)-jet rate R_{2+1} [%]	9.06 ± 0.18	9.39 ± 0.18	7.48 ± 0.21	5.54 ± 0.12	3.479 ± 0.097	2.487 ± 0.081
600 MeV :	$d\sigma^{tot}_{DIS}/dQ^2$ [pb/GeV²]	209 ± 60	116 ± 24	37.5 ± 4.2	8.17 ± 0.65	1.690 ± 0.095	0.0851 ± 0.0016
	: $d\sigma^{(2+1)}_{DIS}/dQ^2$ [pb/GeV²]	23.0 ± 6.7	12.8 ± 2.6	3.31 ± 0.37	0.502 ± 0.043	0.0682 ± 0.0044	0.00232 ± 0.00012
	: (2+1)-jet rate R_{2+1} [%]	11.0 ± 0.36	11.0 ± 0.27	8.83 ± 0.16	6.15 ± 0.19	4.03 ± 0.13	2.73 ± 0.13
800 MeV :	$d\sigma^{tot}_{DIS}/dQ^2$ [pb/GeV²]	203 ± 59	114 ± 23	36.6 ± 4.1	8.00 ± 0.63	1.666 ± 0.094	0.0842 ± 0.0016
	: $d\sigma^{(2+1)}_{DIS}/dQ^2$ [pb/GeV²]	28.0 ± 8.1	14.7 ± 3.0	3.80 ± 0.43	0.566 ± 0.047	0.0752 ± 0.0067	0.00254 ± 0.00013
	: (2+1)-jet rate R_{2+1} [%]	13.80 ± 0.35	12.91 ± 0.29	10.39 ± 0.20	7.08 ± 0.17	4.52 ± 0.31	3.02 ± 0.14

(header spanning all bin columns: **MEPJET version 2.0 predictions using GRV(HO)**)

Table D.1: *MEPJET version 2.0 predictions of total DIS cross sction $d\sigma^{tot}_{DIS}/dQ^2$, exclusive (2+1)-jet cross section $d\sigma^{(2+1)}_{DIS}/dQ^2$ and the derived (2+1)-jet rate R_{2+1} using the PDF GRV(HO).*

Appendix D

The MEPJET Predictions

This chapter gives the numerical results of the NLO predictions obtained with MEPJET version 2.0. This version was slightly modified with respect to the original code provided by [MZ97b]. The default behavior is that MEPJET gets the value of Λ_{QCD}, i.e. the value of α_s, from the selected parton density function (PDF) to use it internally for the matrix element calculations. In order to provide predictions for different values of α_s the possibility was added to override the value of Λ_{QCD} obtained from the PDF from the usual input card file.

For each of the chosen bins in the phase space a set of predictions was obtained for the six values of $\Lambda^4_{QCD} = 100, 200, 300, 400, 600, 800$ MeV. With the defined default phase space cuts of this analysis the predictions for the total DIS cross section was obtained. By the application of the KTCLUS implementation of the exclusive $K_\perp$ jet finding algorithm and the default jet selection the exclusive (2+1)-jet cross section was calculated. The errors quoted with the cross section predictions are the numerical uncertainties as they were given by MEPJET.

From the calculated cross sections the (2+1)-jet rate R_{2+1} is derived and given in addition. The errors are calculated by error propagation.

The MEPJET predictions were calculated with three different parton density functions: GRV(HO), which was taken as default in this analysis, MRSA and CTEQ4M, which were used for systematic checks. These three sets of results are listed in the following tables. Not listed here are the results on the variation of the jet finding parameters and jet selection cuts which had to be calculated for various additional systematic checks.

MEPJET version 2.0 predictions using CTEQ4M						
	bin 1	bin 2	bin 3	bin 4	bin 5	bin 6
$\Lambda^4_{QCD} = :$ Q^2-range [GeV^2]	44...56	56...80	80...160	160...320	320...640	640...3600
100 MeV : $d\sigma^{tot}_{DIS}/dQ^2$ [pb/GeV^2]	236±68	133±27	42.7±4.8	9.23±0.73	1.88±0.11	0.0946±0.0018
: $d\sigma^{(2+1)}_{DIS}/dQ^2$ [pb/GeV^2]	11.2±3.3	6.5±1.3	1.86±0.21	0.303±0.024	0.0435±0.0027	0.001535±0.000049
: (2+1)-jet rate R_{2+1} [%]	4.77±0.10	4.92±0.11	4.363±0.056	3.287±0.051	2.310±0.063	1.622±0.043
200 MeV : $d\sigma^{tot}_{DIS}/dQ^2$ [pb/GeV^2]	233±67	132±27	42.3±4.7	9.18±0.73	1.87±0.10	0.0944±0.0018
: $d\sigma^{(2+1)}_{DIS}/dQ^2$ [pb/GeV^2]	13.8±4.0	8.0±1.6	2.16±0.24	0.352±0.030	0.0501±0.0032	0.001802±0.000063
: (2+1)-jet rate R_{2+1} [%]	5.91±0.12	6.06±0.10	5.117±0.077	3.84±0.12	2.683±0.085	1.908±0.058
300 MeV : $d\sigma^{tot}_{DIS}/dQ^2$ [pb/GeV^2]	232±67	131±27	41.9±4.7	9.11±0.72	1.86±0.10	0.0939±0.0018
: $d\sigma^{(2+1)}_{DIS}/dQ^2$ [pb/GeV^2]	15.6±4.5	8.9±1.8	2.43±0.28	0.381±0.033	0.0540±0.0034	0.001976±0.000084
: (2+1)-jet rate R_{2+1} [%]	6.70±0.14	6.80±0.15	5.80±0.13	4.19±0.15	2.908±0.089	2.105±0.081
400 MeV : $d\sigma^{tot}_{DIS}/dQ^2$ [pb/GeV^2]	231±67	130±27	41.7±4.7	9.06±0.72	1.85±0.10	0.0936±0.0018
: $d\sigma^{(2+1)}_{DIS}/dQ^2$ [pb/GeV^2]	17.4±5.1	10.2±2.1	2.72±0.31	0.402±0.037	0.0575±0.0040	0.00208±0.00014
: (2+1)-jet rate R_{2+1} [%]	7.55±0.27	7.86±0.15	6.53±0.11	4.44±0.21	3.11±0.13	2.23±0.15
600 MeV : $d\sigma^{tot}_{DIS}/dQ^2$ [pb/GeV^2]	229±66	128±26	41.3±4.6	8.95±0.71	1.84±0.10	0.0921±0.0018
: $d\sigma^{(2+1)}_{DIS}/dQ^2$ [pb/GeV^2]	21.2±6.2	12.1±2.5	3.12±0.36	0.450±0.038	0.0663±0.0043	0.00232±0.00012
: (2+1)-jet rate R_{2+1} [%]	9.28±0.28	9.42±0.22	7.56±0.17	5.03±0.16	3.61±0.12	2.52±0.13
800 MeV : $d\sigma^{tot}_{DIS}/dQ^2$ [pb/GeV^2]	225±65	127±26	41.0±4.6	8.92±0.71	1.82±0.10	0.0919±0.0018
: $d\sigma^{(2+1)}_{DIS}/dQ^2$ [pb/GeV^2]	23.3±6.8	13.5±2.8	3.49±0.40	0.510±0.042	0.0703±0.0055	0.00255±0.00013
: (2+1)-jet rate R_{2+1} [%]	10.38±0.27	10.58±0.25	8.51±0.16	5.72±0.15	3.86±0.21	2.77±0.13

Table D.3: *MEPJET version 2.0 predictions of total DIS cross sction $d\sigma^{tot}_{DIS}/dQ^2$, exclusive (2+1)-jet cross section $d\sigma^{(2+1)}_{DIS}/dQ^2$ and the derived (2+1)-jet rate R_{2+1} using the PDF CTEQ4M.*

MEPJET version 2.0 predictions using MRSA						
	bin 1	bin 2	bin 3	bin 4	bin 5	bin 6
$\Lambda^4_{QCD} = :$ Q^2-range [GeV^2]	44...56	56...80	80...160	160...320	320...640	640...3600
100 MeV : $d\sigma^{tot}_{DIS}/dQ^2$ [pb/GeV^2]	226±65	127±26	41.0±4.6	9.01±0.71	1.87±0.10	0.0955±0.0018
: $d\sigma^{(2+1)}_{DIS}/dQ^2$ [pb/GeV^2]	11.3±3.3	6.7±1.4	1.89±0.21	0.313±0.025	0.0469±0.0028	0.001726±0.000060
: (2+1)-jet rate R_{2+1} [%]	5.01±0.11	5.254±0.078	4.606±0.063	3.473±0.057	2.510±0.058	1.808±0.053
200 MeV : $d\sigma^{tot}_{DIS}/dQ^2$ [pb/GeV^2]	226±65	127±26	40.7±4.6	8.96±0.71	1.86±0.10	0.0950±0.0018
: $d\sigma^{(2+1)}_{DIS}/dQ^2$ [pb/GeV^2]	13.4±3.9	8.0±1.6	2.24±0.25	0.368±0.030	0.0522±0.0033	0.001928±0.000090
: (2+1)-jet rate R_{2+1} [%]	5.94±0.12	6.29±0.11	5.502±0.075	4.106±0.072	2.800±0.077	2.030±0.088
300 MeV : $d\sigma^{tot}_{DIS}/dQ^2$ [pb/GeV^2]	224±65	126±26	40.6±4.5	8.88±0.70	1.85±0.10	0.0946±0.0018
: $d\sigma^{(2+1)}_{DIS}/dQ^2$ [pb/GeV^2]	15.7±4.5	9.1±1.9	2.52±0.29	0.396±0.032	0.0570±0.0038	0.002036±0.000071
: (2+1)-jet rate R_{2+1} [%]	6.98±0.17	7.23±0.17	6.20±0.12	4.464±0.080	3.08±0.12	2.151±0.065
400 MeV : $d\sigma^{tot}_{DIS}/dQ^2$ [pb/GeV^2]	224±65	125±26	40.4±4.5	8.81±0.70	1.84±0.10	0.0944±0.0018
: $d\sigma^{(2+1)}_{DIS}/dQ^2$ [pb/GeV^2]	17.5±5.1	9.6±2.0	2.75±0.31	0.441±0.036	0.0627±0.0039	0.002203±0.000090
: (2+1)-jet rate R_{2+1} [%]	7.85±0.30	7.66±0.15	6.82±0.13	5.00±0.10	3.404±0.090	2.334±0.085
600 MeV : $d\sigma^{tot}_{DIS}/dQ^2$ [pb/GeV^2]	221±64	124±25	40.0±4.5	8.79±0.70	1.82±0.10	0.0937±0.0018
: $d\sigma^{(2+1)}_{DIS}/dQ^2$ [pb/GeV^2]	20.0±5.8	11.4±2.3	3.25±0.37	0.491±0.040	0.0672±0.0044	0.002355±0.000093
: (2+1)-jet rate R_{2+1} [%]	9.02±0.23	9.14±0.24	8.13±0.15	5.59±0.13	3.69±0.13	2.515±0.090
800 MeV : $d\sigma^{tot}_{DIS}/dQ^2$ [pb/GeV^2]	220±64	123±25	39.8±4.4	8.74±0.70	1.81±0.10	0.0928±0.0018
: $d\sigma^{(2+1)}_{DIS}/dQ^2$ [pb/GeV^2]	23.3±6.7	13.3±2.7	3.59±0.41	0.529±0.044	0.0764±0.0054	0.00259±0.00011
: (2+1)-jet rate R_{2+1} [%]	10.55±0.29	10.77±0.25	9.02±0.18	6.05±0.16	4.23±0.18	2.80±0.11

Table D.2: *MEPJET version 2.0 predictions of total DIS cross sction $d\sigma^{tot}_{DIS}/dQ^2$, exclusive (2+1)-jet cross section $d\sigma^{(2+1)}_{DIS}/dQ^2$ and the derived (2+1)-jet rate R_{2+1} using the PDF MRSA.*

α_s from $\sigma^{(2+1)}$ using ZEUS 1995 data, ARIADNE4.08, GRV(HO)							
	bin 1	bin 2	bin 3	bin 4	bin 5	bin 6	total
Q^2-range	44...56	56...80	80...160	160...320	320...640	640...3600	44...3600
$\langle Q^2 \rangle$ [GeV^2]	50	66	110	219	435	1128	140
$\alpha_s(Q^2)$	0.231±0.043	0.229±0.031	0.224±0.017	0.203±0.012	0.148±0.016	0.146±0.018	0.2064±0.0030
$\alpha_s(M_z^2)$	0.130±0.012	0.1326±0.0090	0.1368±0.0058	0.1366±0.0053	0.1156±0.0095	0.123±0.013	0.1330±0.0012
$\Lambda^4_{\mathrm{QCD,\overline{MS}}}$ [MeV]	560±300	620±240	730±170	720±150	290±170	410±280	631±29
$\Lambda^5_{\mathrm{QCD,\overline{MS}}}$ [MeV]	420±260	470±210	560±150	550±130	200±130	290±230	475±25

α_s from $\sigma^{(2+1)}$ using ZEUS 1996 data, ARIADNE4.08, GRV(HO)							
	bin 1	bin 2	bin 3	bin 4	bin 5	bin 6	total
Q^2-range	44...56	56...80	80...160	160...320	320...640	640...3600	80...3600
$\langle Q^2 \rangle$ [GeV^2]	50	66	110	219	435	1128	218
$\alpha_s(Q^2)$	±	±	0.235±0.018	0.212±0.012	0.191±0.012	0.151±0.017	0.2112±0.0035
$\alpha_s(M_z^2)$	±	±	0.1405±0.0058	0.1408±0.0050	0.1393±0.0063	0.126±0.011	0.1402±0.0015
$\Lambda^4_{\mathrm{QCD,\overline{MS}}}$ [MeV]	±	±	830±180	840±150	800±190	480±270	826±44
$\Lambda^5_{\mathrm{QCD,\overline{MS}}}$ [MeV]	±	±	650±160	660±140	620±170	350±230	643±38

Table E.1: $\alpha_s(Q^2)$ and $\alpha_s(M_z^2)$ from exclusive (2+1)-jet cross section $\sigma^{(2+1)}$ using ZEUS 1995 & 1996 data, ARIADNE4.08 for the correction and GRV(HO) in MEPJET. To correct the ZEUS 1996 data the 1996 sample of ARIADNE4.08 was used. Also given are the corresponding values for Λ^4_{QCD} and Λ^5_{QCD} in the $\overline{MS}$ renormalization scheme. Only statistical errors are quoted.

fits to the results on α_s in bins of Q^2			
sample	$\langle Q^2 \rangle$	α_s	χ^2/dof
constant α_s assumed			
ZEUS 1995	140 GeV^2	0.1886±0.0074	4.0/5
ZEUS 1996	218 GeV^2	0.1979±0.0070	4.7/3
running α_s assumed			
ZEUS 1995	8315 GeV^2	0.1326±0.0031	0.98/5
ZEUS 1996	8315 GeV^2	0.1392±0.0031	0.49/3

Table E.2: Fits to the results on α_s from the exclusive (2+1)-jet cross section $\sigma^{(2+1)}$ in bins of Q^2 in order to judge on the running of α_s using ARIADNE4.08 for the correction.

Appendix E

Further Results on α_s

This chapter contains the numerical results of the approaches to determine α_s which turned out to exhibit some problems, preventing the results to be taken as reliable. The following explicit listing of these results is given here for completeness. The behavior of these results is discussed in the sections 10.3 and 10.4. In detail, the results given are for:

• the determination of α_s from the differential exclusive (2+1)-jet section $d\sigma^{(2+1)}_{DIS}/dQ^2$ using the ZEUS 1995 & 1996 data,

• the corresponding fit results to judge on the tendency of the data to support the running of α_s and

• the determination of α_s from the differential rate D_2 using the ZEUS 1995 data, performing the jet finding around the two center values $\langle y_{cut} \rangle = 0.45$ and $\langle y_{cut} \rangle = 0.55$ of the jet resolution parameter ($\Delta y_{cut} = 0.1$).

Appendix F

Results with correction by LEPTO6.3tuned

This chapter summarizes the results obtained for the determination of α_s from the exclusive (2+1)-jet rate R_{2+1} by utilizing the LEPTO6.3$^{\text{tuned}}$ MC for the correction of the ZEUS 1995 data. As the exchange of the ARIADNE4.08 to the LEPTO6.3$^{\text{tuned}}$ MC model provides the largest contribution to the systematic errors of this analysis, it was decided to work out a complete analysis using the LEPTO6.3$^{\text{tuned}}$ model including all systematic checks in order to see whether here a different behavior can be found. This is discussed in the sections 10.2.1 and 11.5.1.

The results are presented in complete analogy to the results of the default analysis and comprise:

- the table with the numerical results on α_s,
- the table with the fit results to judge on the tendency of the data to support the running of α_s,
- the table with the systematic uncertainties,
- the plot showing graphically the systematic errors on α_s in the full phase space of the analysis,
- the plot showing graphically the systematic errors on α_s in the bins of Q^2,
- the plot showing the final results on $\alpha_s(Q^2)$ and $\alpha_s(M_z^2)$ including the statistical and the total errors.

α_s from D_2 using ZEUS 1995 data, ARIADNE4.08, GRV(HO): $\langle y_{cut} \rangle = 0.45$, $\Delta y_{cut} = 0.1$							
	bin 1	bin 2	bin 3	bin 4	bin 5	bin 6	total
Q^2-range	$44\ldots56$	$56\ldots80$	$80\ldots160$	$160\ldots320$	$320\ldots640$	$640\ldots3600$	$44\ldots3600$
$\langle Q^2 \rangle$ [GeV^2]	50	66	110	219	435	1128	140
$\alpha_s(Q^2)$	$\pm$	0.236 ± 0.063	0.197 ± 0.028	0.195 ± 0.032	0.160 ± 0.023	0.164 ± 0.027	0.218 ± 0.031
$\alpha_s(M_z^2)$	$\pm$	0.135 ± 0.017	0.126 ± 0.010	0.133 ± 0.013	0.123 ± 0.013	0.135 ± 0.017	0.137 ± 0.011
$\Lambda^4_{\text{QCD},\overline{\text{MS}}}$ [MeV]	$\pm$	680 ± 510	480 ± 250	640 ± 380	410 ± 290	680 ± 530	750 ± 330
$\Lambda^5_{\text{QCD},\overline{\text{MS}}}$ [MeV]	$\pm$	510 ± 460	350 ± 210	480 ± 340	290 ± 240	520 ± 470	570 ± 290

α_s from D_2 using ZEUS 1995 data, ARIADNE4.08, GRV(HO): $\langle y_{cut} \rangle = 0.55$, $\Delta y_{cut} = 0.1$							
	bin 1	bin 2	bin 3	bin 4	bin 5	bin 6	total
Q^2-range	$44\ldots56$	$56\ldots80$	$80\ldots160$	$160\ldots320$	$320\ldots640$	$640\ldots3600$	$44\ldots3600$
$\langle Q^2 \rangle$ [GeV^2]	50	66	110	219	435	1128	140
$\alpha_s(Q^2)$	0.167 ± 0.056	0.169 ± 0.039	0.197 ± 0.022	0.162 ± 0.023	$\pm$	0.127 ± 0.047	0.168 ± 0.020
$\alpha_s(M_z^2)$	0.108 ± 0.020	0.111 ± 0.015	0.1268 ± 0.0084	0.117 ± 0.011	$\pm$	0.109 ± 0.033	0.1164 ± 0.0091
$\Lambda^4_{\text{QCD},\overline{\text{MS}}}$ [MeV]	180 ± 320	210 ± 240	490 ± 200	310 ± 220	$\pm$	200 ± 670	300 ± 160
$\Lambda^5_{\text{QCD},\overline{\text{MS}}}$ [MeV]	120 ± 250	140 ± 190	360 ± 170	220 ± 170	$\pm$	130 ± 550	210 ± 130

Table E.3: $\alpha_s(Q^2)$ and $\alpha_s(M_z^2)$ from differential (2+1)-jet rate D_2 using ZEUS 1995 data, ARIADNE4.08 for the correction and GRV(HO) in MEPJET. Also given are the corresponding values for Λ^4_{QCD} and Λ^5_{QCD} in the $\overline{\text{MS}}$ renormalization scheme. Only statistical errors are quoted.

systematic errors on α_s from R_{2+1} using ZEUS 1995 data, LEPTO6.3, GRV(HO)							
	bin 1	bin 2	bin 3	bin 4	bin 5	bin 6	total
Q^2-range	44...56	56...80	80...160	160...320	320...640	640...3600	44...3600
$\langle Q^2 \rangle$ [GeV²]	50	66	110	219	435	1128	140
$\alpha_s(M_z^2)$	0.1138	0.1166	0.1172	0.1163	0.0985	0.1332	0.1158
statistical error $\quad ^{stat}\Delta\alpha_s$	±0.0016	±0.0016	±0.0016	±0.0027	±0.0094	±0.0077	±0.0012
experimental uncertainty $\quad ^{exp}\Delta\alpha_s$	$^{+0.0025}_{-0.00097}$	$^{+0.0025}_{-0.00084}$	$^{+0.0024}_{-0.0017}$	$^{+0.0032}_{-0.0014}$	$^{+0.0055}_{-0.018}$	$^{+0.0042}_{-0.011}$	$^{+0.0023}_{-0.00086}$
jet finding uncertainty $\quad ^{jet}\Delta\alpha_s$	$^{+0.0072}_{-0.00}$	$^{+0.0036}_{-0.00}$	$^{+0.0026}_{-0.0046}$	$^{+0.0054}_{-0.0040}$	$^{+0.0089}_{-0.0094}$	$^{+0.0051}_{-0.0062}$	$^{+0.0044}_{-0.00}$
hard scale uncertainty $\quad ^{scale}\Delta\alpha_s$	$^{+0.010}_{-0.00}$	$^{+0.0056}_{-0.0013}$	$^{+0.0034}_{-0.00}$	$^{+0.014}_{-0.011}$	$^{+0.031}_{-0.00}$	$^{+0.025}_{-0.031}$	$^{+0.0045}_{-0.0018}$
theoretical uncertainty $\quad ^{theo}\Delta\alpha_s$	$^{+0.010}_{-0.0012}$	$^{+0.0089}_{-0.0013}$	$^{+0.0092}_{-0.0015}$	$^{+0.012}_{-0.00013}$	$^{+0.012}_{-0.0089}$	$^{+0.0075}_{-0.015}$	$^{+0.0094}_{-0.0012}$
systematic error $\quad ^{syst}\Delta\alpha_s$	$^{+0.016}_{-0.0015}$	$^{+0.011}_{-0.0020}$	$^{+0.010}_{-0.0051}$	$^{+0.012}_{-0.012}$	$^{+0.035}_{-0.022}$	$^{+0.027}_{-0.037}$	$^{+0.012}_{-0.0023}$
total error $\quad ^{tot}\Delta\alpha_s$	$^{+0.016}_{-0.0022}$	$^{+0.011}_{-0.0026}$	$^{+0.011}_{-0.0053}$	$^{+0.019}_{-0.012}$	$^{+0.036}_{-0.024}$	$^{+0.028}_{-0.038}$	$^{+0.012}_{-0.0026}$

Table F.3: *Systematic errors on $\alpha_s(M_z^2)$ from exclusive (2+1)-jet rate R_{2+1} using ZEUS 1995 data, LEPTO6.3 for the correction and GRV(HO) in MEPJET. The errors are added in quadrature.*

α_s from R_{2+1} using ZEUS 1995 data, LEPTO6.3^{tuned}, GRV(HO)							
	bin 1	bin 2	bin 3	bin 4	bin 5	bin 6	total
Q^2-range	44...56	56...80	80...160	160...320	320...640	640...3600	44...3600
$\langle Q^2 \rangle$ [GeV²]	50	66	110	219	435	1128	140
$\alpha_s(Q^2)$	0.1826±0.0044	0.1838±0.0041	0.1746±0.0037	0.1600±0.0052	0.121±0.015	0.161±0.012	0.1668±0.0026
$\alpha_s(M_z^2)$	0.1138±0.0016	0.1166±0.0016	0.1172±0.0016	0.1163±0.0027	0.0985±0.0094	0.1332±0.0077	0.1158±0.0012
$\Lambda^4_{QCD,\overline{MS}}$ [MeV]	260±24	302±25	313±27	298±43	99±87	640±210	290±19
$\Lambda^5_{QCD,\overline{MS}}$ [MeV]	177±18	209±20	217±21	206±33	61±61	480±180	199±14

Table F.1: *$\alpha_s(Q^2)$ and $\alpha_s(M_z^2)$ from exclusive (2+1)-jet rate R_{2+1} using ZEUS 1995 data, LEPTO6.3^{tuned} for the correction and GRV(HO) in MEPJET. Also given are the corresponding values for Λ^4_{QCD} and Λ^5_{QCD} in the $\overline{MS}$ renormalization scheme. Only statistical errors are quoted.*

fits to the results on α_s in bins of Q^2			
sample	$\langle Q^2 \rangle$	α_s	χ^2/dof
constant α_s assumed			
ZEUS 1995	140 GeV²	0.1749±0.0021	6.2/5
running α_s assumed			
ZEUS 1995	8315 GeV²	0.1160±0.0010	2.2/5

Table F.2: *Fits to the results on α_s from exclusive (2+1)-jet rate R_{2+1} in bins of Q^2 in order to judge on the running of α_s using LEPTO6.3^{tuned} for the correction.*
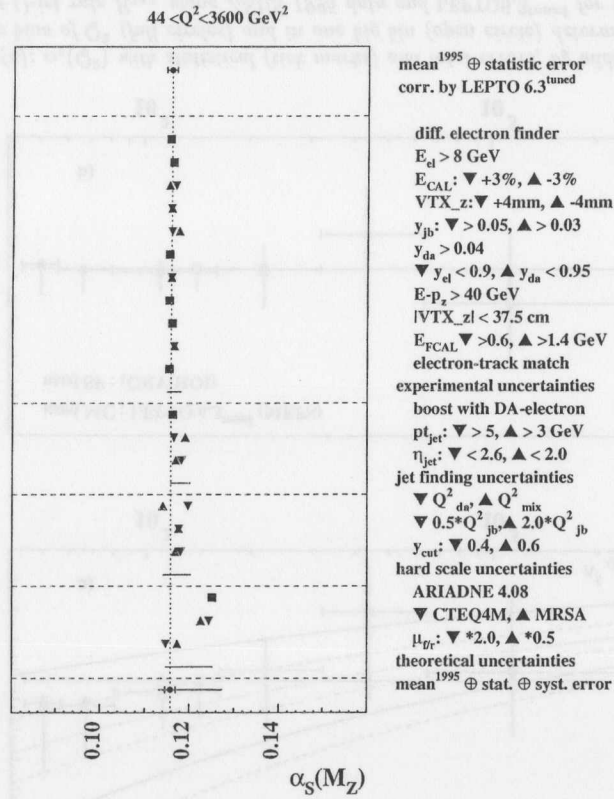
Figure F.1: *Summary of systematic checks for the determination of $\alpha_s(M_z^2)$ in one big bin of Q^2 from the exclusive (2+1)-jet rate R_{2+1} using ZEUS 1995 data, LEPTO6.3$^{\text{tuned}}$ for the correction and GRV(HO) in MEPJET.*

Figure F.2: *Summary of systematic checks for the determination of $\alpha_s(M_z^2)$ in six bins of Q^2 from the exclusive (2+1)-jet rate R_{2+1} using ZEUS 1995 data, LEPTO6.3$^{\text{tuned}}$ for the correction and GRV(HO) in MEPJET.*
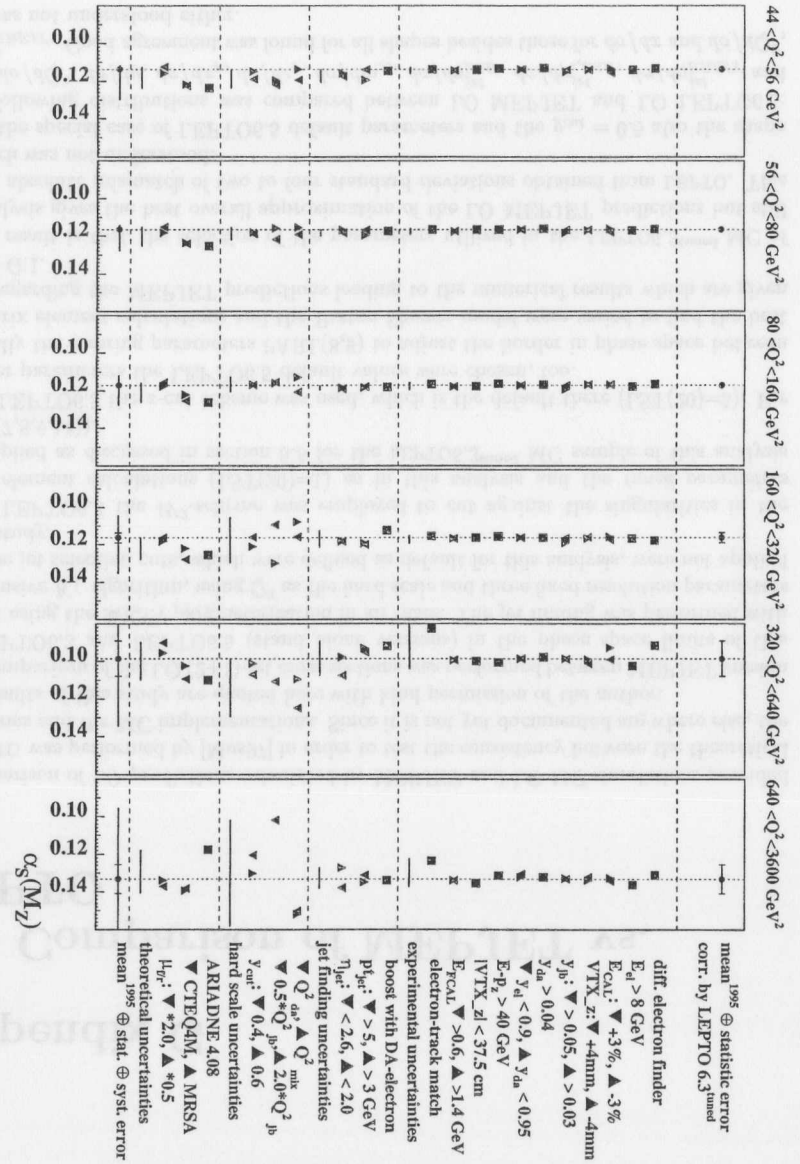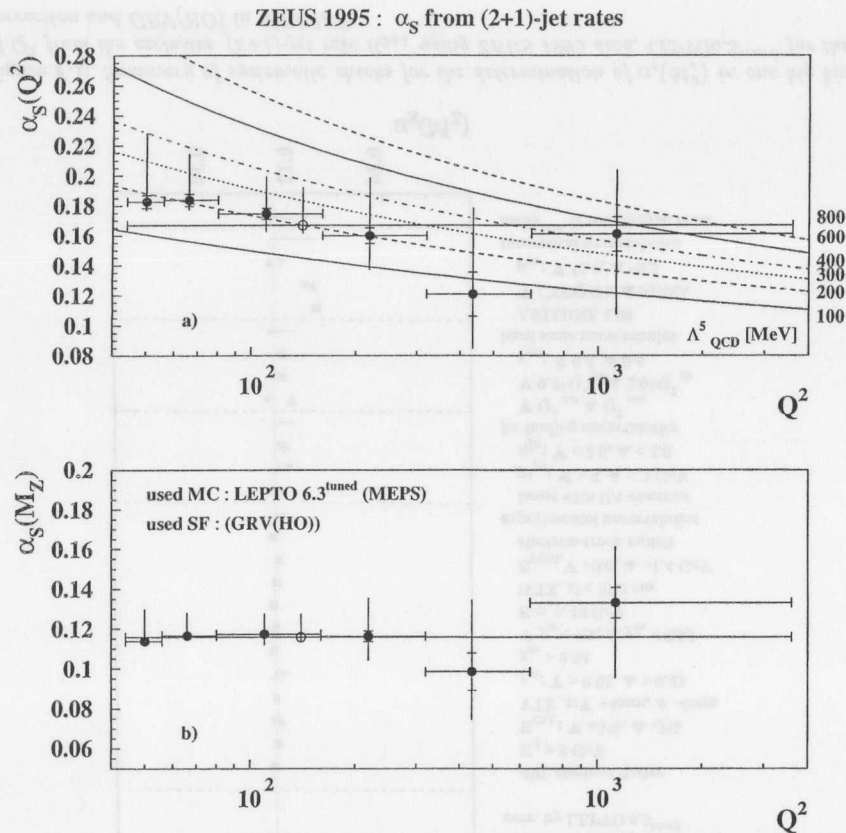
Figure F.3: *(a): $\alpha_s(Q^2)$ with statistical (tick marks) and total errors, by addition in quadrature, in six bins of Q^2 (full circles) and in one big bin (open circle) determined from the exclusive (2+1)-jet rate R_{2+1} using ZEUS 1995 data and LEPTO6.3^tuned for the correction and GRV(HO) in MEPJET. (b): the same data evolved to $\alpha_s(M_z^2)$.*

Appendix G

LO Comparison of MEPJET vs. LEPTO

A comparison of LO predictions calculated by MEPJET and LO MC simulations provided by LEPTO was performed by [Mus97] in order to test the consistency between the theoretical predictions and the MC implementations. Since it is not yet documented anywhere else, the main results of this study are quoted here with kind permission of the author.

A comparison of the LO (2+1)-jet cross sections was performed between MEPJET version 1.4, LEPTO6.3 and LEPTO6.5 (stand alone versions) in the phase space limits of this analysis using the MRSA parameterization in all cases. The jet finding was performed with the exclusive $K_\perp$ algorithm, using Q^2 as the hard scale and three fixed resolution parameters y_{cut}. The jet selection cuts, which were defined as default for this analysis, were not applied in this study.

For LEPTO6.3 the W^2-scheme was employed to cut against the singularities in the matrix element calculations (LST(20)=1) as in this analysis and the *tuned parameters* were applied as discussed in section 8.5 for the LEPTO6.3^tuned MC sample of this analysis (PARL(7,8,9,14)).

For LEPTO6.5 the z-cut scheme was used, which is the default there (LST(20)=5). For the other parameters the LEPTO6.5 default values were chosen, too.

Finally the steering parameters PARL(8,9) to adjust the border in phase space between the matrix element calculations and the Parton Shower model were varied to find the best match regarding the MEPJET predictions leading to the numerical results which are given in table G.1.

The result is that the selection of the parameters utilized in the LEPTO6.3^tuned MC of this analysis gives the best overall approximation of the LO MEPJET predictions but still with an absolute mismatch of two to four standard deviations obtained from LEPTO. This mismatch was not understood.

For the special case of LEPTO6.5 default parameters and the $y_{cut} = 0.5$ also the shape of the following distributions was compared between LO MEPJET and LO LEPTO6.5: $d\sigma/dx$, $d\sigma/dQ^2$, $d\sigma/dy$, $d\sigma/dx_p$, $d\sigma/dz_p$, $d\sigma/dm_{jj}$, $d\sigma/d\eta_{LAB}^{jet}$, $d\sigma/dp_{t,LAB}^{jet}$, $d\sigma/d\eta_{BREIT}^{jet}$ and $d\sigma/dp_{t,BREIT}^{jet}$. Good agreement was found for all shapes besides those for $d\sigma/dx$ and $d\sigma/dQ^2$, which was not understood either.

generator			absolute (2+1)-jet cross section [nb]		
	PARL(8)	PARL(9)	$y_{cut} = 0.3$	$y_{cut} = 0.5$	$y_{cut} = 0.8$
MEPJET			1481±	785±	390±
LEPTO6.3	0.005	4.0	1435±25	839±19	446±14
LEPTO6.3 ‡	0.005	2.0	1435±25	839±19	446±14
LEPTO6.3	0.005	1.0	1435±25	839±19	446±14
LEPTO6.3	0.005	0.5	1435±25	839±19	446±14
LEPTO6.3	0.005	0.1	1435±25	839±19	446±14
LEPTO6.3	0.001	2.0	1820±28	937±20	462±14
LEPTO6.3	0.0005	2.0	1883±28	962±20	479±14
LEPTO6.3	0.0005	0.5	2270±28	965±20	477±14
LEPTO6.3 †	0.0001	2.0	1914±28	935±20	459±14
LEPTO6.3	0.0001	1.0	1912±28	954±20	465±14
LEPTO6.5	0.15	2.0	1560±25	788±18	381±12
LEPTO6.5	0.15	1.0	1526±25	749±18	364±12
LEPTO6.5	0.15	0.5	1530±25	736±18	367±12
LEPTO6.5	0.1	2.0	1702±27	853±19	428±13
LEPTO6.5	0.1	1.0	1699±27	841±19	433±13
LEPTO6.5	0.1	0.5	1618±26	795±18	400±13
LEPTO6.5 †	0.04	4.0	1873±18	915±20	458±14
LEPTO6.5	0.04	0.1	1618±18	794±18	395±13
LEPTO6.5	0.01	4.0	1903±28	942±20	494±14
LEPTO6.5	0.01	2.0	1843±27	918±19	488±14
LEPTO6.5	0.01	0.5	1724±27	875±19	440±13
LEPTO6.5	0.01	0.1	1596±26	798±18	388±12

Table G.1: *Comparison of the LO (2+1)-jet cross sections between MEPJET version 1.4, LEPTO6.3 and LEPTO6.5, by [Mus97]. Here † denotes the corresponding default parameters of the release version of LEPTO and ‡ the tuned parameters applied to the* LEPTO6.3[tuned] *MC used in this analysis. Not that LEPTO6.3 was run with LST(20)=1, while LEPTO6.5 was run with LST(20)=5. See text for other conditions.*

Bibliography

[A+91]   A. Andresen et al. Response of a uranium-scintillator calorimeter to electrons, pion and protons in the momentum range 0.5-10 GeV/c. *Nucl. Inst. Meth.*, A309:101, 1991.

[A+97]   P. Abreu et al. Measurement of event shape and inclusive distributions at $\sqrt{s} = $ 130 GeV and 136 GeV. *Z. Phys.*, C73:229, 1997. for DELPHI-Collaboration, CERN-PPE-96-130.

[ABF+92] U. Amaldi, W. de Boer, P. H. Frampton, H. Fürstenau, and J. T. Liu. Consistency checks of grand unified theories. *Phys. Lett.*, B281:374, 1992. CERN-PPE-91-233.

[ACS95]   H. Abramowicz, A. Caldwell, and R. Sinkus. Neural network based electron identification in the ZEUS calorimeter. *Nucl. Inst. Meth.*, A365:508, 1995. DESY-95-054,hep-ex/9505004.

[ADKT85] Ya. I. Azimov, Yu. L. Dokshitser, V. A. Khoze, and S. I. Troian. The string effect and QCD coherence. *Phys. Lett.*, B165:147, 1985.

[AGIS83] B. Andersson, G. Gustafson, G. Ingelman, and T. Sjöstrand. Parton fragmentation and string dynamics. *Phys. Rept.*, 97:31, 1983. LU-TP-83-10.

[AGLP89] B. Andersson, G. Gustafson, L. Lönnblad, and U. Pettersson. Coherence effects in deep inelastic scattering. *Z. Phys.*, C43:625, 1989. LU-TP-88-14.

[AP77]   G. Altarelli and G. Parisi. Asymptotic freedom in parton language. *Nucl. Phys.*, B126:298, 1977. LPTENS 77-6.

[AQ98]   O. Ruske A. Quadt. A new method to measure vertex distributions, 1998. ZEUS Note 98-036.

[B+87]   W. Bartel et al. Determination of semimuonic branching ratios and fragmentation functions of heavy quarks in e^+e^- annihilation at $\sqrt{s} = 34.6$ GeV . *Z. Phys.*, C33:23, 1987. for JADE-Collaboration, DESY-86-129.

[B+88]   S. Bethke et al. Experimental investigation of the energy dependence of the strong coupling strength. *Phys. Lett.*, B213:235, 1988. for JADE-Collaboration, DESY-88-105.

[B+93a]   B. Bernstein et al. Beam tests of the ZEUS barrel calorimeter. *Nucl. Inst. Meth.*, A336:23, 1993.

[B+93b]   H. Boterenbrood et al. A two-transputer VME module for data acquisition and online event selection in ZEUS. *Nucl. Inst. Meth.*, A332:263, June 1993. NIKHEF-H-01-1993A.

[B+96]   P. N. Burrows et al. Prospects for the precision measurement of α_s. *hep-ex/9612012*, 1996. Presented at 1996 DPF / DPB Summer Study on New Directions for High-Energy Physics (Snowmass 96), Snowmass, CO, 25 Jun - 12 Jul 1996, SLAC-PUB-7371.

[BEK91]   S. Betvelsen, J. Engelen, and P. Kooijman. Reconsruction of (x, Q^2) and extraction of structure functions in neutral current scattering at HERA. In W. Buchmüller and G. Ingelman, editors, *Proceedings of the Workshop 'Physics at HERA'*, volume 1, page 23, Notkestraße 85, D-22607 Hamburg, Germany, October 1991. DESY.

[Bet95]   S. Bethke. Summary of α_s measurements. *Nucl. Phys. Proc. Suppl.*, 39BC:198, 1995. PITHA-94-30, QCD 94, Montpellier, France, Jul 7-13, 1994.

[BHV93]   U. Behrens, L. Hagge, and W. O. Vogel. The eventbuilder of the ZEUS experiment. *Nucl. Inst. Meth.*, A332:253, February 1993. DESY-93-008.

[BIS87]   M. Bengtsson, G. Ingelman, and T. Sjöstrand. Parton cascade evolution and event structure at HERA. In R. D. Peccei, editor, *Proceedings of the HERA Workshop*, volume 1, page 149, Notkestraße 85, D-22607 Hamburg, Germany, August 1987. DESY.

[BK92]   T. Brodkorb and J.G. Korner. Lepton-hadron correlations to $\mathcal{O}(\alpha_s^2)$ in (2+1) jet production at electron-proton colliders. *Z. Phys.*, C54:519, 1992. DESY-91-147.

[BKP96]   M. Botje, M. Klein, and C. Pascaud. Future precision measurements of $F_2(x, Q^2)$, $\alpha_s(Q^2)$ and $xg(x, Q^2)$ at HERA. In G. Ingelman, A. De Roeck, and R. Klanner, editors, *Proceedings of the Workshop 'Future Physics at HERA'*, volume 1, page 33, Notkestraße 85, D-22607 Hamburg, Germany, September 1996. DESY.

[BM94]   T. Brodkorb and E. Mirkes. DISJET 1.0: A Monte Carlo program for jet cross-section calculations in deep inelastic scattering, 1994. MAD-PH-821, hep-ph/9404287.

[BM95]   T. Brodkorb and E. Mirkes. Complete $\mathcal{O}(\alpha_s^2)$ in deep inelastic scattering. *Z. Phys.*, C66:141, 1995. MAD-PH-820.

[BN68]   J. D. Bjorken and M. Nauenberg. Current algebra. *Ann. Rev. Nucl. Sci.*, 18:229, 1968. SLAC-PUB-0400.

[Bru87]   R. Brunner. *GEANT 3.13*. CERN, CH-1211 Geneva 23, Switzerland, 1987. CERN DD/EE/84-1.

[BS87]   H.-U. Bengtsson and T Sjöstrand. The Lund Monte Carlo for hadronic processes: PYTHIA version 4.8. *Comput. Phys. Commun.*, 46:43, 1987.

[BS88]   M. Bengtsson and T. Sjöstrand. Parton showers in leptoproduction events. *Z. Phys.*, C37:465, 1988. LU-TP-87-10.

[Bur97]   P. N. Burrows. Review of α_s measurements. *Acta Phys. Pol.*, B28:701, 1997. SLAC-PUB-7293, hep-ex/9612007.

[C+91]   S. Catani et al. New clustering algorithm for multi-jet cross-sections in e^+e^- annihilation. *Phys. Lett.*, B269:432, 1991. CAVENDISH-HEP-91-5.

[CDW92]   S. Catani, Yu. L. Dokshitzer, and B. R. Webber. The $K_\perp$-clustering algorithm for jets in deep inelastic scattering and hadron collisions. *Phys. Lett.*, B285:291, May 1992. CERN-TH-6473-92.

[CR96]   J. Chýla and J. Rameš. On the consistent determination of α_s from jet rates in DIS. In G. Ingelman, A. De Roeck, and R. Klanner, editors, *Proceedings of the Workshop 'Future Physics at HERA'*, volume 1, page 529, Notkestraße 85, D-22607 Hamburg, Germany, September 1996. DESY.

[CS96a]   S. Catani and M. H. Seymour. The dipole formalism for the calculation of QCD jet cross-sections at next-to-leading order. *Phys. Lett.*, B378:287, 1996. CERN-TH-96-28, hep-ph/9602277.

[CS96b]   S. Catani and M. H. Seymour. NLO QCD calculations in DIS at HERA based on the dipole formalism. In G. Ingelman, A. De Roeck, and R. Klanner, editors, *Proceedings of the Workshop 'Future Physics at HERA'*, volume 1, page 519, Notkestraße 85, D-22607 Hamburg, Germany, September 1996. DESY. CERN-TH-96-240, hep-ph/9609521.

[CS97]   S. Catani and M. H. Seymour. A general algorithm for calculating jet cross-sections in NLO QCD. *Nucl. Phys.*, B485:291, 1997. CERN-TH-96-029, hep-ph/9605323, Erratum-ibid.B510:503-504,1997.

[CSZ91]   H. Chaves, R. J. Seifert, and G. Zech. Kinematic fitting of neutral current events. In W. Buchmüller and G. Ingelman, editors, *Proceedings of the Workshop 'Physics at HERA'*, volume 1, page 57, Notkestraße 85, D-22607 Hamburg, Germany, October 1991. DESY.

[D+91]   M. Derrick et al. Design and construction of the ZEUS barrel calorimeter. *Nucl. Inst. Meth.*, A309:77, 1991.

[DDVZ97] W. A. De Wolf, A. T. Doyle, N. Varelas, and D. Zeppenfeld. QCD effects in hadronic final states. In José Repond and Danny Krakauer, editors, *Deep Inelastic Scattering and QCD - 5th international workshop - Chicago, IL April 1997*, number 407 in AIP conference proceedings, page 175. American Institute of Physics, Woodbury, New York, 1997.

[DES95]   DESY. Scientific annual report 1994 of Deutsches Elektronen Synchrotron DESY. Technical report, DESY, July 1995.

[DLMW97] Yu. L. Dokshitzer, G. D. Leder, S. Moretti, and B. R. Webber. Better jet clustering algorithms. *hep-ph/9707323*, 1997. Cavendish-HEP-97/06.

[Dok90]   Yu. L. Dokshitzer, 1990. presented at the Workshop on JET STUDIES at LEP and HERA, Durham England, 1990, (unpublished); see summary by W.J. Styrling, J. Phys G 17. 1572 (1991).

[DW98]   M. Dasgupta and B. R. Webber. Power corrections to event shapes in deep inelastic scattering. *Eur. Phys. J.*, C1:539, 1998. Cavendish-HEP-96/5, hep-ph/9704297.

[EIR96]   A. Edin, G. Ingelman, and J. Rathsman. Soft Color Interactions as the origin of rapidity gaps in DIS. *Phys. Lett.*, B366:371, 1996. TSL-ISV-95-0125, hep-ph/9508386.

[EIR97]   A. Edin, G. Ingelman, and J. Rathsman. Unified description of rapidity gaps and energy flows in DIS final states. *Z. Phys.*, C75:57, 1997. DESY-96-060, hep-ph/9605281.

[EKS92]   S. D. Ellis, Z. Kunszt, and D. E. Soper. Jets at hadron colliders at order α_s^3: A look inside. *Phys. Rev. Lett.*, 69(25):3615, December 1992.

[ES93]   S. D. Ellis and D. E. Soper. Succesive combination jet algorithm for hadron collisions. *Phys. Rev. D*, 48(7):3160, October 1993. CERN-TH.6860/93.

[ESW96]   R. K. Ellis, W. J. Stirling, and B. R. Webber. *QCD and Collider Physics*. Number 8 in Cambrigde Monographs on Particle Physics, Nuclear Physiscs and Cosmology. Cambrige University Press, The Edinburgh Building, Cambridge CB2 2RU, United Kingdom, 1996.

[F$^+$93]   B. Foster et al. The design and construction of the ZEUS central tracking detector. *Nucl. Inst. Meth.*, A338:254, 1993.

[FM90]   B. Flaugher and K. Meier. A compilation of jet finding algorithms. In *Proceedings of '1990 Summer Study on High Energy Physics - Research Directions for the Decade'*, Snowmass, Colorado, 1990. June 25 - July 13.

[FP92]   S. M. Fisher and P. Palazzi. The ADAMO data system. Technical report, CERN, June 1992.

[FW80]   G. C. Fox and S. Wolfram. A model for parton showers in QCD. *Nucl. Phys.*, B168:285, 1980. CALT-68-755.

[GG92]   W. T. Giele and E. W. N. Glover. Higher order corrections to jet cross-sections in e^+e^- annihilation. *Phys. Rev.*, D46:1980, 1992. FERMILAB-PUB-91-100-T.

[GGK93]   W. T. Giele, E. W. N. Glover, and D. A. Kosower. Higher order corrections to jet cross-sections in hadron colliders. *Nucl. Phys.*, B403:633, 1993. FERMILAB-PUB-92-230-T, hep-ph/9302225.

[GP88]   G. Gustafson and U. Pettersson. Dipole formulation of QCD cascades. *Nucl. Phys.*, B306:746, 1988. LU-TP-87-9.

[Gra91]   D. Graudenz. Three jet production in deep inelastic electron-proton scattering to order $\mathcal{O}(\alpha_s^2)$. *Phys. Lett.*, B256:518, 1991. DESY-90-095.

[Gra94]   D. Graudenz. Next-to-leading order QCD corrections to jet cross-sections and jet rates in deeply inelastic electron proton scattering. *Phys. Rev.*, D49:3291, 1994. LBL-34147, hep-ph/9307311.

[Gra95]   D. Graudenz. PROJET: Jet cross sections in deeply inelastic electron proton scattering version 4.1. *Comput. Phys. Commun.*, 92:65, 1995. CERN-TH-7420-94, hep-ph/9408383.

[Gra97]   D. Graudenz. *DISASTER++ 1.0.1*. Paul Scherrer Institut, 5232 Villingen, PSI, Switzerland, 1997. Information and code via WWW *http://wwwcn.cern.ch/ graudenz/disaster.html*, hep-ph/9710244.

[Gre89]   M. G. Green. CERN, 1989.

[GRV95]   M. Glück, E. Reya, and A. Vogt. Dynamical parton distributions of the proton and small x physics. *Z. Phys.*, C67:433, 1995. DO-TH-94-24,.

[Gus86]   G. Gustafson. Dual description of a confined color field. *Phys. Lett.*, B175:453, 1986. LU TP 86-5, Moriond 1986: Hadronic v.2:193 (QCD161:R34:1986:V.2).

[H193]   H1-Collaboration. Measurement of the proton structure function $F_2(x,Q^2)$ in the low x region at HERA. *Nucl. Phys.*, B407:515, 1993. DESY-93-117.

[H195]   H1-Collaboration. Determination of the strong coupling constant from jet rates in deep inelastic scattering. *Phys. Lett.*, B346:415, 1995.

[H197a]   H1-Collaboration. Evolution of *ep* fragmentation and multiplicity distributions in the Breit frame. *Nucl. Phys.*, B504:3, 1997. DESY-97-108, hep-ex/9707005.

[H197b]   H1-Collaboration. Measurement of event shape variables in deep inelastic *ep* scattering. *Phys. Lett.*, B406:256, 1997. DESY-97-098, hep-ex/9706002.

[H198]   H1-Collaboration. Multi-jet event rates in deep inelastic scattering and determination of the strong coupling constant. Abstract 527 for ICHEP98, XXIX International Conference on High Energy Physics, Vancouver, 23-29 July 1998, hep-ex/9807019, 1998.

[H$^+$90]   J. E. Huth et al. Towards a standarization of jet definitions. In *Proceedings of '1990 Summer Study on High Energy Physics - Research Directions for the Decade'*, Snowmass, Colorado, 1990. June 25 - July 13.

[HIJJ94]   V. Hedberg, G. Ingelman, C. Jacobsson, and L. Jönsson. Study of jet reconstruction algorithms for deep-inelastic events at HERA. *Z. Phys.*, C63:49, January 1994.

[HM84]   F. Halzen and A. D. Martin. *Quarks and Leptons: An introductory Course in Modern Particle Physics*. John Wiley & Sons, New York, Chichester, Brisbane, Toronto, Singapore, 1984.

[Hoe91]   K. C. Hoeger. Measurement of x, y, Q^2 in neutral current events. In W. Buchmüller and G. Ingelman, editors, *Proceedings of the Workshop 'Physics at HERA'*, volume 1, page 43, Notkestraße 85, D-22607 Hamburg, Germany, October 1991. DESY.

[Hol97]   B. Holzer, 1997. private comunications.

[HZ89]   K. Hagiwara and D. Zeppenfeld. Amplitudes for multiparton processes involving a current at e^+e^-, $e^\pm p$ and hadron colliders. *Nucl. Phys.*, B313:560, 1989. KEK-TH-199.

[IER95] G. Ingelman, A. Edin, and J. Rathsman. *LEPTO version 6.3 — The Lund Monte Carlo for Deep Inelastic Lepton-Nucleon Scttering*. DESY, Notkestraße 85, D-22607 Hamburg, Germany, August 1995.

[IER96] G. Ingelman, A. Edin, and J. Rathsman. *LEPTO 6.5 — A Monte Carlo Generator for Deep Inelastic Lepton-Nucleon Scttering*. DESY, Notkestraße 85, D-22607 Hamburg, Germany, April 1996. DESY-96-057. Information and code via WWW page *http://www3.tsl.uu.se/thep/lepto/*.

[Ing91] G. Ingelman. LEPTO version 6.1 — the Lund Monte Carlo for deep inelastic lepton-nucleon scttering. In W. Buchmüller and G. Ingelman, editors, *Proceedings of the Workshop 'Physics at HERA '*, volume 3, page 1366, Notkestraße 85, D-22607 Hamburg, Germany, October 1991. DESY.

[IR94] G. Ingelman and J. Rathsman. Renormalization scale uncertainty in the DIS (2+1) jet cross-section. *Z. Phys.*, C63:589, 1994. TSL-ISV-94-0096.

[JAD91] JADE-Collaboration. A comparison of measured jet cross-sections with QCD calculations for e^+e^- annihilation. *Z. Phys.*, C49:29, 1991. DESY-90-089.

[JB+79] F. Jacquet, A. Blondel, et al. Report from the study group on detectors for charged current events. In U. Amaldi, editor, *Hamburg 1979, Proceedings, Study of an ep Facility for Europe*, page 377. DESY 79/48, 1979.

[KMS89] J. G. Körner, E. Mirkes, and G. A. Schuler. QCD jets at HERA I. $O(\alpha_s)$ radiative corrections to electroweak cross sections and jet rates. *Int. J. Mod. Phys. A*, 4(7):1781, 1989.

[Krü92] J. Krüger. *The Uranium Scintillator Calorimeter for the ZEUS Detector at the Electron-Proton Collider HERA*. Habilitationsschrift, Universität Hamburg, DESY, D-22607 Hamburg, Germany, 1992. DESY F35-92-02.

[KS92] Z. Kunszt and D. E. Soper. Calculation of jet cross-sections in hadron collisions at $\mathcal{O}(\alpha_s^3)$. *Phys. Rev.*, D46:192, 1992. OITS-475.

[KSM92] A. Kwiatkowski, H. Spiesberger, and H. J. Mohring. HERACLES: An event generator for *ep* interactions at HERA energies including radiative processes: version 1.0. *Comput. Phys. Commun.*, 69:155, 1992. also DESY HERA Workshop 1991:1294-1310.

[LHK+97] H. L. Lai, J. Huston, S. Kuhlmann, F. Olness, J. Owens, D. Soper, W. K. Tung, and H. Weerts. Improved parton distributions from global analysis of recent deep inelastic scattering and inclusive jet data. *Phys. Rev.*, D55:1280, 1997. MSUHEP-60426, CTEQ-604, hep-ph/9606399.

[Lön92] L. Lönnblad. ARIADNE version 4: A program for simulation of QCD cascades implementing the Color Dipole Model. *Comput. Phys. Commun.*, 71:15, 1992. DESY-92-046.

[Lön95] L. Lönnblad. Rapidity gaps and other final state properties in the color dipole model for deep inelastic scattering. *Z. Phys.*, C65:285, 1995. CERN-TH-7307-94.

[M+92] G. Marchesini et al. HERWIG: A Monte Carlo event generator for simulating Hadron Emission Reactions With interfering Gluons, version 5.1 - april 1991. *Comput. Phys. Commun.*, 67:465, 1992. CAVENDISH-HEP-91-26, DESY-91-048.

[Mag96] S. Magill, 1996. private comunications.

[Mar84] W. J. Marciano. Flavor thresholds and lambda in the modified minimal subtraction prescription. *Phys. Rev.*, D29:580, 1984.

[Mir97a] E. Mirkes. private communications, August 1997.

[Mir97b] E. Mirkes. *Theory of Jets in Deep Inelastic Scattering*. Habilitationsschrift, Institut für Theoretische Teilchenphysik, Universität Karlsruhe, D-76128 Karlsruhe, Germany, October 1997. TTP97-39.

[MRS94] A. D. Martin, R. G. Roberts, and W. J. Stirling. Parton distributions of the proton. *Phys. Rev.*, D50:6734, 1994. hep-ph/9406315.

[Mus97] B. Musgrave. ZEUS internal presentation, October 1997. private comunications.

[MW84] G. Marchesini and B. R. Webber. Simulation of QCD jets including soft gluon interference. *Nucl. Phys.*, B238:1, 1984. CERN-TH-3525.

[MWZ97] E. Mirkes, S. Willfahrt, and D. Zeppenfeld. Jet productions in DIS at NLO including Z and W exchange. *hep-ph/9711366*, August 1997. TTP 97-47, Talk given by E. Mirkes at the International Europhysics Conference on High Energy Physics (HEP 97), Jerusalem, Israel, 19-26 Aug 1997.

[MZ96a] E. Mirkes and D. Zeppenfeld. Dijet production at HERA in next-to-leading order. *Phys. Lett.*, B380:105, 1996. hep-ph/9511448, TTP 95-42, MADPH-95-916.

[MZ96b] E. Mirkes and D. Zeppenfeld. Jet production in deep inelastic scattering at HERA. *Acta Phys. Pol.*, B27:1393, April 1996. hep-ph/9604281, TTP 96-10, MADPH-96-935, Invited talk given at the Cracow Epiphany Conference on Proton Structue, Krakow, January 5-6. 1996; presented by E. Mirkes.

[MZ96c] E. Mirkes and D. Zeppenfeld. NLO corrections to jet cross sections in DIS. *hep-ph/9608201*, April 1996. TTP 96-30, MADPH-96-955, Talk presented by E. Mirkes at the 'International Workshop on Deep Inelastic Scattering and Related Phenomena' (DIS 96), April 1996, Rome.

[MZ96d] E. Mirkes and D. Zeppenfeld. QCD corrections to jet cross sections in DIS. *hep-ph/9606332*, June 1996. TTP 96-24, MADPH-96-946, Invited talk presented by E. Mirkes. To appear in the proceedings of 'QCD and QED in Higher Orders' 1996 Zeuthen Workshop on Elementary Particle Theory, April 22-26, 1996.

[MZ97a] E. Mirkes and D. Zeppenfeld. E_T production in DIS at NLO. In José Repond and Danny Krakauer, editors, *Deep Inelastic Scattering and QCD - 5th international workshop - Chicago, IL April 1997*, number 407 in AIP conference proceedings, page 175. American Institute of Physics, Woodbury, New York, 1997. MADPH-97-1002, hep-ph/9706437.

[MZ97b]   E. Mirkes[a] and D. Zeppenfeld[b]. *MEPJET 2.0 — A next-to-leading order event generator for ep → n jets.* [a]Inst. für Theor. Teilchenphysik, Univ. Karlsruhe, D-76128 Karlsruhe, Germany; [b]Physics Department, University of Wisconsin, Madison WI 53706, USA, 1997. Information and code via anonymous ftp *ftp ttpax2.phusik.uni-karlsruhe.de; cd mirkes.*

[Nis94]   R. Nisius. *Measurement of the strong coupling constant α_s from jet rates in deep inelastic scattering.* Dissertation, Physikalische Institute RWTH Aachen, Sommerfeldstr., 52056 Aachen, Germany, June 1994. PITHA 94/21.

[OB98]   J. Okrasinski and J. Bromely, 1998. private comunications.

[PB93]   H. Plothow-Besch. *PDFLIB: A library of all available parton density functions of the nucleon, the pion and the photon and the corresponding α_s calculations. Comput. Phys. Commun.,* 75:396, 1993. CERN-PPE-92-123.

[PB96]   H. Plothow-Besch. *PDFLIB: Nucleon, Pion, Photon Parton Density Fubctions and α_s Calculations - Users's Manual - Version 7.06.* CERN, 1996. CERN-PPE-1996.11.14.

[PDG98]   PDG - Particle Data Group. Review of particle physics. *Phys. Rev. D,* 54(1), 1998.

[Per87]   D. H. Perkins. *Introduction to High Energy Physics.* The Advanced Book Program. Addison-Wesley Publishing Company, Inc., Menlo Park, California, 1987.

[Qua96]   A. Quadt. *Measurement and QCD Analysis of the Proton Structure Function F_2 from the 1994 HERA Data Using the ZEUS Detector.* Dissertation, University of Oxford, 1996. DESY-THESIS-1998-007, RAL-TH-97-004.

[Rep96]   J. Repond. Jet energy corrections, 1996. ZEUS Note 96-133.

[Rep98a]   J. Repond. Calculation of errors on correction factors, 1998. ZEUS Note 98-015.

[Rep98b]   J. Repond. How to determine correction factors, 1998. ZEUS Note 98-019.

[S⁺89]   W. H. Smith et al. The ZEUS trigger system. Technical report, DESY, 1989. DESY 92-150-B.

[S⁺95]   G. Sterman et al. Handbook of perturbative QCD. *Rev. Mod. Phys.,* 67(1):157, January 1995.

[Sch96]   M. Schmelling. Status of the strong coupling constant. *ICHEP,* page 91, 96. MPI-H-V39-1996, hep-ex/9701002.

[Sey95]   M. H. Seymour. Jets in QCD. *hep-ph/9506421,* June 1995. CERN-TH/95-176, Talk given at the 10th Topical Workshop on Proton-Antiproton Collider Physics, Batavia, IL, May 9-13, 1995.

[Sey96]   M. H. Seymour. The subjet multiplicity in quark and gluon jets. *Phys. Lett.,* B378:279, 1996. CERN-TH-95-225, hep-ph/9603281.

[Sey97a]   M. H. Seymour. *DISENT 0.1.* Rutherford Appleton Laboratory, UK, October 1997. Information and code via WWW *http://hepwww.rl.ac.uk/theory/seymour/nlo/.*

[Sey97b]   M. H. Seymour. Jet phenomenology. *hep-ph/9707349,* 1997. contributed to Proceedings of Les Rencontres de la Valée d'Aoste: Results and Persectives in Particle Physics, La Thuile, Italy, March 2-8, 1997.

[Sey97c]   M. H. Seymour. Jet shapes in hadron collisions: Higher orders, resummation and hadronization. *hep-ph/9707338,* July 1997. RAL-97-026.

[Sey97d]   M. H. Seymour. *KTCLUS revised version from October 1997.* Rutherford Appleton Laboratory, UK, October 1997. Information and code via WWW *http://hepwww.rl.ac.uk/theory/seymour/ktclus/.*

[Sjö93]   T. Sjöstrand. *PYTHIA 5.7 and JETSET 7.4, Physics and Manual.* CERN, CH-1211 Geneva 23, Switzerland, December 1993. CERN-TH.7112/93, LU TP 95-20.

[SS91]   G. A. Schuler and H. Spiesberger. DJANGO: The interface for the event generators HERACLES and LEPTO. In W. Buchmüller and G. Ingelman, editors, *Proceedings of the Workshop 'Physics at HERA',* volume 3, page 1419, Notkestraße 85, D-22607 Hamburg, Germany, October 1991. DESY.

[Sti97]   W. J. Stirling. α_s : from DIS to LEP. *hep-ph/9709429,* 1997. DTP-97-80.

[Str91]   J. Straver. *Design, Construction and Beam Tests of the High Resolution Uranium Scintillator Calorimeter for ZEUS.* Dissertation, Universiteit van Amsterdam, March 1991.

[Sur98]   B. Surrow. *Measurement of the Proton Structure Function F_2 at low Q^2 and Very Low x with the ZEUS Beam pipe Calorimeter at HERA.* Dissertation, Universität Hamburg, Notkestr. 85, 22607 Hamburg, Germany, January 1998. DESY-THESIS-1998-004.

[Tas97]   E. Tassi. An ODBMS based event store for ZEUS, April 1997. Talk given at Computing in High-energy Physics (CHEP 97), Berlin, Germany.

[Tas98]   E. Tassi, July 1998. private comunications.

[Tob98]   N. Tobien. Determination of α_s from (2+1) jet event rates with the H1 detector at HERA. DIS 98, April 5th 1998, 1998.

[Tre96]   T. M. Trefzger. *Messung der Kopplungskonstanten α_s der starken Wechselwirkung aus Jetraten in der tiefinelastischen ep-Streuung bei HERA.* Inauguraldissertation, Albert-Ludwigs-Universität Freiburg i. Br., Hermann-Herder-Str. 3, 79104 Freiburg, Germany, March 1996. DESY F35D-96-08.

[Uij92]   H. A. J. R. Uijterwaal. *The Global Second Level Trigger.* Dissertation, Universiteit van Amsterdam, 1992.

[Web84]   B.R. Webber. A QCD model for jet fragmentation including soft gluon interference. *Nucl. Phys.,* B238:492, 1984. CERN-TH-3713.

[Wol93] G. Wolf. HERA physics. In *Proceedings of the Scottish Summer School 1993*, page 135, St. Andrews, Scotland, August 1993. Lectures given at 42nd Scottish Universities Summer School in Physics (SUSSP 93): High Energy Phenomenology (NATO Advanced Study Institute), QCD161:S37: 1993, DESY-94-022, Feb 1994.

[You92] C. Youngman. The ZEUS data acquisition system. Technical report, DESY, October 1992. DESY-92-150A.

[ZEU93a] ZEUS-Collaboration. Measurement of the proton structure function F_2 in ep scattering at HERA. *Phys. Lett.*, B316:412, 1993. DESY-93-110.

[ZEU93b] ZEUS Collaboration. The ZEUS detector, status report 1993 - The Blue Book. Technical report, DESY, February 1993.

[ZEU95a] ZEUS-Collaboration. Measurement of α_s from jet rates in deep inelastic scattering at HERA. *Phys. Lett.*, B363:201, 1995.

[ZEU95b] ZEUS-Collaboration. Measurement of the diffractive structure function in deep inelastic scattering at HERA. *Z. Phys.*, C68:569, 1995. DESY-95-093.

[ZEU97] ZEUS-Collaboration. Observation of scaling violations in scaled momentum distributions at HERA. *Phys. Lett.*, B414:428, 1997. DESY-97-183, hep-ex/9710011.

[ZEU98] ZEUS-Collaboration. Measurement of event shapes in deep inelastic scattering at HERA. Abstract 808 for ICHEP98, XXIX International Conference on High Energy Physics, Vancouver, 23-29 July 1998, 1998.

Acknowledgments

I would like to express my gratitude to all the colleagues I worked with on various hardware, software or physics projects for their great cooperation, especially there should be mentioned Adolf Bornheim, Henk Boterenbrood, Dr. Jane Bromley, Dr. Guy Cases, Douglas Chapin, Joanne Cole, Cathy Farrow, Dr. Peter Göttlicher, Wladimir Hain, Dr. Herrmann Hessling, Dr. Andres Kruse, Marc St. Laurent, Dr. Jitning Lim, Mohsen Khakzad, Dr. Ulrich Kötz, Dr. Steve Magill, Dr. Mario Martinez, Jan Okrasinski, Dr. Nikolai Pavel, Dr. Juan Puga, Patrick Saull, Dr. Tara Shah, David Simmons, Dr. Laurel Sinclair, Dr. Bernd Surrow, Dr. Esther Strickland, Dr. Song Ming Wang and Dr. Rik Yoshida and from the technical staff Hans-Helmut Sabbat and Klaus Westphal as well as our ZEUS secretaries Birgit Bahr and Irmgard Harm who do a dedicated, diligent job.

Special thanks go to Dr. B. Musgrave and Dr. S. Wölfle for reading the whole thesis draft and giving so many valuable comments.

And very special thanks go to my wife Petra for her trust, her encouragement and patience with me and my „sweetheart" DESY.

Last, but not least, I would like to thank the German tax payer who financed this basic research project which does not lead to short-term economical profit but is knowledge oriented, even though we are living in economically difficult times.

THANK YOU ALL!!

Ich versichere ausdrücklich, daß ich die vorliegende Arbeit selbst angefertigt und dabei nur die darin erwähnten Unterstützungen und Hilfsmittel benutzt habe. Es ist mir bekannt, daß meine Promotion für ungültig erklärt wird, falls meine Angaben nicht der Wahrheit entspechen.

Ich habe mich bisher an keiner deutschen oder außerdeutschen Hochschule um Promotion beworben.

Stephan Eisenhardt